

Design and Analysis of a Practical Large-Force Piezoelectric Inchworm Motor with a Novel Force Duplicator

E. F. Williams

94236641

M.Eng Dissertation

Submitted to

University of Pretoria

Department of Mechanical and
Aeronautical Engineering

February 2014

Abstract

The work presented in this dissertation on piezoelectric inchworm motors (IWM) is part of a process to gain an understanding of the design, analysis and testing of this smart actuator technology. This work will form the foundation of what will hopefully lead to the realisation of a production-ready IWM design to be used in energy-scarce, battery-operated Unmanned Aerial Vehicles (UAVs), and forms part of a larger national drive to expand the UAV industry in South Africa. Although the principles used in the design of IWMs are well known, a new innovation is employed. A novel way to increase the force capacity of IWMs without compromising on the speed or displacement when compared to conventional methods is shown to be effective, and was used for the first time on IWMs. The use of a simple design equation is demonstrated to be useful in predicting the load limits and step displacements. Challenges of finding a correlation between predicted and measured performance values are discussed and solutions are presented. The history of IWMs and some background on piezoelectricity are given for the reader not familiar with these. The use of micro ridges on the clamp mechanisms is explored. The effects of the control signals on the mechanism of the motor are discussed in detail and some important comments on electrical controllers are made. The emphasis is on designing a strong motor that capitalises on the high-force density of piezoelectric material.

Acknowledgements

Special thanks are due to my dissertation advisors Dr Philip Loveday and Prof. Nico Theron for their guidance, encouragement, support and patience.

I would also like to thank Icron Engineering services and AGV Engineering for the mechanical manufacturing. Also thanks to the CSIR Laser Centre and the CSIR's Mechatronics and Micro Manufacturing (MMM) department for their assistance with the manufacturing and measuring of the micro ridges.

Also thanks to Mark de Villiers from CSIR MMM for the use of his controller design.

Special thanks to all those who assisted with the proofreading and editing.

Contents

Abstract.....	i
Acknowledgements.....	i
List of Figures.....	v
List of Tables.....	xi
1 Introduction	1
1.1 Motivation.....	1
1.2 Objective	3
1.3 Scope.....	3
2 Literature review	5
2.1 About piezoelectricity	5
2.2 About IWMs	11
2.3 Some history of IWMs.....	13
2.4 Electrical control of piezoelectric IWMs	24
3 Two novel IWM designs.....	34
3.1 Overview	34
3.2 The conventional IWM design	34
3.3 An IWM with force duplicator mechanism.....	35
4 Analysis of piezoelectric actuators	40
4.1 Finite Element Analysis (FEA).....	40
4.2 Principles of analysing a Piezo-electric element.....	40
4.3 Analysis of the conventional IWM flextensional extender	44
4.4 Analysis of the IWM design with force duplicator mechanism	48

5	Testing the IWM extenders used for the IWM extenders	51
5.1	Testing of the flextensional actuator	51
5.1.1	Investigation into the effect on stiffness due the thickness differences of the flexures 54	
5.1.2	Investigation into the effect of the flextensional arms being at different angles	55
5.1.3	Investigation into the effect of the attachment ends of the actuator not being aligned 56	
5.2	Testing an improved flextensional actuator	58
5.3	Testing of the beam actuator used in the IWM design with force duplicator mechanism ..	61
6	Designing the IWMs.....	65
6.1	Load limit of an IWM.....	66
6.2	Calculating the load limits of the IWM designs	72
6.3	Signal events and their effect on the speed of an IWM	72
6.4	The use of micro ridges on the clamp mechanisms.....	75
6.4.1	Laser ablation.....	76
6.4.2	Micro machining – milling.....	78
6.4.3	Discussion and conclusion on micro ridges	79
7	Testing the IWMs	81
7.1	Velocity measurements during event time changes	81
7.2	Load testing of the conventional IWM	81
7.3	Load testing of an IWM with force duplicator mechanism	86
8	Conclusions and observations	89
9	References	92
10	Appendices.....	96
A.	Behaviour of a piezoelectric element	96

B. Matlab programs.....	106
C. State space representation of a Single Degree of Freedom (SDOF) piezoelectric system.....	115
D. Spring acting through a ratio.....	118
E. Material and load properties	119
F. Piezoelectric load input in Nastran	123
G. Detail design of the flextensional actuator	125
H. Detail design of the beam actuator with force duplicator mechanism	134
I. Measurement equipment	142
J. Manufacturing drawings for the conventional IWM.....	143
K. Manufacturing drawings for the IWM with force duplicator.....	151
L. UAV outline.....	159

List of Figures

Figure 1: Speed and force characteristics of piezo motors (Spanner & Koc, 2010).....	1
Figure 2: Lattice structure of PZT (1) above Curie temperature, (2) below Curie temperature (Smith C, 2005)	6
Figure 3: Electric dipoles in domains. (1) unpoled ferroelectric, (2) during and (3) after poling (Physikinstrumente, n.d.).....	6
Figure 4: Stress directions definition	7
Figure 5: Typical deformation of a piezoelectric material (Piezomechanik, 2011)	8
Figure 6: Electrical design of a stack actuator (“Physikinstrumente,” 2011).....	9
Figure 7: Relationship between force and displacement of piezoelectric material (Piezomechanik, 2011)	10
Figure 8: Inchworm motion (Vaughan, 2001).....	12
Figure 9: The three different IWM groups.....	13
Figure 10: Incremental feed mechanism patented by Stibitz (Stibitz, 1964)	14
Figure 11: Linear actuator patented by Lochner (Locher, 1967)	14
Figure 12: <i>Walker</i> motor patented by Brisbane (Brisbane, 1968).....	15
Figure 13: Burleigh Instruments Inc. Inchworm Actuator (Bizzigotti, 1975)	15
Figure 14: Electromotive actuator (Lafayette & Foster, 1980)	16
Figure 15: Inchworm motor using stacked piezoelectric actuators (Hara et al., 1986).....	16
Figure 16: Inchworm motor with flexure-hinged mechanisms 1988 (Fujimoto, 1988).....	17
Figure 17: Concept for a rotational inchworm motor (Van Nuys, 1990)	17
Figure 18: Inchworm motor with linear gear rack (Yokohama, 1990).....	18
Figure 19: Inchworm motor with monolithic frame (Zhang, 1994)	18
Figure 20: Hydro inchworm motor with both piezoelectric and magnetostrictive materials (Miesner & Teter, 1994)	19
Figure 21: Micro-scaled inchworm motor (Lee & Esashi, 1995)	20

Figure 22: Caterpillar motor (1996) (Pandell & Garcia, 1996)	20
Figure 23: Actuator device containing microscale components (1999) (Chen et al., 1999)	21
Figure 24: Inchworm motor with a specific power of 99 W/kg (2000) (Park et al., 2000)	21
Figure 25: A MEMS inchworm actuator (2002-2003) (Yang et al., n.d.)	22
Figure 26: Inchworm motor with reduction lever mechanism (2004) (Kwon, Cho, & Jang, 2004)	22
Figure 27: Inchworm motor for high loads (2004) (Liess et al., 2004)	23
Figure 28: High-power inchworm motor (2005) (Powers et al., 2004)	23
Figure 29: Piezoelectric actuator using a feed screw (2007) (Loverich et al., 2007)	24
Figure 30: Typical signals required for each of the three actuators making up an IWM	25
Figure 31: Typical hysteresis response of a piezo ceramic actuator (Piezomechanik, 2011)	26
Figure 32: Typical linear stroke response of a piezo stack under electrical charge control (Piezomechanik, 2011)	26
Figure 33: Electrical representation of a linear amplifier (Newton & Main, 1996)	28
Figure 34: Switching amplifier (Newton & Main, 1996)	28
Figure 35: Current controlled switching amplifier (Chandrasekaran & Lindner, 2001)	29
Figure 36: Comparison of input power of different amplifiers (Lindner, Zhu, Vujic, et al., 2002)	29
Figure 37: Circuit topology (Lindner, Zhu, Song, et al., 2002)	30
Figure 38: Square clamp waveforms and sine extender waveform (Frank et al., 1999)	31
Figure 39: CSIR's switch-mode power supply (Williams et al., 2010)	32
Figure 40: Measured and simulated voltage vs. time (Williams et al., 2010)	32
Figure 41: CSIR's switch-mode power supply connected to an IWM	33
Figure 42: Side view of piezoelectric inchworm motor (PIM)	35
Figure 43: Isometric view of inchworm motor	35
Figure 44: Schematic of the basic operations of the IWM with force duplicator	37

Figure 45: New IWM design showing the lever mechanism connecting both sides of the extender to the load 37

Figure 46: Diagram showing the action of the lever mechanism (two events) 38

Figure 47: Finite element analysis showing the exaggerated action of the extender and lever mechanism (Blue is zero displacement, red is most displacement)..... 38

Figure 48: Photo of the IWM lever mechanism 39

Figure 49: Mathematical model of a piezoelectric element acting against a mechanical stiffness load 41

Figure 50: Theoretical limit of a piezo actuator 42

Figure 51: The flextensional actuator used in the conventional IWM design 45

Figure 52: The manufactured flextensional actuator 45

Figure 53: The beam actuator with the beam mechanism used in the IWM with force duplicator 48

Figure 54: Free displacement measurement set-up..... 51

Figure 55: Flextensional actuator in Instron Servohydraulic mechanical testing machine during stiffness testing 52

Figure 56: Free displacement laser measurement within the motor 53

Figure 57: Measured stiffness data and regression line of the flextensional actuator 53

Figure 58: Flexure thickness..... 54

Figure 59: Initial (green) and adjusted geometry (brown) used in the analyses..... 55

Figure 60: Displacement due to a unit force applied to the adjusted geometry 56

Figure 61: Designed (green) and traced geometry (magenta) of the flextensional actuator..... 57

Figure 62: Deformation of traced geometry..... 57

Figure 63: Comparison between the designed geometry (green) and the new geometry (brown) after manufacturing improvements 58

Figure 64: Location of gaps 59

Figure 65: Stiffness measurement of the second flextensional actuator 60

Figure 66: Free displacement testing of the extender..... 61

Figure 67: Measured input signal and displacement output in volts	62
Figure 68: Stiffness testing of extender	63
Figure 69: Extender stiffness results: measured and calculated	63
Figure 70: Photo of the conventional IWM	65
Figure 71: Conventional IWM design showing the two load paths	66
Figure 72: New inchworm design showing the two load paths.....	67
Figure 73: Stepping of an IWM with, and without loading.....	68
Figure 74: Displacement of load attachment point at a load less than the load limit of the motor	70
Figure 75: Displacement of load attachment point at stall	70
Figure 76: Actuating events indicating the shortest event time for a given step-change time	74
Figure 77: Effect of the Matlab filtering function on a square input signal.....	75
Figure 78: Micro ridges (Park et al., 2000).....	76
Figure 79: Micro ridge samples (dimensions in millimetres).....	77
Figure 80: 3D scan of laser ablation in steel	77
Figure 81: Measurement of laser ablation in steel.....	78
Figure 82: Laser ablation in aluminium.....	78
Figure 83: Milled micro teeth	79
Figure 84: Milled micro teeth measurement.....	79
Figure 85: The conventional IWM during load testing	82
Figure 86: Measurement positions	82
Figure 87: Load side measurement.....	84
Figure 88: Load side displacement.....	84
Figure 89: Far side measurement	85
Figure 90: Far side displacement	85

Figure 91: Load testing set-up showing load cell attached to the IWM	86
Figure 92: Load testing set-up showing all the equipment	87
Figure 93: Extender behaviour at an intermittent load.....	88
Figure 94: Extender behaviour at stall load	88
Figure 95: Equivalent electrical circuit of a piezoelectric vibrator (Meeker, 1996).....	96
Figure 96: Testing of preloaded piezo element	98
Figure 97: Load measurements on a single piezo stack.....	99
Figure 98: Laser displacement measurement.....	100
Figure 99: Voltage and current measurement for a single piezo stack	101
Figure 100: Power calculation from measured voltage and current for a single piezo stack.....	101
Figure 101: Comparison between measured and simulated displacement	103
Figure 102: Comparison between measured and simulated current	103
Figure 103: Comparison between measured and simulated power	104
Figure 104: Hysteresis effect.....	104
Figure 105: Comparison voltage and current for measured and simulated results	105
Figure 106: Diagram for SDOF system	115
Figure 107: Spring acting through a ratio	118
Figure 108: Flextensional actuator from Cedrat Technologies (“Cedrat Technologies,” 2012)	125
Figure 109: Domain used in the topology optimisation	126
Figure 110: Result of the topology optimisation	127
Figure 111: Final design of the flextensional actuator	128
Figure 112: Free displacement.....	129
Figure 113: Free displacement stresses.....	129
Figure 114: Blocked stresses.....	130

Figure 115: Blocked force reaction	130
Figure 116: Force applied and constraints used for the stiffness calculation	131
Figure 117: Displacement due to unit load (stiffness analysis)	131
Figure 118: The element representing the piezo stacks is replaced with rigid elements	132
Figure 119: Displacement of the frame with rigid elements due to an applied unit force	132
Figure 120: First natural mode at 831 Hz	133
Figure 121: FEA model of extender	134
Figure 122: Constraints used in the analysis.....	135
Figure 123: Exaggerated Displacement at Blocked force	135
Figure 124: Free displacement.....	136
Figure 125: Stresses due to free displacement.....	136
Figure 126: Stresses due to blocked force conditions	137
Figure 127: Constraint and force applied for stiffness calculation	138
Figure 128: Displacement result due to unit force	138
Figure 129: Constraint and force applied for stiffness calculation of only the extender	139
Figure 130: Displacement result due to unit force of only the extender	139
Figure 131: Element representing the piezo stacks is replaced with rigid elements	140
Figure 132: Displacement of the frame with rigid elements due to an applied unit force	140
Figure 133: First modal shape at 335 Hz.....	141

List of Tables

Table 1: Different loading conditions applied to a piezo stack.....	43
Table 2: Summary of FEA results for the flextensional actuator	46
Table 3: Summary of FEA results for the beam actuator with force duplicator mechanism	48
Table 4: Summary of FEA results for the second flextensional actuator	59
Table 5: Extender stiffness summary	64
Table 6: Explanation of simplified diagrams representing the two IWM designs.	69
Table 7: Comparison between the working principles of the two IWM designs.....	71
Table 8: Different times used during velocity testing.....	81
Table 9: Load and displacement results of IWM load measurements	85
Table 10: Properties for PSt 150/5x5/20	119
Table 11: Table of available piezoelectric stacks (Piezomechanik, 2008).....	119
Table 12: Properties for PZT-4	120
Table 13: Values used for the piezoelectric stacks' material properties	121
Table 14: Patran input form for the piezoelectric stacks' material properties	121
Table 15: Patran input form for the stainless steel properties.....	122
Table 16: Summary of FEA results for the flextensional actuator	128
Table 17: Summary of FEA results for the beam actuator with force duplicator mechanism	141
Table 18: Testing equipment	142

1 Introduction

1.1 Motivation

The research field of actuators is growing worldwide. In particular, the use of small actuators has increased significantly in recent times. Small actuators are broadly defined as actuators with an output of below 1 kW. This growth can be attributed to increasing mechanisation and automation, a general growth in consumer goods, and a steady need for increased accuracy and precision in machine technologies (Stölting & Kallenbach, 2008).

As such, two categories of actuators can be distinguished: those working with fields and those changing their shapes (Ouyang, Tjiptoprodo, Zhang, & Yang, 2007). The first category uses forces created by fields such as electrostatic, magnetostatic and electro-dynamic. Conventional motors, such as direct current (DC) motors, alternating current (AC) motors, and stepper motors fall into this category. The second category of actuators primarily generates a strain in the material, which can be converted into a force. Piezoelectric actuators, shape memory alloy (SMA) actuators, magnetostrictive actuators, thermal actuators, and hydraulic and pneumatic actuators fall into this category.

With the focus on piezoelectric technology, this second category of actuators may be further classified into three categories according to the functional principals employed. The categories are: 1) Inchworm motors and piezo walk-drives where various piezo actuators are used for clamping and shifting alternatively to produce a movement. 2) Stick-slip-drives, where a movement is generated by speed-dependent friction factors. 3) Ultrasonic motors, where vibration at ultrasonic frequency range on an oscillating element is transferred to moving element through frictional coupling (Spanner & Koc, 2010). The difference of these in terms of speed and force is graphically shown in Figure 1.

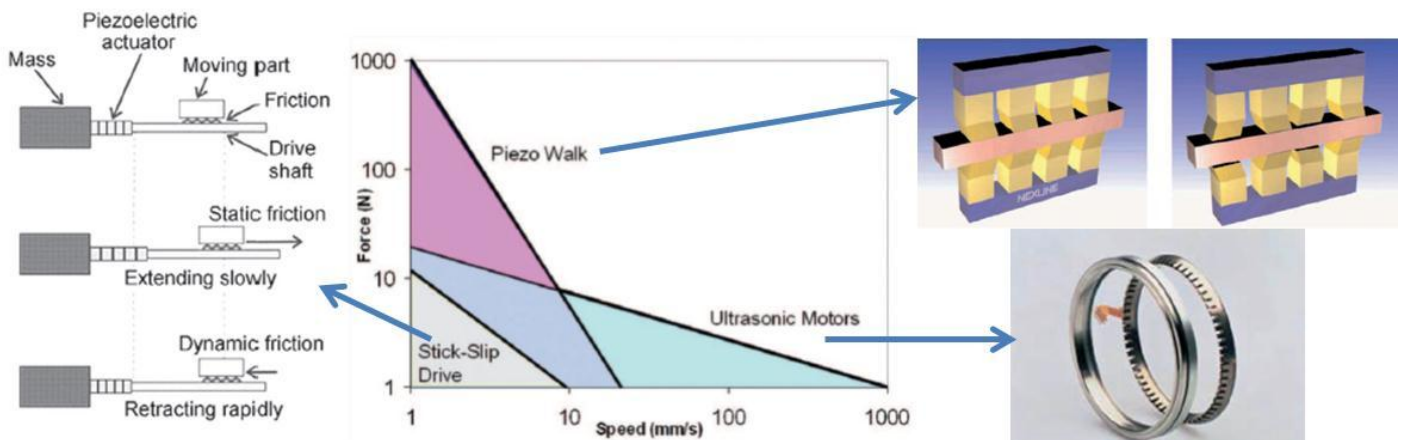


Figure 1: Speed and force characteristics of piezo motors (Spanner & Koc, 2010)

In general, piezo actuators offer some unique advantages:

- Sub-micrometre resolution
- Large force generation (high force density)
- Sub-millisecond response
- No magnetic fields
- Extremely low steady state power consumption
- No wear and tear
- Vacuum and clean room compatibility
- Holding function without significant power consumption.

However, there are also some disadvantages:

- Highly nonlinear input/output behaviour
- Creep
- Hysteresis
- Very small motion range
- Relatively complex electronic controllers are required.

In the field of piezoelectric motors, many designs with various operating principles have been invented and many patents have been, and still are, being registered. However, the number of commercially successful inventions is limited. This indicates that the operating principles described in those inventions were not sufficiently developed to make commercially viable motors. “The commercial success of a piezoelectric motor is hidden in the details” (Spanner & Koc, 2010).

Actuation is used in many vehicles (aircraft, spacecraft, ground vehicles, etc.) to control the position and/or attitude of the vehicle, and also to deploy or retract equipment. In spacecraft, space robots and unmanned aerial vehicles, small actuators are greatly in demand, because on the one hand they allow the structures to become smarter or adaptronic, and on the other hand, more actuators add mass and the risk of equipment failure. These contradictory properties encourage research in both conventional electromagnetic actuators and smart material actuators. Both groups of actuator technologies are making progress in their development, and each has different advantages and limitations (Claeyssen et al., 2010).

Their large-force generation and force-holding capability makes piezoelectric inchworm motors (IWM) of particular interest for Unmanned Aerial Vehicle (UAV) applications, specifically for actuating a morphing wing on a long-endurance, battery-operated UAV.

The use of morphing wings has a history as long as that of manned powered flight. In 1903 the Wright Flyer, the first practical aircraft to fly, maintained lateral control by twisting the wings in opposite directions to each other. An increase in aircraft performance, and the consequent need to increase structural stiffness, meant that the use of wing twisting soon became impractical. In 1910 Henri Farman introduced the use of the aileron and in 1919 the first flaps were introduced. Subsequently all aircraft have made use of these, or modifications of these basic devices to change the aerodynamic profile of the wing. A major disadvantage of this design concept is that fixed geometry wings are optimised for a single design point based on altitude, Mach number and aircraft weight. During a typical mission these parameters will vary continuously, meaning that the wing is rarely performing at its optimal point. Wing design represents a compromise between design point and off-design point performance, with better performance at the design point resulting in worse performance at the off-design points. This problem can be overcome by varying the camber of the wing during flight so that a near optimal geometry can be maintained for all flight conditions. The use of variable cambering would lead to significant improvements in aircraft aerodynamic and structural efficiency (Coetzer & Harris, 2010).

The typical aerodynamic force experienced by a wing requires a relatively strong actuator to morph a wing against such forces. Strong actuators come with a weight penalty which is, of course, undesirable in an aircraft. Another challenge is that the wing needs to be held in its morphed condition for a long time, which in the case of electromagnetic actuators would require a large and heavy power source or complicated design if a constant supply of current to the actuator is to be avoided. In a battery-operated UAV, such as the one developed by CSIR Meraka Institute and CSIR Defence, Peace, Safety and Security, the limitations of batteries, coupled with conventional power-hungry electromagnetic actuators, make the use of a morphing wing difficult (see Appendix L). A piezoelectric IWM

that is both strong, relatively light, and has the ability to hold a large force without consuming significant power, would make the use of morphing wings in energy-scarce UAVs much more feasible.

Before the advantages of using a piezoelectric IWM can be illustrated, a practical understanding of the design and workings of such devices is needed. As part of the work by CSIR Materials Science and Manufacturing on smart materials, this research into IWMs was undertaken to gain competence in their design and operation. If an IWM can be produced that meets the specifications as mentioned, it will open the door to the development of a morphing wing for UAVs, thus supporting the CSIR's and national South African strategic initiatives of establishing a broader UAV industry (Department of Science and Technology - Republic of South-Africa, 2010).

1.2 Objective

The objective of this dissertation is to lay the foundation for building a local competency across the cycle of innovation of piezoelectric IWMs. The work concentrates on developing a high-force linear motor with precision positioning potential and power-off force-holding capability. The focus is on gaining a proper understanding of all that is involved in the analysis, manufacturing and testing of this unconventional type of motor. This dissertation concentrates on how the mechanics of an IWM operate and respond when supplied with practical signals, and less on how to generate ideal signals. Since the application in mind requires high force, it was important to try to find a correlation between predicted force calculations and measurements for a design that operates at a practical speed. This study serves to identify which parameters are important in producing and operating an IWM and which parameters affect the force capability, and identifies the challenges that need to be overcome to realise a production-ready and easily manufacturable IWM.

The objectives can be summarised as follows:

1. Analyse the IWM designs to predict the force capability.
2. Measure the IWM's performance to confirm the analysis results.
3. Apply the analysis and measurements techniques to two IWM designs.

1.3 Scope

As one first needs to have a proper understanding of the underlying principles, the designs presented here are concept demonstrators, which were designed to allow the testing and evaluation of the basic operation of an IWM. Many of the principles treated apply to IWMs in general, but the focus is primarily on relatively large *piezoelectric* IWMs. The force capability of the design, the force calculation and the experimental verification thereof are given preference. Of less importance are the speed, precision, power consumption and durability as far as this study is concerned.

Two IWM designs are analysed, experimentally verified and critically discussed in detail. Both are novel designs. The one design is based on a conventional IWM design, but the second is an inventive new embodiment that will double the force capability and improve the precision capability, without compromising on the speed of an IWM when compared with the conventional design.

An introduction to piezoelectricity is also given, the history of IWMs is discussed and questions of particular interest to the author are investigated, such as the use of micro ridges and the effects of intentional and unintentional filtering of

the control signals. Some background information on control strategies and some details on driving piezoelectric elements are also provided.

Although the working of an IWM is relatively simple, seemingly insignificant details have a substantial effect on its operation. The presence of any compliance in the load paths will reduce the force capability of an IWM. The force capability is to a large extent dependent on the stiffness of the extender. To predict the force capability of the IWM, it is necessary to accurately analyse the stiffness of the extender. Initially, poor correlation between the measured and calculated results was obtained. Therefore a lot of emphasis is placed on identifying the cause of these discrepancies and how to avoid them during the analytical phase of such designs.

Only some attempts are made to optimise the structure for weight and stiffness, and the designs are intended to be overly stiff. Topology optimisation techniques were employed in the design of the flextensional actuator that is used as an extender in the one design, but it is by no means an optimised design.

The power consumption is to a large extent dependent on the topology and strategy employed in the control electronics and amplifier(s). Some research and experimentation were done to understand the response to variables concerning the control signals, but no conclusion has been reached into the best control strategy.

The repetitive motion of the clamp in the IWM requires materials that are wear resistant if longevity is required. The work presented does not address the selection of wear-resistant material.

The work presented is divided into ten chapters. The first chapter outlines the motivation, objective and scope of the work. Chapter two gives an introduction into piezoelectricity and provides a description on IWM in general, followed by some history about this technology. This chapter ends with a section on the control signals required to drive and power an IWM. At this point the reader would need an overview on the actual IWM designs being discussed further in the dissertation, which is provided in chapter three. The main theme of the dissertation is about the analysis methodology used in calculating the performance of an IWM, in particular calculating the load stall limit. This is discussed in chapter four and applied to the extender mechanisms of the motors which were introduced in chapter three. In chapter five the extender mechanisms is tested and compared to the theoretical values calculated in the previous chapter. Practical challenges that arouse during testing are presented in some detail since it provides insight in the workings of piezo actuators and highlights potential pitfalls to be avoided by IWM designers. How the behaviour of the extender mechanism influence the operation of the IWM as a whole is discussed in chapter six. Signal events and their effect on the speed of an IWM and the use of micro ridges as a possible method to increase the force capability is also presented here. In chapter seven, the complete motors are tested. Conclusions and observations is given in chapter eight, followed by the references in chapter nine, and the appendices in chapter ten.

2 Literature review

2.1 About piezoelectricity

Piezoelectricity is the ability of some materials to generate an electrical potential when pressure is applied. The effect is reversible in that, when an electrical field is applied, a mechanical stress and/or strain is produced. This behaviour is exhibited in a few natural materials, although by a small amount, such as quartz, tourmaline, Rochelle salt, cane sugar, etc. Polycrystalline ferroelectric ceramic materials such as barium titanate and lead (plumbum) zirconate titanate (PZT) have been developed that have improved properties (“Physikinstrumente,” 2011). PZT is the most common piezoelectric material in use today.

The lattice structure of PZT is shown in Figure 2 in its paraelectric phase (above the Curie temperature), and in its ferroelectric phase (below the Curie temperature.) The Curie temperature is the temperature at which the phase change occurs, and ranges from 240 °C to 480 °C for PZT depending on the molar fraction. A plot of internal energy over the position of the Ti^{4+} ion shows minima that correspond to the equilibrium state of the Ti^{4+} ion. In its paraelectric state, only one equilibrium state exists in the centre of the structure, but in its ferroelectric state, two equilibrium conditions exist. If sufficient electrostatic or elastic energy is provided, the Ti^{4+} ion will move across the unstable centre position to the other stable position, i.e. a dipole switch occurs (Smith C, 2005).

Individual PZT crystallites are piezoelectric, i.e. the positive and negative electrical charges of the crystallites are separate, but symmetrically distributed. The term crystallites or crystal applies to a solid in which the atoms are arranged in a single pattern throughout the body. Small groups of atoms in a crystal that are similarly orientated and regularly aligned are known as Weiss domains, and can be regarded as bounded by a parallelepiped. The orientation of the Weiss domains is random so that the overall crystal is electrically neutral, and no piezoelectric behaviour is observable. By applying a strong electrical field at elevated temperature, permanent alignment of the domains are forced in the direction in which the field was applied. This is known as poling (“Physikinstrumente,” 2011; Smith C, 2005). After poling, the material will exhibit piezoelectric behaviour.

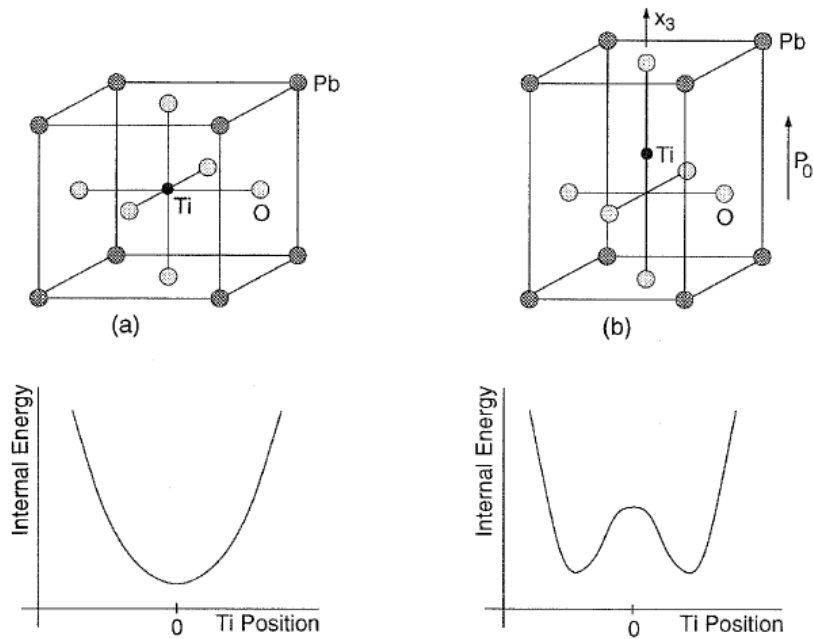


Figure 2: Lattice structure of PZT (1) above Curie temperature, (2) below Curie temperature (Smith C, 2005)

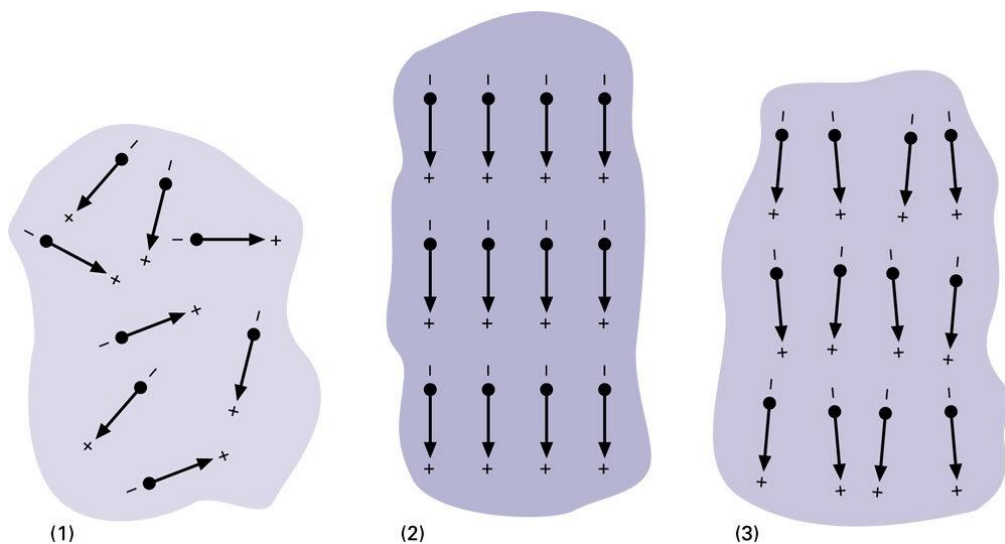


Figure 3: Electric dipoles in domains. (1) unpoled ferroelectric, (2) during and (3) after poling (Physikinstrumente, n.d.)

The linear theory of Piezoelectricity stems from the first law of thermodynamics that is derived from the conservation of energy principle, and results in the piezoelectric constitutive (matrix) equation:

$$\begin{aligned}
 T &= c^E \cdot S - e^t \cdot E \\
 D &= e \cdot S + \epsilon^S \cdot E
 \end{aligned}
 \tag{Equation 2-1}$$

where E is the electrical field strength, D is the electrical charge density, T is the stress, S is the strain, c is the elastic stiffness matrix (constant), e is a piezoelectric matrix (constant) and ϵ is the permittivity (Meeker, 1996). The superscript values indicate whether the matrix applies at a constant electrical field (E) or at a constant strain field (S). Superscript t is for the matrix transpose. Equation 2-1 can also be written in an alternative form in terms of strain:

$$S = s^E \cdot T + d^t \cdot E$$

Equation 2-2

$$D = d \cdot T + \varepsilon^T \cdot E$$

where s is the elastic compliance matrix, and d is another piezoelectric matrix. (There are four forms of these equations in total). The superscript (T) indicates that the permittivity was measured under free displacement conditions.

A poled ceramic such as PZT can be classified as a tetragonal crystal system and is transversely isotropic, i.e. at every point in the material there is one plane in which the mechanical properties are equal in all directions. These symmetrical material planes reduce the number of independent constants required to fully describe the material mathematically.

For the plane of transverse isotropy being defined as the 1-2 plane, the first part of Equation 2-2 can then be written as:

$$\begin{bmatrix} S_1 \\ S_2 \\ S_3 \\ S_4 \\ S_5 \\ S_6 \end{bmatrix} = \begin{bmatrix} s_{11}^E & s_{12}^E & s_{13}^E & 0 & 0 & 0 \\ s_{21}^E & s_{22}^E & s_{23}^E & 0 & 0 & 0 \\ s_{31}^E & s_{32}^E & s_{33}^E & 0 & 0 & 0 \\ 0 & 0 & 0 & s_{44}^E & 0 & 0 \\ 0 & 0 & 0 & 0 & s_{55}^E & 0 \\ 0 & 0 & 0 & 0 & 0 & s_{66}^E = 2(s_{11}^E - s_{12}^E) \end{bmatrix} \begin{bmatrix} T_1 \\ T_2 \\ T_3 \\ T_4 \\ T_5 \\ T_6 \end{bmatrix} + \begin{bmatrix} 0 & 0 & d_{31} \\ 0 & 0 & d_{32} \\ 0 & 0 & d_{33} \\ 0 & d_{24} & 0 \\ d_{15} & 0 & 0 \\ 0 & 0 & 0 \end{bmatrix} \begin{bmatrix} E_1 \\ E_2 \\ E_3 \end{bmatrix}$$

with $s_{23}^E = s_{13}^E$, $s_{21}^E = s_{12}^E$, $s_{31}^E = s_{13}^E$, $s_{32}^E = s_{13}^E$, $s_{22}^E = s_{11}^E$ and with $d_{32} = d_{31}$ and $d_{24} = d_{15}$

where the stress (T) (similar for strain (S) and electrical field (E)) directions are defined as shown below:

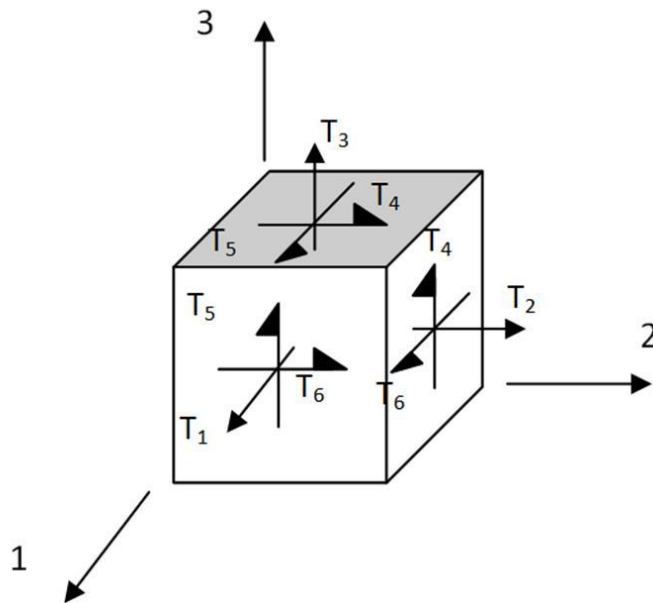


Figure 4: Stress directions definition

If, for instance, an electrical field is applied in the 3-direction ($E_1 = E_2 = 0$ and $E_3 \neq 0$) of a mechanically unconstrained ($T = 0$) piezoelectric material, a strain condition, and thus a dimensional change, will occur in the 1-, 2- and 3-directions, but no shear behaviour will occur.

If an electrical field is applied only in the 1-direction, only S_5 will be non-zero, and the material will be in a state of shear.

For a typical piezoelectric material like PZT, d_{33} , d_{15} and d_{24} will be positive and d_{32} and d_{31} will have negative values.

A typical piezoelectric material also has relatively low elastic compliance constants (s^E , which have units of length²/force). As a result, piezoelectric material has high stress values for a given strain condition, and as such can produce very high forces for its relatively small size.

Commonly used piezoelectric materials have a strain of up to 0.2%. Consider an example where an actuator consists of a single-layer piezoelectric ceramic disk, which has an electrical field applied in the 3-direction (Figure 5). The change in length for an unloaded single-layer piezo actuator can be estimated by:

$$\Delta L = S_3 \cdot L_0$$

$$\Delta L = \pm E_3 \cdot d_{33} \cdot L_0 = \pm V \cdot d_{33}$$

Equation 2-3

where ΔL is the change in length, L_0 is the original length and V is the applied voltage.

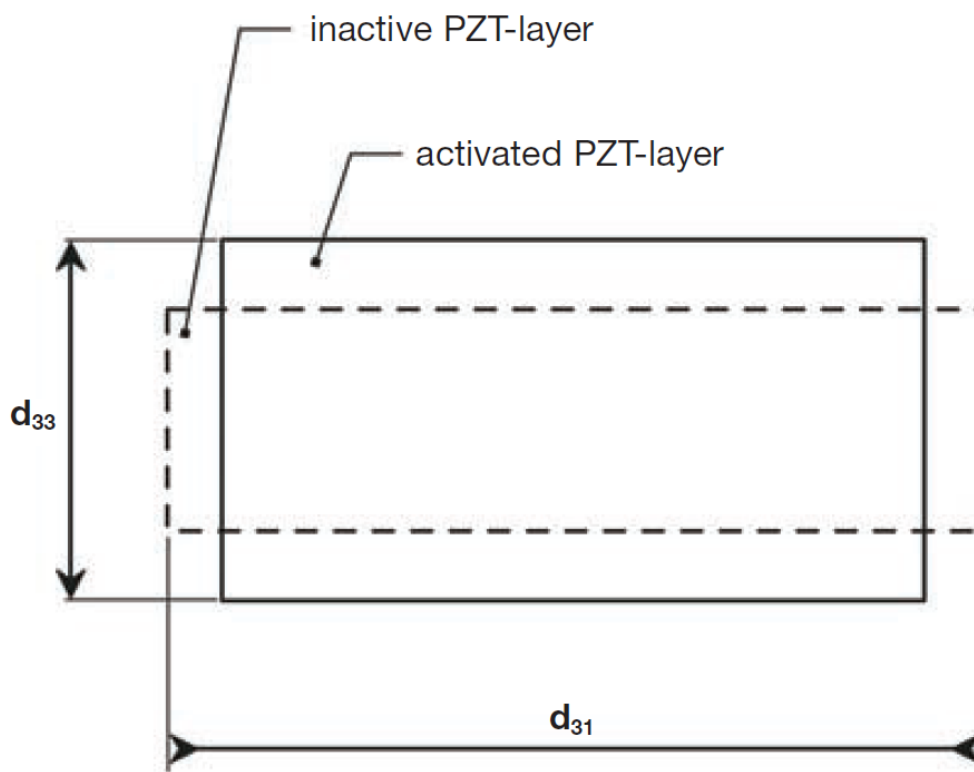


Figure 5: Typical deformation of a piezoelectric material (Piezomechanik, 2011)

The displacement is a function of the applied voltage. The maximum operating voltage is also proportional to the thickness of the disk. A too thin layer will cause electrical arcing between the end surfaces of the layer, therefore the

thinner the layer is, the lower the maximum voltage that may be used. The displacement of an actuator may be increased (for the same applied voltage) by using a number of stacked piezoelectric layers that are poled together (Figure 6).

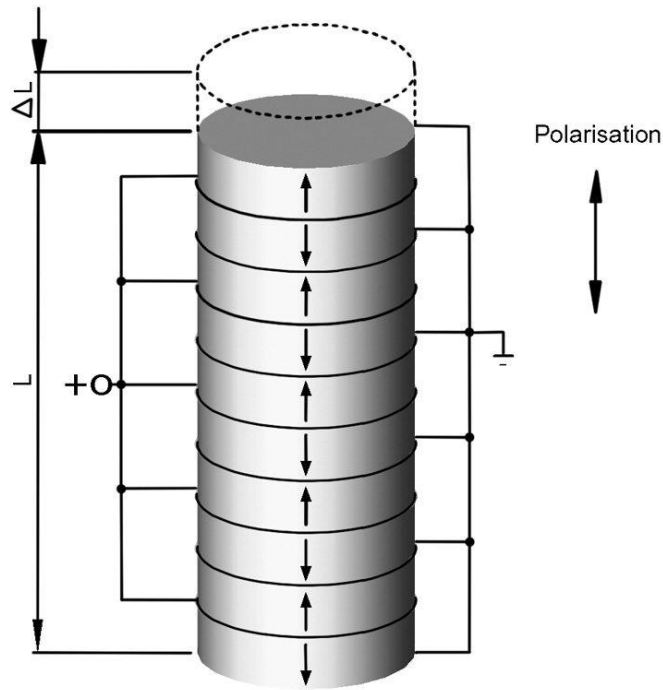


Figure 6: Electrical design of a stack actuator (“Physikinstrumente,” 2011)

The displacement now becomes from Equation 2-3:

$$\Delta L = \pm E_3 \cdot d_{33} \cdot L_0 \cdot N \quad \text{Equation 2-4}$$

where N is the number of layers

Stacked piezoelectric actuators have roughly the same displacement that a single-layer piezo actuator of the same length would have, but at a much lower applied voltage.

Despite the increase in displacement of stacked piezoelectric actuators, displacement values are still fairly small. A typical PZT stack actuator of dimensions 5 mm x 5 mm x 18 mm has a free displacement of only 27 μm , for an applied voltage ranging from -30 V to 150 V. For its small size, it can produce a blocked force of 1 600 N. The relationship between displacement and force produced is shown in Figure 7.

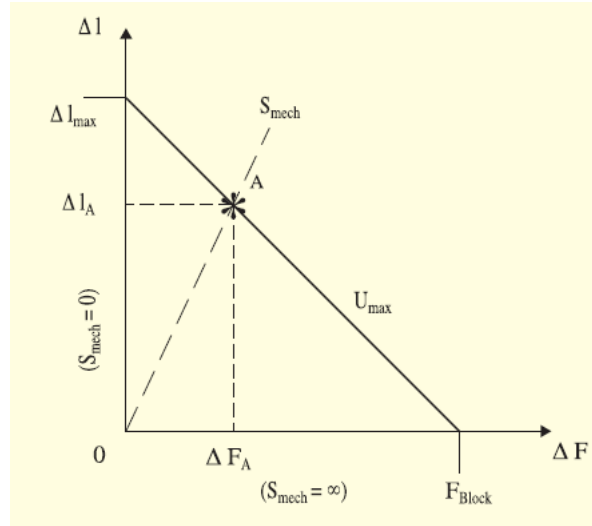


Figure 7: Relationship between force and displacement of piezoelectric material (Piezomechanik, 2011)

Due to their low mass and high force properties, piezoelectric materials also have very good dynamic properties. The piezoelectric stack in the previous example has a natural frequency of 50 kHz.

When using PZT stacks, it is sometimes useful to simplify Equation 2-2 so that it is only applicable to one dimension along the length of the stack (chosen to be the 3-direction), i.e. the stresses and the electrical field in the 1- and 2-directions are assumed to be zero, and the strains in the 1- and 2- directions are ignored. Equation 2-2 can thus be written as:

$$S_3 = s_{33}^E \cdot T_3 + d_{33} \cdot E_3 \quad \text{Equation 2-5}$$

If the PZT stack is further simplified to be of a homogeneous material, the strain can be written as $S_3 = \frac{\delta}{L}$ and $E_3 = \frac{V_{out}}{L}$, where δ is the displacement of the stack and L is the original length of the stack. V_{out} is the applied voltage. The stress in the stack is expressed in terms of force over area, $T_3 = \frac{F}{area}$. The equation can now be written in terms of displacement:

$$\delta = \frac{s_{33}^E \cdot L}{area} \cdot F + d_{33} \cdot V \quad \text{Equation 2-6}$$

By setting $a = \frac{s_{33}^E \cdot L}{area}$ and $b = d_{33}$, the simplified equation is now:

$$\delta = a \cdot F + b \cdot V \quad \text{Equation 2-7}$$

A practical means to determine the constant “ a ” when working with a PZT stack is to keep V constant (or zero, for instance by short-circuiting the stack), vary F , and measure δ . The slope of the line δ versus F would be equal to the constant a . “ a ” is thus the compliance of the stack. Similarly, b can be determined by keeping F constant (or zero, i.e. free displacement conditions), varying V , and again measuring δ . The slope of the line, δ versus V would be equal to the constant b .

When Equation 2-7 is written in terms of force (F) and internal stiffness (k_p), it becomes:

$$F = k_p \cdot \delta - k_p \cdot b \cdot V \quad \text{Equation 2-8}$$

The term $k_p \cdot b \cdot V$ is the piezoelectric induced force of the stack and is equal to the blocked force (F_b) (Heverly, Wang, & Smith, 2004) (Ardelean, 2004). Note that blocked force is defined for a certain applied voltage. The external force that the piezoelement exerts on an external load ($F_{ext} = -F$) is the blocked force minus the internal load required to displace the element against its own stiffness.

$$F_{ext} = F_b - k_p \cdot \delta \quad \text{Equation 2-9}$$

As an example, consider a piezoelectric stack with a free displacement of $\delta_f = 27 \mu m$, a blocked force of $F_b = 1\,600\,N$ and stiffness of $59.3\,N/\mu m$. If the stack displaces its full free displacement $\delta = \delta_f$, it will not be able to apply any external force, $F_{ext} = 0\,N$. But if it only displaces half its free displacement, the force it can exert on an external load is $F_{ext} = 800\,N$.

2.2 About IWMs

The high force density and good dynamic properties of piezoelectric material makes it an attractive technology for actuator applications. However, its very small displacement limits its usefulness. To increase the displacement, mechanical amplification may be used by attaching a lever to a piezoelectric actuator. This, however, reduces the force capability. Another possibility is to use so-called *Frequency Levering* where an actuator is driven dynamically at a high frequency, and displacement per cycle is added over many repetitions without compromising on the force capability. One such mechanism that accumulates a number of small displacements is known as an inchworm motor (IWM).

Basically, an IWM is three actuators working together. Two of the actuators act as brakes or clamps (labelled A and B), and the third is an extender mechanism that produces the linear (or rotational) displacement.

A single operational cycle consists of six steps as shown in Figure 8:

1. Clamp A is activated while clamp B is disengaged.
2. The extender extends.
3. Clamp B is activated. Both clamps are now on.
4. Clamp A relaxes.
5. The extender relaxes / returns to its original shape.
6. Clamp A is engaged.

At the end of the cycle, the motor has been displaced by a small amount. The cycle is then repeated. The large bandwidth of typical piezoelectric material allows this cycle to be repeated at high frequencies. The motion is reminiscent of the movement of a worm in nature from which the name is derived. The motor mimics continued linear motion and relatively high frequencies (>30 Hz) and small step sizes (<0.1 mm). The travel distance is only limited by the length of the guide for the extender and/or moving clamp(s).

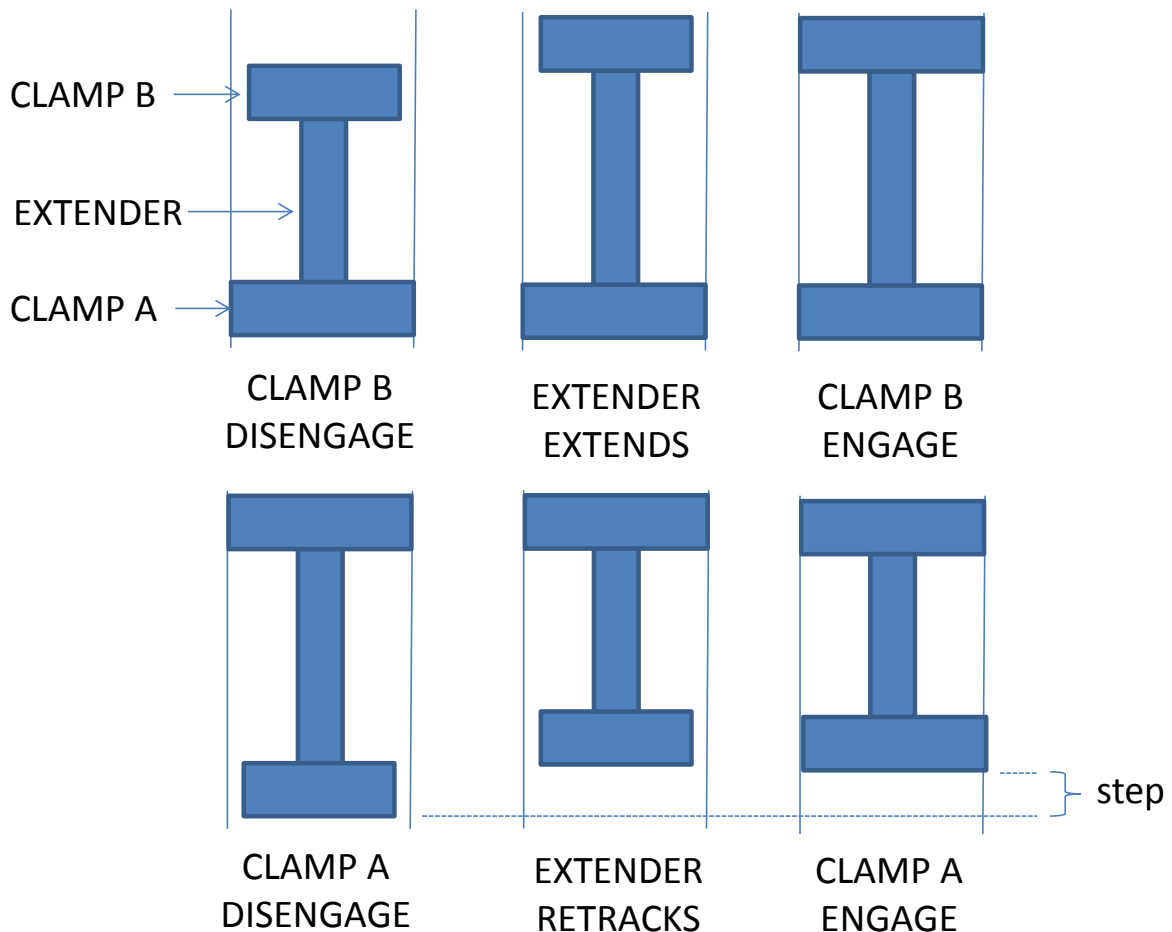


Figure 8: Inchworm motion (Vaughan, 2001)

Linear motors utilising the inchworm principle may have different embodiments that can be broadly grouped into three groups as shown in Figure 9:

1. Both clamps and extender are connected directly. This group includes configurations where the clamps and extender are mounted to a common base or are attached directly to form a single unit. This unit may be stationary and move a shaft or a guide, or the shaft or guide may be stationary and the clamps-extender unit moves. The extender causes the clamps to be displaced relative to each other with each step.
2. The second group includes configurations where the clamps are separate from the extender but both clamps are connected to each other or mounted on a common base. The extender may be part of the guide or shaft and cause it to extend and contract rather than changing the distance between the clamps. The relative position between the two clamps is fixed.
3. The third group consists of configurations where only one of the clamps is attached to the extender. The inchworm motion will cause the distance between the clamps to increase or decrease continually as the moving part of the motor travels in the actuation direction.

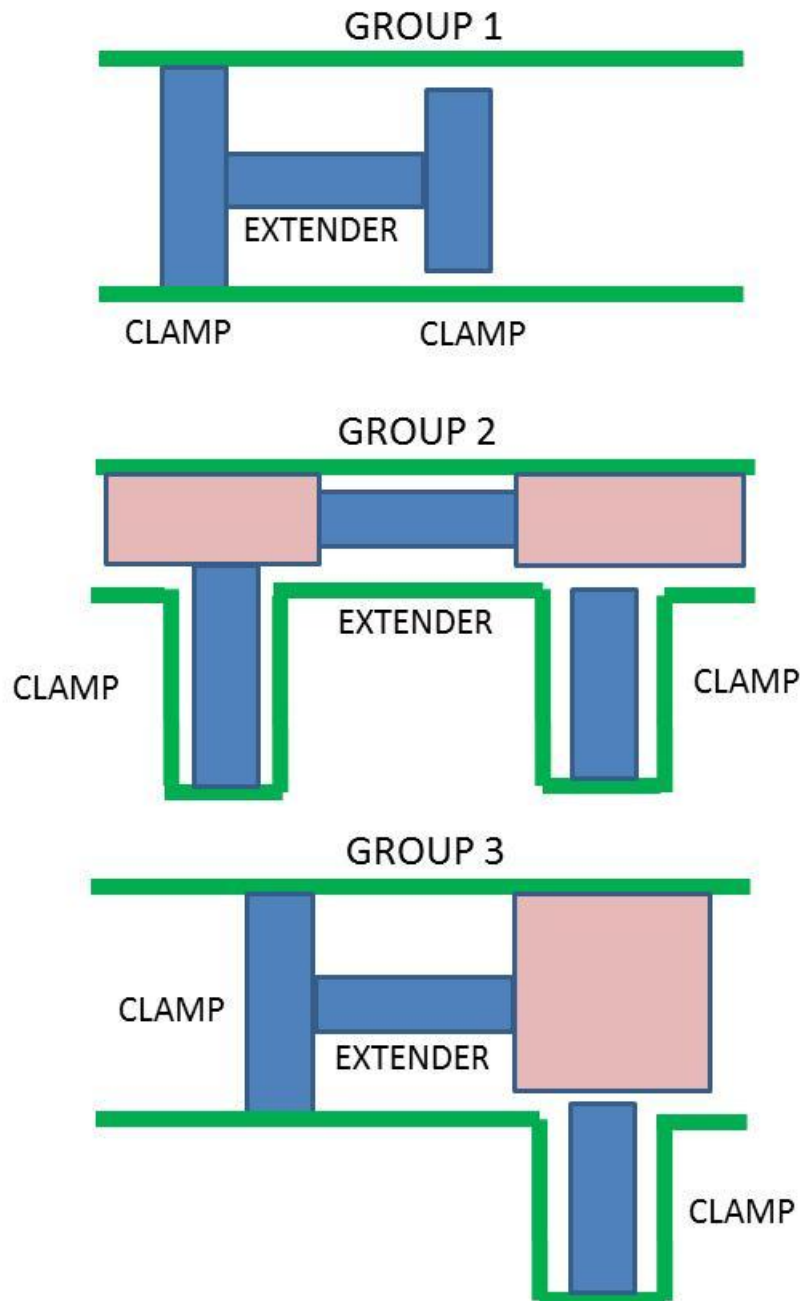


Figure 9: The three different IWM groups

2.3 Some history of IWMs

Linear actuating mechanisms incorporating the inchworm principle for translation into movement can be traced back in registered patents to the early 1960s. Stibitz was perhaps the first to design such an actuator (Stibitz, 1964). His *incremental feed mechanism* employs magnetic fields and frictional connections to obtain “precisely controlled, microscopically small motions” aimed at the machine tool industry. The shaft (#2 in Figure 10) moves due to friction between couplers (#4, #5 and #6) and the shaft. Electromagnetic coils (#10, #11 and #12) cause magnetostrictive materials and the couplers to displace axially by a small amount. When two of the actuators move against the third, the shaft makes an incremental step. By activating the three actuators in different combinations so that two always work against one, the shaft will move in a particular direction by small increments.

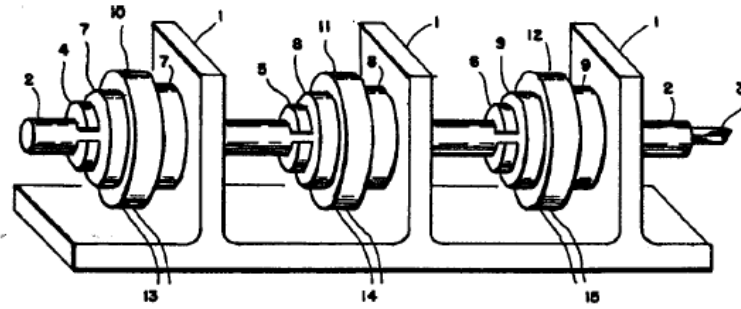


Figure 10: Incremental feed mechanism patented by Stibitz (Stibitz, 1964)

Locher's *linear actuator* was patented in 1967 (Locher, 1967), and provided "controlled rectilinear" displacement with an accuracy of about 13 μm . His motivation for his design was to improve the backlash behaviour of lead screw arrangements when linear actuation was required in dynamic applications (up to 20 Hz). Actuation was obtained through piezoelectric materials that moved a shaft or bar. An "oscillator" provided a sine wave from which a "trigger pulse shaper" generated pulses that formed square waves. The sine waves were phase shifted to obtain typical inch worm motion between the clamps (12a and 12b in Figure 11) and the pusher extender (14). The piezoelectric materials in the clamps would extend when activated, causing part 70 to pivot around part 72 and wedge onto the pushrod (26L). Compliance in the clamps was obtained through threaded rods (48) that returned the wedge part (70) to its starting position when the clamps were relaxed. The extender simply pushed the bar when the piezoelectric material was energised. This design also provided a holding force when power is off.

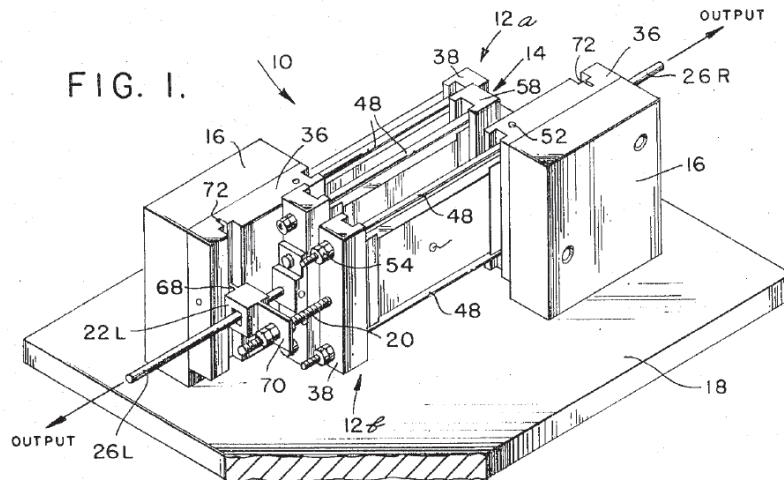


Figure 11: Linear actuator patented by Lochner (Locher, 1967)

A design for a "position control device" by Brisbane is the first piezoelectric *walker* motor (Brisbane, 1968). A voltage applied to any of the disks (4 and 5 in Figure 12) will cause a radial expansion, which will clamp the disk onto the housing (2). A length expansion is obtained by the extender (6) when a voltage is applied to it. The object of the invention is to position a work table both accurately (5 μm) and at a reasonable high speed (50 mm/s).

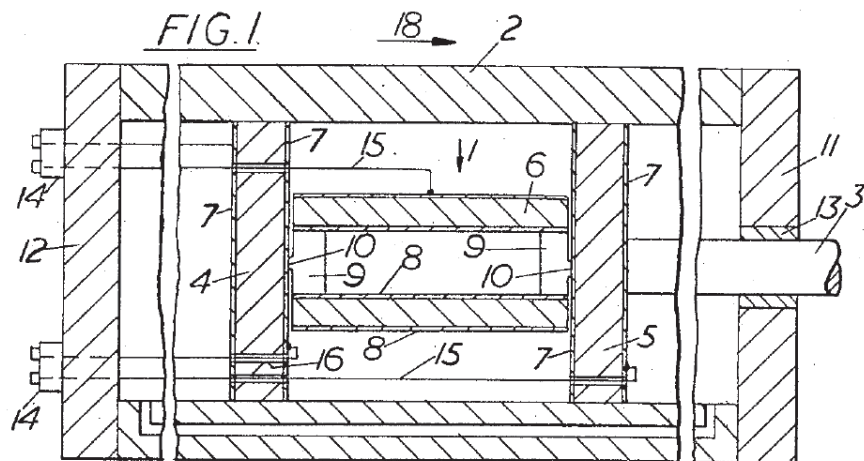


Figure 12: Walker motor patented by Brisbane (Brisbane, 1968)

An important landmark in the development of piezoelectric inchworm motors was the design by Bizzigotti for Burleigh Instruments Inc who introduced the term “Inchworm” (Bizzigotti, 1975). The design employed a pusher configuration and used “staircase waveforms” for actuation. Applications are when either continuous or incremental precision actuation is required. The piezoelectric materials are in the shape of a ring for both the clamps and extender. When a voltage is applied to the clamps (54 and 56 in Figure 13) the rings will shrink onto the shaft (18). The extender part has sufficient clearance between the extender ring and shaft and undergoes axial expansion with applied voltage.

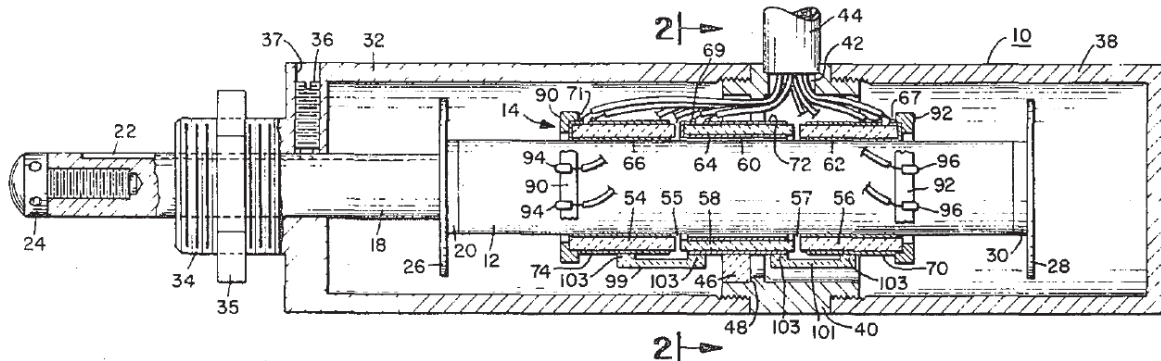


Figure 13: Burleigh Instruments Inc. Inchworm Actuator (Bizzigotti, 1975)

The piezoelectric inchworm motor presented by Lafayette & Foster (1980) and shown in Figure 14 introduced an actuator that had full clamping abilities when not activated, and could be driven at frequencies up to 1 000 Hz (Lafayette & Foster, 1980). Two drive signal electronics were proposed, the first using a single sine wave and two-phase shifters together with “peak clipping pulse shapers” to obtain the three driving signals. The second uses a control signal that enables one or two gates to a cyclic counter. The counter controls three “flip-flops” respectively. Both circuits are in essence a series of switches that generate square control waves.

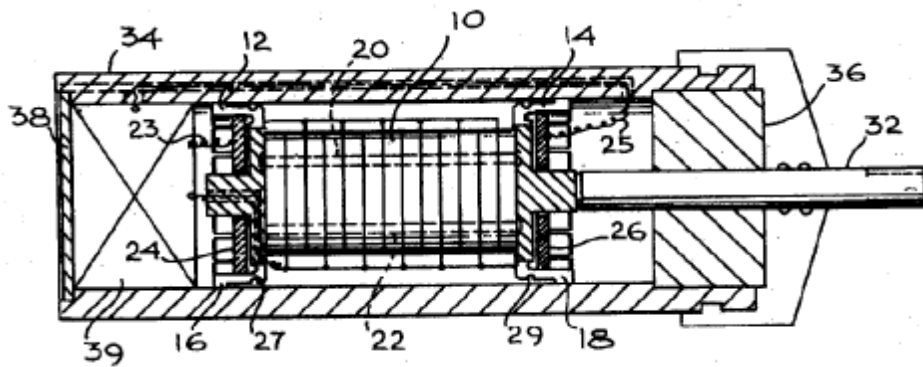


Figure 14: Electromotive actuator (Lafayette & Foster, 1980)

The inchworm motor in Figure 15 by Hara et al. makes use of *stacked piezoelectric actuators* (Hara, Horinchi, Yamada, Takahashi, & Nakamura, 1986). The result was a motor with similar performance to that of Burleigh's IWM, with the exception that the design can operate at a lower maximum voltage of 200 volts, compared to Burleigh's 600 V. A precision of 1 μm and a speed of 2 mm/s with a range of over 50 mm were achieved.

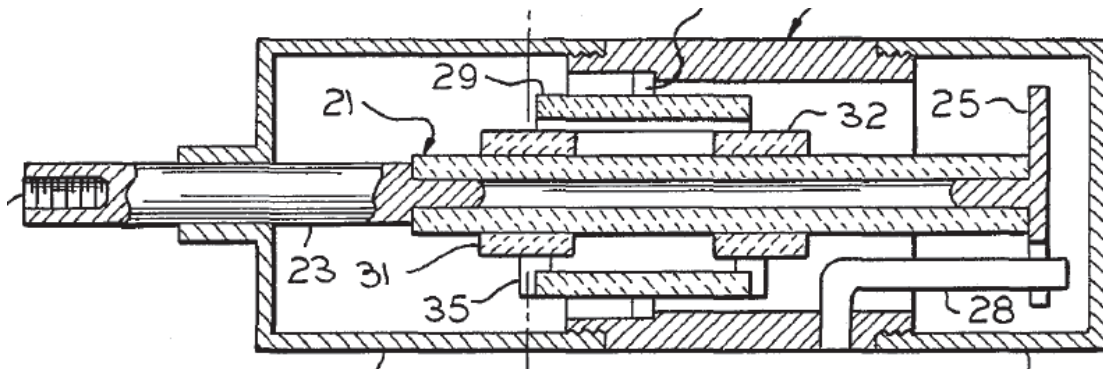


Figure 15: Inchworm motor using stacked piezoelectric actuators (Hara et al., 1986)

The use of a flexure-hinged mechanism to amplify the clamp mechanism displacement was employed by Fujimoto (1988) on a linear motor device (Fujimoto, 1988) (Figure 16). This is typically done to exchange the force capacity of piezoelectric materials to gain larger displacement. Amplifying the clamps could also lead to lower power consumption, since the voltage applied to the clamps can be lower than it would otherwise be, as was the object of this design. The amplified displacement will also allow less stringent machining tolerances.

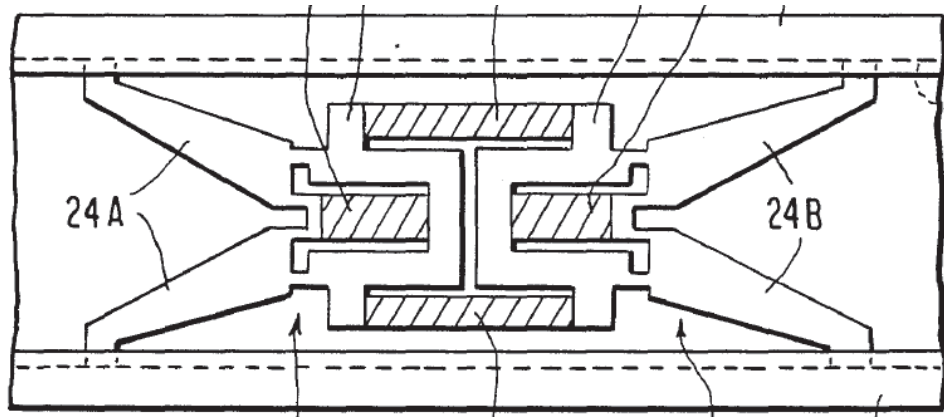


Figure 16: Inchworm motor with flexure-hinged mechanisms 1988 (Fujimoto, 1988)

The inchworm principle may also be employed to obtain rotation as in Figure 17. Van Nuys proposed and patented a device that combines translational piezo elements with shear piezo elements (Van Nuys, 1990). The translation elements act as the clamp mechanism while the actual actuation is obtained by the shear elements. Both elements are combined in a single wedge actuator where the translation element provides axial movement for clamping and the shear element provides the angular motion. These wedges can then be arranged around an axis. Every second wedge is driven in phase, but 90° out of phase to the wedges next to it, to obtain the rotation of the axis.

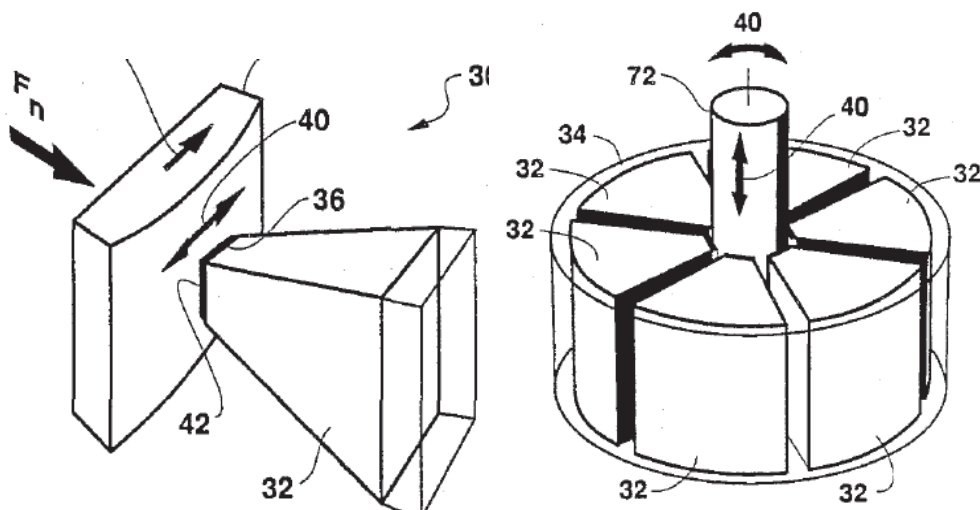


Figure 17: Concept for a rotational inchworm motor (Van Nuys, 1990)

The load capability of an IWM is in general hampered by the limitations of the friction contact between the clamp mechanisms and the sliding component. Murata proposed the use of a linear gear rack with an extremely small pitch to improve the force transfer between the clamps and slide (Yokohama, 1990) (Figure 18). Applications for this design are limited to applications where required step size is at the increments of the rack pitch.

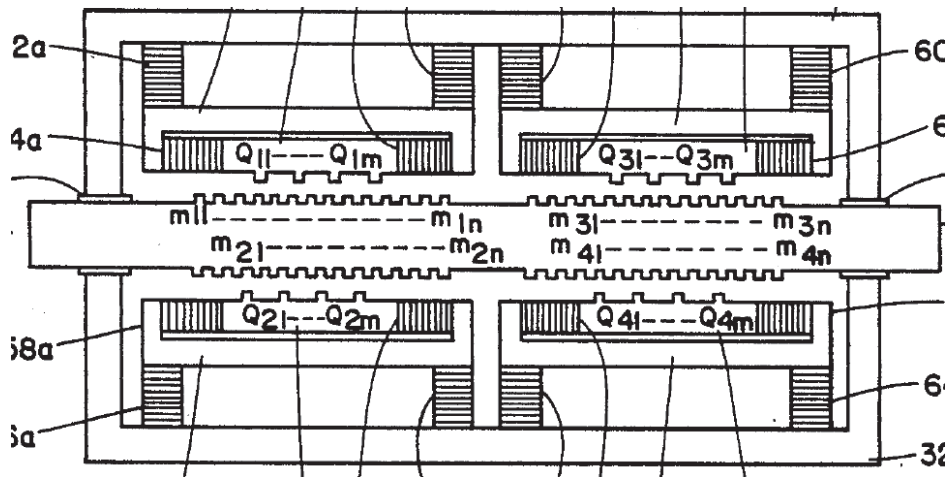


Figure 18: Inchworm motor with linear gear rack (Yokohama, 1990)

Zang and Zhu used a monolithic structure with elastic hinge flexures in their design shown in Figure 19. Three piezoelectric actuators are integrated into the frame. The linear motor is capable of travelling at a speed of 1.6 mm/s over a range of 300 mm with a positioning resolution of 5 nm. It also provides a stiffness of 90 N/ μ m and an output force of 200 N (Zhang, 1994).

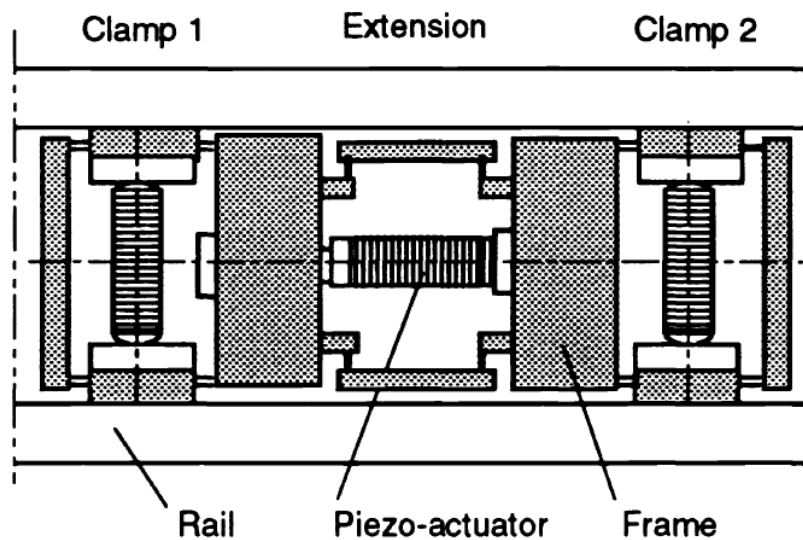


Figure 19: Inchworm motor with monolithic frame (Zhang, 1994)

A hybrid design demonstrated by Meisner and Teter in Figure 20 makes use of the normal electrical phase relationship between piezoelectric and magnetostrictive materials (Miesner & Teter, 1994). The coil of the magnetostrictive material behaves as an inductor, whereas the stacks of piezoelectric discs separated by conductive plates act as a capacitor. Together a resonant circuit is formed. At the resonant frequency, large currents exist inside the motor with power flowing back and forth between the inductor and capacitor. The prototype achieved a stall load of 115 N and a no-load speed of 25 mm/s, but experienced electrical noise problems.

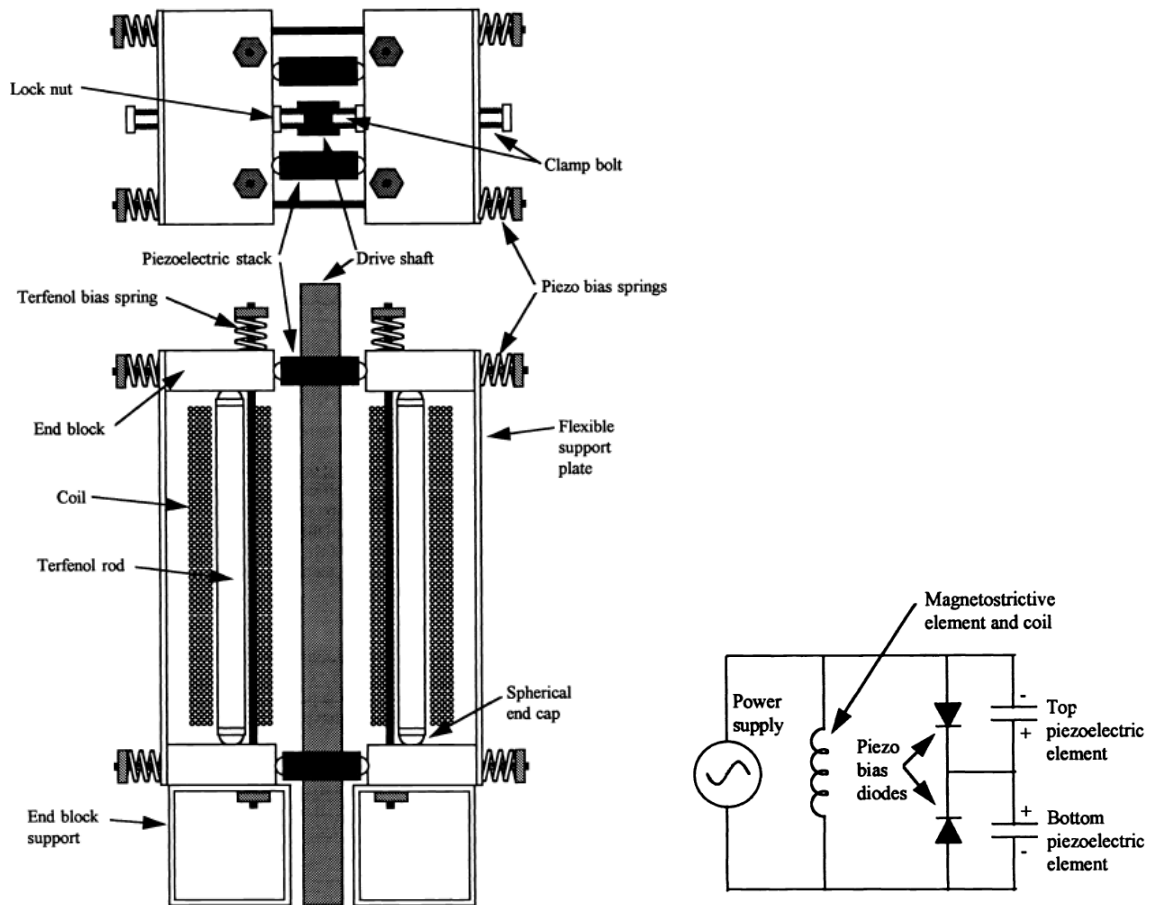


Figure 20: Hydro inchworm motor with both piezoelectric and magnetostrictive materials (Miesner & Teter, 1994)

By using micro-scaled etching methods, Lee and Esashi developed an inchworm motor that is less than 25 mm long from silicon and glass (Figure 21). The device makes use of electrostatics as the driving force. It was found that the designed structure can produce a generating force of a few mN and a moving speed of 2.2 mm/s when it is operated with a voltage of 100 V and at a frequency of 1.4 kHz (Lee & Esashi, 1995).

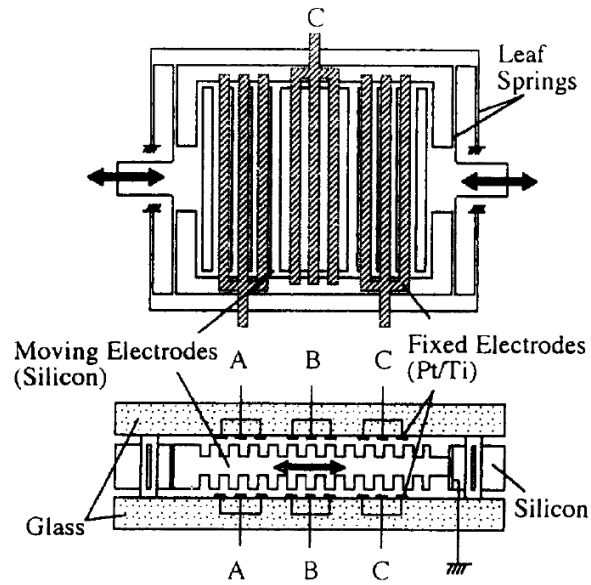


Figure 21: Micro-scaled inchworm motor (Lee & Esashi, 1995)

Pandell and Garcia (1996) added another clamp and extender mechanism to the typical inchworm design and called it a *piezoelectric caterpillar motor* (Figure 22). This offered improved operation over the inchworm design in that it helped to eliminate slippage. The performance of the device claimed a stall load of approximately 2.5 N and an unloaded speed of 10 mm/s.

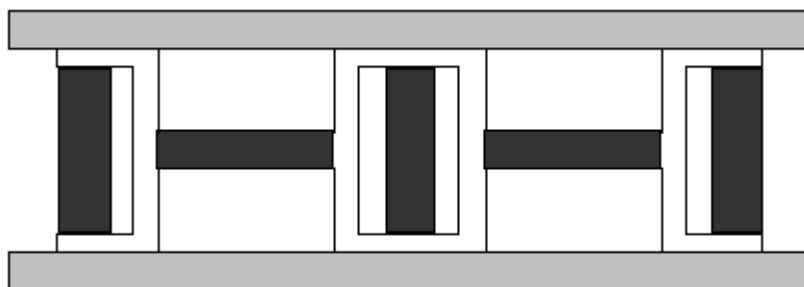


Figure 22: Caterpillar motor (1996) (Pandell & Garcia, 1996)

A novel concept mesoscale actuator device containing microscale components was developed by Chen, Yao, Kim, & Carman (1999). Shear force transfer between the clamping mechanism and the frame was through *interlocked micro ridges* fabricated from single crystal silicon, with a pitch of 10 μm (Figure 23). An open-loop control signal was used to synchronise the locking and unlocking of the micro ridges. The proof of concept prototype supported a 500 N load and was operated at 5 mm/s or 500 Hz. (Chen, Yao, Kim, & Carman, 1999)

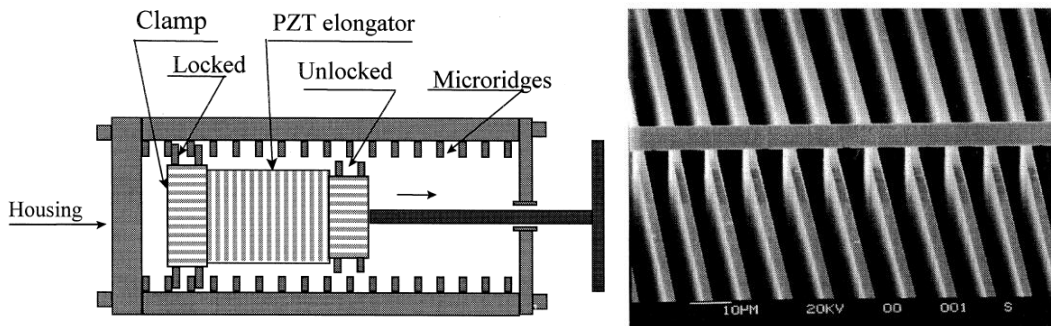


Figure 23: Actuator device containing microscale components (1999) (Chen et al., 1999)

An improvement on the previous device was made by Park, Carman, & Hahn and is shown in Figure 24. It produced a peak-to-peak amplitude of 900 N at 11 mm/s with a weight of 100 g or specific power of 99 W/kg. The total length of the device was 72 mm. Trapezoidal MEMS (micro-electromechanical) ridges were fabricated from single-crystal silicon at a pitch of 11 μm (Park, Carman, & Hahn, 2000).

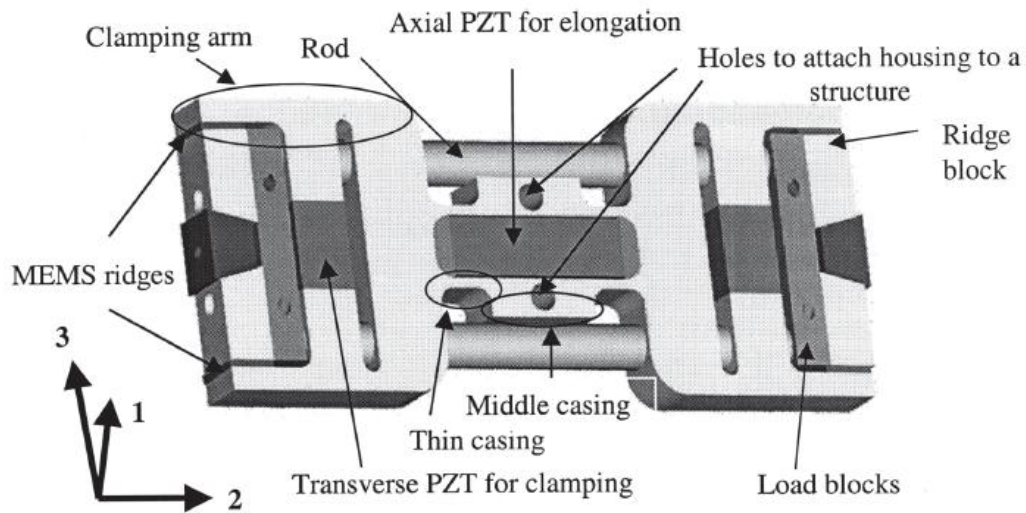


Figure 24: Inchworm motor with a specific power of 99 W/kg (2000) (Park et al., 2000)

A MEMS inchworm actuator for application in an ultra-light space telescope with segmented silicon mirrors was proposed by Yang et al (2002–2003). (Yang, Dekany, & Padin, n.d.). The actuator is capable of a relatively large stroke of 250 μm , with a resolution of a few nm, and occupies only about 2 mm^3 and weighs only about 10 mg. The holders act as the clamps, and the driver acts as the extender as illustrated in Figure 25. Movement is normal to the view as in Figure 25. Contact between the slider and driver, and between the driver and clamps, is by electrostatics.

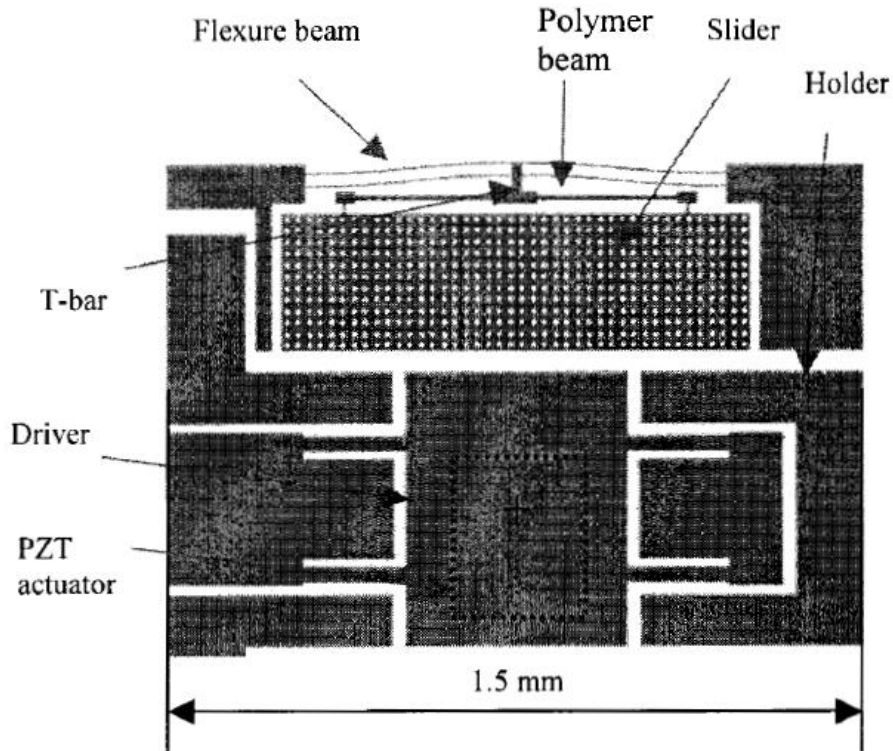


Figure 25: A MEMS inchworm actuator (2002-2003) (Yang et al., n.d.)

To improve positional accuracy, Kwon et al. took the unusual step of having a reduction lever within a monolithic flexure mechanism. An advantage of reducing the displacement of the piezo stacks is a reduction in positioning errors caused by control voltage fluctuations. At an applied voltage of 20 V, the device had a resolution of less than 2 nm. Clamping device A (shown in expanded view in Figure 26) is displaced by the lever mechanism after having engaged the shaft. Clamping device B is the fixed clamp and is active during the return movement of Clamp A.

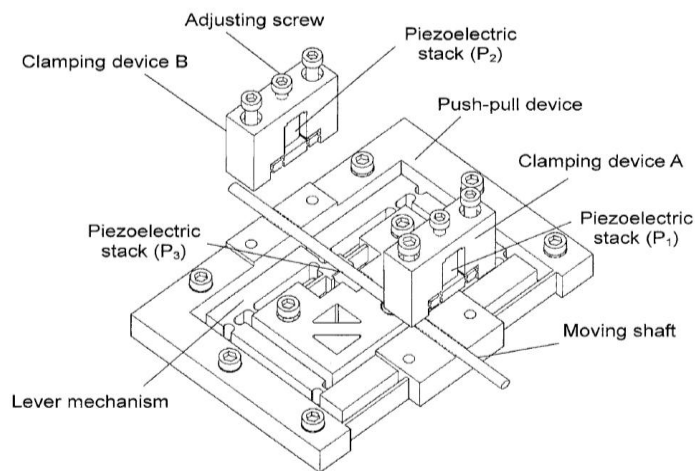


Figure 26: Inchworm motor with reduction lever mechanism (2004) (Kwon, Cho, & Jang, 2004)

An IWM designed for high loads used laser ablation to manufacture micro ridges (Figure 27). Liess et al. used piezoelectric actuators for the extender part, but electromagnets for the clamps for simplicity. Bidirectional continuous motion with loads up to 200 N was achieved. (Liess et al., 2004)

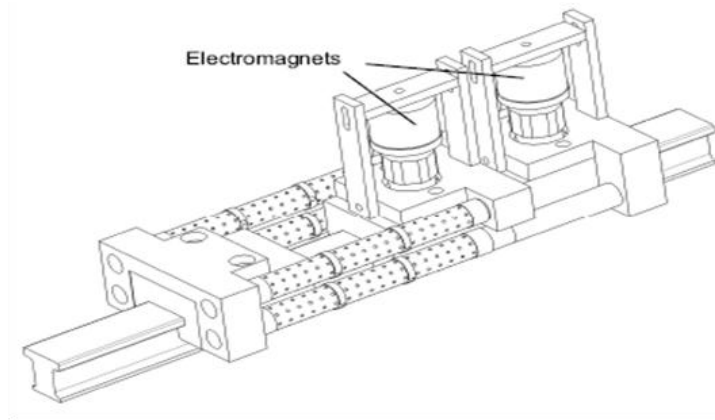


Figure 27: Inchworm motor for high loads (2004) (Liess et al., 2004)

Powers, Xu, Guidarelli, & Smith present an impressive single small actuation system (Figure 28) that provides high resolution of 2 nm over an extended range of 20 mm with consistent forces of 100 N and peak values exceeding 180 N. It also has an integral power-off hold capability. Speeds of 60 mm/s have been achieved. The maximum mechanical power was achieved at around 2 kHz and at an average peak power of 2.2 W. Materials used in the clamp design are silver bearing pads and silicon carbide shaft surfaces (silicon carbide has an excellent stiffness-to-mass ratio). The use of pseudoelastic nickel-titanium is proposed in future for even better clamp performance. The extender forms part of the shaft assembly. The current version is measured at over 300 times the power density of a commercial inchworm motor. Possible application is in deployable optical telescopes (Powers, Xu, & Smith, 2004).



Figure 28: High-power inchworm motor (2005) (Powers et al., 2004)

A novel concept of applying the inchworm principle is reported by Loverich, Koopmann, Lesieutre, Frank & Chen (2007) for a linear actuator (Figure 29). In this design, the two clamps (normally used in classical inchworm designs) are replaced by two nuts acting on a screw thread. An electromagnetic torque motor provides a bias force between the nuts. As the piezoelectric extender engages, force is transferred from the one nut to the other. The “free nut” will then rotate under the bias force until it engages the screw. The extender relaxes; force is transferred to the nut, and the other “free nut” will then turn until it engages the feed screw. The process is then repeated. This design offers reversibility, robustness and simplicity, high force actuation, simple power electronics, insensitivity to wear and a power-off self-locking state. (Loverich, Koopmann, Lesieutre, Frank, & Chen, 2007).

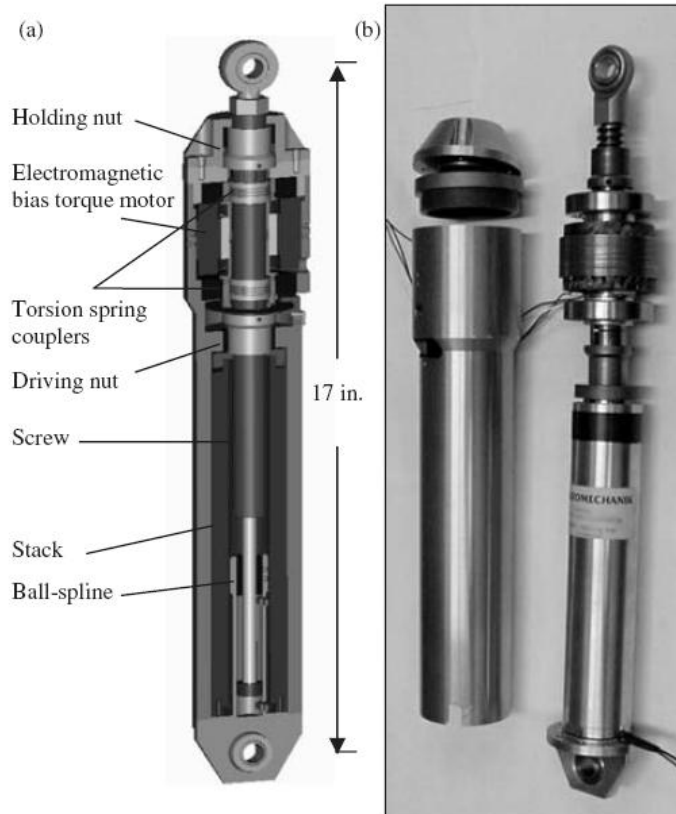


Figure 29: Piezoelectric actuator using a feed screw (2007) (Loverich et al., 2007)

2.4 Electrical control of piezoelectric IWMs

As stated previously, an IWM consists of three mechanisms working together to produce the inchworm motion. It therefore requires three separate electrical signals to drive each of the three mechanisms, or four in the case where the extender uses two oppositely phased piezo stacks. The phase between these signals is very important to produce the inchworm motion as described in Section 2.2. Typical signals are shown in Figure 30, which shows the relative timing between them (for these graphs, a 3 V signal implies activation and -3 V implies deactivation). Each of these control signals requires conditioning and amplification, resulting in the need for replicating electronic hardware. Since only piezoelectric actuators were used during this study, electromagnetic control electronics will not be discussed, but many of the principles also hold true for such devices.

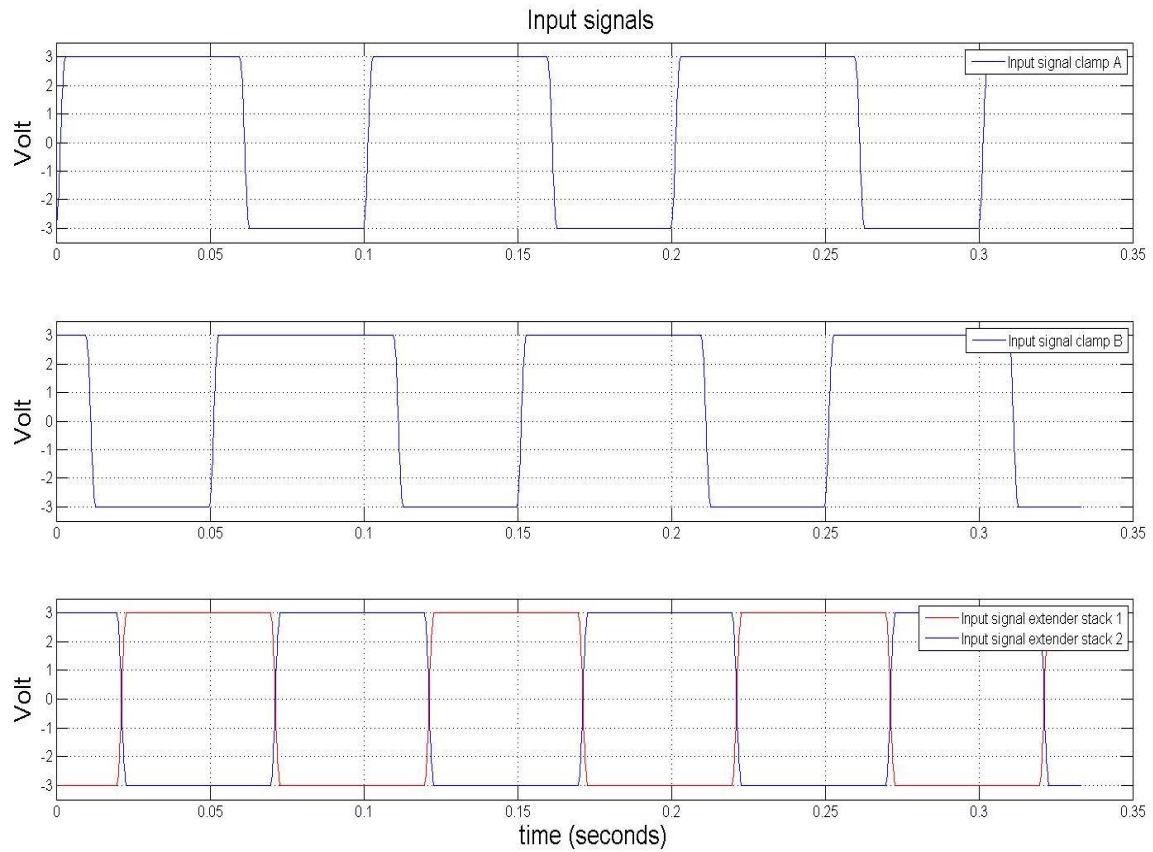


Figure 30: Typical signals required for each of the three actuators making up an IWM

This study focuses mostly on the mechanical design of IWMs, but since the electrical control strategy employed has an important influence on the performance of IWMs, some of the more common control approaches are briefly discussed.

Voltage control strategies (as opposed to current control strategies) are mostly used to operate piezo actuators. In open loop operation, these actuators exhibit a hysteretic nonlinearity between the displacement and the electrical field that limits their accuracy (Ge & Jouaneh, 1995). This effect becomes increasingly noticeable the higher the electrical field strength and the higher the piezoelectric sensitivity of the material are. A typical hysteresis response is shown in Figure 31.

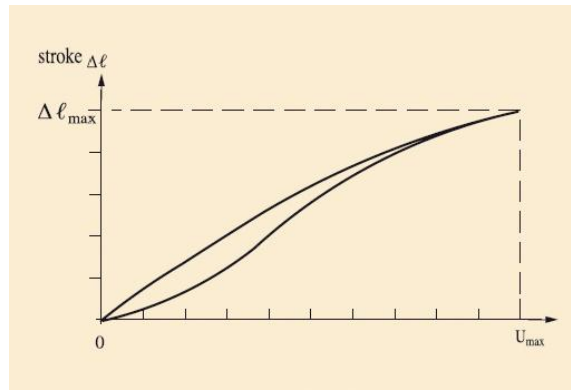


Figure 31: Typical hysteresis response of a piezo ceramic actuator (Piezomechanik, 2011)

Hysteresis can virtually be eliminated if an applied electrical charge, rather than an applied voltage, is varied to control the expansion of the piezo element (Newcomb & Flinn, 1982). Yi and Veillette have demonstrated that an inverting charge control circuit was successful in linearising piezoelectric actuation movement. (Yi & Veillette, 2005) A compliance feedback current driver was built and tested by Fleming and Moheimani to improve the low-frequency performance of charge amplifiers. (Fleming & Moheimani, n.d.)

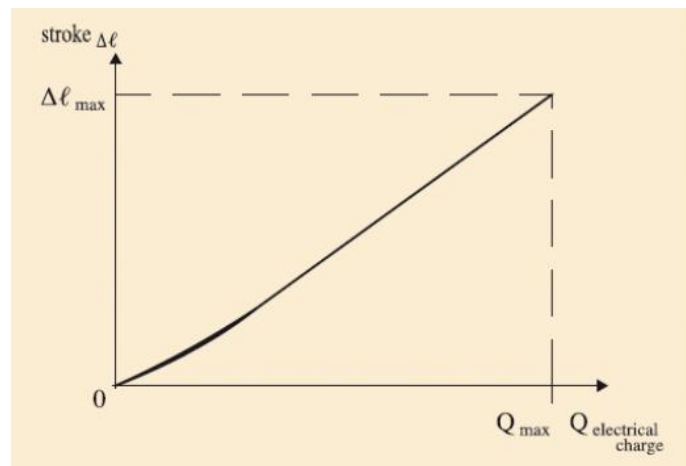


Figure 32: Typical linear stroke response of a piezo stack under electrical charge control (Piezomechanik, 2011)

Another approach to eliminate the effect of hysteresis relies upon using closed-loop controllers (Okazaki, 1990). Piezo stacks are commercially available with strain gauges in Wheatstone bridge configurations for linearising the expansion of the actuator (Piezomechanik, 2011). By using feedback control, the input signal to the piezo actuator is altered to compensate towards a linear displacement response.

Traditionally, the *piezoelectric equation* is used to describe piezo actuators, and comes from linear piezoelectric theory derived from thermodynamic principles ((Meeker, 1996) and Section 2.1). The equation gives the relationship between applied voltage, strain and displacement, and is given by Equation 2-2:

$$S = s^E \cdot T + d^t \cdot E$$

Where

$$E = \frac{V}{m} \quad \text{Equation 2-10}$$

and m is the thickness of the piezoelectric element. This equation implies a linear relationship between displacement and input voltage, and ignores hysteretic effects by equating the electrical field in the piezoelectric material to the field applied to the material ($E = V/m$).

When piezoelectric actuators are used in IWMs, the tolerance for many applications is such that hysteresis does not significantly affect the operations of the motor. IWMs only need to be accurate over a number of steps, and not necessarily for every step. Hysteresis would, however, play a role where the use of micro ridges is considered, since accurate meshing of ridges for every step would have to be achieved.

The topology of the amplifier being used has a great impact on its power consumption, and therefore on the power consumption of a piezoelectric motor. The most common type of amplifier is the linear amplifier, which uses a simple voltage-feedback strategy. Most laboratory amplifiers are of this type. When such an amplifier is used to drive a capacitive load, large currents flow in and out of the amplifier output resistor. The power dissipation requirements of the amplifier can be estimated by (Newton & Main, 1996):

$$P_{out,max} = \frac{V_s^2}{2Z_L} \cdot \left| \frac{4}{\pi} - \cos(\theta) \right| \quad \text{Equation 2-11}$$

where V_s is the amplifier supply voltage, Z_L is the magnitude of the load impedance, and θ is the phase angle of the load impedance.

The current requirement is given by:

$$I = 2\pi f_{max} \cdot V \cdot C \quad \text{Equation 2-12}$$

where C is the capacitance and f_{max} is the maximum driving frequency.

For a purely capacitive load it becomes:

$$P_{out,max} = 4V_s^2 \cdot f_{max} \cdot C \quad \text{Equation 2-13}$$

The amount of power that needs to be supplied is a function of the capacitance and the driving frequency; both are generally high for a piezoelectric IWMs. This will also result in a large and heavy heat sink. Linear amplifiers are generally designed to drive resistive loads and not capacitive loads, and will dissipate all of the regenerated energy as heat.

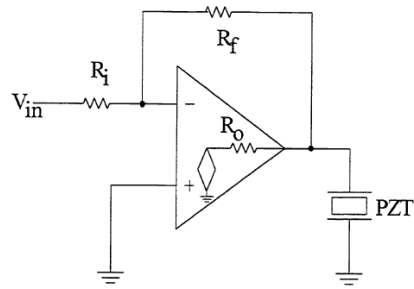


Figure 33: Electrical representation of a linear amplifier (Newton & Main, 1996)

An alternative to linear amplifiers is switching amplifiers. Switching amplifiers recycle the regenerative energy back to the power source, resulting in a very efficient amplifier.

A voltage control switching amplifier saves power by maintaining a phase angle of 0° or 180° . Only two phases are possible with this topology. Power is consumed only during switching from one state to the other (Newton & Main, 1996).

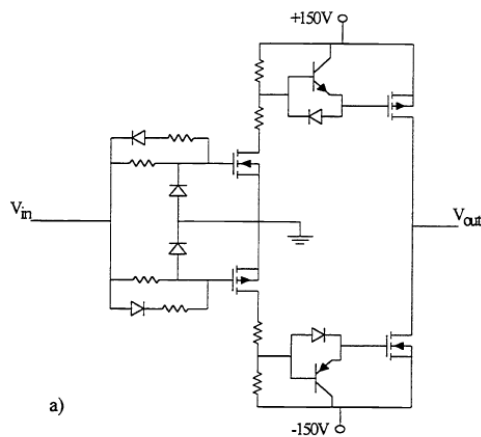


Figure 34: Switching amplifier (Newton & Main, 1996)

Chandrasekaran and Lindner (2001) designed a light-weight current controlled switching amplifier. Because of the high efficiency, switching current amplifiers are recognised as promising amplifier topology for driving piezoelectric actuators. (Chandrasekaran & Lindner, 2001).

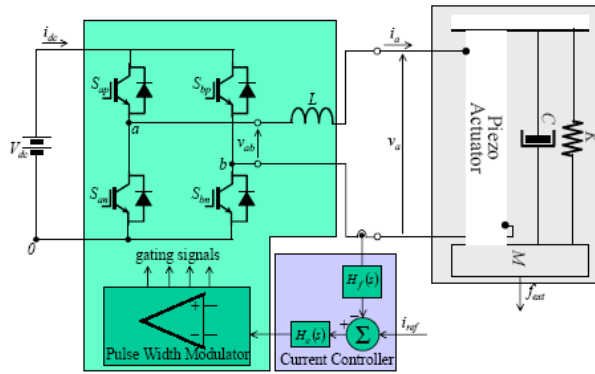


Figure 35: Current controlled switching amplifier (Chandrasekaran & Lindner, 2001)

The power consumption of linear and switching amplifiers was compared by Lindner and Zhu in (Lindner, Zhu, Vujic, & Leo, 2002). Four amplifiers were compared when driving a very small but similar piezoelectric load. The first two amplifiers were low-voltage (200 V max) (AMP1) and high-voltage (750 V max) (AMP2) linear amplifiers. The third was a hybrid topology designed for current control operations (AMP3). AMP4 was a current controlled switching amplifier similar to the topology shown in Figure 35. The graphs are shown in Figure 36.

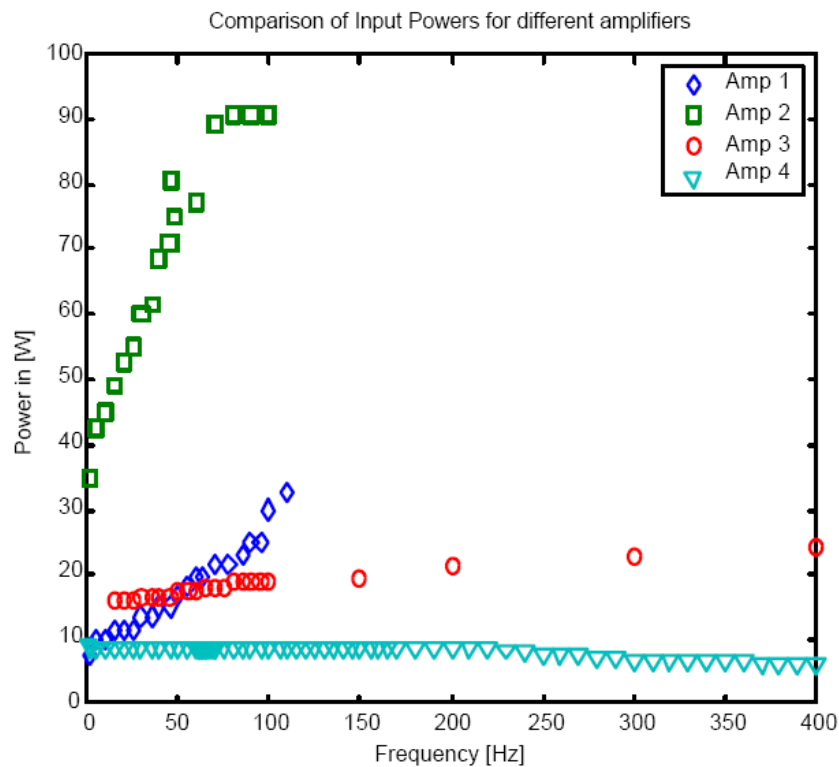


Figure 36: Comparison of input power of different amplifiers (Lindner, Zhu, Vujic, et al., 2002)

Amplifiers 1, 2 and 3 exhibit linear dependence with frequency because the piezoelectric actuators draw more current at higher frequencies. The switching amplifiers show approximately constant power consumption over frequency because they recycle the energy through storage capacitors. The constant power consumption represents (small) fixed losses in the amplifiers.

A control amplifier especially suitable for low voltage input, high-voltage PZT actuators was designed by Lindner et al. (Lindner, Zhu, Song, Huang, & Cheng, 2002). This amplifier is designed for an inertially stabilised rifle and the topology is selected for its light weight and low power consumption properties. Power is supplied from batteries. This makes this design also attractive to small battery-operated UAVs, where piezoelectric actuators are very attractive for control applications. The amplifier is based on switching technology so it efficiently handles the regenerative energy from the piezoelectric actuator. This amplifier consists of two stages. The first stage is a flyback converter which boosts the (low) input voltage to the maximum voltage required by the piezoelectric actuator. The second stage is a half-bridge amplifier which delivers the output voltage to the actuator as commanded by a reference signal.

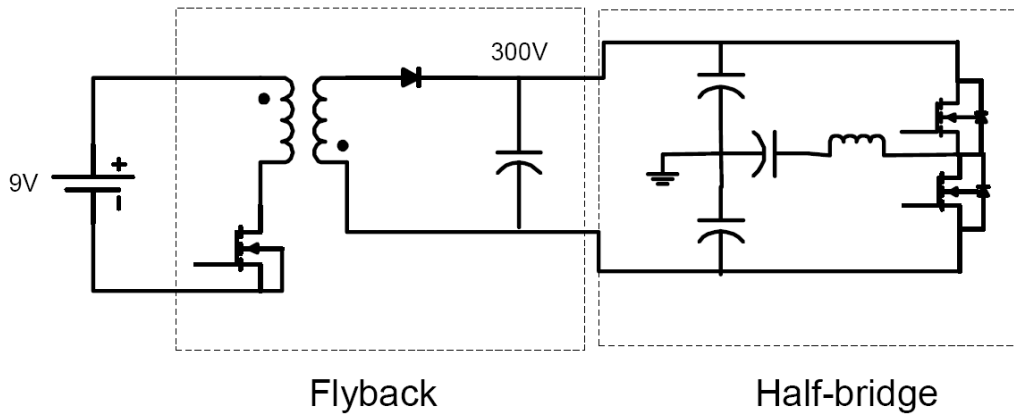


Figure 37: Circuit topology (Lindner, Zhu, Song, et al., 2002)

Different waveform shapes may be used to drive each actuator. Square waveforms or waveforms approaching square waveform are typically used for controlling the clamps (Powers et al., 2004) (Suleman, Burns, & Waechter, 2004) (Frank, Koopmann, Chen, & Lesieutre, 1999) (Canfield, Edinger, Frecker, & Koopmann, 1999). To control the extender, square (Suleman et al., 2004), sine (Frank et al., 1999), or ramp (Powers et al., 2004) (Suleman et al., 2004), waveforms have been used.

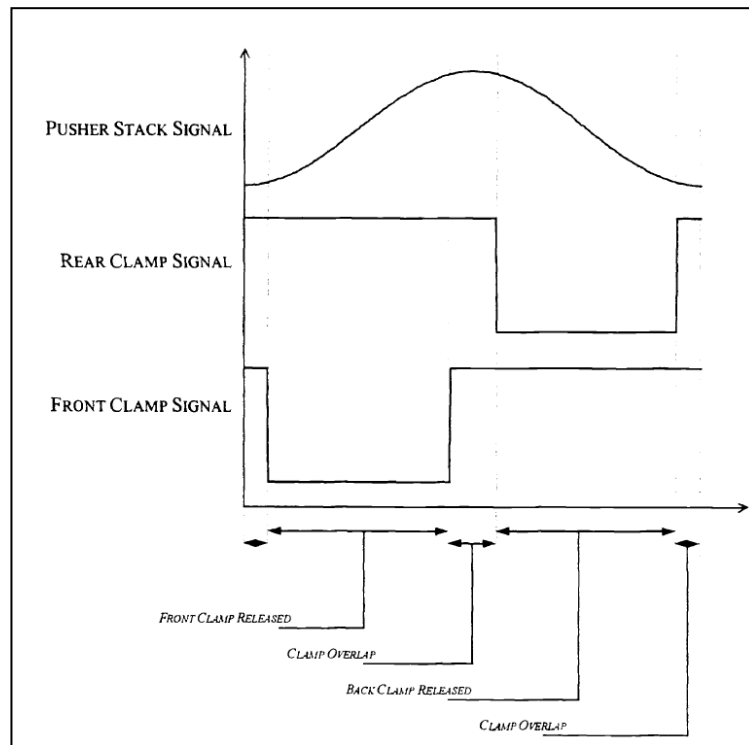


Figure 38: Square clamp waveforms and sine extender waveform (Frank et al., 1999)

By overlapping the square waveforms for the clamps (see Figure 38), back slip is prevented when driving an external load. The need for this overlap is one of the reasons why a square waveform for the clamp actuators is preferred. Square waves on the other hand require a power amplifier with large bandwidth and could deteriorate in shape at larger frequencies (Frank et al., 1999).

As part of the CSIR's IWM research, a switch-mode power supply was designed to provide the voltages required to drive the piezo stacks (Figure 41). The flyback topology was chosen from the many switch-mode power supply topologies, as it uses the fewest components and can be designed for high efficiency. (Williams, Loveday, & de Villiers, 2010).

The piezo stack voltage can be alternated between 0 V and 120 V using a square wave. This allows the application of a relatively simple resonant charge recovery method which was proposed for use on micro-insect wings (Campolo, 2001). The circuit was adapted slightly for use on a single, uni-polar actuator. A large capacitor, C_s in Figure 39, was used to store charge. The voltage on this capacitor changed very little when charging or discharging the piezo stack. This decreased the voltage over the inductor, and hence the current spikes into and out of the stack. As explained by (Campolo, 2001), the circuit uses the LC resonant properties to move most of the charge from the piezo stack to the storage capacitor, C_s on the left in Figure 39. The charging speed is determined by considering the piezo stack and the storage capacitor as two capacitors in series. The resulting resonant frequency is given by $\omega = 1/\sqrt{LC}$, where $C = \frac{C_p \cdot C_s}{C_p + C_s}$.

The charge recovery takes place in a half period $\frac{T}{2} = \frac{\pi}{\omega}$. A 100 μH inductor (L), and a 1 mF storage capacitor (C_s) results in a half period of 42 μs . This corresponds to the simulation results shown in Figure 40. The measured and simulated results showed some differences. The measured half period is close to 100 μs . It is believed that this is due to non-linearity and internal resistance being neglected in the modelling of the piezo stack.

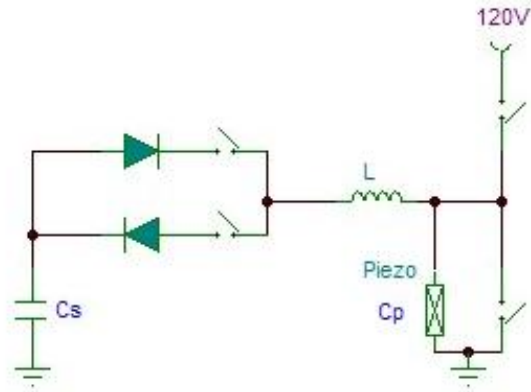


Figure 39: CSIR's switch-mode power supply (Williams et al., 2010)

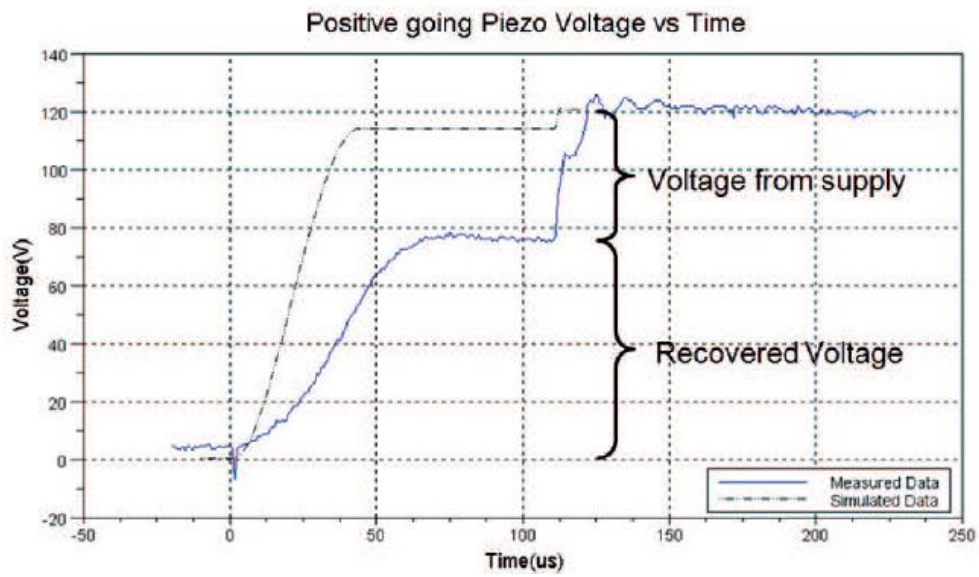


Figure 40: Measured and simulated voltage vs. time (Williams et al., 2010)

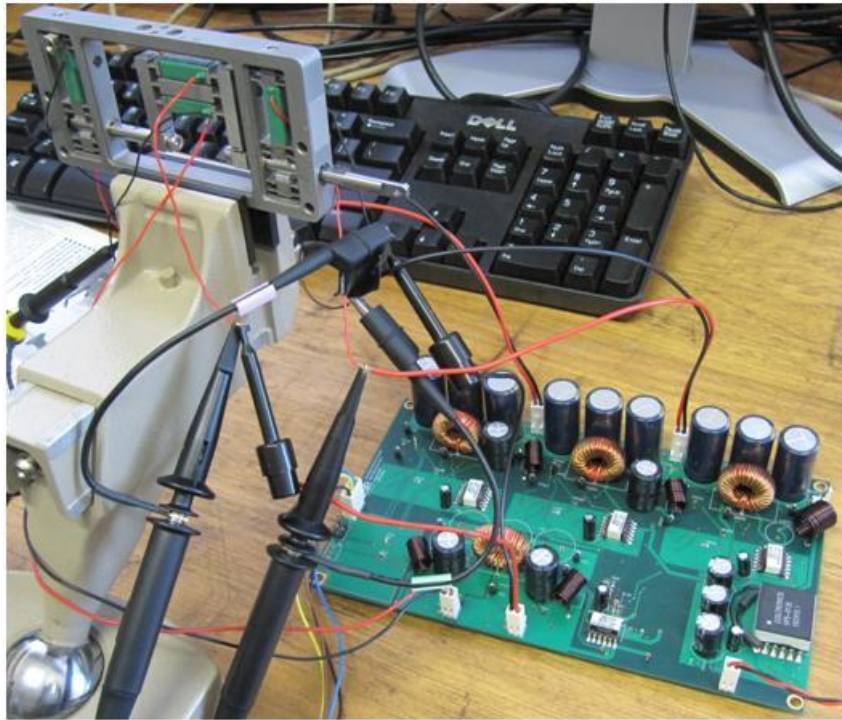


Figure 41: CSIR's switch-mode power supply connected to an IWM

3 Two novel IWM designs

3.1 Overview

Two IWM designs are presented. Both designs are novel, and both fall in the first IWM type group as described in Section 2.2. The basic layout of the IWM was selected since it is best suited to the morphing wing UAV application that is briefly discussed in Section 1.1 (also see Appendix L). Also the size of the IWM and the selection of the specific piezoelectric elements used were (loosely) driven by this application. The first design is based on a conventional IWM design, but the second design is an inventive new embodiment that will double the force capability and improve the precision capability, without compromising on the speed of an IWM when compared with the conventional design.

In this dissertation, it is not the intention to develop an IWM that is perfectly suited to the UAV application mentioned, but the design presented should be viewed as an experimental platform, specifically designed to gain a deeper understanding of aspects that were not clear at the outset of the project. The parameters of the designs are determined by the space available, and the speed, stroke and force requirements estimated from the wing parameters used in Coetzer & Harris (2010). The specification initially used is for an IWM with a stroke of 20 mm, a holding force capability of 140 N and a speed of 3.8 mm/s when driven at 50 Hz. Some compromise was made between these specifications due to the power ability of the available electronic amplifiers (which affect the maximum possible drive frequency) and the need to accommodate the available piezoelectric stacks. The two IWM designs are roughly similar in size, but were designed with different extender amplifications, and therefore have different speed and force characteristics. These discrepancies do not, however, compromise the objectives of this work as described in Section 1.2.

A description of the designs is required at this point to give an understanding of some of the concepts used in the following sections.

3.2 The conventional IWM design

The conventional piezoelectric IWM developed for this investigation consists of two stationary clamps without any mechanical amplification, and a mechanically amplified extender (Figure 42). The actuator used for the extender is known as a flextensional or Moonie actuator (Newnham et al., 1993). The clamp mechanism is integrated in the frame and consists of small blocks that are suspended by four flexures each. The clamps have aluminium “shoes” that press onto the hardened, precision-made steel shafts which are in turn supported by brass bushes. The two shafts are attached to the extender. Set screws are in contact with the blocks at the top of the piezo stack and opposite the shaft. These blocks and set screws allow tension adjustment, but are stationary during operation. The third block moves during operation and is actuated by the clamp’s piezo stack. The two pairs of parallel flexures on each block constrain the block to translate only. The outer frame with integrated clamps and the extender of the motor were made from Stainless Steel 431 and manufactured mostly by wire eroding. The shoes are permanently glued onto the blocks.

This configuration allows a rigid and robust design that has a low part count (Figure 43). An external load can be attached to one shaft.

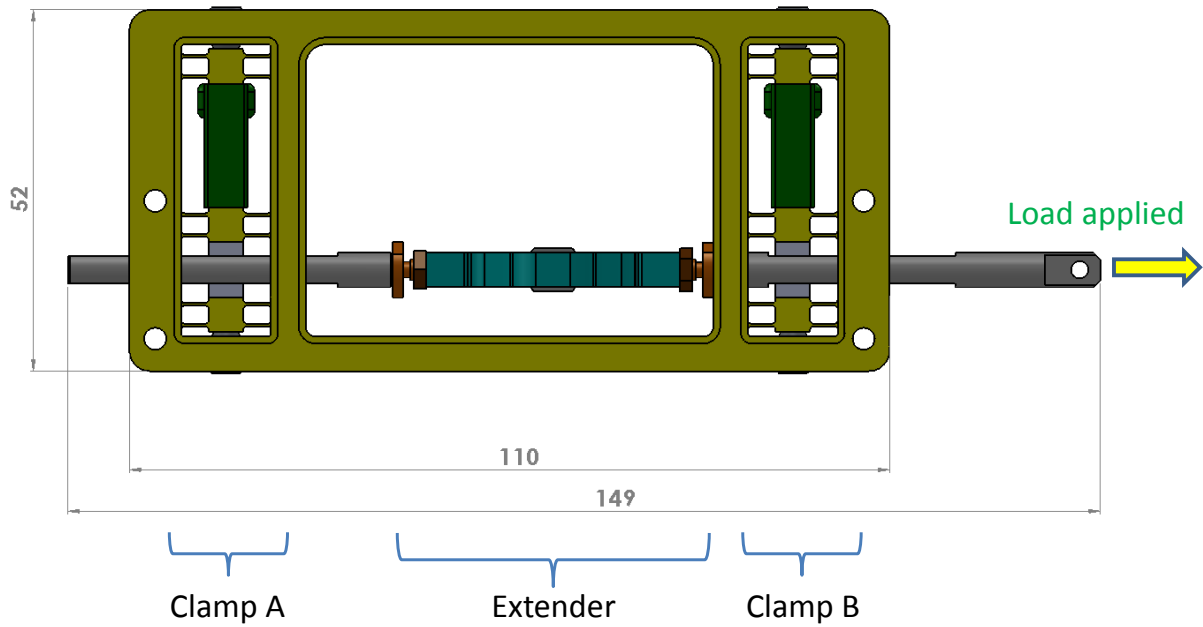


Figure 42: Side view of piezoelectric inchworm motor (PIM)

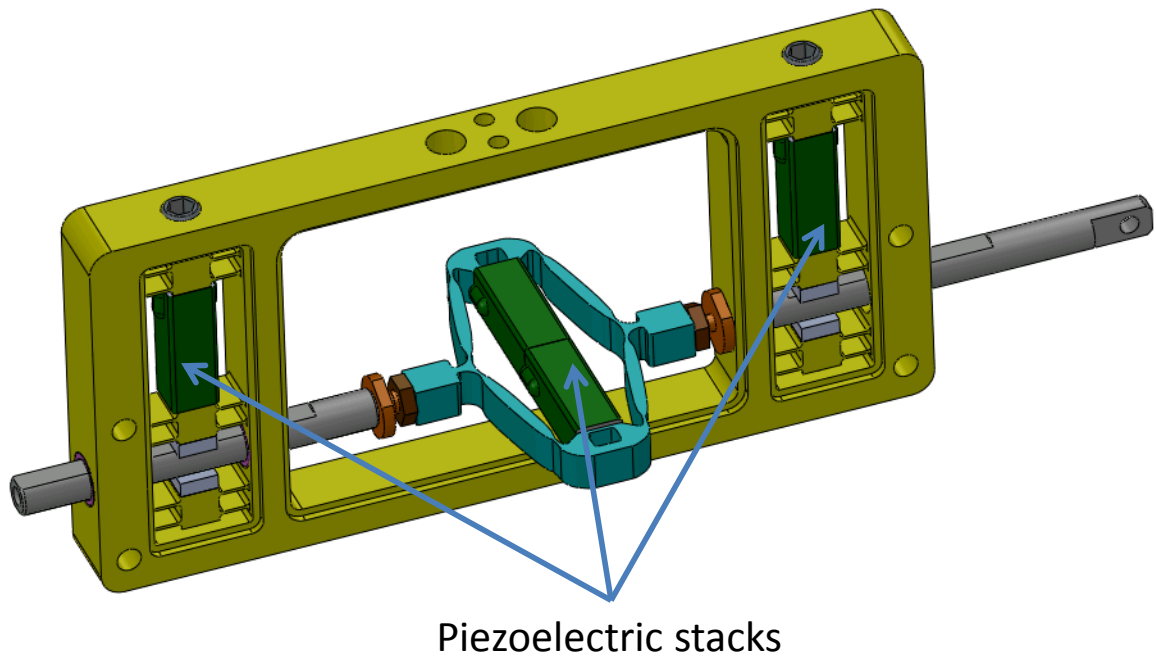


Figure 43: Isometric view of inchworm motor

3.3 An IWM with force duplicator mechanism

The second IWM design also consists of two integrated clamp mechanisms and an extender mechanism. The important difference between the classical IWM design and this one is the presence of a lever mechanism between the extender and applied external load.

A different type of actuator is used for the extender and is referred to as a beam actuator. This type of actuator was designed and patented by the CSIR (Loveday, 2003; Wallis & Loveday, 2004). It allows similar (symmetrical) behaviour

in both directions (push and pull) and has an overall stiffer construction. An optimisation algorithm previously developed in-house was used to determine the optimal position and thickness of the flexures (Loveday, 2003). The flexure positions determined from the algorithm ensure that the output movement of this actuator is a purely translation movement without any rotation. The actuator is designed to amplify the piezoelectric stack displacement by a factor of ten. The stacks in this type of beam actuator is working in parallel and operated in opposite phase with each other. The force capacity of each stack is thus added within the actuator. In the flextensional actuator the two stacks is in series and the displacement of each stack is added.

The clamp mechanisms are in essence the same as before, except that the use of a lever introduces a mechanical amplification between the piezo stack displacement input and the output of the shoe. The clamp mechanisms are designed with a mechanical amplification factor of two. Amplification is realised by a pivot mechanism, where the pivot action is obtained by two perpendicular flexures. This allows more displacement of the shoe clamps and makes the design a bit less sensitive to machining and assembly tolerances. As with the previous design, adjustment is made with set screws, but because of the higher amplification, adjustment is less sensitive and allows better control over the pre-loading of the clamps. A schematic of the basic operations is shown in Figure 44 and the operational steps of section 2.2. are again repeated here:

A single operational cycle consists of six steps:

1. Clamp A is activated while clamp B is disengaged.
2. The extender extends.
3. Clamp B is activated. Both clamps are now on.
4. Clamp A relaxes.
5. The extender contracts.
6. Clamp A is engaged.

Another improvement is the use of a novel force duplicator that doubles the force capability without sacrificing the displacement. This new IWM design interacts with the external load through a beam mechanism in such a way that the beam acts as a lever (Figure 45). Rotations are achieved through flexures as shown in Figure 47. The beam connects both sides of the extender to a single external load through a ratio of 2:1. This leverage allows twice the load to be displaced compared to the conventional design, although at only half the displacement step size of the extender (Figure 46 and Figure 48). However, this specific layout also allows the extender to act against the load during both the actuating events (Section 2.2) concerning the extender stepping for each cycle. The extender acts against the load in both its extension and compression events, whereas in the conventional design it only acts against the load for one of these. This means that the external load displaces twice with each cycle, instead of only once compared to the conventional design. The displacement per event is only half that of the conventional design, but since each cycle now has two displacement events, the displacement per cycle remains unchanged while the force capability is doubled.

A further advantage is that since the step size experienced by the external load is half that of one extender step event, the step resolution is thus twice as good as it is in the conventional design, i.e. the smallest precision step that the motor can make is half that of a similar conventional design. This is particularly important, for instance where the IWM is used as a precision actuator, which is one of the typical applications of IWMs.

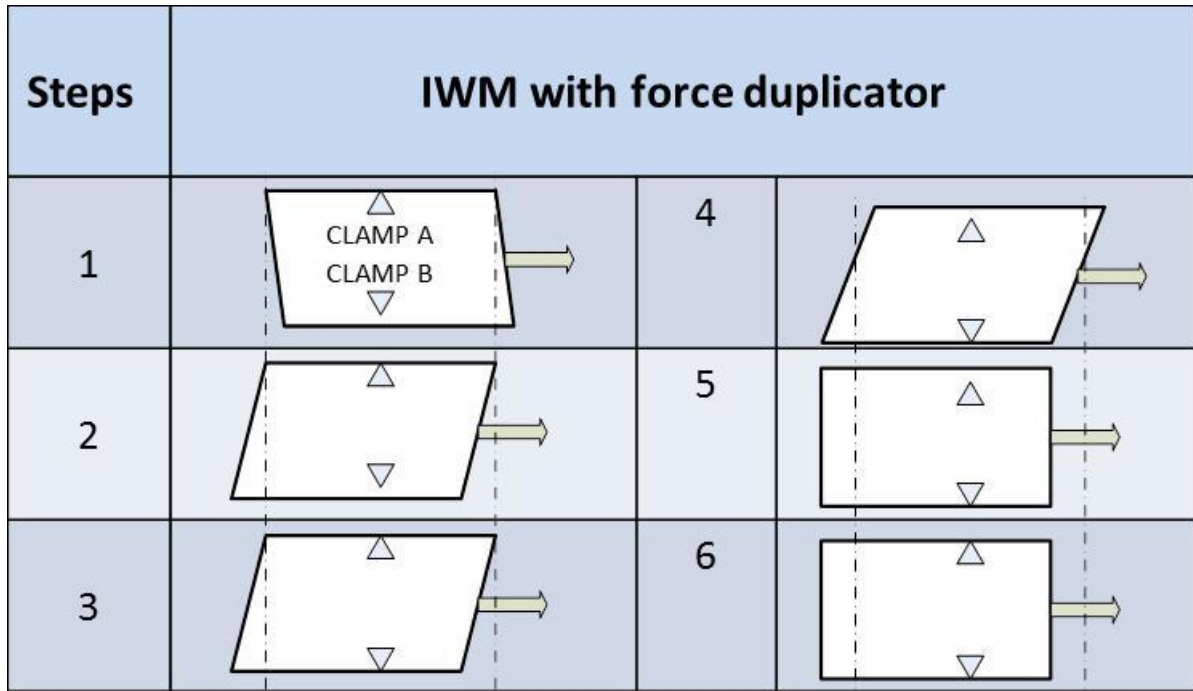


Figure 44: Schematic of the basic operations of the IWM with force duplicator

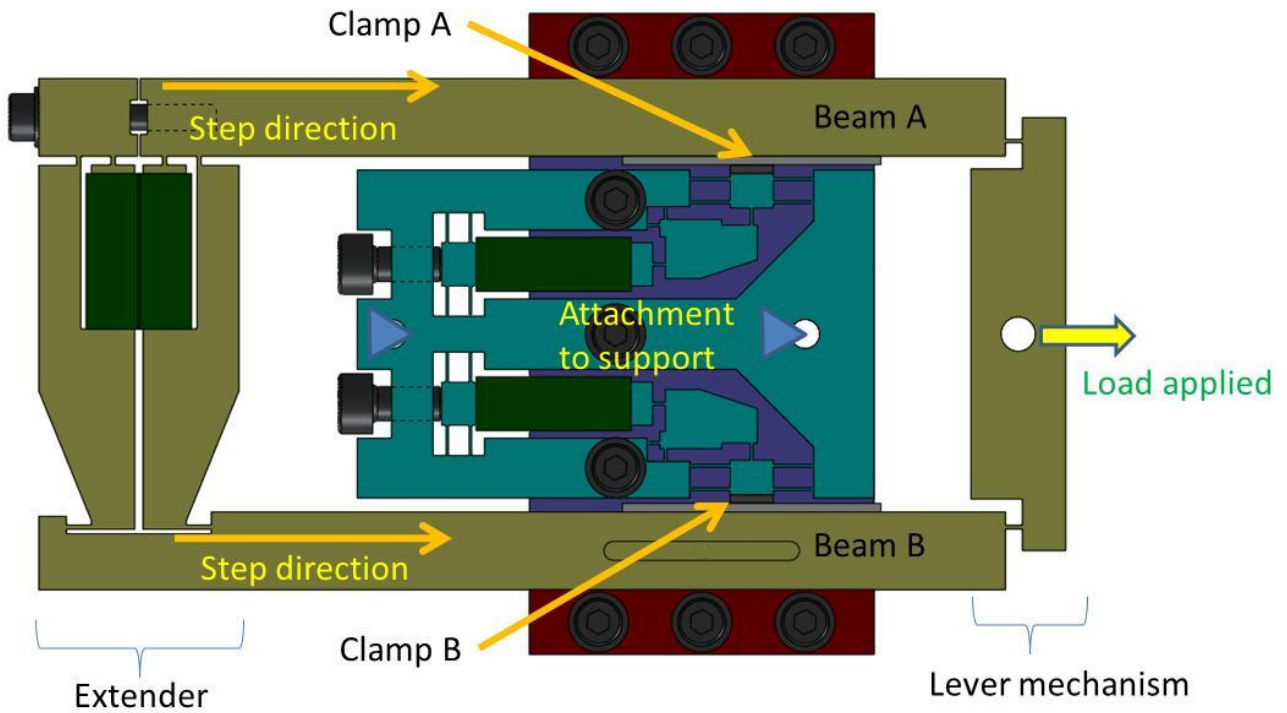


Figure 45: New IWM design showing the lever mechanism connecting both sides of the extender to the load

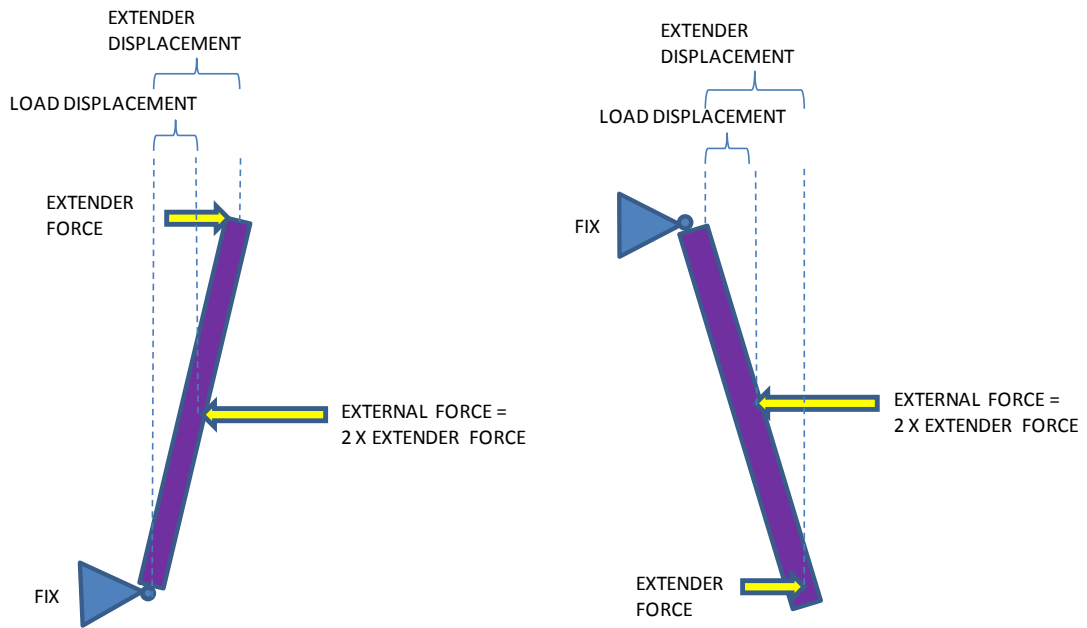


Figure 46: Diagram showing the action of the lever mechanism (two events)

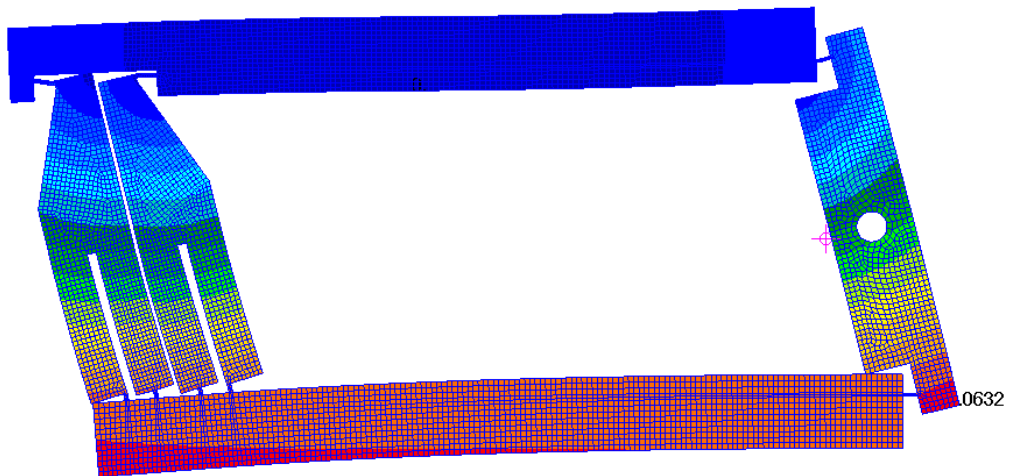


Figure 47: Finite element analysis showing the exaggerated action of the extender and lever mechanism (Blue is zero displacement, red is most displacement).

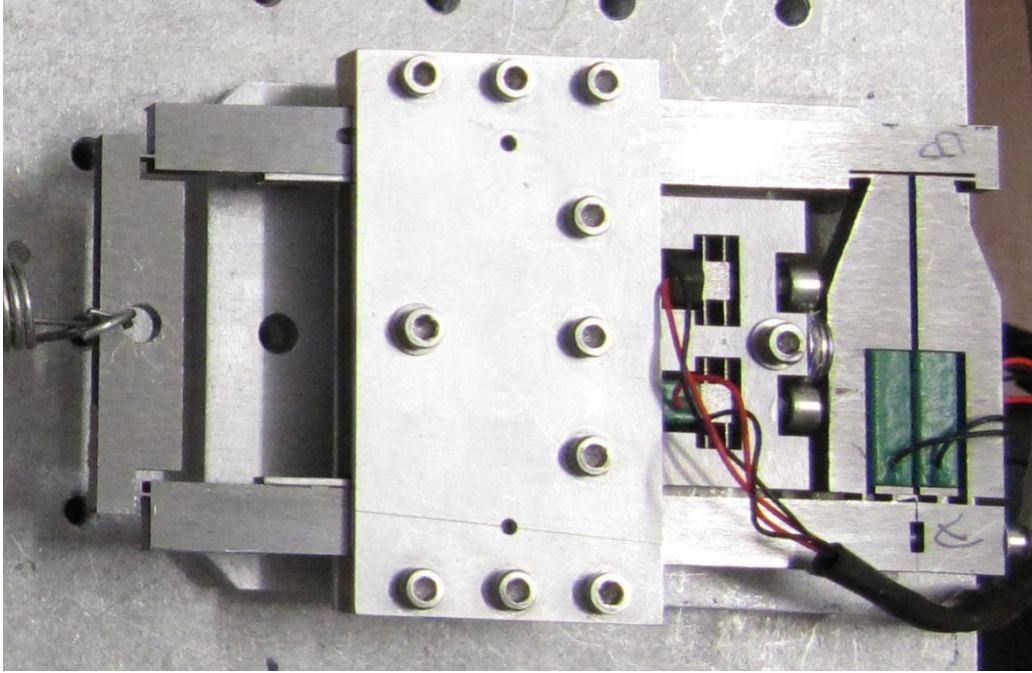


Figure 48: Photo of the IWM lever mechanism

4 Analysis of piezoelectric actuators

To calculate the load limit of a piezo electric actuator or an IWM, the blocked force and free displacement is required. Both of these can be calculated using a finite element analysis (FEA). Another approach is to use simple linear equations. If the stiffness's of the extender actuator and of the piezo stacks is known, the load limit of the extender and hence the IWM utilizing the extender can be determine. The stiffness's can be measured directly, or calculated using FEA. Both methods are shown in the following sections.

4.1 Finite Element Analysis (FEA)

MSC Nastran 2010 solver 101 was used for linear static analysis, solver 103 was used for modal analysis and solver 200 was used for the topology optimisation analysis. MSC Patran 2010 was used as the pre- and post-processor.

The piezo actuators presented often utilised flexures as pivots since a flexure has no backlash or dead zones. These flexures are typically as thin as 0.3 mm on a design with a global dimension in the order of 200 mm. Previous investigations have shown that when modelling thin flexures, at least two higher-order FEA elements (eight node quad elements) or three lower-order elements (four node quad elements) are required through the thickness of the member to accurately calculate stresses in such thin members. FEA stress values have been compared to simple beam theory hand calculations to reach these conclusions. (This investigation is not presented as part of this document.) The thickness of the flexures therefore determines the size and number of FEA elements required to analyse these small actuators. Four node and eight node quadrilateral plate elements with six degrees of freedom at each node were used in the analysis presented. The four node plate elements, known at QUAD4 elements in Nastran, were used in the topology analysis for the classical IWM (Appendix G). Since the results from the topology analysis have more than three elements at the flexure area, these elements were also used in the linear static analysis of this design. Eight node plate elements, known at QUAD8 elements in Nastran, were, however used in the design of the beam actuator motor which has thin flexures requiring at least two high-order elements through the thickness.

The use of the quadrilateral plate elements allowed three dimensional analyses, which were considered important for performing natural vibration modal analysis. A simpler two dimensional analysis would have missed natural vibration modes that involve out-of-plane motion.

Only the results are presented in the main body of this document, but more details of the FEA analysis are given in the appendix.

4.2 Principles of analysing a Piezo-electric element

A simple one-degree-of-freedom linear mathematical model of a piezo-electric element (stack) acting against an inertia mass, internal stiffness and external stiffness, is derived in Appendix C. This model can be used to evaluate frequency dependent characteristics, like calculating the first resonant frequency. When a piezoelectric element is used in static or quasi-static conditions, frequency and mass effects can be neglected and the static characteristics can be derived. The mathematical model shown in Figure 106 can be reduced to the model shown in Figure 49, where k_m is the external stiffness, k_p is the internal piezo stack stiffness, $f(t)$ is the applied force and $\delta(t)$ is the displacement.

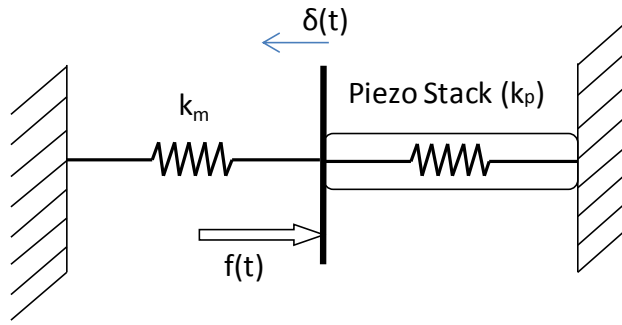


Figure 49: Mathematical model of a piezoelectric element acting against a mechanical stiffness load

Since induced-strain piezoelectric stacks have a finite internal stiffness, the application of an external spring load will always be accompanied by a loss of actuation displacement. The output displacement will thus only be a fraction of its free displacement (Giurgiutiu & Rogers, 1997). Using the stiffness ratio $r = \frac{k_m}{k_p}$, the output displacement is:

$$\delta = \frac{1}{1 + r} \cdot \delta_{free} \quad \text{Equation 4-1}$$

When the output displacement is known, the load capacity of the piezoelectric element can be calculated from Equation 2-9:

$$F_{ext} = F_b - k_p \cdot \delta.$$

A piezoelectric actuator can be viewed as a piezoelectric element with stiffness, within a structure with its own stiffness associated to it. This structure acts as an external spring force being applied to the piezoelectric element. From Equation 4-1 it can be seen that the output displacement of the piezoelectric element will diminish the larger the stiffness of this external structure. Once the output displacement is known, the force that the piezoelectric element can deliver can be calculated. These equations are graphically illustrated in Figure 50.

Characteristics of an Piezo Actuator

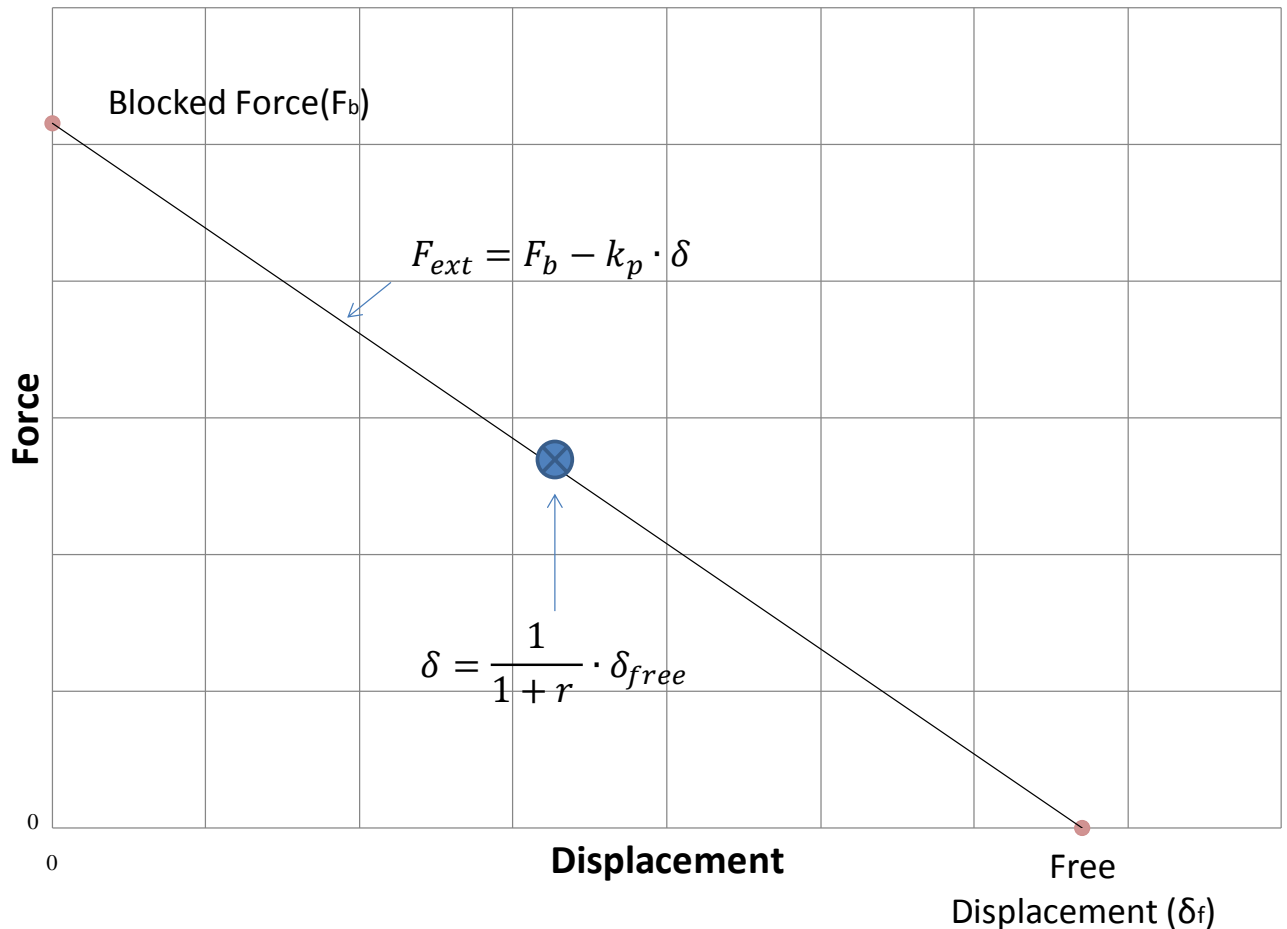


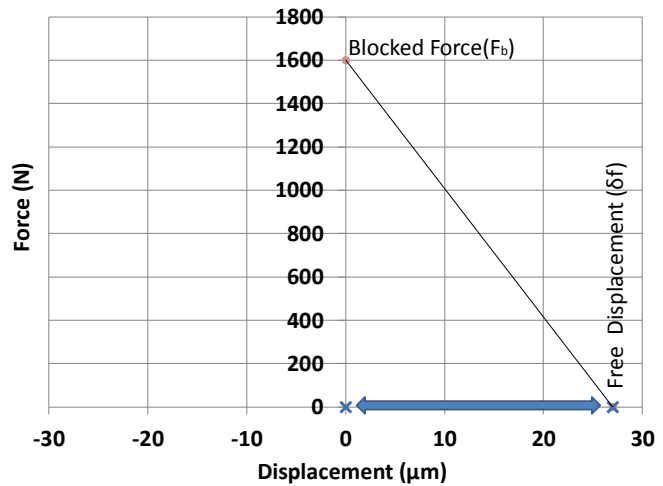
Figure 50: Theoretical limit of a piezo actuator

The “blocked force” is an abstract term since no constraint is infinitely stiff, and will always have some compliance, resulting in a produced load that is less than the blocked force. The blocked force is calculated by measuring the force and displacement at an arbitrary point and extrapolating to a point that represents the zero displacement of the actuator. The free displacement however, could be measured directly in the absence of any external load. Both the blocked force and free displacements is defined at a certain applied voltage. Typically, catalogue values is given at the maximum applied voltage range for a particular piezo element and should be adapted if the applied voltage is different from the voltage at which the blocked force and free displacement values is defined at.

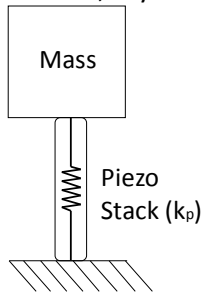
As an example, consider a piezoelectric stack undergoing the three different loading conditions. Table 1 illustrates the different displacement responses of a piezoelectric stack under a constant and proportional loading. The stack properties in Table 10 are used for this illustration. This example shows that regardless of the same magnitude load being applied through a stiffness (variable load), or as a constant load, the piezo stacks displacement reduced to a displacement less than its free displacement, but to the same displacement point relative to the zero loading reference position for both instances. This principle can similarly be applied to a piezo actuator.

Table 1: Different loading conditions applied to a piezo stack

1. No load is being applied. A cyclic control signal is applied to the stack that alters between the minimum and maximum voltage. The stack is displacing between the zero position and its free displacement position.



2. A constant load is applied by placing a mass on the stack, say 800N.



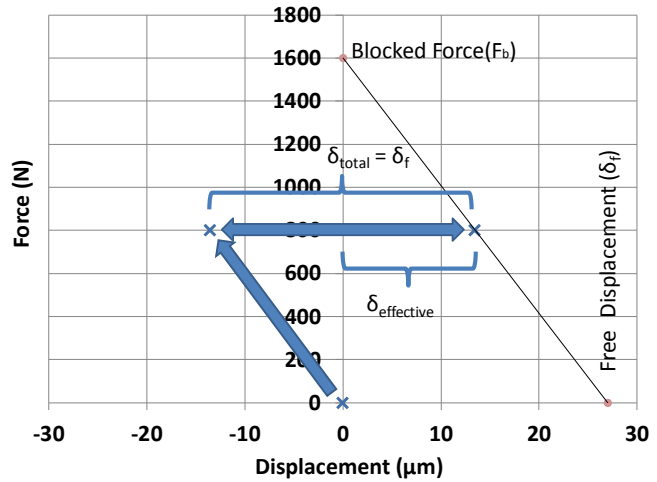
The load will compress the stack proportional to its internal stiffness (k_p).

$$\delta_{loaded} = \frac{F_{ext}}{k_p}$$

$$\delta_{loaded} = \frac{800}{59.3} = 13.5 \mu m$$

A cyclic control signal is again applied that alters between the minimum and maximum voltage. The stack will now displace from its compressed position, by an amount equal to its free displacement.

$$\delta_{total} = \delta_{free} = 27 \mu m$$



Note that the constant load applied does not alter the total displacement¹, but does affect the reference point from which the total displacement is viewed, and therefore the effective displacement. Also refer to Appendix A, and Figure 98.

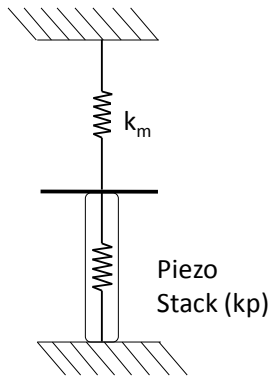
The effective displacement is therefore

$$\delta_{effective} = \delta_{free} - \delta_{loaded}$$

$$\delta_{effective} = 27 - 13.5 = 13.5 \mu m$$

¹ This is strictly speaking not accurate, since preloading the stack would slightly improve the piezoelectric constant and thus slightly increase the displacement.

3. The loading is applied through an external stiffness or spring. A cyclic control signal is again applied that alters between the minimum and maximum voltage.



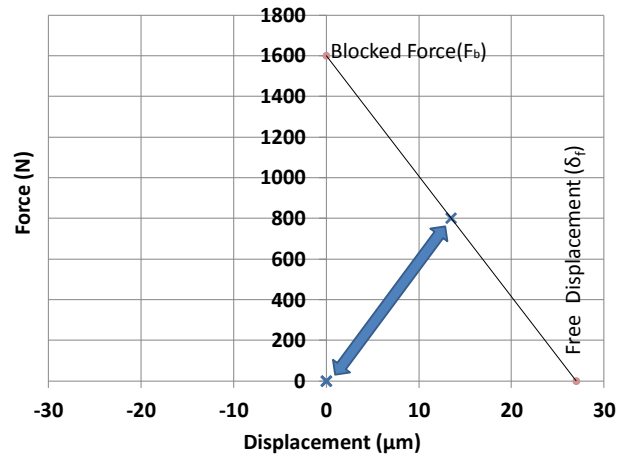
The spring prevents the stack from reaching its free displacement according to Equation 4-1

If we select the stiffness of the spring to limit the displacement to $13.5\mu\text{m}$, the external stiffness is calculated to be:

$$r = \frac{\delta_{free}}{\delta} - 1$$

$$r = \frac{27}{13.5} - 1$$

$$r = 1$$



$$\therefore k_m = k_p = 59.3\text{N}/\mu\text{m}$$

The force at the max displacement point is thus

$$F = k_m \cdot \delta$$

$$F = 59.3 \cdot 13.5$$

$$F = 800\text{N}$$

This is the same force magnitude as in the previous loading condition.

4.3 Analysis of the conventional IWM flextensional extender

The flextensional actuator is a well-known type of actuator and is often used as a way to amplify the small displacements of piezoelectric stacks (Newnham et al., 1993). This type of actuator is used for the IWM design since it is a proven concept and was considered low risk. Since the actuator can only be operated in tension, the IWM could only be used in a similar tension fashion when using the flextensional actuator as the extender. A compression force will result in the piezo stack being under tension, which is not allowed as it renders the device unusable.

The design consists of two piezoelectric stacks in series within a Stainless Steel 431 frame as shown in Figure 51. A topology optimisation finite element analysis (FEA) was done to determine the actual shape of the actuator (Appendix G). The actuator is designed to amplify the piezoelectric stack displacement by a factor of four. This amplification is an input for the topology optimisation, which then calculated the material distribution that would result in a minimum compliance design with such an amplification factor. A linear static FEA was then used to verify the displacement and the blocked force, and to calculate the stiffness and verify that the stresses are well below yield limits. An iterative process was followed between selecting a weighing factor for the material distribution problem that resulted in a

topology with sufficiently low stresses, i.e. the higher the weighing factor, the more elements in the FEA were removed from the initial design domain (Figure 109). Just enough elements were retained to result in a maximum stress limit of about 350 MPa. The stress limit of 350 MPa for Stainless Steel 431 is an in-house design rule of thumb, and has been empirically found through previous experience to be a good compromise between fatigue limitations and practical manufacturing constraints. A proper detailed investigation into this might result in a better stress value that could be used, but this was not attempted as part of the work presented here. Details of the FEA analysis can be found in appendix G. The results are summarised in Table 2.

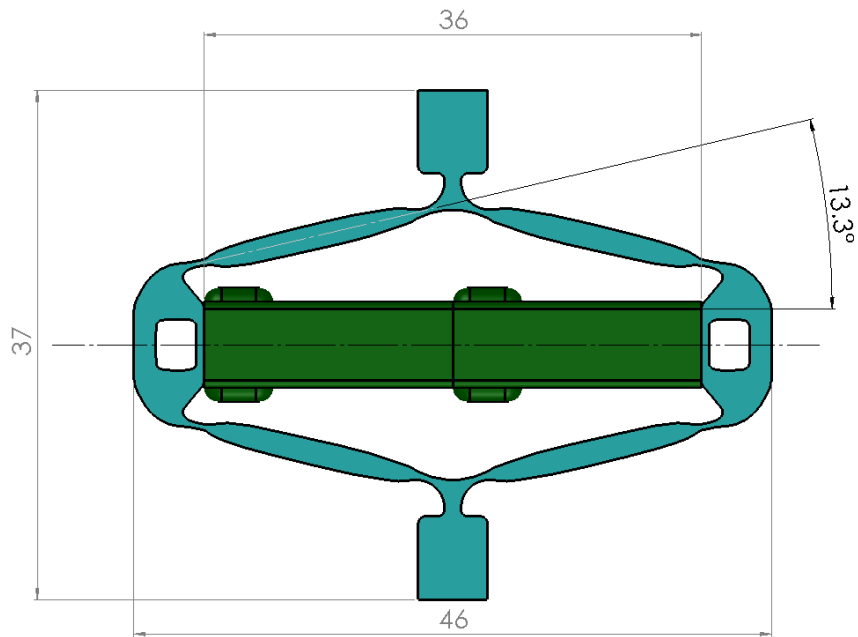


Figure 51: The flextensional actuator used in the conventional IWM design

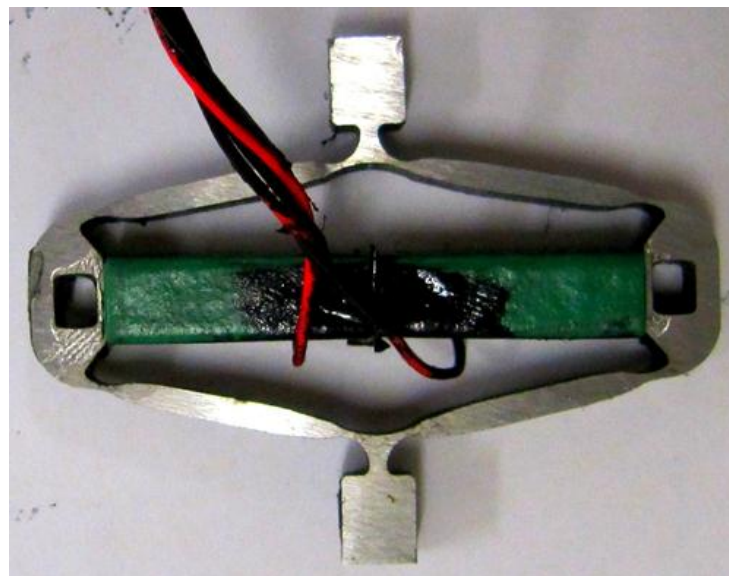


Figure 52: The manufactured flextensional actuator

Table 2: Summary of FEA results for the flextensional actuator

Blocked force	187.4 N
Free displacement	220 μm
Maximum stress (free displacement)	206 MPa
Maximum stress (blocked)	302 MPa
Stiffness in actuating direction	847.5 N/mm
Amplification (mechanical)	4.074

The blocked force and free displacement of the flextensional actuator may also be calculated using the theory developed in Section 4.2 provided the stiffness's is known. To apply the theory developed in Section 4.2, the flextensional actuator stiffness needs to be expressed by two stiffness values (see Figure 49). The first stiffness value represents the internal stiffness's of the piezo elements (k_p), while the second stiffness value represents the external stiffness of the frame (k_m). The stacks stiffness, k_p , may be calculated directly using the stiffness values from Table 10. To calculate the stiffness of the frame, a FEA analysis is constructed of the flextensional actuator. The details of the FEA are shown in Appendix G. To calculate k_m , the piezo stacks was represented with rigid FEA elements (see Figure 118). This was done so that the total stiffness of the FEA model equal the external stiffness of the frame, since the internal stack stiffness's is now effectively infinite. A unit force is applied and the displacement is calculated to be (Figure 119):

$$k_m = 1/5.6483 \cdot 10^{-4} = 1770.44 \text{ N/mm} \quad \text{Equation 4-2}$$

This stiffness is orders lower than the stiffness of the stack, and during free displacement conditions, the frame offers insignificant resistance to the displacement of the piezo stacks, so that the free displacement of the actuator is the free displacement of the two stacks combined, times the mechanical amplification of the frame ($\delta_{\text{free}} = 27 \mu\text{m}$, see Table 10).

$$\begin{aligned} \delta_{\text{flex_free}} &= 2 \times 27 \mu\text{m} \times 4.074 \\ \delta_{\text{flex_free}} &= 220 \mu\text{m} \end{aligned} \quad \text{Equation 4-3}$$

The free displacement calculated in this manner is the same as the free displacement calculated by the FEA (Table 2).

Before Equation 4-1 can be applied, the stiffness of the stacks first needs to be expressed at the same displacement position that the frame stiffness is expressed at, i.e. the mechanical amplification of the frame needs to be accounted for. The stack stiffness relative to the output position is derived in Appendix D and is given as:

$$k_{p_{\text{amp}}} = \frac{k_p}{N^2} \quad \text{Equation 4-4}$$

Where $N = 4.074$ is the amplification of the frame, and the stiffness k_p of the dual stacks is found in Table 10 to be:

$$\begin{aligned} k_p &= \frac{59.3 \cdot 10^3}{2} \\ k_p &= 29650 \text{ N/mm} \end{aligned}$$

Therefore

$$k_{p_amp} = \frac{29650}{4.074^2}$$

$$k_{p_amp} = 1786.42 \text{ N/mm}$$

The stiffness ratio is thus:

$$r = \frac{k_m}{k_{p_amp}}$$

Equation 4-5

$$r = \frac{1770.44}{1786.42} = 0.991$$

The free displacement at maximum applied voltage range of -30V to +150V of the two piezo stacks combined is $\delta_{free} = 2 \cdot 27 = 54 \mu\text{m}$ (from Table 10). Using Equation 4-1 and adapting it to account for the mechanical amplification, δ_{flex} is calculated as:

$$\delta_{flex} = \frac{1}{1+r} \cdot (\delta_{free} \cdot N)$$

$$\delta_{flex} = \frac{1}{1+0.991} \cdot (54 \cdot 4.074)$$

Equation 4-6

$$\delta_{flex} = 110.5 \mu\text{m}$$

To calculate the blocked force of the actuator, the compliance of the frame needs to be accounted for. This is done by viewing the actuator blocked force as an external force being applied to a rigid frame. If the frame was indeed rigid, the blocked force would have simply been the blocked force of the stacks, divided by the amplification. The blocked force of the actuator can thus be calculated by adapting Equation 2-9.

$$F_{flex_blocked} = \frac{F_{b_stack}}{N} - k_{p_amp} \cdot \delta_{flex}$$

$$F_{flex_blocked} = \frac{1600}{4.074} - 1786.42 \cdot 110.5 \cdot 10^{-3}$$

Equation 4-7

$$F_{flex_blocked} = 195.34 \text{ N}$$

The theoretical blocked force of the flextensional actuators calculated using the individual stiffness's compared reasonably well with the FEA-calculated blocked force of 187.4 N presented in Table 2.

Another approach is to consider the stiffness of the piezo stacks as a spring in series with the second frame stiffness condition. This approach is shown for interest sake. Applying the springs-in-series equation gives the following value:

$$\frac{1}{k_{flextensional}} = \frac{1}{k_m} + \frac{1}{k_{p_amp}}$$

Equation 4-8

$$\frac{1}{k_{flextensional}} = \frac{1}{1770.44} + \frac{1}{1786.42}$$

$$k_{flexional} = 889.2 \text{ N/mm}$$

The total flexional stiffness compares reasonably with the FEA value of 847.5 N/mm (Table 2).

4.4 Analysis of the IWM design with force duplicator mechanism

The use of a piezoelectric beam actuator makes for a simpler integration with the beam mechanism, which is the characteristic feature of the extender of this innovative IWM (Figure 53). The relative positions, lengths and thicknesses of the flexures are calculated using an in-house developed optimisation algorithm (Loveday, 2003). An amplification of ten times is the input to the algorithm. A linear static FEA was used to verify the displacement and the blocked force, and to calculate the stiffness and verify that the stresses are well below yield limits (less than 350 MPa as a design goal). Details of the FEA analysis can be found in Appendix H. A summary of the results is shown in Table 3.

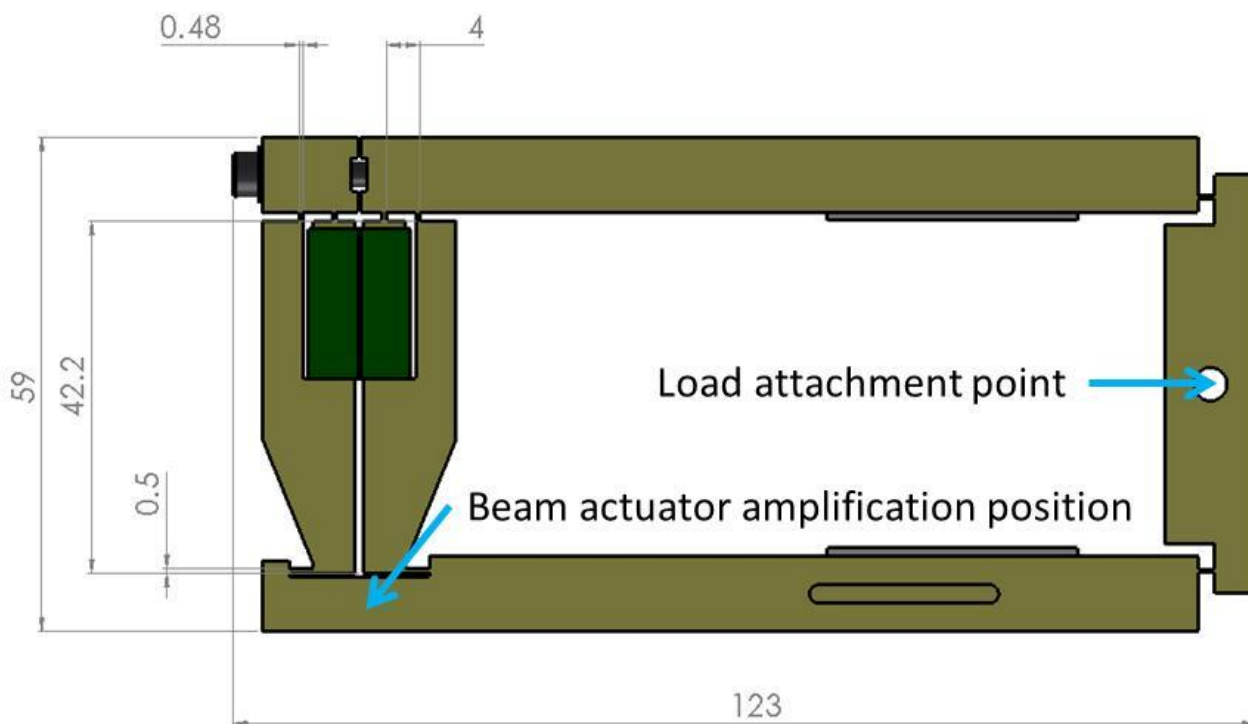


Figure 53: The beam actuator with the beam mechanism used in the IWM with force duplicator

Table 3: Summary of FEA results for the beam actuator with force duplicator mechanism

Blocked force (at load attachment point)	103 N
Free displacement (at load attachment point)	134 μm
Maximum stress (free displacement)	240 MPa
Maximum stress (blocked)	342 MPa
Stiffness in actuating direction (at load attachment point)	768 N/mm
Amplification (beam mechanical)	9.92
Amplification (at load attachment point)	4.96

As before, the blocked force and free displacement of the beam actuator with force duplicator may also be calculated using the theory developed in Section 4.2 provided the stiffness's is known. Again the theory developed in Section 4.2 is applied by expressing the beam actuator by two stiffness values similar as for the flextensional actuator in section 4.3 (also see Figure 49). The first stiffness value represents the internal stiffness's of the piezo elements (k_p), while the second stiffness value represents the external stiffness of the frame (k_m). To find the stiffness of the structure without the influence of the stacks, the elements representing the piezo stacks in the FEA model are replaced with rigid elements (see Appendix H and Figure 131). A unit force is applied at the load attachment point and the stiffness relative to this point is calculated to be (Figure 132):

$$k_m = 1/9.335 \cdot 10^{-4} = 1071.2 \text{ N/mm} \quad \text{Equation 4-9}$$

The two stacks used in this actuator are placed in parallel and therefore the displacement is not added as with the previous actuator. The free displacement of the beam actuator (between the top and bottom beam) is the free displacement of the stack, times the mechanical amplification of the frame ($\delta_{free} = 27 \mu\text{m}$, see Table 10).

$$\delta_{beam_free} = 27 \mu\text{m} \times 9.92 \quad \text{Equation 4-10}$$

$$\delta_{beam_free} = 268 \mu\text{m}$$

The free displacement calculated in this manner is the same as the free displacement calculated by the FEA, taking into account the half reduction due to the beam mechanism action (Table 3).

Before Equation 4-1 can be applied, the stiffness's of the stacks first needs to be expressed at the same displacement position at which the frame stiffness is expressed, i.e. the mechanical amplification of the frame needs to be accounted for. For this actuator, the reduction caused by the beam mechanism also needs to be accounted for. The amplification between the stacks in the extender and the load attachment point is thus $N = \frac{9.92}{2} = 4.96$. Applying Equation 4-4:

$$k_{p_{amp}} = \frac{59.3 \cdot 10^3 \cdot 2}{4.96^2} \quad \text{Equation 4-11}$$

$$k_{p_{amp}} = 4820.8 \text{ N/mm}$$

The stiffness ratio is:

$$r = \frac{k_m}{k_{p_{amp}}} \quad \text{Equation 4-12}$$

$$r = \frac{1071.2}{4820.8} = 0.222$$

Applying Equation 4-1:

$$\delta_{dup} = \frac{1}{1+r} \cdot (\delta_{free} \cdot N)$$

$$\delta_{dup} = \frac{1}{1+0.222} \cdot (27 \cdot 4.96) \quad \text{Equation 4-13}$$

$$\delta_{dup} = 109.6 \mu m$$

To calculate the blocked force of the actuator, the compliance of the frame needs to be accounted for. This is done by viewing the actuator blocked force as an external force being applied to a rigid frame. If the frame was indeed rigid, the blocked force would have simply been the blocked force of the stacks, divided by die amplification. The blocked force of the actuator can thud be calculated using Equation 2-9 similar as with the flextensional actuator:

$$F_{dup_blocked} = \frac{F_{b_stack}}{N} - k_{p_amp} \cdot \delta_{dup}$$

$$F_{dup_blocked} = \frac{1600 \cdot 2}{4.96} - 4820.8 \cdot 109.6 \cdot 10^{-3} \quad \text{Equation 4-14}$$

$$F_{dup_blocked} = 116.8 N$$

Another approach is to consider the stiffness of the piezo stacks as a spring in series with the second frame stiffness condition. Applying the springs-in-series equation, we obtain:

$$\frac{1}{k_{beam}} = \frac{1}{k_m} + \frac{1}{k_{p_amp}}$$

$$\frac{1}{k_{beam}} = \frac{1}{1071.2} + \frac{1}{4820.8} \quad \text{Equation 4-15}$$

$$k_{beam} = 876.4.0 N/mm$$

The total beam actuator stiffness compares acceptably with the FEA value of 768 N/mm (Table 3).

5 Testing the IWM extenders used for the IWM extenders

5.1 Testing of the flextensional actuator

Before the actuators are assembled into an IWM, their performance is first measured independently and compared with the calculated values. Since any experimental setup will have some compliance, the blocked force cannot be measured directly. Only the free displacement and actuator stiffness is therefore measured.

To measure the free displacement, one end of the actuator is clamped while the other can displace freely. A laser vibrometer is aimed at the other end (Figure 54) (see Appendix I for a list of test equipment). A -30 V to 150 V sine signal at 3 Hz is supplied to the actuator using a function generator and a PosiCon amplifier. The laser vibrometer suffers from integration drift when attempting to measure at static conditions, which is why a slow sine wave, below the first natural vibration mode of the structure is used instead.



Figure 54: Free displacement measurement set-up

For the stiffness measurement, the actuator is slowly pulled while recording the force applied and the displacement across the actuator ends. For this, the actuator was taken to the CSIR structural laboratory and placed in an Instron Servohydraulic mechanical testing machine. The force was recorded using the Instron's internal load cell, and the displacement was measured using a clip gauge. The slope of the force–displacement line is the stiffness of the actuator being tested. The load was applied at a rate of less than 0.1 mm/min and up to a load of about 100 N.

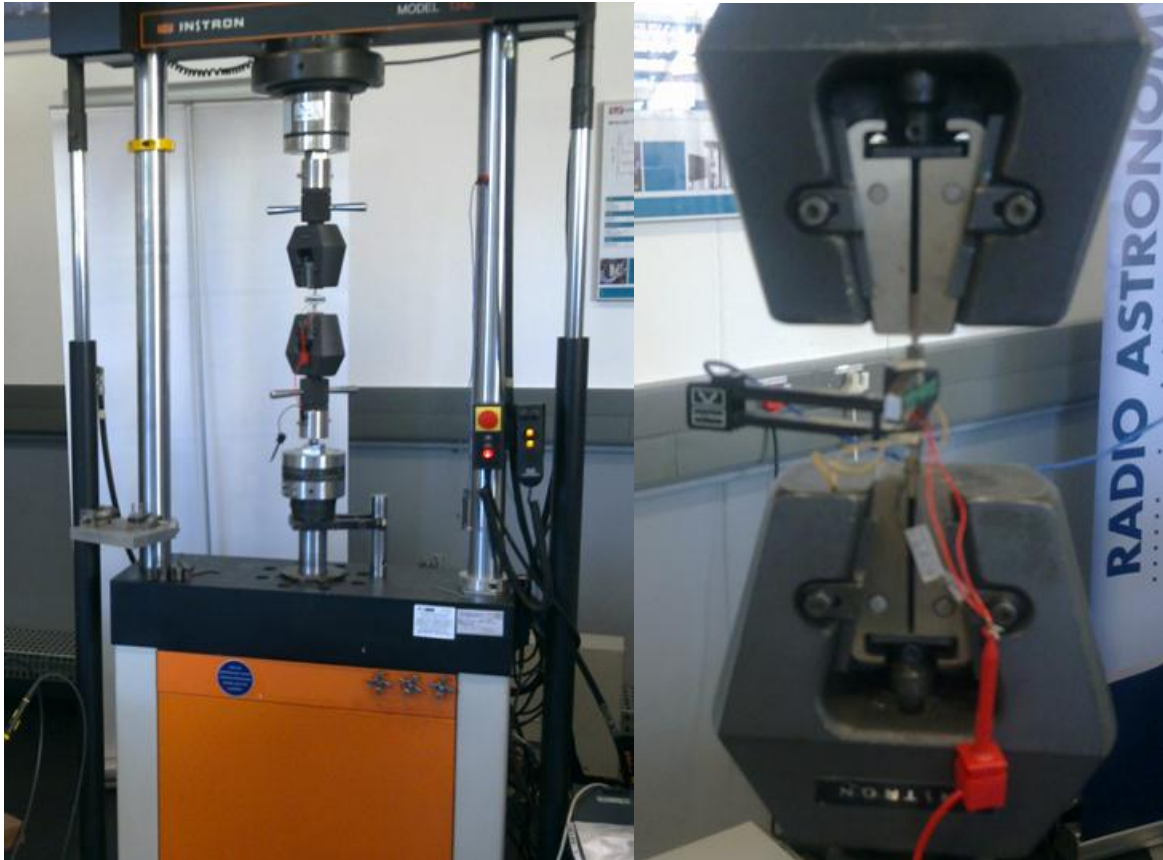


Figure 55: Flextensional actuator in Instron Servohydraulic mechanical testing machine during stiffness testing

The response of the actuator when supplied with a -30 V to +150 V sine wave is shown in Figure 56. The frequency of the sine wave was 3 Hz, well below the first natural frequency of the actuator at 831 Hz (Figure 120) so that no dynamic effects are present. The measured free displacement is 224.5 μm , which correlates with the calculated free displacement (220 μm).

A linear best-fit regression line through the measured data obtained during the stiffness testing had a slope of 395.2 N/mm as shown in Figure 57. This is significantly less than the calculated stiffness of 847.5 N/mm (Table 2).

One way to calculate the actual blocked force is to multiply the calculated blocked force with the ratio between the measured stiffness and the calculated stiffness (Table 2). The free displacement has not been affected by the difference in stiffness.

$$F_{b_conv1} = 187.4 \cdot \frac{395.2}{847.5}$$

Equation 5-1

$$F_{b_conv1} = 87.4\text{N}$$

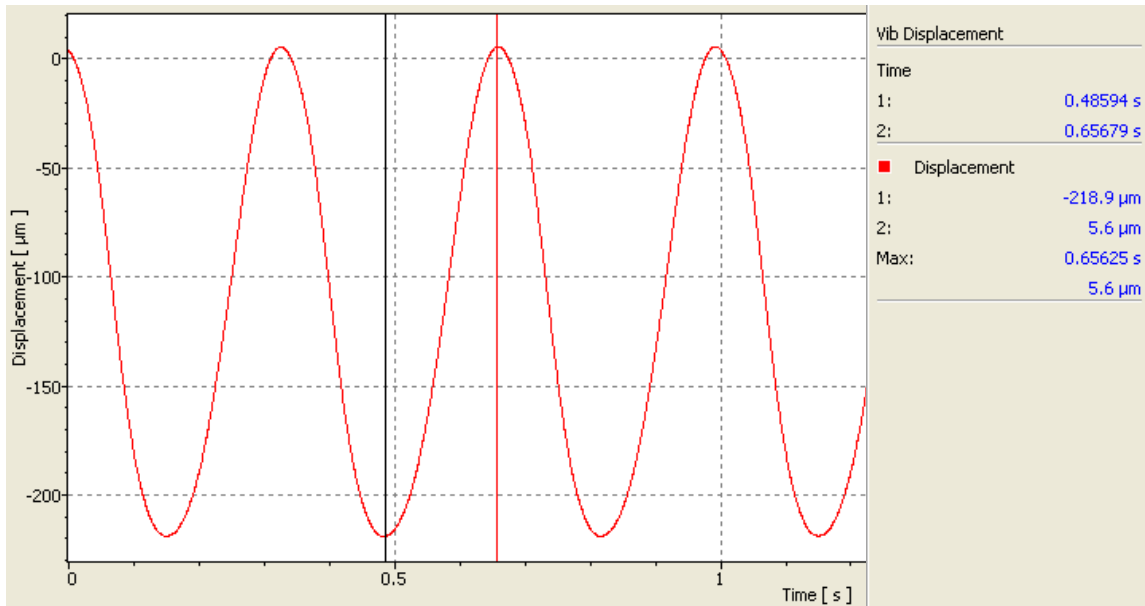


Figure 56: Free displacement laser measurement within the motor

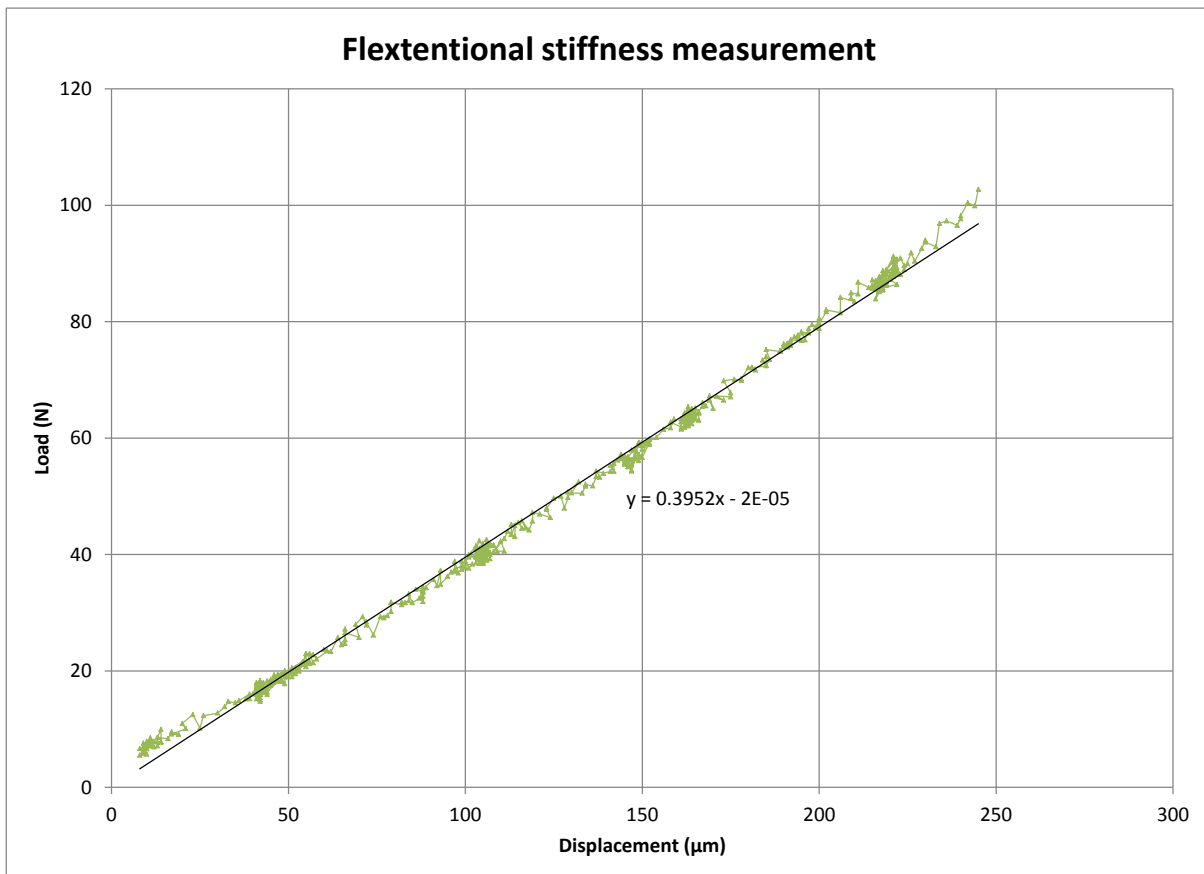


Figure 57: Measured stiffness data and regression line of the flextensional actuator

In an attempt to explain the difference between the calculated and analysed stiffness, three possible causes were identified and investigated. Since these investigations provide further insight into the design and workings of flextensional actuators, each is discussed in more detail in the following section.

The possible causes are:

1. Geometrical difference between the tested and analysed geometry of the thin flexure section of the actuator frame.
2. A possible change in the stiffness of the actuator due to the arms of the actuator being at different angles to the design used in the FEA.
3. The attachment ends of the actuator not being collinear with each other.

It should be mentioned that stiffness loss due to the interface between the piezo-stack and the metal structure have also been investigated, and was found to have a negligible effect. This investigation is not presented as part of this document.

5.1.1 Investigation into the effect on stiffness due the thickness differences of the flexures

Comparing the actual flextensional actuator with the CAD models, it was observed that the flexure's thickness at its thinnest position varied from 0.35 mm to 0.65 mm. The intended thickness of the design was 0.4 mm (Figure 58).

To evaluate the effect of this discrepancy, the flexures in the FEA model were changed by removing a row of elements from the flexure region with a thickness of 0.1mm, i.e. the remaining flexures' thickness was 0.3 mm. The stiffness calculation showed an insignificant change in stiffness value from 847.5 N/mm (Table 2) to 846.3 N/mm due to the thinner flexures. The change in the flexures' thickness between the initial analysis and the tested geometry is unlikely to account for the lack of stiffness.

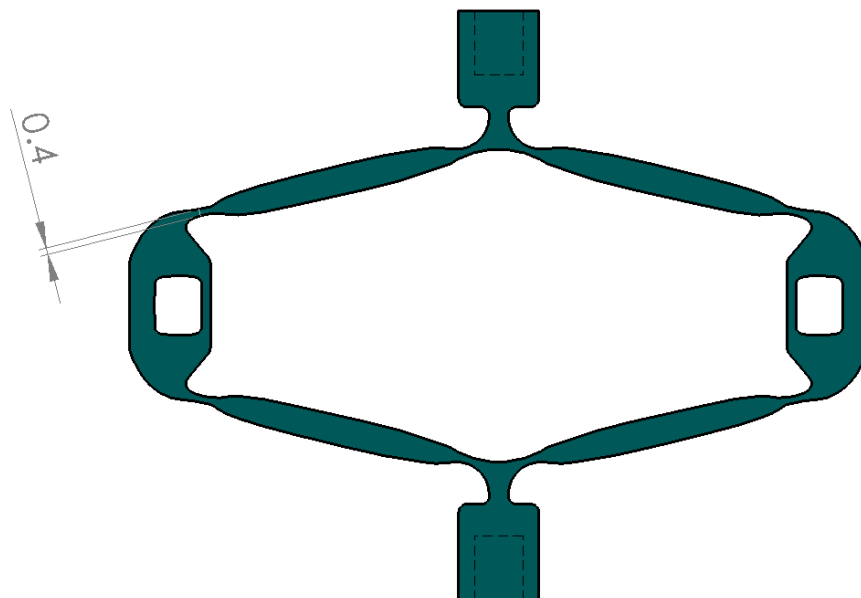


Figure 58: Flexure thickness

5.1.2 Investigation into the effect of the flextensional arms being at different angles

The installation of the piezo stacks in the stainless steel frame resulted in a shape change of the flextensional actuator. This meant that the geometry that was analysed was different from the geometry that was tested. The most notable change was that the arms of the frame were at a different angle than that which was intended. To evaluate the effect of this, a new FEA model was constructed, which was the same as the previous model, except that the angle of the arms was changed so that the overall height of the actuator resembled the actual part (Figure 59). A unit force was again applied (Figure 60) and the stiffness was calculated as:

$$k_m = 1/2.08 \cdot 10^{-3} = 480.8 \text{ N/mm} \quad \text{Equation 5-2}$$

It is clear that the difference between the shape of the designed and tested actuator is a major contributor to the differences in stiffnesses when comparing the initial value of 847.5 N/mm (Table 2) with the adjusted calculated value of 480.8 N/mm, although it is still short of the measured stiffness of 395.2 N/mm (Figure 57).

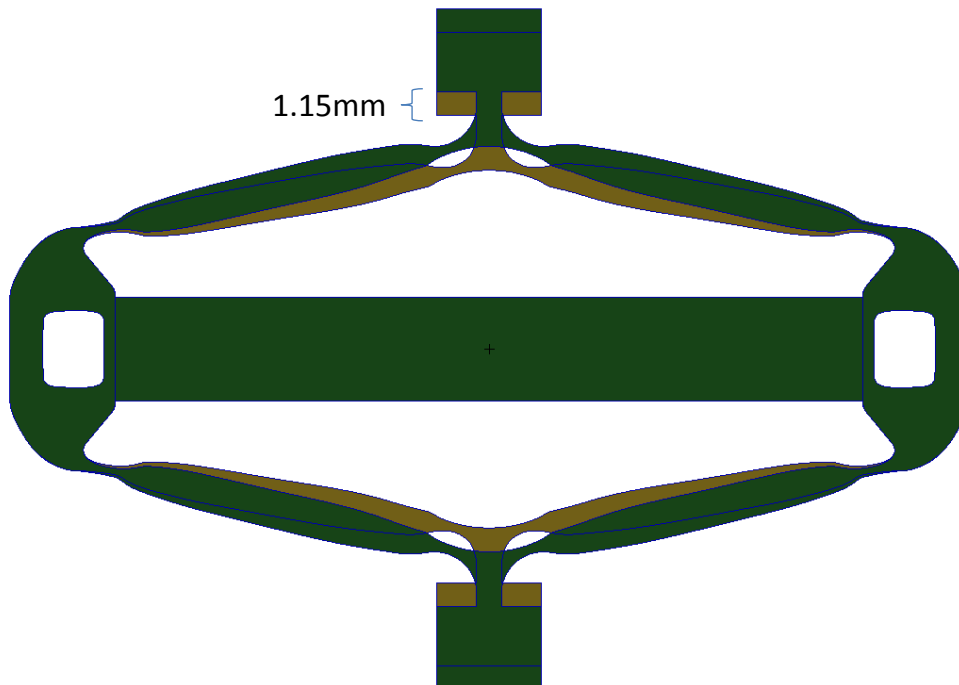


Figure 59: Initial (green) and adjusted geometry (brown) used in the analyses

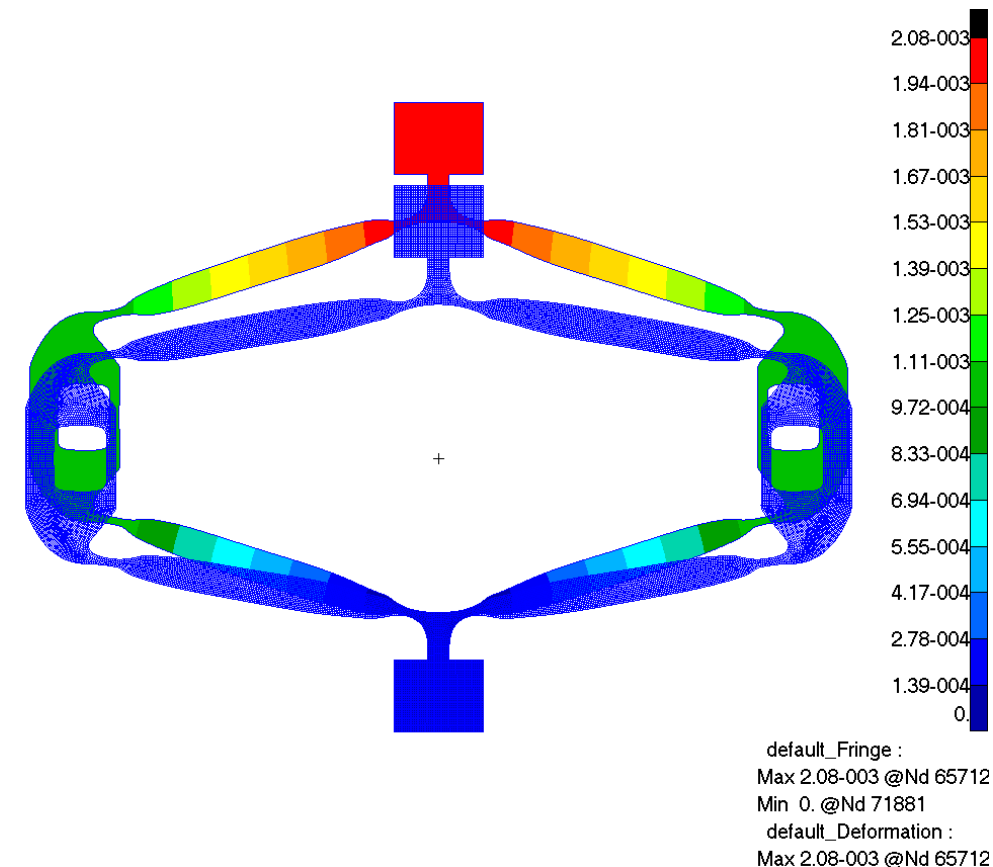


Figure 60: Displacement due to a unit force applied to the adjusted geometry

5.1.3 Investigation into the effect of the attachment ends of the actuator not being aligned

In the previous section it is shown that the differences in the geometry of the arms of the structure have a significant effect on the stiffness of the structure. To investigate if other geometric discrepancies could account for the missing stiffness, an attempt was made to further improve the geometric representation of the actual structure in the FEA. By tracing the outlines of the actuator, and using it to build a new model to be used in a new FEA, a more representative geometry was achieved (Figure 61). Note that this operation followed after the angle of the arms was corrected by plastically deforming the device, so that the arms were the same as the (original) analysed geometry. The stiffness of the actual device should now represent the stiffness associated with the analysed geometry (Table 2).

A unit force was again applied and the stiffness is calculated as:

$$k_m = 1 / 1.33 \cdot 10^{-3} = 751.9 \text{ N/mm} \quad \text{Equation 5-3}$$

As can be seen in Figure 62, the structure is unsymmetrical and also responds unsymmetrically. A loss of stiffness is still associated with this unsymmetrical behaviour when compared to the initial value of 847.5 N/mm (Table 2). This unsymmetrical behaviour is the likely culprit causing the stiffness loss.

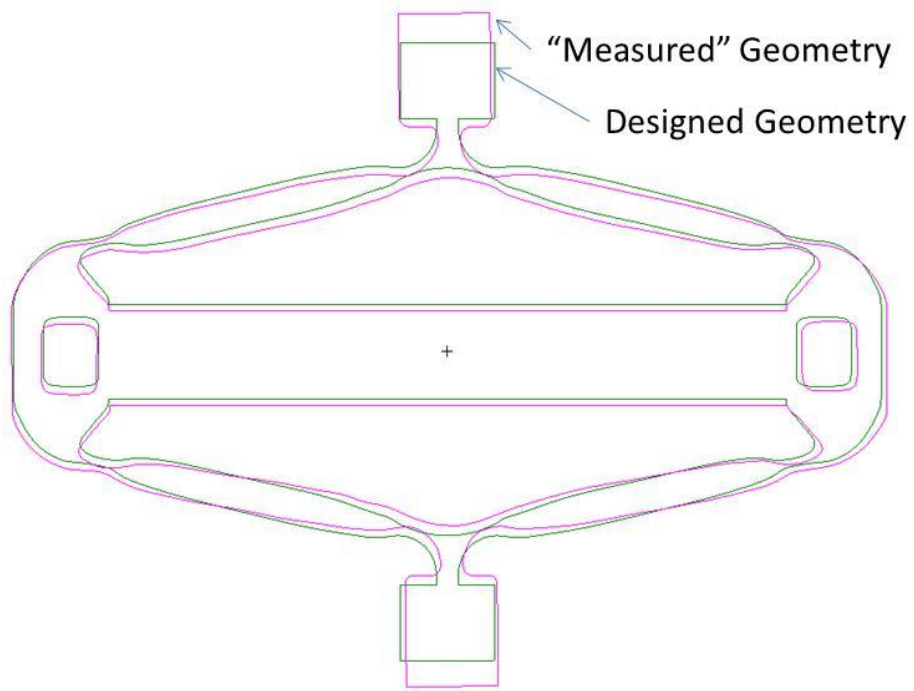


Figure 61: Designed (green) and traced geometry (magenta) of the flextensional actuator

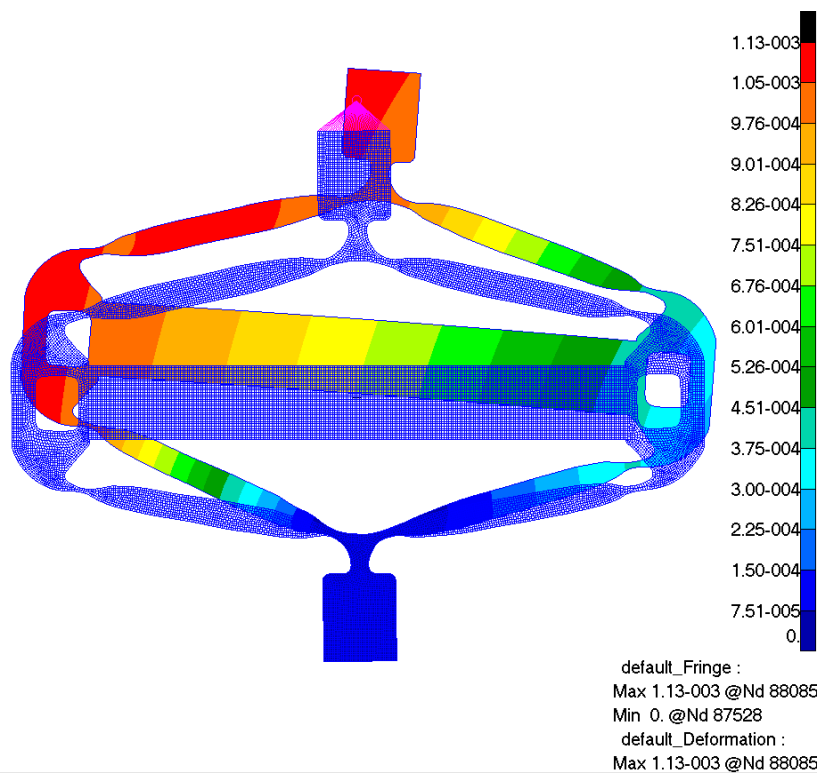


Figure 62: Deformation of traced geometry

5.2 Testing an improved flextensional actuator

Further investigations into the cause of the geometrical discrepancies revealed that material deformation due to insufficient support during the wire cutting manufacturing of the structure was to blame. Another attempt was made at manufacturing a second frame. Two changes were made to the manufacturing process, but the design was kept the same. Firstly, the material was stress-relieved through heat treatment prior to wire cutting. Secondly, small structural supports were introduced at crucial positions to support the frame during cutting, and only removed after the final machining operation. This ensured a much more symmetrical frame and better agreement with the designed geometry.

After manufacturing, the frame was scanned using a 3D scanner. The scanned data were then used in a new FEA to show that the theoretical analysis and the practical testing did correlate. In Figure 63 the design geometry and the geometry resulting from the scanned data is overlaid, showing a much-improved comparison.

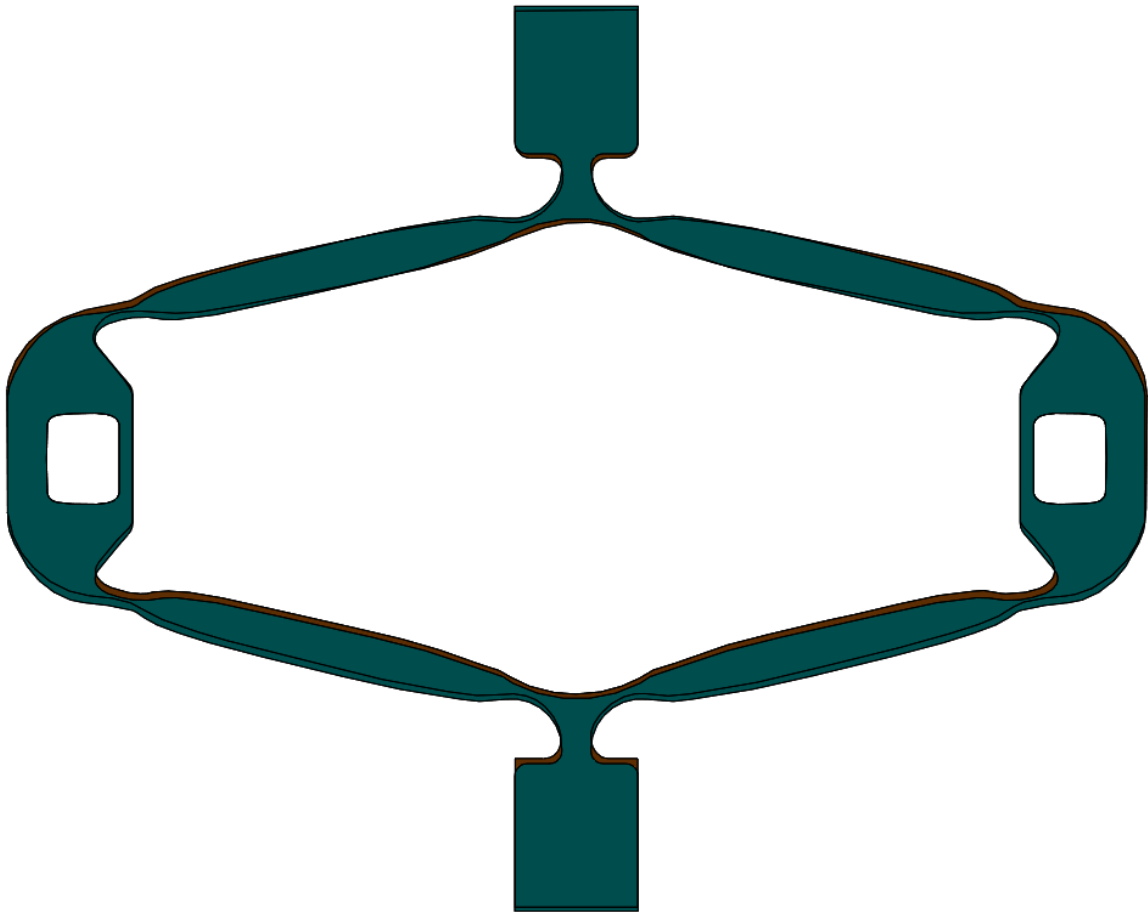


Figure 63: Comparison between the designed geometry (green) and the new geometry (brown) after manufacturing improvements

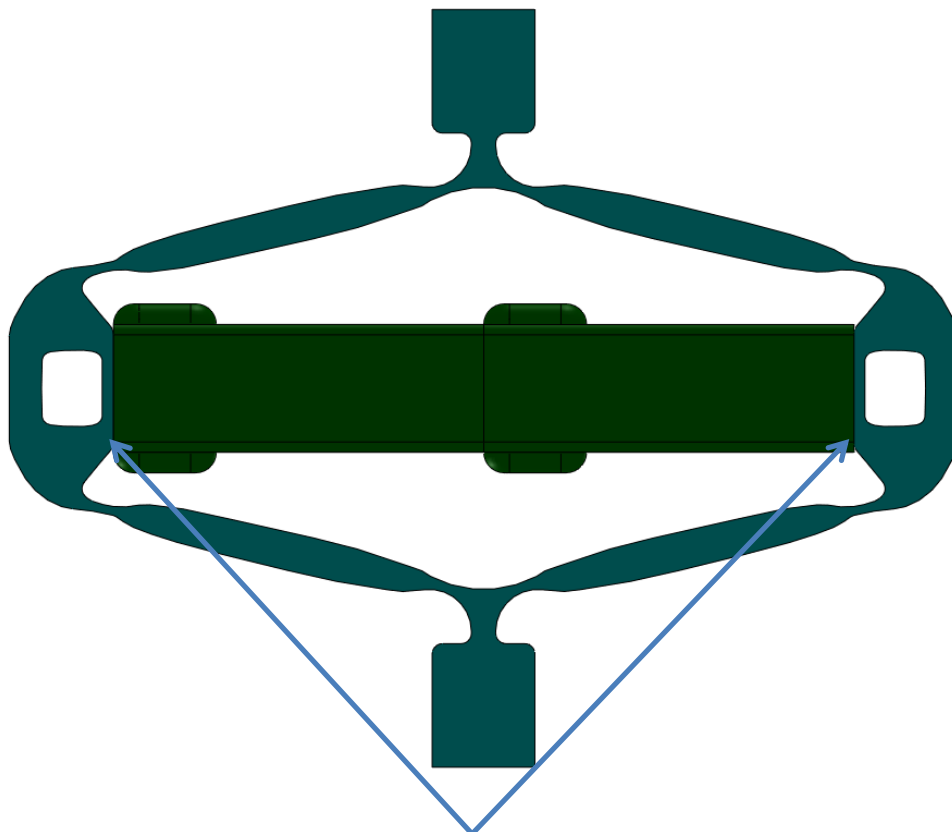
A new FEA mesh was created based on the scanned geometry. The displacement response of the FEA showed that the structure behaves symmetrical as intended. The results from the FEA are shown in Table 4.

Table 4: Summary of FEA results for the second flextensional actuator

Blocked force	160.9 N
Free displacement	231 μm
Maximum stress (free displacement)	233 MPa
Maximum stress (blocked)	559 MPa
Stiffness in actuating direction	694.4 N/mm
Amplification (mechanical)	4.278

In a similar manner as in Section 5.1, the stiffness of the second flextensional actuator was measured. The result is shown in Figure 65. It appears that the stiffness of the actuator increased with applied load. Initially, the stiffness was about 190 N/mm, and increased until about 50 N, after which it appeared to become linear. The stiffness from 50 N to about 100 N was 664.5 N/mm as shown in Figure 65.

Closer inspection shows the presence of gaps between the piezo stacks and the stainless steel frame due to unparallel surface on the frame. The location of the gaps is shown in Figure 64. These gaps are the likely cause of the change in stiffness observed during testing. As the applied load increases, the gaps get smaller. Once the gaps have fully closed, the structure behaves more linearly and at its intended stiffness.



Gaps due to un-parallel surfaces

Figure 64: Location of gaps

The measured stiffness of 664.5 N/mm of the linear part of the data from about 50 N compared reasonably well with the calculated stiffness of 694.4 N/mm. The changes introduced into the manufacturing process were successful, although new issues concerning gaps between contacting surfaces arose. Provided that accurate and applicable geometry is used in the FEA, the linear static analysis methodology is shown to be a sufficiently useful tool to analyse the behaviour and predict the stiffness, free displacement and stresses of this type of structure for IWM applications. The adjusted blocked force was again determined by scaling the calculated blocked force with the ratio between the measured and calculated stiffnesses, thus:

$$F_{b_conv2} = 160.9 \cdot \frac{664.5}{694.4}$$

Equation 5-4

$$F_{b_conv2} = 154.0N$$

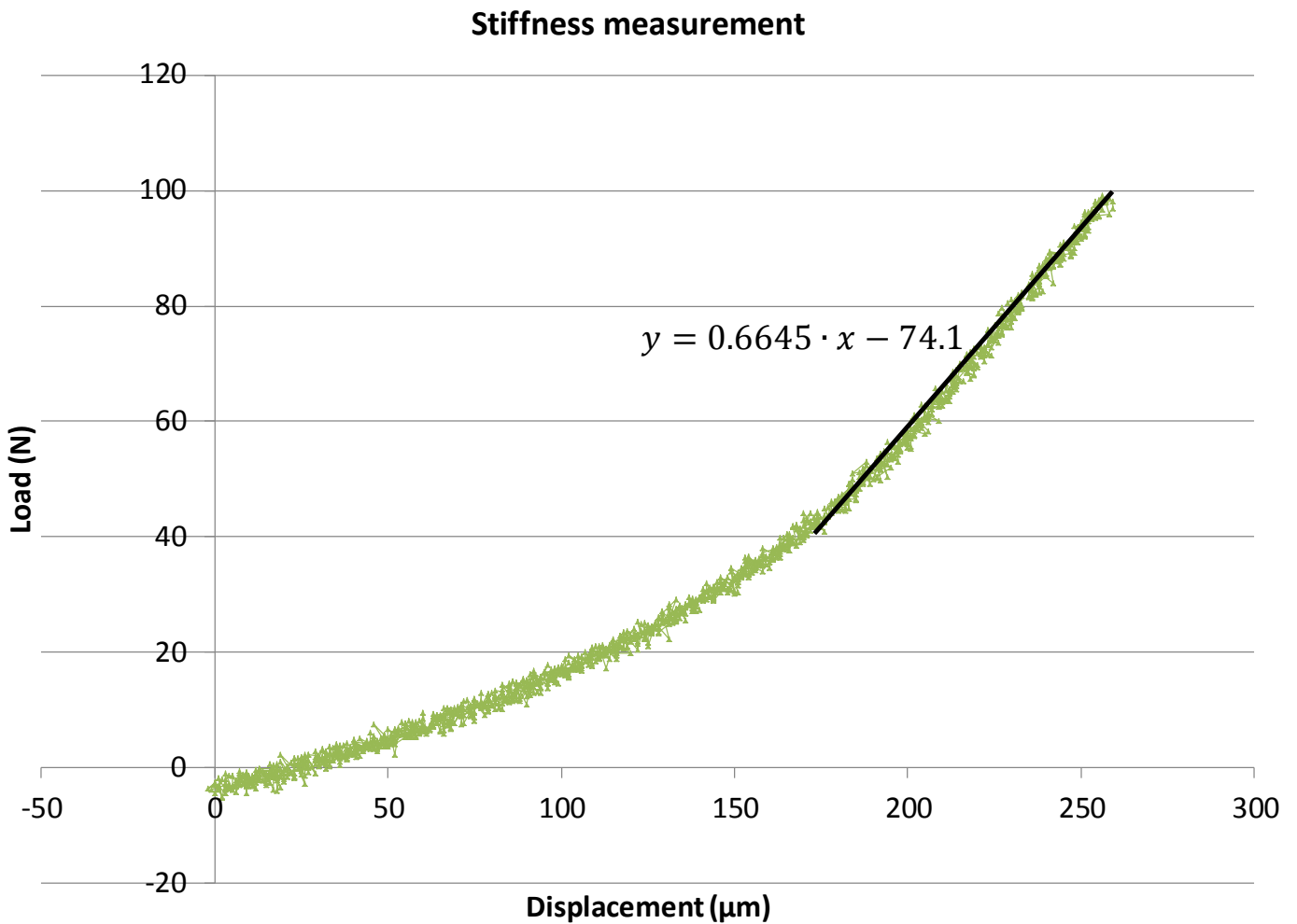


Figure 65: Stiffness measurement of the second flextensional actuator

5.3 Testing of the beam actuator used in the IWM design with force duplicator mechanism

To verify the working of this extender, the free displacement was measured using OFV-552 Fiber Vibrometer laser (Figure 66). A -30V to +150V excitation at 10 Hz frequency sine wave input was supplied to the extender. The signal was generated using a signal generator, and amplified with the PosiCon power amplifier. A custom-built inverter was used to invert and split the signal before amplifying it to supply oppositely phased signals to the two piezo stacks in the extender. The signal supplied and the displacement measured was captured with a Tektronic oscilloscope (Figure 67). The output scale of the displacement signal is 1 mm/V. The measured displacement was 288 μm and compared adequately with the calculated free displacement of 268 μm . The free displacement of the actuator at the load attachment point is thus $\frac{288}{2} = 144 \mu\text{m}$.

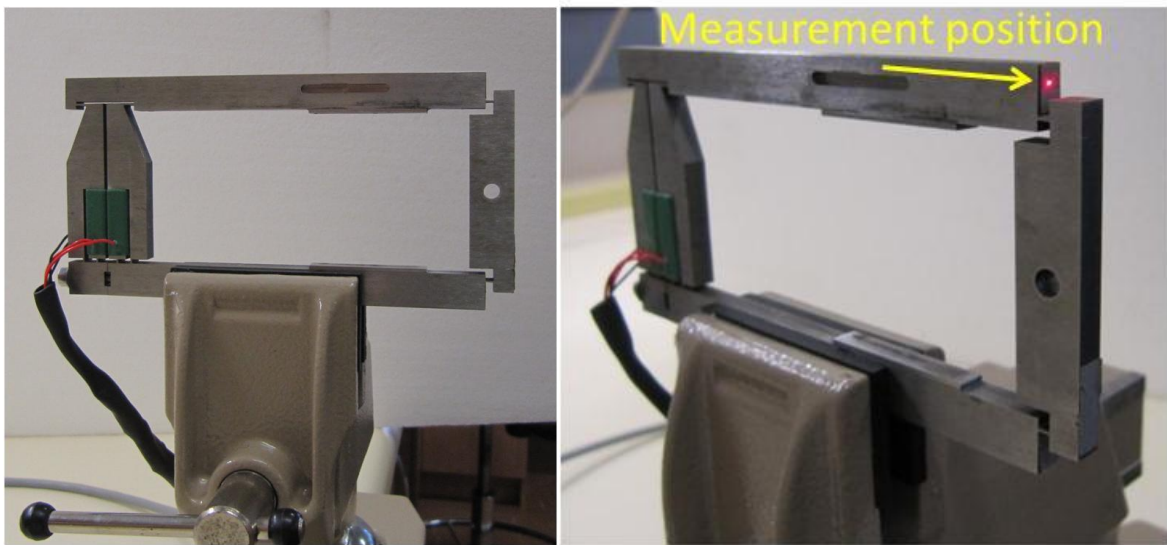


Figure 66: Free displacement testing of the extender

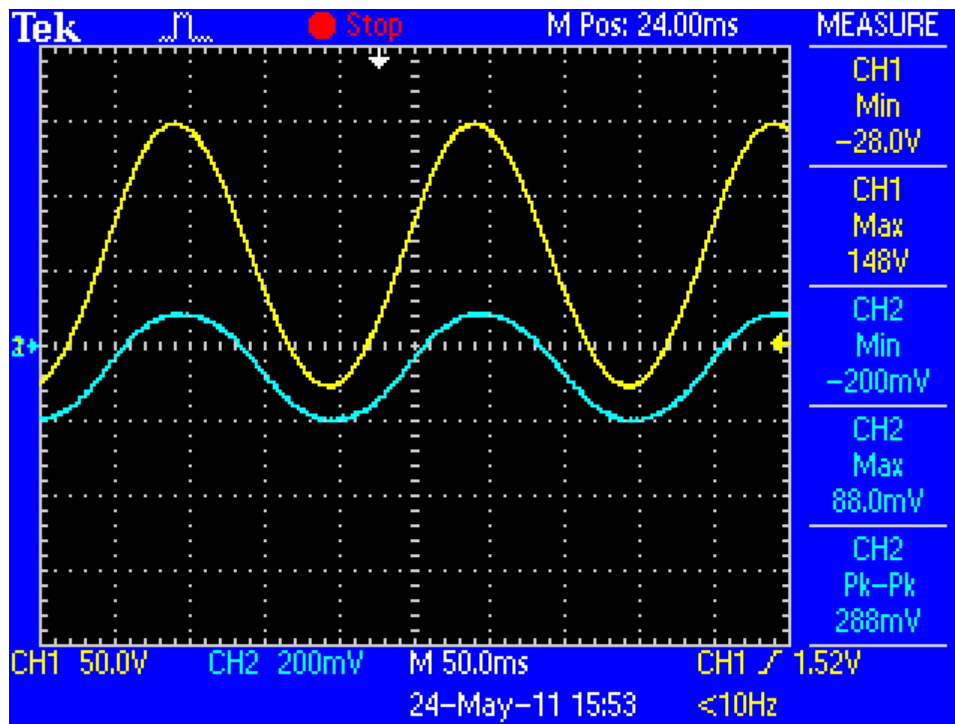


Figure 67: Measured input signal and displacement output in volts

To measure the stiffness of the extender, it was clamped rigidly to a mounting bracket at the same position where the clamp mechanism engages. The load cell was attached to the extender and pulled using a wheel screw as shown in Figure 68. The loading was applied at intervals from roughly 10 N up to 100 N. At each interval, the displacement between the top and bottom beam of the extender was recorded. Displacement was measured using the Polytec differential fibre optic vibrometer laser (OFV-5). The reference probe of the laser was pointed at the clamped beam, and the measuring probe was aligned with the unclamped beam. This ensured that only the relative displacement between the two beams was measured. The displacement measured was divided by two to obtain the displacement at the load attachment position. The results for the two sets of measurements are plotted together with the calculated stiffness in Figure 69. A line is fitted to the measured data. The slope of this line is the measured stiffness of the extender.

A summary of the results is shown in Table 5.

Differential measuring positions

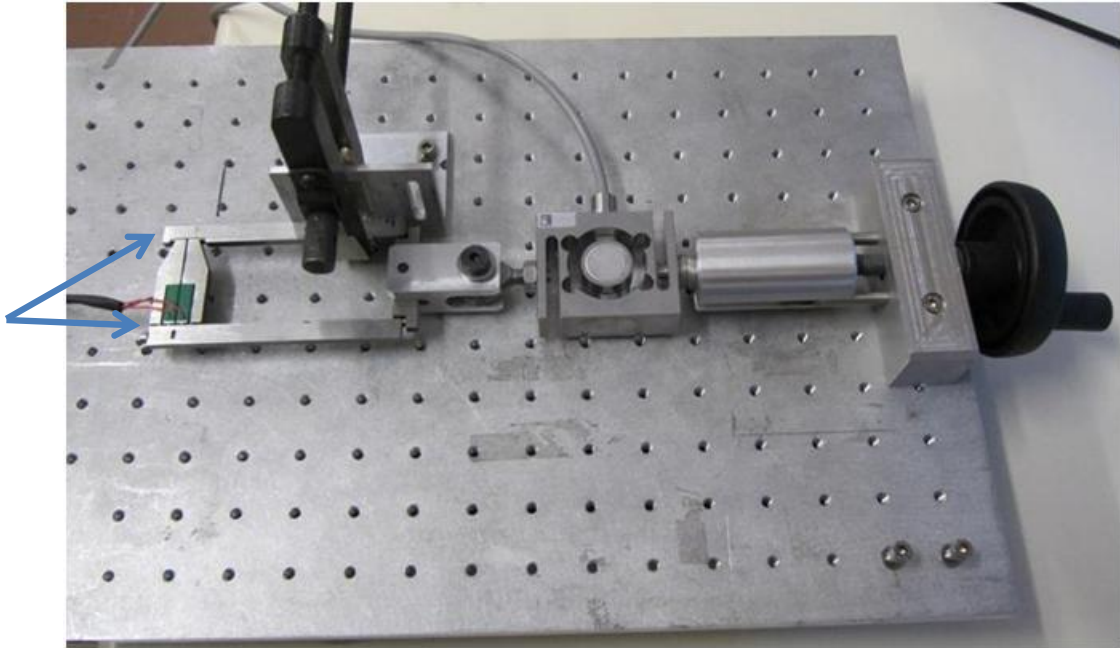


Figure 68: Stiffness testing of extender

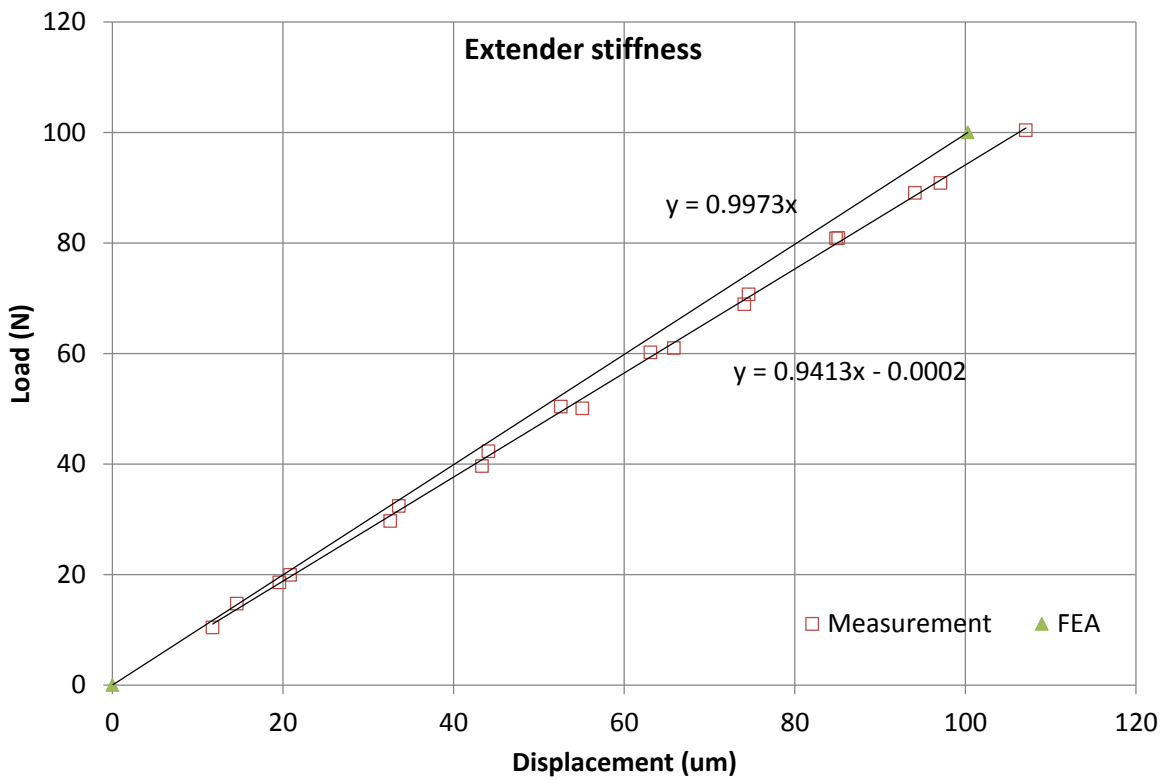


Figure 69: Extender stiffness results: measured and calculated

Table 5: Extender stiffness summary

Calculated (FEA)	Measurement (line fit)
997.3 N/mm	941.3 N/mm

The adjusted blocked force scaled from the calculated blocked force using the calculated and measured stiffness (Table 3) is thus:

$$F_{b_dup} = 103 \cdot \frac{941.3}{997.3}$$

Equation 5-5

$$F_{b_dup} = 97.2N$$

6 Designing the IWMs

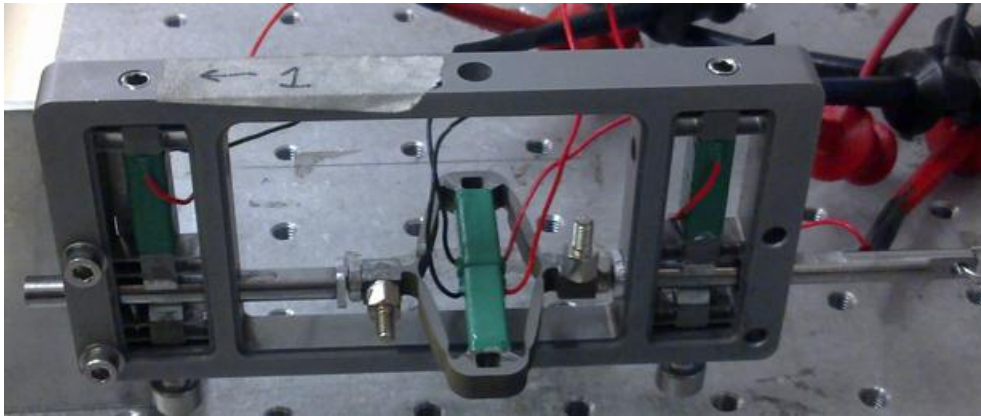


Figure 70: Photo of the conventional IWM

In the previous sections, the actuators that are used for the extenders in the IWM designs were characterised in terms of their stiffness, free displacement and blocked force. The following section relates these properties to the performance of an IWM.

The characteristic properties of an IWM, which are of particular importance to the designs presented, are the following:

1. The load capacity of the motor
2. The speed of the motor
3. The step size of the motor

All of these properties are affected by the frequency at which the motor is driven, which is to a large extent a function of the performance of the electronic controller and amplifier design. The work presented is limited to drive frequencies well below the resonant frequencies of the actuators and structures used, so that dynamic effects can be considered as negligible, i.e. the IWM is only driven at quasi-static conditions. The design and operation of the electronic controller, although very important to the overall workings of the motor, have been omitted from these investigations. All testing was performed at drive frequencies of 30 Hz or less and the properties of the designs were evaluated at these frequencies. Results and conclusions reached are thus only valid for similar instances where dynamic effects can be neglected. In general, an IWM is often driven at frequencies well below its first natural frequency.

Besides the driven frequency and the ability of the electronic amplifier to deliver sufficient power to the piezo elements, the performance of the IWM is further influenced by the following aspects:

1. The blocked force of the extender and its free displacement directly affect the force capability of the extender and thus the IWM, as can be seen by the equations in Section 4.2.
2. The stiffness of primarily the extender, as well as the overall stiffness of the load path that the extender forms part of, affects the force capability.

3. The stiffness of the structural load path (that the extender does not form part of) could also affect the force capability.
4. The clamps should be able to hold the force applied to the IWM and is generally designed to have a larger holding force than the blocked force of the extender.
5. The maximum force capability can only be reached if the supplied signals are such that events do not overlap (see Sections 2.2, 2.4 and 6.3), i.e. a clamp must only engage when the extender is finished stepping, and the clamp should only release when the other clamp has engaged.

6.1 Load limit of an IWM

An IWM can essentially be described as a device that consists of two alternating load paths (Figure 71 and Figure 72). In the conventional IWM design, the first load path (shown in blue) is from the motor's interface or attachment point, through the engage clamp towards the point at which the load is applied. The second load path (shown in orange) starts again at the point at which the motor is attached to its supporting structure, through the engage clamp (once the clamps have alternated their engage states), but now goes through the extender before flowing to the point at which the external load is applied. An IWM operates by alternating between these two load paths.

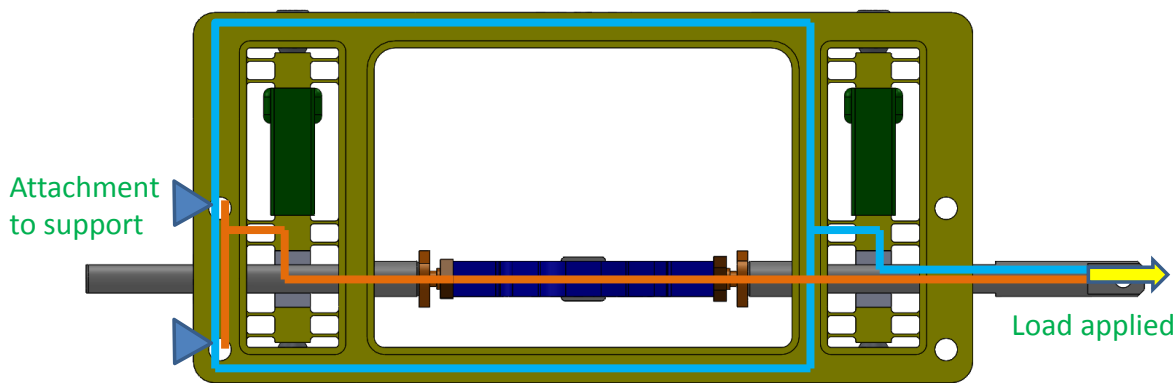


Figure 71: Conventional IWM design showing the two load paths

The new IWM, which has a force multiplication lever, behaves in a similar way, the difference being that both load paths go through the extender (Figure 72). Since the extender acts against the external load twice in each cycle it is necessary for both load paths to act through the extender. This is the main difference between the new design and the conventional design: in the conventional design, the extender acts against the external load only once in each cycle.

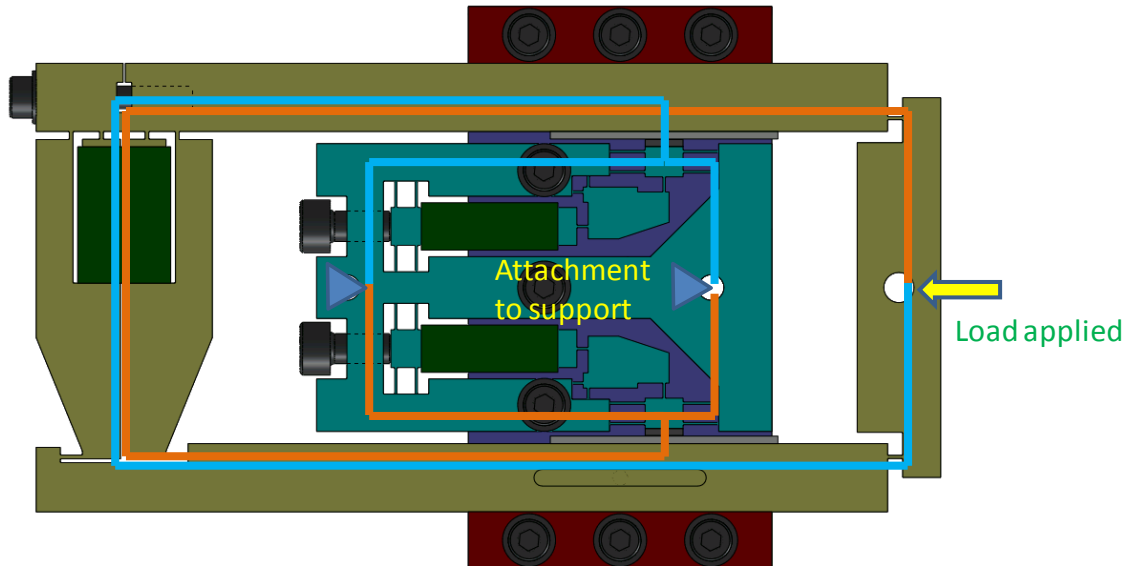


Figure 72: New inchworm design showing the two load paths

With each cycle, each alternating load path is strained and unstrained as the clamps open and close and the load paths alternate. In other words, each load path expands due to its non-zero compliance as a result of the externally applied load, but relaxes when the load is transferred to the second load path through the action of the clamps. That load path then returns to its relaxed position when the load is transferred. As the load path relaxes, the point at which the load is applied will as a result have a negative displacement, i.e. for a pushing load, the attachment point will move in the opposite direction to the actuating direction, which is also the direction in which the load is applied to the motor. When the load is pulling against the motor, the same behaviour is evident, but obviously the load attachment will now have a small displacement in the direction of the movement.

In section 4.2 and specifically in Table 1, the effect of a constant load and of a proportional load on a piezo element, and by extension, on a piezo actuator has been demonstrated. In summary, a constant load will not reduce the total step size that a piezoelectric element or actuator makes, but a proportional load will. However, it was observed during testing of different IWM's that the presence of a load did reduce the step size taken by the extender. Also the reduction of step size was in proportion to the size of the load. During testing of the IWM's, the load was applied to the extender in a manner that closer resembled a constant load condition. It is suspected that the combination of the external load together with friction on the clamps resulted in the extender experiencing the load as a proportional load, hence causing the step size reduction. During load testing, the clamps preloading were adjusted such that a maximum load capacity was realised. The preloading was determined through trial and error. When the no load step size was measured at the clamp pre load settings for maximum load conditions, the free displacement step size was observed. However the combination of the external load, together with the clamps and maximum load capacity preloading, resulted in some unwanted friction load between the disengage clamp and the part of the extender moving. This friction load is suspected to be the cause of the step size reduction observed during load testing. A definite explanation of this phenomenon is still unidentifiable but that the load did reduce the extender step size have been observed during different testing conditions and on different designs.

The stepping behaviour of a point on the extender of an IWM with no loading; and under loading can be graphically shown as in Figure 73. When no loading is present, the extender is capable of stepping its free displacement (δ_f). The presence of load acting against the extender will prevent the extender of realising its free displacement. The reduction in step size (labelled "a" in Figure 73), is determined by the stiffness of the extender. The distance "a" may be viewed

as the distance the compliant extender contracts (or extend, depending on load direction) under the influence of the load. When the load is removed, the strained extender will recover by distance “a”, but because of the action of the motor’s clamp having altered the constraint conditions, the direction is reversed. When the load paths alters, a back movement happens as the previously loaded load paths relaxes, labelled “b” in Figure 73. This brings us to an important realisation, in that $a = b$.

As the external load is increased, a load will be reached when the negative movement caused by the compliance of the extender equals the ability of the motor to displace against that load. The motor effectively stalls and will no longer be able to have a nett positive displacement over a full actuation cycle. The stall load of an IWM therefore occurs at half the free displacement of the extender when $a=b$ and $b=c$. The label “c” is the step size of the extender as shown in Figure 73.

$$\delta_{stall} = \frac{1}{2} \cdot \delta_{free} \quad \text{Equation 6-1}$$

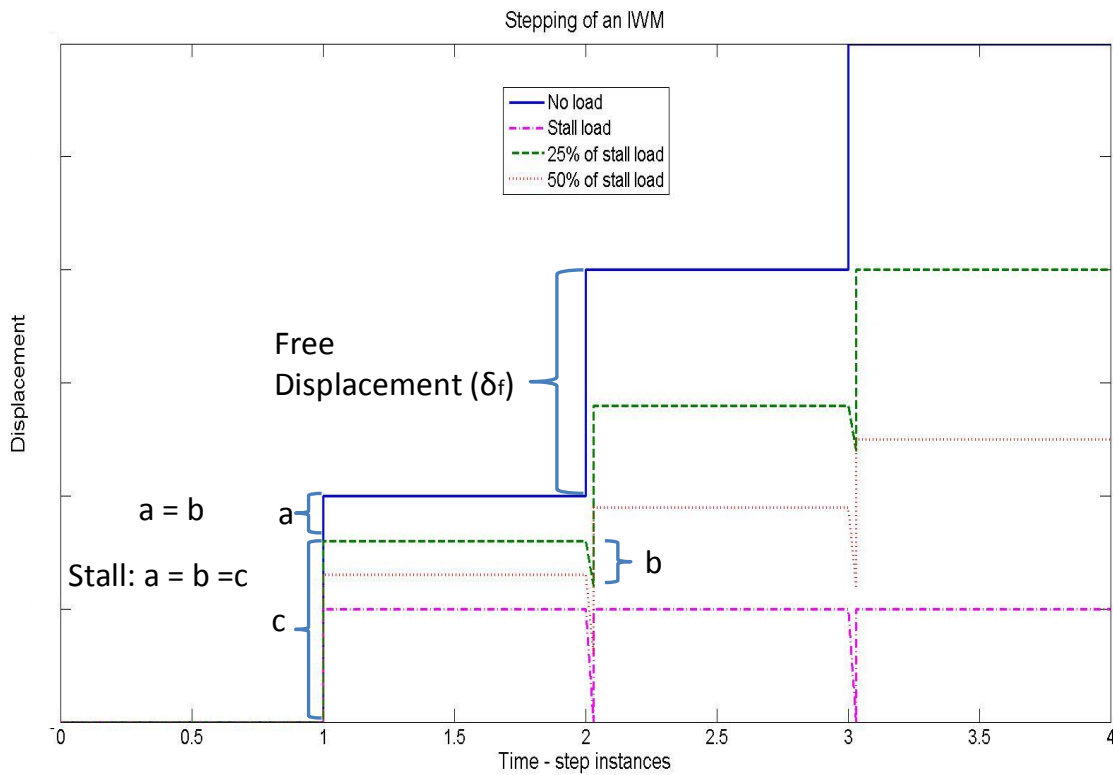


Figure 73: Stepping of an IWM with, and without loading

Substituting Equation 6-1 into Equation 2-9 gives the stall load of an IWM.

$$F_L = F_b - k_p \cdot \frac{1}{2} \delta_{free} \quad \text{Equation 6-2}$$

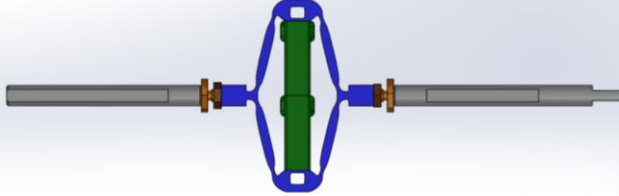
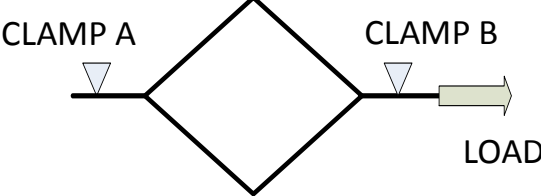

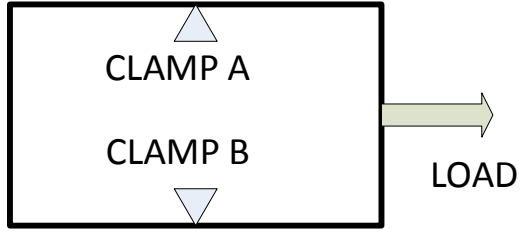
The force limit of an IWM against a stiffness load calculated from Equation 2-9 is the blocked force of the actuator minus the product of half the free displacement, times the stiffness of the extender.

The design equations (Equation 6-1 and Equation 6-2) as well as the behaviour graphically shown in Figure 73, applies to both the classical IWM design and the IWM with the force duplicator. To illustrate that both types of motors is governed by the same operating principles, a chart is presented using simplified diagrams representing the two

designs (Table 7). Refer to section 2.2 for the operation steps that an operational cycle consists off, and Table 6 for an explanation of the simplified diagrams used in the chart. Note that the graphs in the chart represent a point on the extender at the location of clamp B. A point on the extender located at clamp A would have displayed similar behaviour.

This behaviour was confirmed by the experimental measurements and is shown in Figure 74 for a load less than the stall load or limit load, and in Figure 75 for at the stall load (these graphs only show the principle, and do not apply to the designs presented).

Table 6: Explanation of simplified diagrams representing the two IWM designs.

Actual design	Simplified diagram
	
	

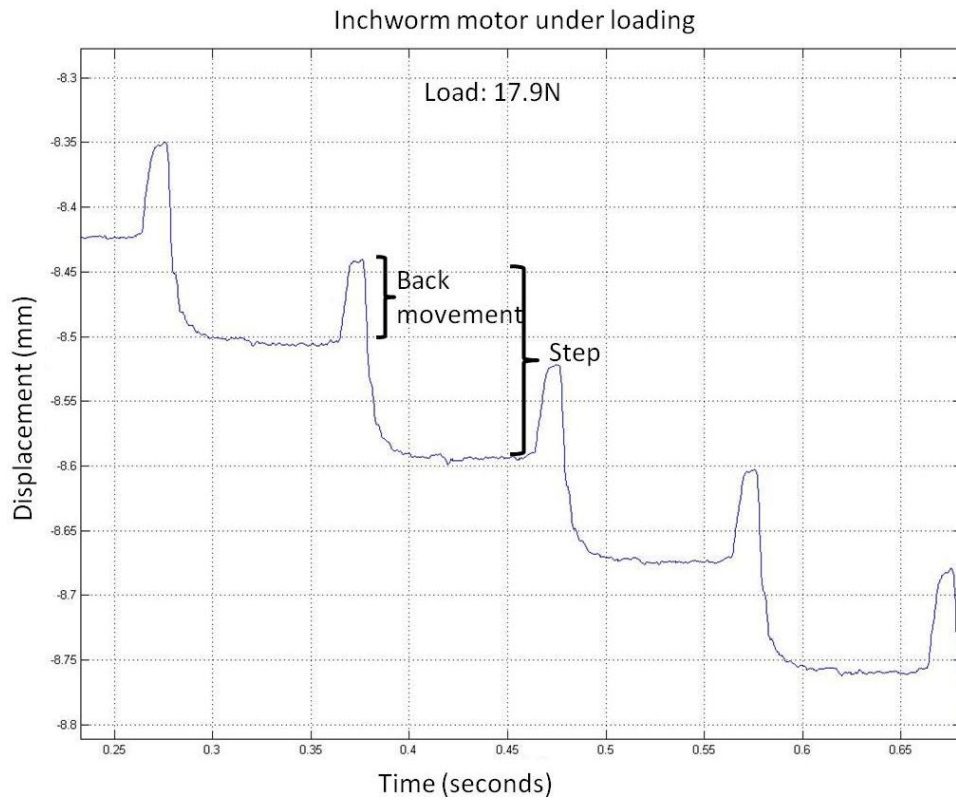


Figure 74: Displacement of load attachment point at a load less than the load limit of the motor

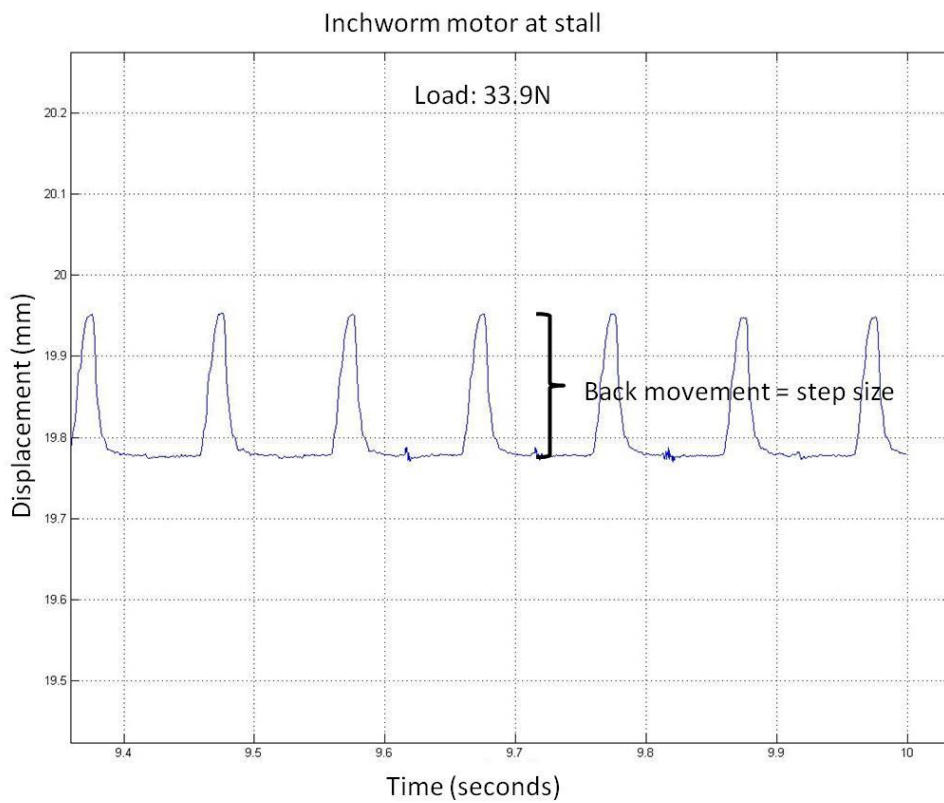
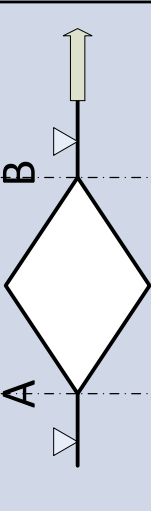
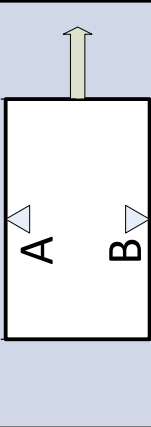
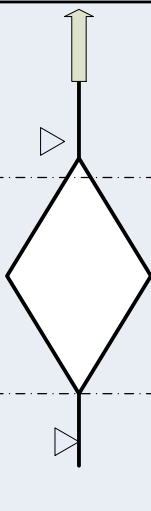
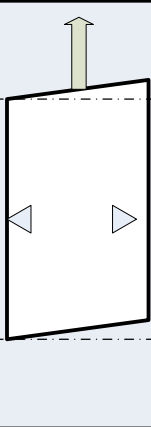
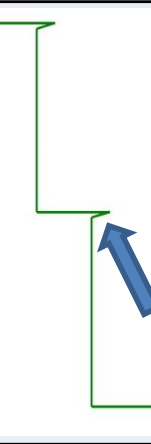
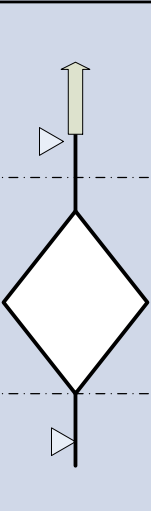
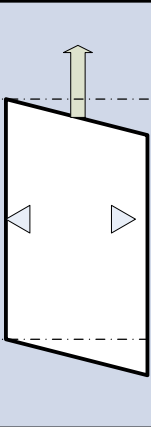

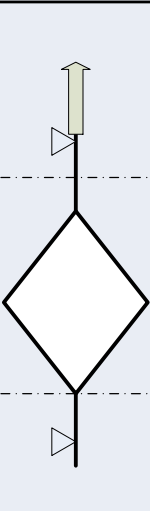
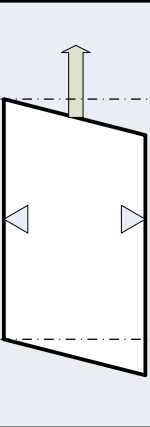
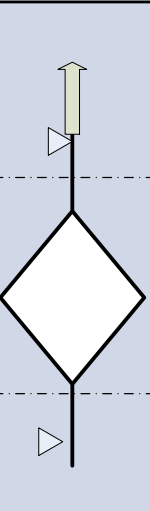
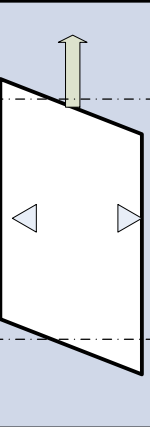
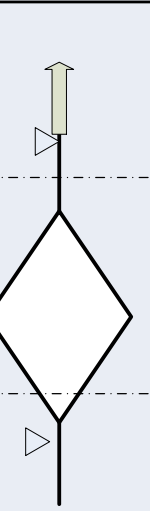
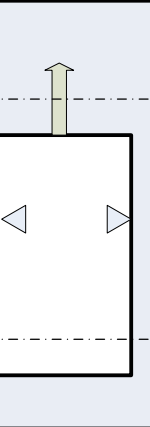
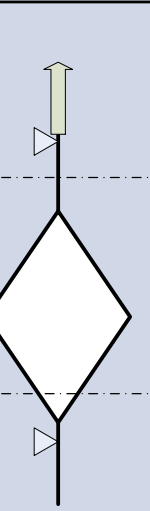
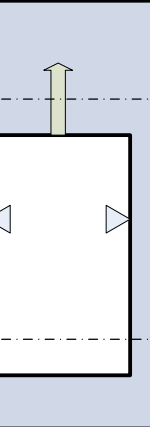


Figure 75: Displacement of load attachment point at stall

Table 7: Comparison between the working principles of the two IWM designs

Steps	Conventional IWM	IWM with force duplicator	Snap shot from graph	
START				Start position
1				Clamp A is activated, while clamp B is disengaged. Load results in displacement due to compliance.
2				The extender extends.
3				Clamp B is activated
4				Clamp A relaxes. Load is transferred to 2 nd load path. Extender displaces due to compliance..
5				The extender returns to its original shape
6				Clamp A is engaged. A step against the load have been made.

6.2 Calculating the load limits of the IWM designs

Equation 6-2 is used to calculate the expected load capacity of the IWMs.

$$F_L = F_b - k_p \cdot \frac{1}{2} \delta_{free}$$

For the conventional IWM design with the original flextensional actuator, the blocked force, free displacement and stiffness values determined in Section 5.1 are used. This actuator was installed in the IWM during testing.

$$F_{L_conv1} = 87.4 - 0.395 \cdot \frac{1}{2} \cdot 224.5$$

$$F_{L_conv1} = 43.1N$$

For the conventional IWM design with the improved flextensional actuator, the blocked force, free displacement and stiffness values determined in Section 5.2 are used.

$$F_{L_conv2} = 154.0 - 0.665 \cdot \frac{1}{2} \cdot 231$$

$$F_{L_conv2} = 77.2N$$

The design improvements increased the expected IWM load limit significantly. The IWM testing was only performed with the original flextensional actuator. Better results would have been obtained if the improved flextensional actuator were to be used.

For the load limit calculation of the IWM design with the force duplicator mechanism, the blocked force, free displacement and stiffness values calculated in section 4.4 is used, and also the values measured in Section 5.3.

For the calculated instance:

$$F_{L_dup_calc} = 103 - 0.768 \cdot \frac{1}{2} \cdot 134$$

$$F_{L_dup_calc} = 51.2N$$

And for the measured instance:

$$F_{L_dup_meas} = 97.2 - 0.941 \cdot \frac{1}{2} \cdot 144$$

$$F_{L_dup_meas} = 29.4N$$

6.3 Signal events and their effect on the speed of an IWM

The voltage signals used to drive an IWM comprising two clamp mechanisms and one extender can in general be divided into six events. These events are discussed in Section 2.2, and are plotted graphically in Figure 76.

The overall speed of an inchworm motor is therefore a function of the following:

1. Step size of the extender.
2. Number of steps per second or driving frequency.
3. Slippage or reverse stepping between the clamps and extender mechanism.
4. Load applied to the extender.

To prevent slippage of the extender mechanism or guide relative to the clamps (depending on the particular IWM configuration), the stepping event can only execute after the clamps have fully engaged, i.e. the following extender event has to wait a certain amount of time for the clamp to complete its motion. Similarly, the next clamp event has to allow sufficient time for the extender to complete its motion. An increase in required stroke, as well as an increase in inertia, will increase the time needed to complete the motion of a particular mechanism. These parameters place a mechanical limit on the maximum frequency at which an IWM can be driven. Mechanical inertia in a piezoelectric mechanism has the effect of “rounding the edges” of a square wave input due to the electrical and mechanical coupling, and behaves like a low pass filter.

Besides the inherent inertia of the mechanism, there are other reasons that might limit the maximum driving frequency. These include the power available and the current limit of the power amplifier electronics. Mechanical noise caused by the hammer action of the clamps could also indirectly affect the motor speed. The closer the input signals approach a square wave, the faster the possible frequency at which the IWM can be driven, but the noisier the clamps become, and more bandwidth, current and power are required from the power supply. By filtering the signals, i.e. rounding the sharp edges, a reduction in power is achieved and a smoother motion is obtained from the mechanisms, making them quieter.

The maximum possible speed at which the IWM can be driven is limited by the time it takes for a step change of the signal to change from low to high, or high to low, since following signals have to wait for such a step change to be completed before its step change can be started as shown in Figure 76.

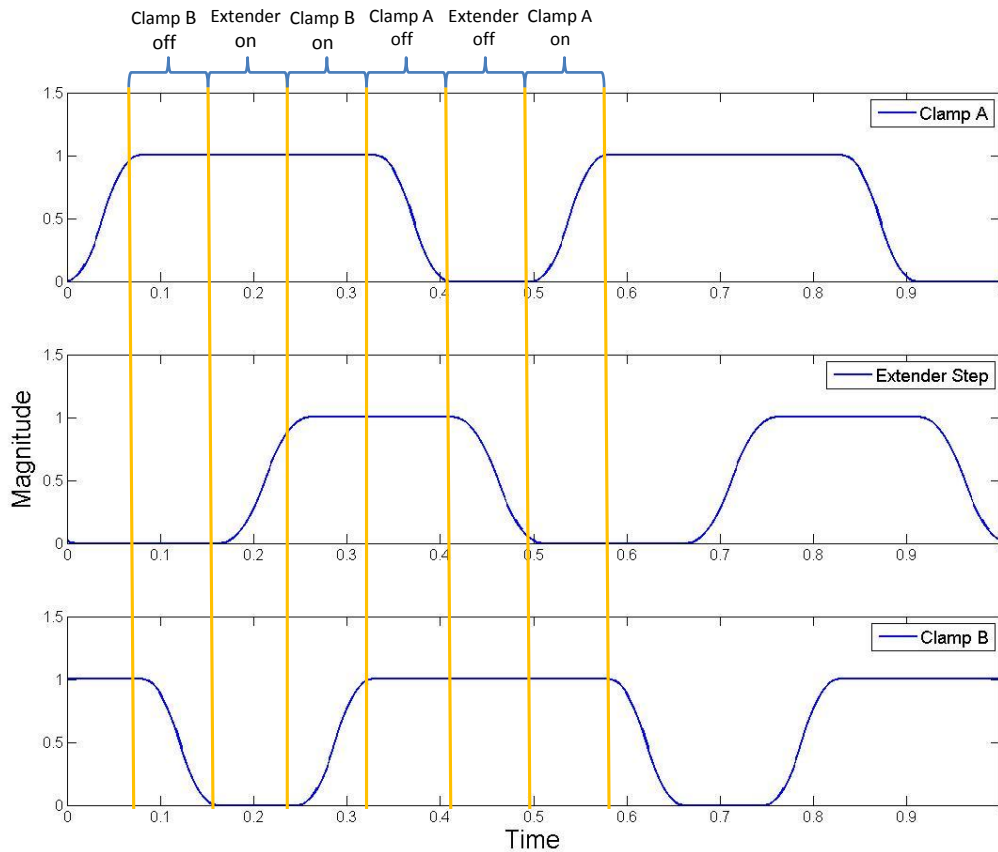


Figure 76: Actuating events indicating the shortest event time for a given step-change time

To investigate the effects of rounding (filtering) that the input signals have on the overall performance of the IWM, a Matlab program was written to generate the input signals that are sent to the amplifiers that drive the IWM. This program allows the frequency and amplification to be changed, as well as the time of an individual event to be adjusted within a fix duration cycle that comprises the six events. The program also filtered the signal using Matlab's filter.m function. See Appendix B for the Matlab program. The effect of the filtering function on a square input is shown in Figure 77. An excessive amount of filtering will result in a sine wave signal.

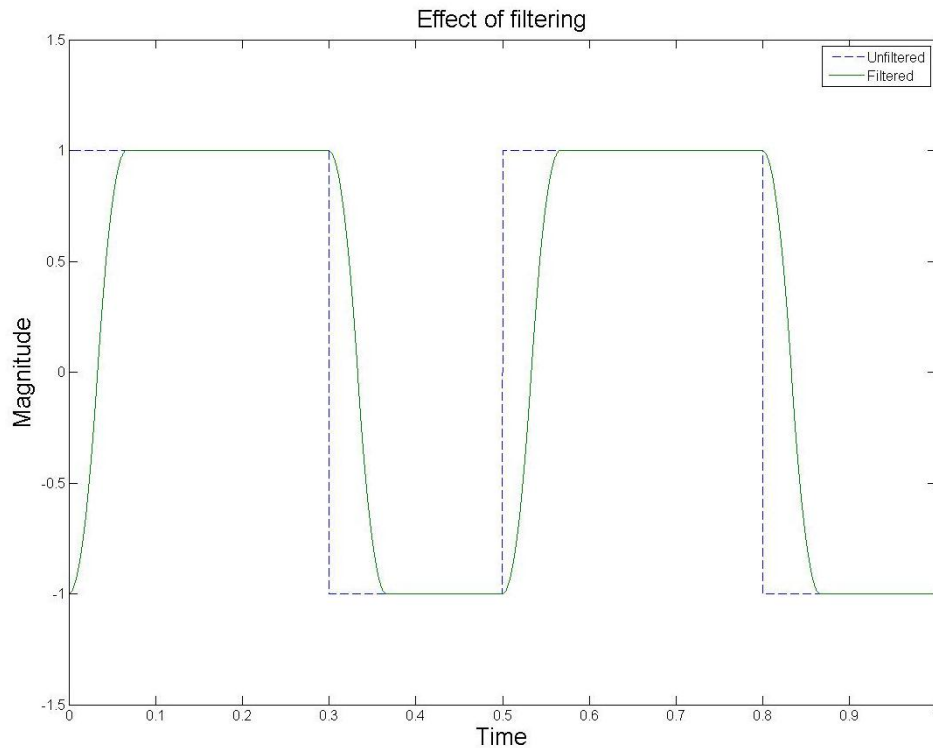
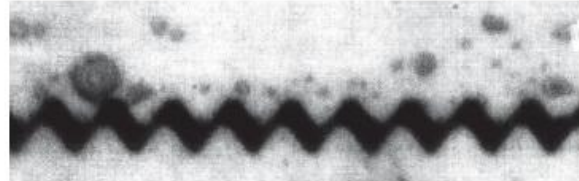
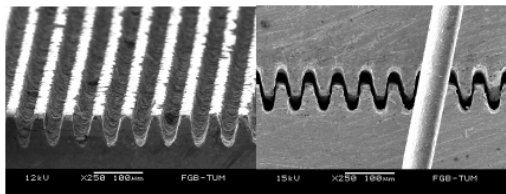
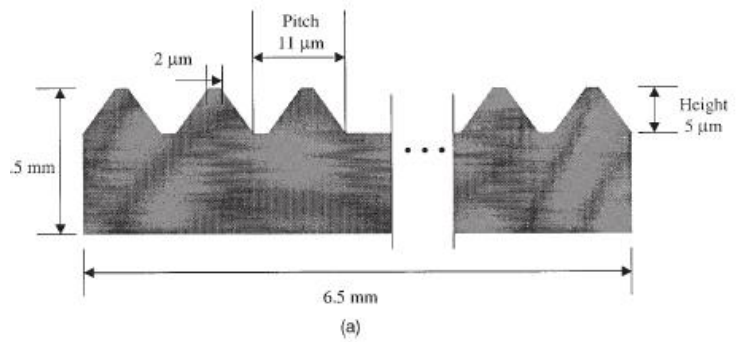


Figure 77: Effect of the Matlab filtering function on a square input signal

Even a small amount of filtering had a significant effect on the noise created by the clamps of the motor. Filtering did not affect the load performance or directly the speed of the motor, as long as the individual event in a signal cycle was allowed to complete its motion before the next event took effect. The more filtering that was used, the lower the maximum frequency at which the motor could be driven, since each event requires more time before the next event can execute. It was, however, noted that filtering allowed operation at a higher frequency before clipping problems occurred, given the power-limited amplifiers that were used. This is because filtered signals require less power to drive resulting in faster possible signals.

6.4 The use of micro ridges on the clamp mechanisms

The force output of IWM mechanisms is to a large extent determined by the efficiency of the clamping system. An inherent disadvantage of IWMs is the limiting coefficient of friction between the clamping system and moving shaft. Most IWMs make use of the principle of static friction for the clamping systems. Increasing the coefficient of friction by roughening the surfaces and applying a clamping preload improves load transfer, but causes other problems associated with positioning, engaging/disengaging of the clamps and wear of the contact surfaces. The use of micro ridges has been proposed to overcome this problem. Micro scale ridges are created on the contact surfaces. These ridges interlock to transfer the shear load. Two likely processes to obtain such small ridges are laser ablation or micro-electromechanical system (MEMS) processes. Pitches that varied from 11 μm to 60 μm have been found in the literature (Chen et al., 1999) (Park et al., 2000).



(b)

Figure 78: Micro ridges (Park et al., 2000)

If micro ridges are used, the clamp mechanisms should be able to mesh the micro teeth with every step taken by the extender. This implies firstly that the clamps should displace at least by a distance exceeding the height of the teeth to enable the teeth to disengage and move over their mating teeth. Secondly, the smallest step that the extender could take must be at least the pitch of the micro teeth, otherwise the same teeth will just mesh repeatedly, and no forward motion will occur. It was thus necessary to know the smallest practical size teeth that can be manufactured through processes that are realistically available in South-Africa.

Two possible manufacturing processes were identified and considered:

1. Laser ablation
2. Micro machining – milling.

6.4.1 Laser ablation

Laser ablation is the process of selectively removing material from a surface with a laser. The National Laser Centre of the CSIR was asked to demonstrate the manufacture of square or trapezoidal teeth onto aluminium and steel. The samples that were prepared for the laser process are shown in Figure 79. Samples were taken to CSIR Material Science and Manufacturing for measurements on a Zeiss Axiovert 200M laser scanning microscope. The microscope scans and measurements that were done on the steel parts are shown in Figure 80 and Figure 81. The process was not successful on the aluminium parts as can be seen in Figure 82.

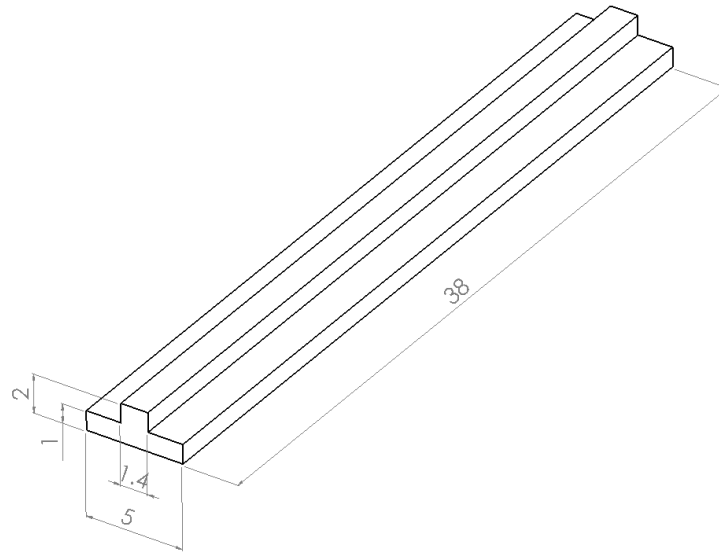


Figure 79: Micro ridge samples (dimensions in millimetres)

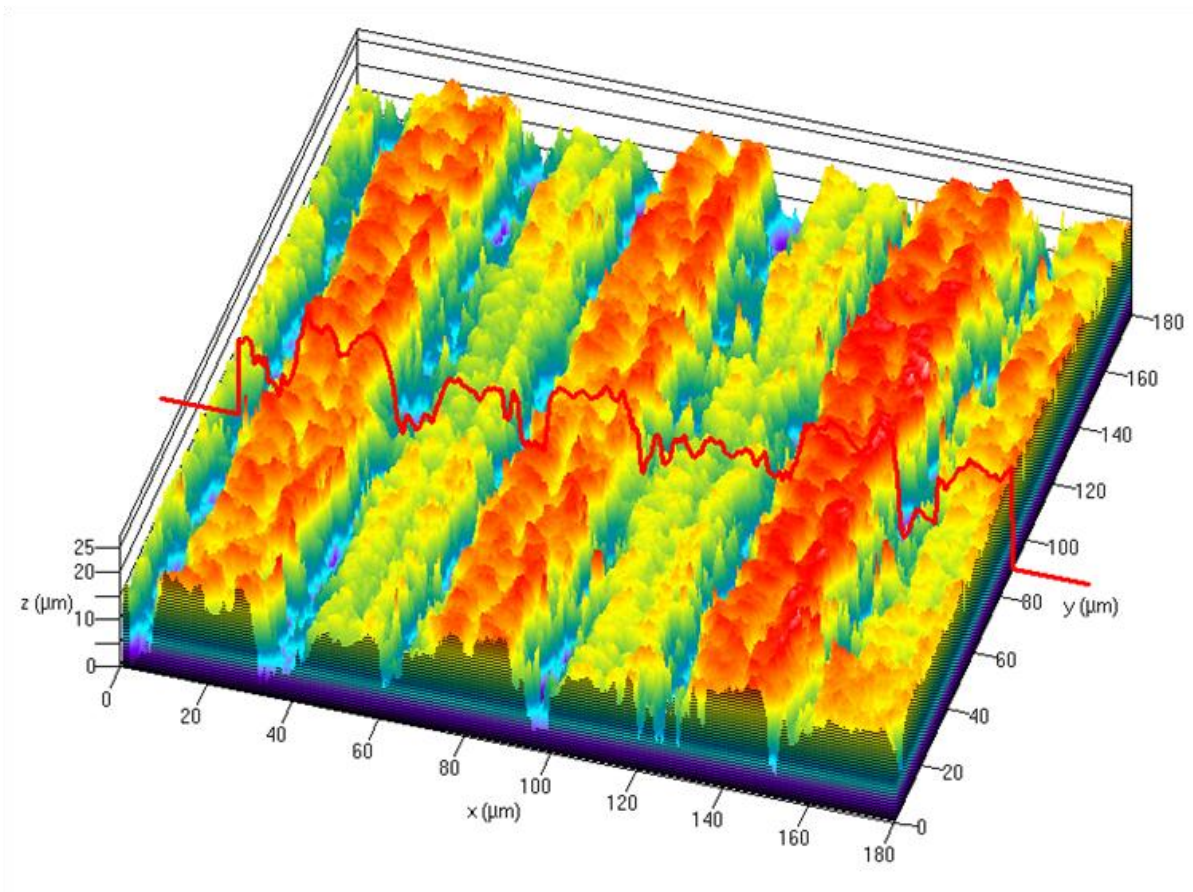


Figure 80: 3D scan of laser ablation in steel

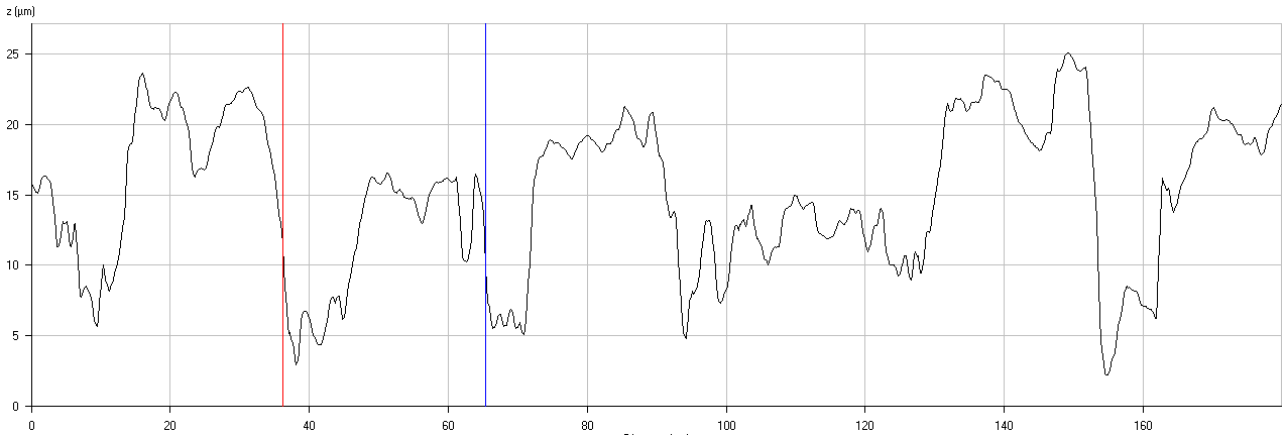


Figure 81: Measurement of laser ablation in steel

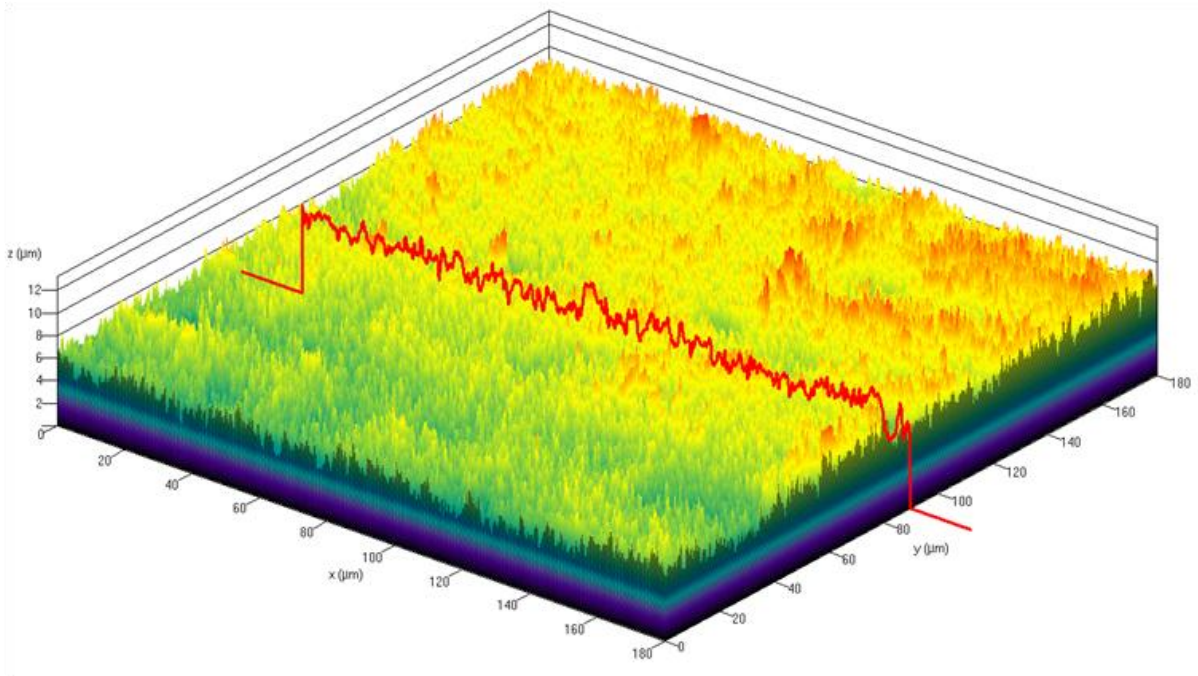


Figure 82: Laser ablation in aluminium

6.4.2 Micro machining – milling

ICRON Precision Engineering was challenged to machine teeth as small as possible onto 3 mm thick aluminium. A conventional CNC (Computer Numerical Control) milling operation was employed with a modified cutting tool. The sample was again measured at the CSIR using the laser scanner microscope and is shown in Figure 83 and Figure 84.

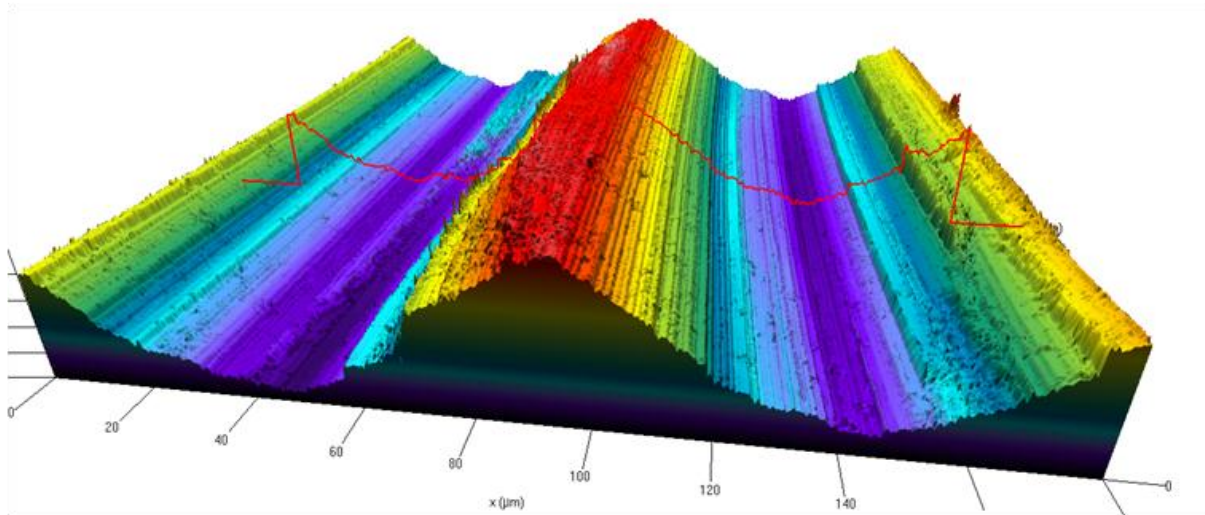


Figure 83: Milled micro teeth

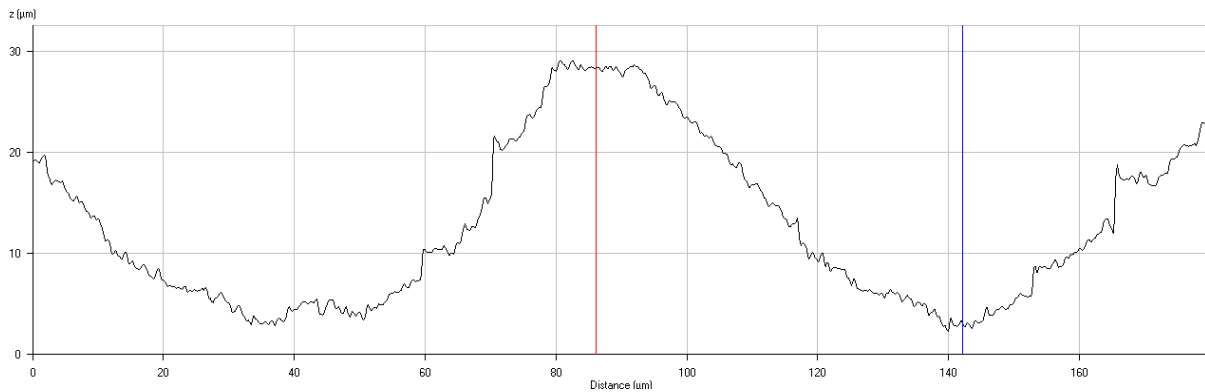


Figure 84: Milled micro teeth measurement

6.4.3 Discussion and conclusion on micro ridges

With laser ablation it was possible to cut measurable ridges at a pitch of $30\ \mu\text{m}$ at a height of approximately $15\ \mu\text{m}$ onto the steel. The shape of the ridges would still need to be improved substantially to be considered in an actual design. It did, however, demonstrate the capability of the process in a material that is considered wear resistant.

The shape of the ridges obtained from micro milling appears better than the ridges obtained from laser ablation. The pitch of these ridges is, however larger at $56\ \mu\text{m}$ and at a height of $25\ \mu\text{m}$, and was only demonstrated in aluminium, which is not likely to have the required wear resistance. Micro milling is more suited to possible future production, since the cost is less than laser ablation and longer lengths of ridges can be obtained more easily.

Ridges manufactured practically by technology to which the author had access are unlikely to have a pitch smaller than $30\ \mu\text{m}$. Useful ridges would possibly have ridges at a pitch larger than $50\ \mu\text{m}$. The extender of an IWM would have to be able to make a step of $50\ \mu\text{m}$ and do so under maximum loading. The clamps would have to displace a distance of about $25\ \mu\text{m}$ to be able to pull the teeth from each other to move to the next position.

When we consider the piezo stack used for the IWM design presented in this dissertation, the measured free displacement is $27\ \mu\text{m}$, so the clamp mechanism will have to reach a clean gap of at least $27\ \mu\text{m}$ to enable the teeth to disengage. If allowance has to be made for the internal compliance of the clamp mechanism, as well as the

compression of all the materials in the load paths of the mechanism, a much bulkier clamp mechanism will be required. The extender should also be able to displace about 60 μm to step to the next teeth interval, and this under full load. This will also result in a fairly bulky overdesign and will compromise the force density of the IWM. It was therefore decided not to use micro ridges. To overcome these considerations, micro ridges would have to have a pitch and height two or three times less than was achieved. This implies the use of MEMS technology in the manufacture of such smaller micro ridges, and will not be investigated at this point.

7 Testing the IWMs

7.1 Velocity measurements during event time changes

The following tests were performed to see whether the effects of differently timed events would influence the speed of the IWM. For these tests, the frequency and shape of the signal ramp up and down was kept the same, but the duration of the events within the fixed timed cycle was changed. The conventional IWM design was used.

The IWM was driven with a 25 Hz signal at 0 V to 120 V without any external loading. The total amount of time of each cycle was kept constant for all five tests, but the time of the individual events was changed between the different tests as indicated in Table 8. The IWM was allowed to travel its full range of 20 mm. The signals were also filtered to reduce the current required from the supply amplifier to within a limit of 50 mA. The OFV-552 Fiber Vibrometer laser was then used to measure the displacement of the IWM as a function of time. From these data the average velocity was calculated.

Measurements showed no significant change in the overall speed of the IWM, as long as enough time was allowed between events within a cycle to allow the extender and clamp mechanisms to complete their motion. Measured velocity results are shown in Table 8 for the different event times.

Table 8: Different times used during velocity testing

TEST NO	EVENT TIME (MILLI-SECONDS)						TOTAL TIME	AVERAGE VELOCITY (mm/s)
	CLAMP B OFF	EXTENDER EXTENDS	CLAMP B ON	CLAMP A OFF	EXTENDER CONTRACTS	CLAMP A ON		
1	1.4	1.4	17.1	1.4	1.4	17.1	40.0	1.12
2	1.7	1.7	16.7	1.7	16.7	1.7	40.0	1.14
3	1.8	1.8	16.4	1.8	1.8	16.4	40.0	1.13
4	2.0	2.0	16.0	2.0	2.0	16.0	40.0	1.14
5	2.2	2.2	15.6	2.2	2.2	15.6	40.0	1.14

7.2 Load testing of the conventional IWM

To test the load capacity of the conventional IWM, it was attached to a load cell via a spring as shown in Figure 85. Note that these tests were performed with the same actuator that was tested in Section 5.1 and not the improved actuator tested in Section 5.2. The IWM was then driven at the full allowable voltage of the piezo stacks of -30 V to 150 V for both the clamp mechanisms and the extender mechanism. The clamp adjustment was tweaked until maximum performance was obtained from the motor, i.e. the maximum force against which the motor could just displace was realised. The displacement was measured at the two indicated points in Figure 86, using the laser vibrometer.

Three signals were supplied to the motor, one for each of the two clamps and one for the extender. Each channel was individually amplified using a different amplifier. A 20X amplifier was used for each of the clamps, and a 30X amplifier was used for the extender. This is done because of the limited availability of similar amplifiers. This meant that a larger voltage signal had to be supplied to the 20X amplifiers to obtain the same output to the IWM (i.e. -30 V to 150 V). See Appendix I for a list of test equipment used.

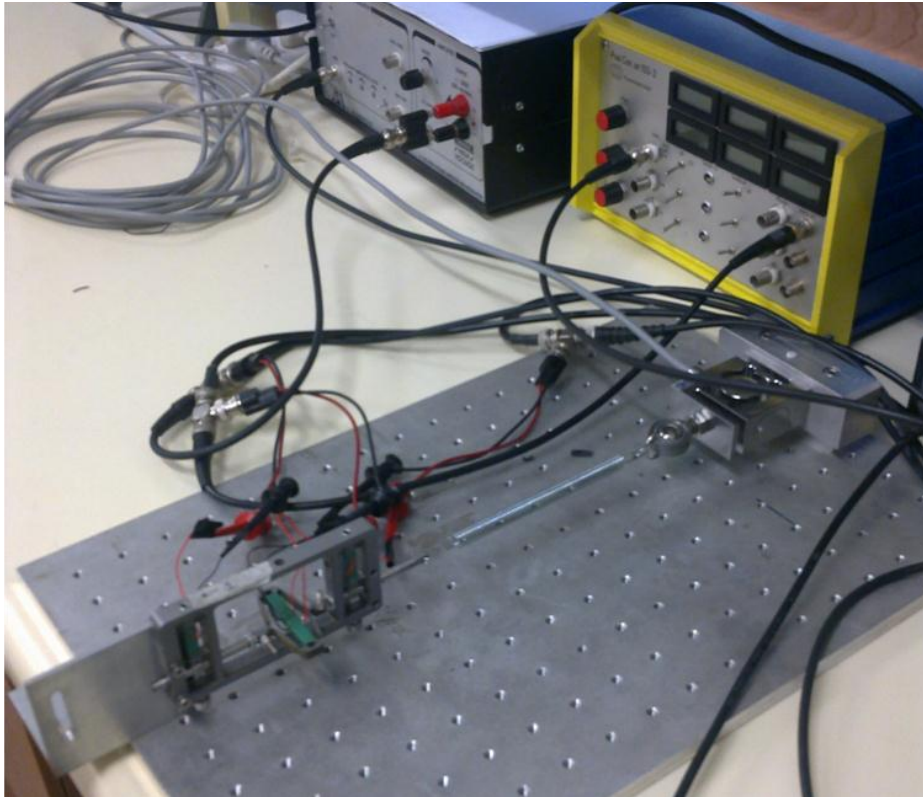


Figure 85: The conventional IWM during load testing

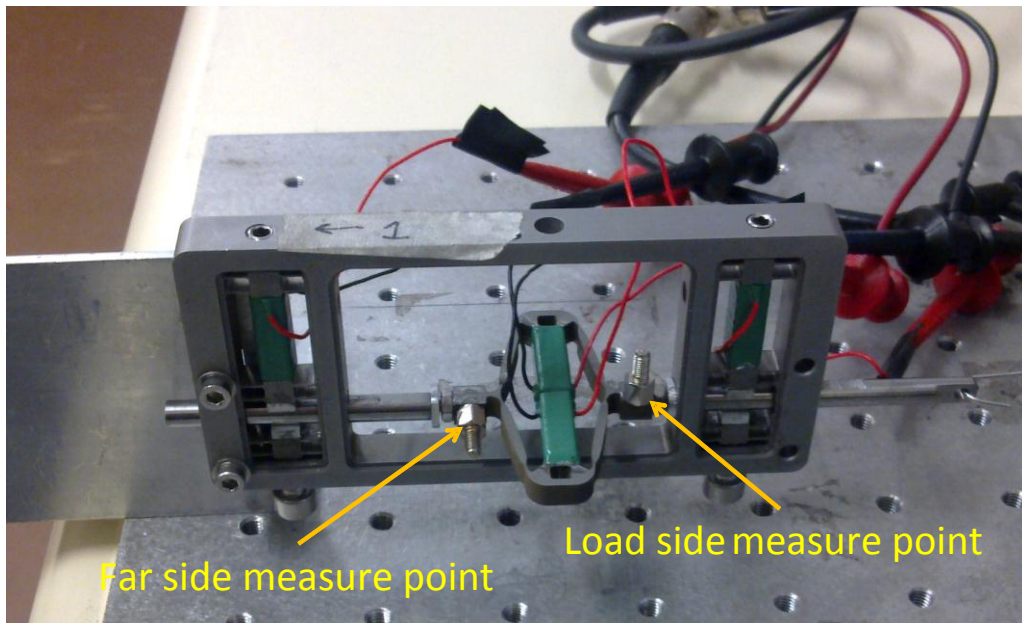


Figure 86: Measurement positions

Since the laser can make only one point measurement at a time, two different tests were performed for the load side measurement and the far side measurement, but at approximately the same loading. The measured results are given for 0.3 seconds, and are shown in Figure 87 for the load side and in Figure 88 for the far side. The reported loading at these instances was 33.9 N and 33.7 N respectively. The first graph in each of these figures is the input voltage signals

supplied to the amplifiers. The second graph shows the output signals after amplifications. (The small notch in the extender signal is a measurement error caused by “signal ghosting” due to too fast sampling. The too high sampling prevented the internal measurement capacitor of the DAQ card to fully discharge before the next voltage was “grabbed”. The notch may be ignored.) The third graph shows the displacement as measured with the laser vibrometer. These graphs are shown more clearly in Figure 88 and Figure 90. The pullback behaviour described in Section 6.1 can be clearly seen at the instance when the clamp opens and the load paths swap.

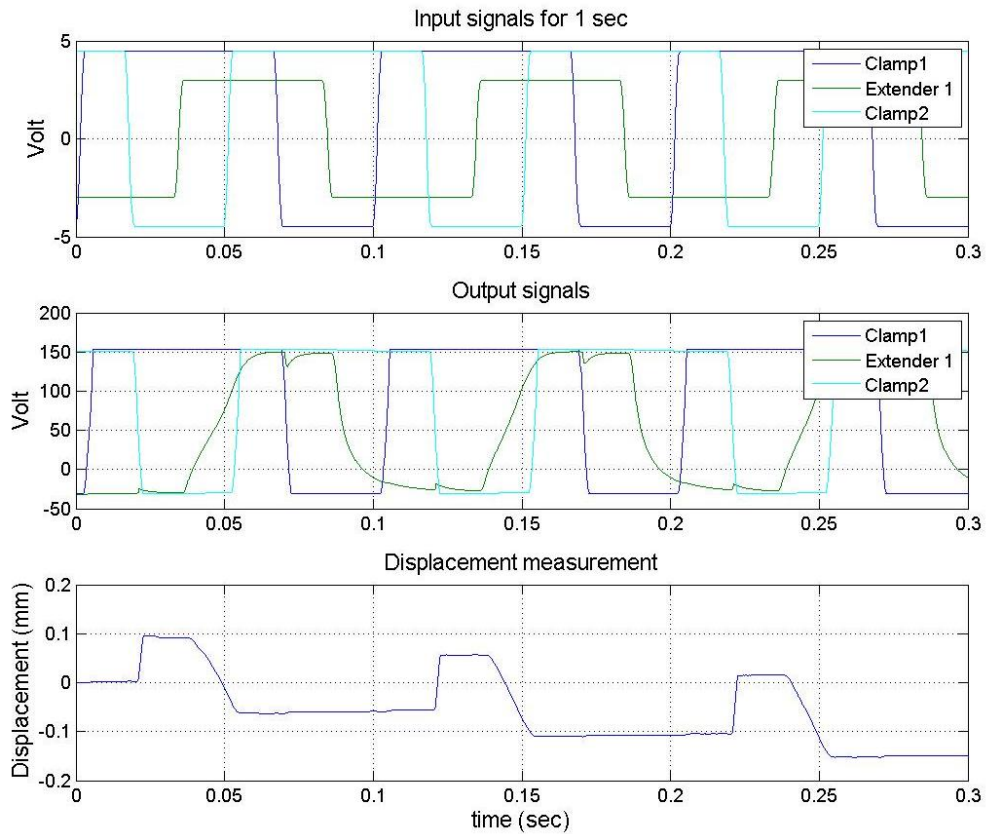


Figure 87: Load side measurement

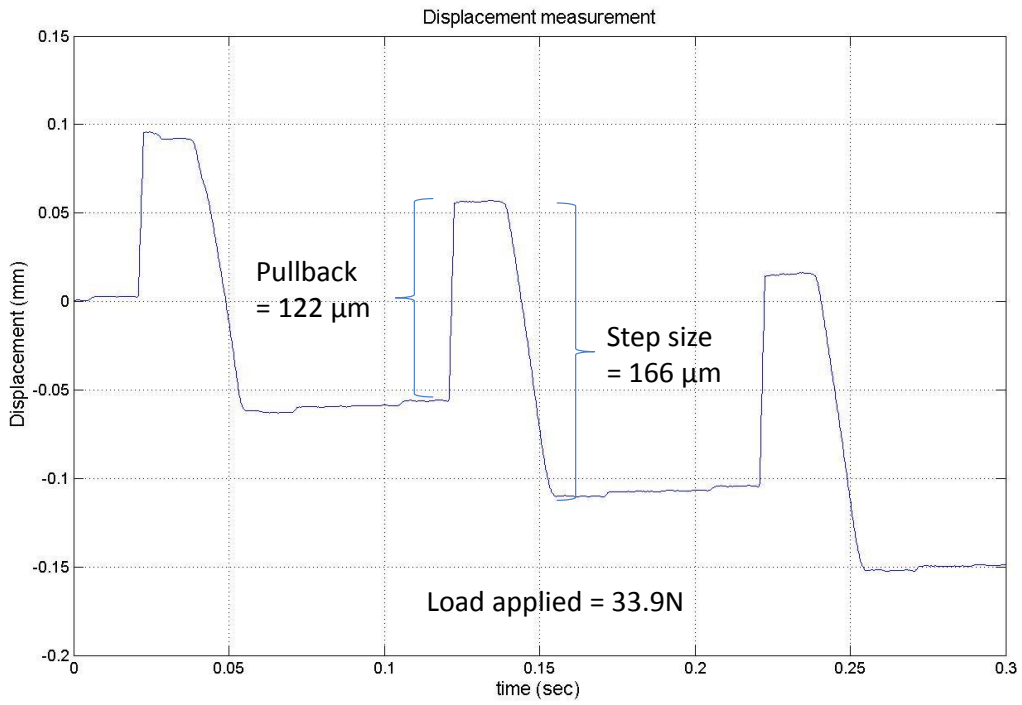


Figure 88: Load side displacement

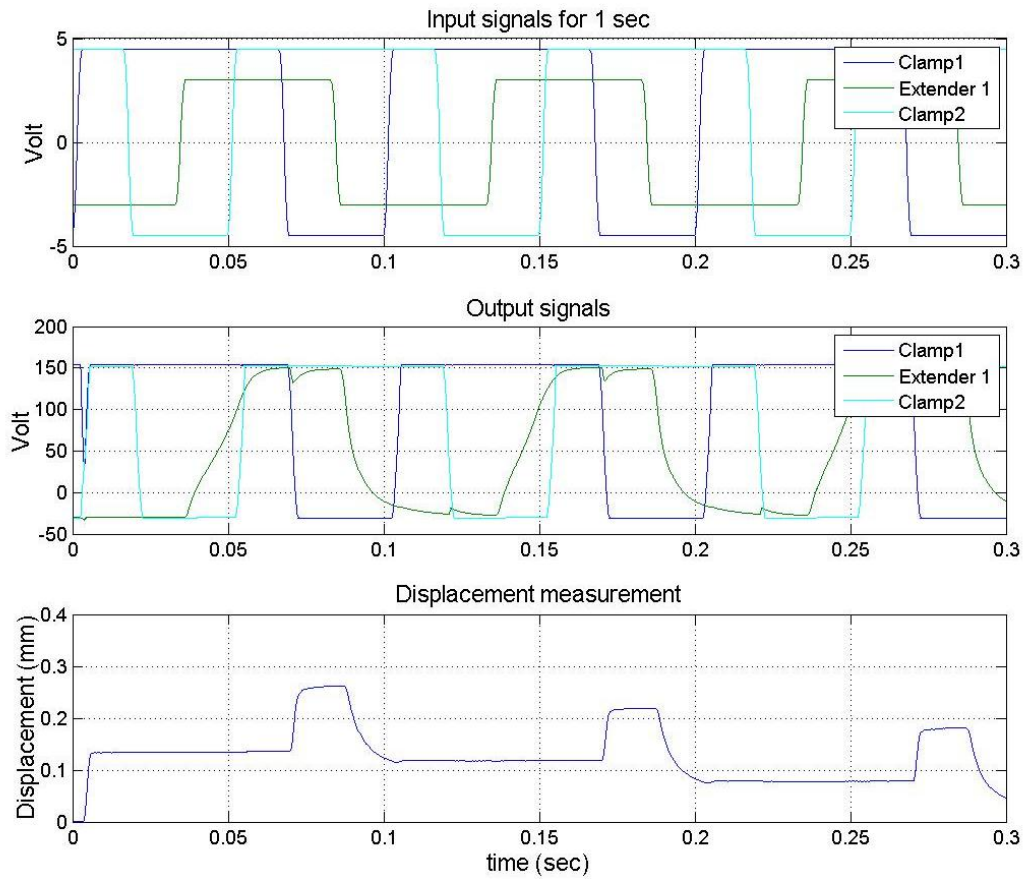


Figure 89: Far side measurement

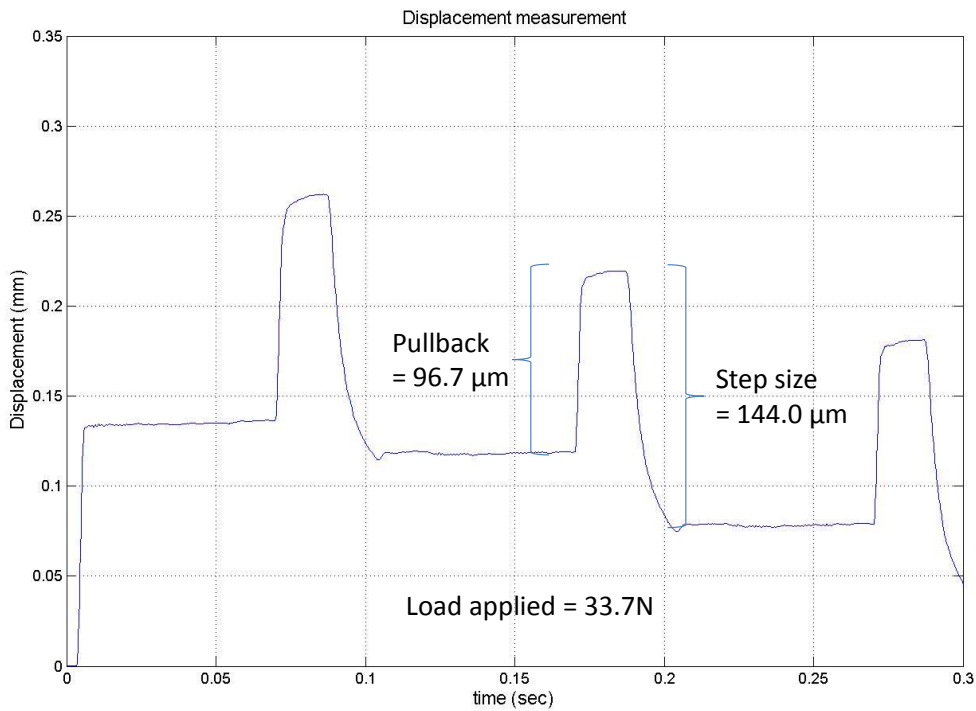


Figure 90: Far side displacement

The load applied divided by the amount of pullback is an indication of the stiffness of the load path being considered and should compare with the stiffness measurement of 395 N/mm obtained on the extender in Section 5.1. The stiffness values are shown for two instances for both measuring positions in Table 9.

Table 9: Load and displacement results of IWM load measurements

Far side			
Load	Pullback	Step size	Stiffness
N	μm	μm	N/mm
33.68	98.69	-144	341.27
Load side			
Load	Pullback	Step size	Stiffness
N	μm	μm	N/ μm
33.86	112	-166	302.32

The maximum load reported by the load cell was 39 N, at which point the motor stalled and no positive displacement could be observed. The step size and pullback are equal at stall at about 120 μm . This compared reasonably well with the predicted stall limit of 43.1 N (section 6.2) at a displacement of 112 μm .

This comparison confirmed that the IWM design methodology used is a useful tool to predict the load limit of this type on an IWM. Using the improved flextensional actuator in an IWM, would have had an expected load limit of over 77 N as calculated in Section 6.2.

7.3 Load testing of an IWM with force duplicator mechanism

The IWM with the force duplicator mechanism was attached via a tension spring to a load cell to measure the load capacity of the IWM. The stiffness, length and preloading of the attachment spring were selected through trial and error to ensure that stall was achieved within the 20 mm displacement range of the motor. The laser OFV-552 Fiber Vibrometer Fiber was used to measure displacement on the top and/or bottom beams of the extender. The top beam is labelled “A”, and the bottom is labelled “B” as indicated in Figure 45. The driving signals were generated with a computer using Matlab and sent to the PosiCon and A-303 amplifiers using a National Instrument PCIe – 6259 A/D data acquisition board (Figure 92). The same card was used to simultaneously record the generated signals, the signals after amplification, the displacement and the load signal output from the load cell. The Matlab program used can be found in Appendix B. All tests were performed at a signal frequency of 10 Hz or less to minimise any possible dynamic effects.

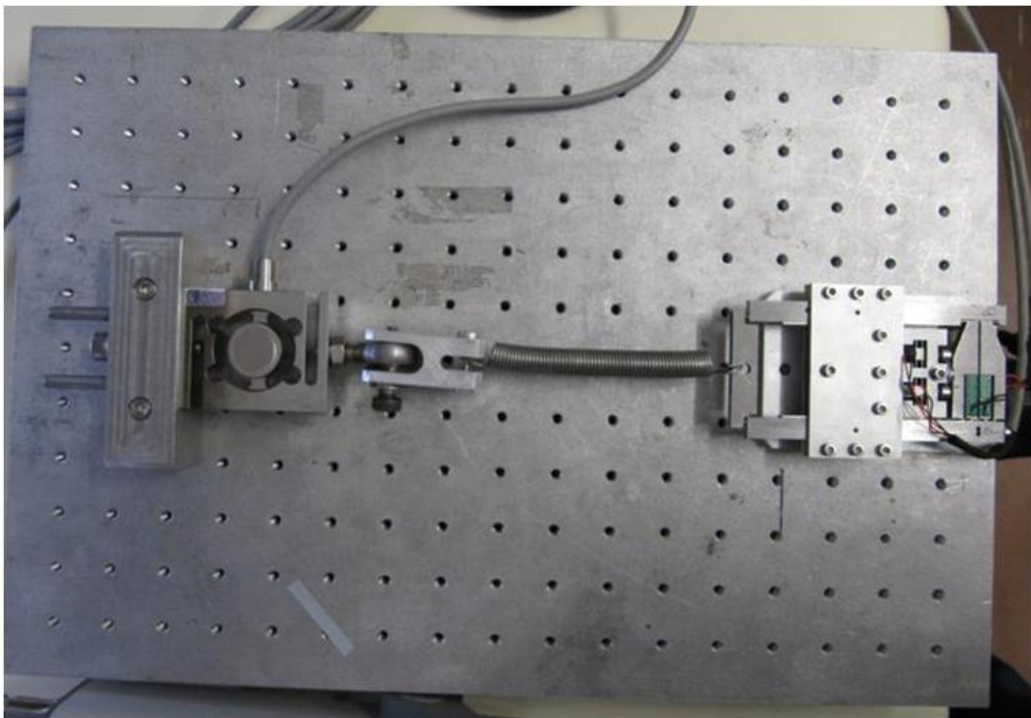


Figure 91: Load testing set-up showing load cell attached to the IWM

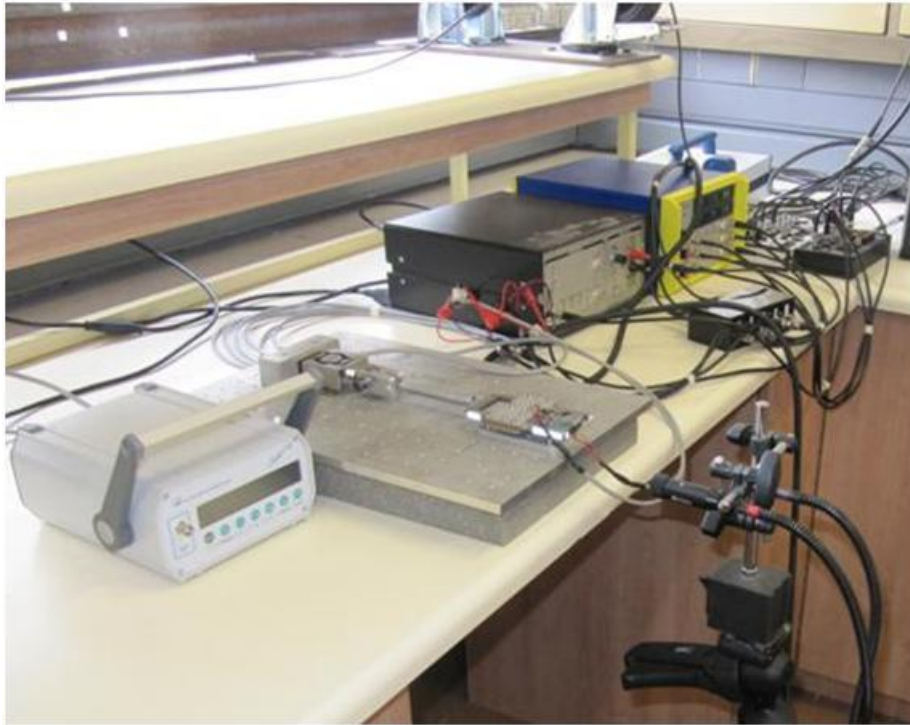


Figure 92: Load testing set-up showing all the equipment

The measured results are shown in Figure 93 for the load at 19.4 N and in Figure 94 for stall conditions which were found to be at 30.5 N. This result compares favourably with the calculated value of 29.4 N in Section 6.2. The displacement at stall was roughly 160 μm .

Referring to Figure 94, when an external load of 19.4N is applied to the relevant load path of the IWM, a back step of 109 μm is observed. Transferring these values to the load attachment position (by dividing the displacement by two, and multiplying the load by two), the stiffness of the load path can be calculated as follows:

$$(19.4 \cdot 2) / (109/2) = 0.711 \text{ N}/\mu\text{m} \quad \text{Equation 7-1}$$

which compares reasonable with the calculated stiffness in Table 3 of 0.768 N/ μm . Similarly, the stiffness from Figure 94 is:

$$(30.5 \cdot 2) / (160/2) = 0.763 \text{ N}/\mu\text{m} \quad \text{Equation 7-2}$$

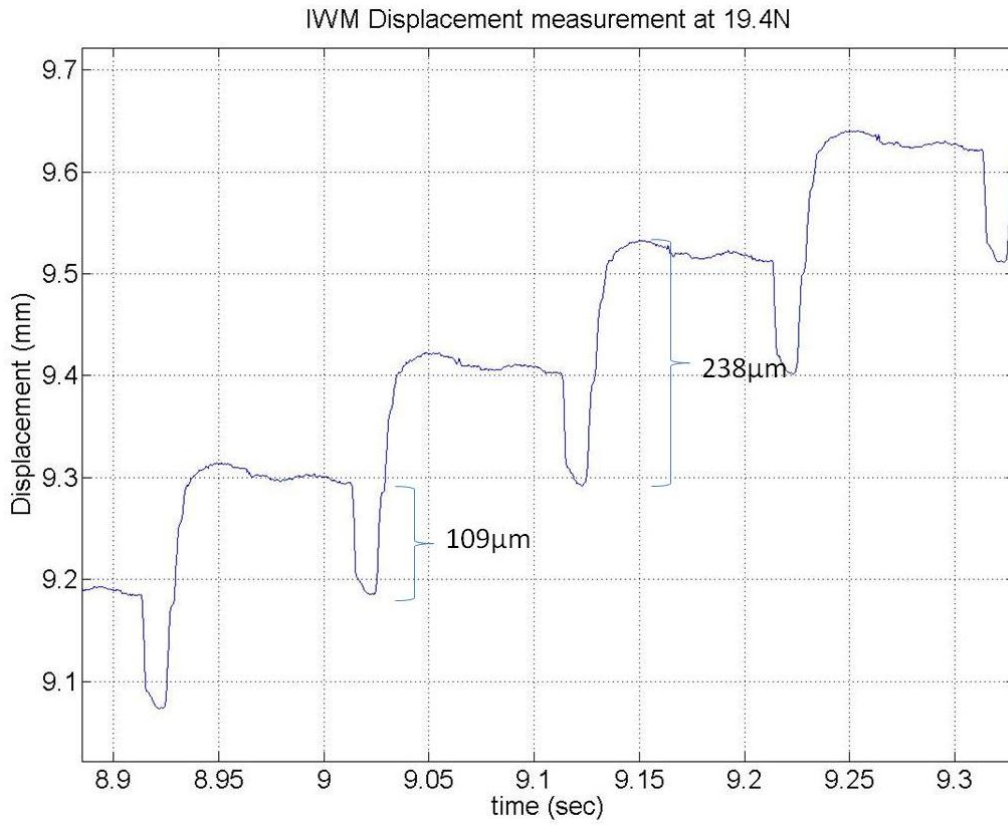


Figure 93: Extender behaviour at an intermittent load

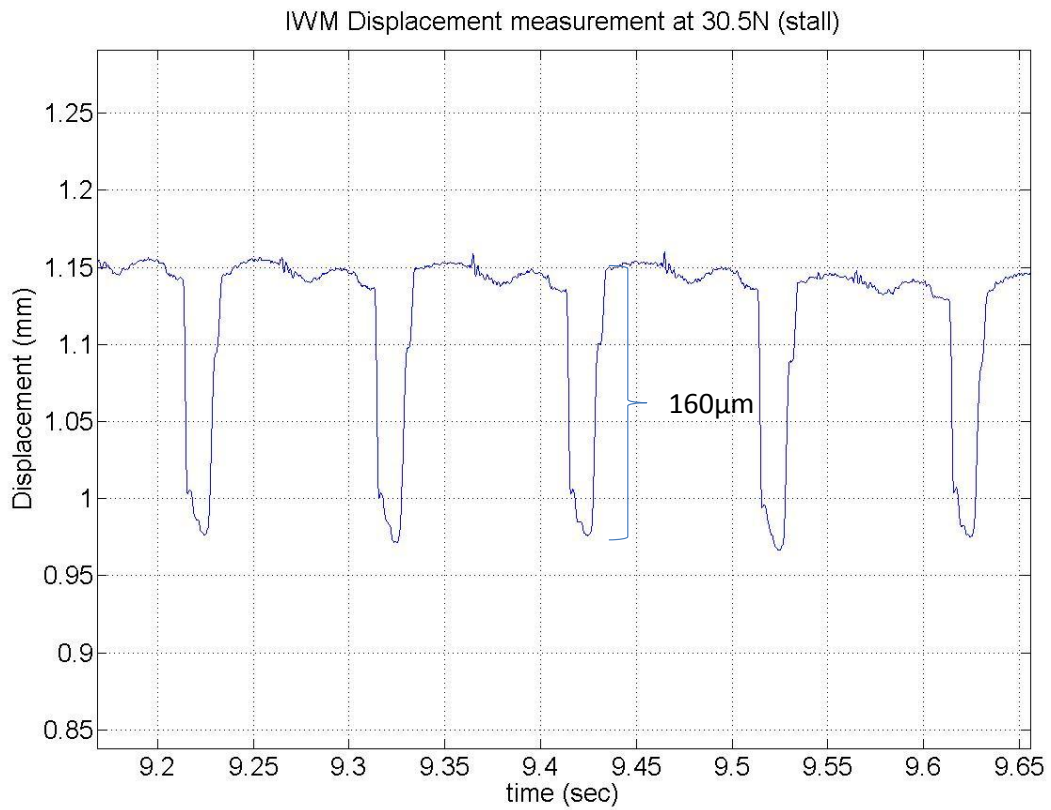


Figure 94: Extender behaviour at stall load

8 Conclusions and observations

The accumulation of small displacement is known, and has again been shown, to be a valid means for linear actuators to use. One type of actuator that makes use of this principle is referred to as an inchworm motor (IWM) due to its resemblance to an inch worm's locomotion. Although the principle works well, there remain a number of practical challenges that limit its usefulness. This is probably why so few of these devices are commercially available, despite the fact that the first inchworm motors appeared in the 1970s.

The unique properties associated with piezoelectric materials, together with the continued need for devices of increased precision and accuracy, have resulted in research on IWMs remaining active. An IWM is a practical device for acquiring useful displacement from the micro displacements of typical piezoelectric materials, without compromising its force capacity. The insignificant power consumption when holding a large load in position, as well as the high power density of piezoelectric materials, have made the piezoelectric IWM of particular interest for use as an actuator to morph a battery-operated UAV's wing.

An IWM requires at least three control signals, two for the clamp mechanism and one for the extender. When the extender actuator makes use of oppositely phased piezo elements, an additional signal is required. Such an actuator is ideal when similar forward and backward behaviour is required. To prevent the motor from slipping back, the clamp operation, and thus the clamp signals, needs to overlap, i.e. one of the clamps must always be engaged. The extender also must be allowed to complete its motion before the next clamp event is activated. Provided that these requirements are met, the shape of the signals and the relative timing of the six events that comprise a cycle do not alter the performance of the motor significantly. Whether a sine, ramp or square signal is used, the overall performance of the IWM remains the same; provided all other parameters are the same, one of the clamps is always in an engage position, and the extender is allowed to complete its motion before a clamp is activated/deactivated.

If an IWM is required to be fast, the shorter the signal events need to be. The fastest possible signals are square signals. It was found that mechanical inertia has a damping or filtering effect on the electrical signals, compromising perfectly square signals by causing the edges to be rounded. Also, to generate a perfect square signal requires an amplifier with infinite bandwidth and thus excessive power requirements. A practical, fast IWM will have less than perfect square signals. The designer needs to strike a balance between speed, mechanical inertia and power requirements when designing an IWM. The closer the signals approach a sine wave as opposed to a square wave, the lower the maximum possible speed, since more time is needed to meet the requirements as mentioned, but the lower the power consumption. It was also found that square waves, together with the mechanical clamp actions, make a lot of noise. If the clamps and extender have a smoother transition, then the noise of the motor is reduced significantly to hardly audible levels during slow operation. One way to obtain signals with smooth transition is to deliberately filter the signals. The noise and power requirements of an IWM could be tailored by filtering the control signals. The penalty for this is a reduction in the maximum speed, but it will not affect the force capacity.

The signals required for demonstrating the working of the IWM presented here were generated with linear laboratory amplifiers. The power consumed by a linear amplifier driving a piezoelectric load is excessive due to the high frequency and large voltage through the output resistor of the amplifier. Energy is lost through heat loss through the resistor. Linear amplifiers are designed for resistive loads and not capacitance loads as when driving piezoelectric elements. A switching amplifier is more suited for driving piezoelectric loads. The use of a novel switch mode power supply that uses a fly-back topology was specifically designed by the CSIR to drive an IWM. This supply was demonstrated to recover and cycle a large part of the power supplied to the piezo elements, and thereby reduces the power to be supplied from the power source for the next signal event. If a battery is used as the power source, one

can expect improved performance due to the switch mode power supply compared to linear amplifiers. Work still remains to shape or filter the signals of the switch mode amplifier to make it more suited for use with an IWM.

The use of micro ridges has been proposed as a means to improve the performance of the clamps. The idea is that very small interlocking teeth be manufactured into the contacting materials. Such interlocking teeth will have superior (shear) force transfer capability compared to when only static friction is depended on to transmit the holding load between the extender mechanism and the clamp mechanism. Since part of the focus of this study was to evaluate practical means of manufacturing an IWM using South African capabilities, the investigation into micro ridges was limited to manufacturing processes that would be both affordable and accessible locally. Two possible processes were identified and evaluated, namely micro milling machining and laser ablation. The study also only looked at aluminium and steel as possible materials to be considered. Both processes could produce ridges smaller than 30 μm , and only the ridges produced by micro milling had a sufficiently good surface finish to be able to interlock with other ridges, but at a pitch of about 60 μm . This means that the clamp mechanism would have to open with a gap of at least greater than 60 μm . The clamps in the second mechanism can displace about 50 μm . This is already insufficient before even making provision for compliance in the structure. It was concluded that it would be a lot simpler to design the clamps to have a force transfer capability through friction contact that matches or exceeds the force capacity of the extender mechanism. At no point during testing and measurement of the two IWMs used in the study could slippage of the clamps be observed. The use of micro ridges is therefore considered unnecessary as they would offer little advantage and add a lot of complexity to these types of IWM designs.

Understanding still lack in explaining the mechanism through which the external load reduces the displacement of the extender when operating within an IWM. The extenders behaved as expected under load when tested not as part of IWM, however, a reduction proportional to the external load have been observed on different IWM's and under different testing conditions when tested as part of a IWM. The load limit of the IWM is based on a stall displacement at half the free displacement of the extender, and has been empirically determine during testing.

The force capability of an IWM is largely a function of the blocked force of the extender, the free displacement of the extender, and the stiffness of the structure following a load path from the load attachment point, through the extender and holding clamp, to the attachment position of the IWM. It was shown that simple equations based on linear piezoelectric theory are very useful for predicting the force capacity of a design when the force is limited by the extender capability. These equations require the free displacement, the blocked force of the actuator and the stiffness of the actuator to be considered as inputs. An IWM stalls when the displacement of the extender under load is half the free displacement of the actuator. A simple linear static FEA was used to calculate the variables required for the design equations. Initially, unsatisfactory comparison with the measured force resulted. Geometrical inaccuracies were found to be the reason for this. It is important that the geometry used in the analysis compares well with the actual geometry if correlation with theory is required.

The use of lump parameter models to describe the dynamics of an IWM can be found in many literature works on IWMs. Little dynamic behaviour was witnessed during testing, and had no significant effect on the global performance of the IWMs. Lump parameter models were abandoned as an analysis tool in favour of the much simpler techniques presented in Section 6.1. Modal analysis of the motors also confirmed the first natural vibration modes about 10 times larger than the frequencies at which the IWM was tested. It should, however, be noted that at higher operational frequencies, dynamic effects become important and lump parameter models are a good way to analyse behaviour when approaching the natural modal frequencies.

Two different embodiments of the IWM are presented. Both were designed with the same application in mind. The first design was based on the conventional IWM layout, where the extender utilises a flextensional actuator. The second design used a novel optimised beam actuator for the extender actuation. It was realised with the previous design that since the extender moves in two parts within each cycle, the full load capacity could be displaced with each movement. By linking the extender's two ends through a lever, it is possible to use this ability to displace twice the load. Such a force duplicator will double the load capacity without compromising the displacement, since the full load is displaced two half displacements in each cycle. A further advantage is that since the step size experienced by the external load is half that of one extender step event, the step resolution is thus twice as good as it is in the conventional design, i.e. the smallest precision step that the motor can make is half that of a similar conventional design. This is particularly important, for instance where the IWM is used as a precision actuator, which is one of the typical applications of IWMs.

9 References

- Ardelean, E. V. (2004). High Performance V-stack'' Piezoelectric Actuator. *Journal of Intelligent Material Systems and Structures*, 15(11), 879–889. doi:10.1177/1045389X04045150
- Berlincourt, D., Krueger, H., & Near, C. (n.d.). Technical Publication TP-226 Properties of Piezoelectricity Ceramics. Retrieved from <http://www.morganelectroceramics.com/resources/technical-publications/>
- Bizzigotti, R. A. (1975). Electromechanical Translation Apparatus. U.S.
- Brisbane, A. D. (1968). Position Control Device. U.S.
- Campolo, D. (2001). *Energy Efficient Driving of Piezoelectric Actuators for the Micromechanical Flying Insect*.
- Canfield, S., Edinger, B., Frecker, M., & Koopmann, G. (1999). Design of Piezoelectric Inchworm Actuator and Compliant End-Effector for Minimally Invasive Surgery. *SPIE*, 3668, 835–843.
- Cedrat Technologies. (2012). Retrieved from www.cedrat.com
- Chandrasekaran, S., & Lindner, D. K. (2001). Optimized Design of Switching Amplifiers for Piezoelectric Actuators. *Journal of Intelligent Material Systems and Structures*, 1–42.
- Chen, Q., Yao, D.-J., Kim, C.-J., & Carman, G. P. (1999). Mesoscale actuator device: micro interlocking mechanism to transfer macro load. *Sensors and Actuators A: Physical*, 73(1-2), 30–36. doi:10.1016/S0924-4247(98)00251-9
- Claeysen, F., Jänker, P., Leletty, R., Sosniki, O., Pages, A., Magnac, G., & Christmann, M. (2010). New Actuators for Aircraft , Space and Military Applications. In *ACTUATOR 2010, 12th International Conference on New Actuators* (pp. 324–330). Bremen, Germany.
- Coetzer, M., & Harris, L. (2010). Progress Report 2009 / 2010 NSIA Smart Structures : Structural Design. (*CSIR Internal report*).
- Department of Science and Technology - Republic of South-Africa. (2010). *Civil / Commercial UAS development proposal*.
- Fleming, A. J., & Moheimani, S. O. R. (n.d.). *Improved current and charge amplifiers for driving piezoelectric loads. Analysis*. The University of Newcastle.
- Frank, J., Koopmann, G. H., Chen, W., & Lesieutre, G. A. (1999). Design and Performance of a High Force Piezoelectric Inchworm Motor. *SPIE*, 3668.
- Fujimoto, T. (1988). Linear Motor Driving Device. U.S.
- Ge, P., & Jouaneh, M. (1995). Modeling hysteresis in piezoceramic actuators. *Precision Engineering*, 17, 211–221.
- Giurgiutiu, V., & Rogers, C. A. (1997). Power and Energy Characteristics of Solid-State Induced-Strain Actuators for Static and Dynamic Applications. *Journal of Intelligent Material Systems and Structures*, 8(9), 738–750. doi:10.1177/1045389X9700800903

- Hara, A., Horinchi, T., Yamada, K., Takahashi, S., & Nakamura, K. (1986). Electromechanical Translation Device Comprising an Electrostrictive Driver of a Stacked Ceramic Capacitor Type. U.S.
- Heverly, D. E., Wang, K. W., & Smith, E. C. (2004). Dual-Stack Piezoelectric Device with Bidirectional Actuation and Improved Performance. *Journal of Intelligent Materials Systems and Structures*, 15(7), 565–574. doi:10.1177/1045389X04044450
- Kwon, K., Cho, N., & Jang, W. (2004). The Design and Characterization of a Piezo-Driven Inchworm Linear Motor with a Reduction-Lever Mechanism. *Jsm International Journal*, 47(3), 803–811.
- Lafayette, C. G. O., & Foster, C. E. F. (1980). Electromotive Actuator. U.S.
- Lee, S., & Esashi, M. (1995). Design of the Electrostatic Linear Microactuator Based on the Inchworm Motion. *Science*, 5(8), 963–972.
- Lies, H., Hegewald, T., Heizl, J., Lerch, R., Kappel, A., Schwebel, T., ... Kraul, R. (2004). Piezo Inchworm Actuator for Heavy Loads. In *International Conference on New Actuators* (pp. 144–147). Bremen.
- Lindner, D. K., Zhu, H., Song, C., Huang, W., & Cheng, D. (2002). Low input voltage switching amplifiers for piezoelectric actuators. *SPIE*, 4698, 282–292. doi:10.1117/12.475075
- Lindner, D. K., Zhu, M., Vujic, N., & Leo, D. J. (2002). COMPARISON OF LINEAR AND SWITCHING DRIVE AMPLIFIERS FOR PIEZOELECTRIC ACTUATORS. *American Institute of Aeronautics and Astronautics*, 1352, 1–5.
- Locher, G. L. (1967). Micrometric Linear Actuator. U.S.
- Loveday, P. W. (2003). Practical optimization of amplification mechanisms for piezoelectric actuators. *Proceedings of SPIE*, 5056, 392–399. doi:10.1117/12.483455
- Loverich, J. J., Koopmann, G. H., Lesieutre, G. a., Frank, J. E., & Chen, W. (2007). A New Piezoelectric Actuator using a Feed-screw for Quasi-static Motion Accumulation Part I: Experimental Development. *Journal of Intelligent Material Systems and Structures*, 19(1), 73–81. doi:10.1177/1045389X06073169
- Meeker, T. R. (1996). IEEE Standard on Piezoelectricity. *Ultrasonics, Ferroelectrics, and Frequency Control.*, 43(5), 9.
- Miesner, J. E., & Teter, J. P. (1994). Piezoelectric/magnetostrictive resonant inchworm motor. *Proceedings of SPIE*, 2190, 520–527. doi:10.1117/12.175212
- Newcomb, C. V., & Flinn, I. (1982). Improving the linearity of piezoelectric ceramic actuators. *Electronics Letters*, 18(11), 442–444.
- Newnham, R. E., Dogan, a., Xu, Q. C., Onitsuka, K., Tressler, J., & Yoshikawa, S. (1993). Flexensional “moonie” actuators. *Proceedings of IEEE Ultrasonics Symposium*, 509–513. doi:10.1109/ULTSYM.1993.339557
- Newton, D., & Main, J. (1996). Piezoelectric Actuation Systems : Optimization of Driving Electronics Cl L1. *SPIE*, 2717, 259–266.
- Okazaki, Y. (1990). A micro-positioning tool post using a piezoelectric actuator for diamond turning machines. *Precision Engineering*, 12(3), 151–156. doi:10.1016/0141-6359(90)90087-F

- Ouyang, P. R., Tjiptoprodjo, R. C., Zhang, W. J., & Yang, G. S. (2007). Micro-motion devices technology: The state of arts review. *The International Journal of Advanced Manufacturing Technology*, 38(5-6), 463–478. doi:10.1007/s00170-007-1109-6
- Pandell, T., & Garcia, E. (1996). Design of a Piezoelectric Caterpillar Motor. *Proceedings of the ASME Aerospace Division*, 52, 627–648.
- Park, J., Carman, G. P., & Hahn, H. T. (2000). Design and Testing of a Mesoscale Piezoelectric Inchworm Actuator with Microridges. *Journal of Intelligent Material Systems and Structures*, 11(9), 671–684. doi:10.1106/J44B-DK25-G57B-RTC5
- Physikinstrumente. (n.d.). Tutorial: Piezoelectrics in Nanopositioning, Designing with Piezoelectric Actuators. PI. Retrieved from http://www.physikinstrumente.com/en/products/piezo_tutorial.php
- Physikinstrumente. (2011). Retrieved from www.physikinstrumente.com
- Piezomechanik. (2008). Low voltage co-fired multilayer stacks , rings and chips for actuation.
- Piezomechanik. (2011). No Title. Retrieved from www.piezomechanik.com
- Powers, G., Xu, Q., Guidarelli, T., & Smith, J. (2005). High-power Inchworm actuators for extended-range precision positioning. *Proceedings of SPIE*, 5762, 287–298. doi:10.1117/12.600584
- Powers, G., Xu, Q., & Smith, J. (2004). The next generation of Inchworm actuators evolves with nanometer resolution, multimillimeter range, and power-off hold. *Proceedings of SPIE*, 5388, 155–166. doi:10.1117/12.540055
- Smith C, R. (2005). *Smart material systems: model development* (Vol. illustrate). SIAM.
- Spanner, K., & Koc, B. (2010). An Overview of Piezoelectric Motors. In *ACTUATOR 2010, 12th International Conference on New Actuators* (pp. 167–176). Bremen, Germany.
- Stibitz, G. R. (1964). Incremental Feed Mechanisms. U.S.
- Stölting, H.-D., & Kallenbach, E. (2008). *Handbook of fractional-horsepower drives* (p. 350). Springer.
- Suleman, A., Burns, S., & Waechter, D. (2004). Design and modeling of an electrostrictive inchworm actuator. *Mechatronics*, 14(5), 567–586. doi:10.1016/j.mechatronics.2003.10.007
- Van Nuys, G. W. C. (1990). US Patent 4928030 Piezoelectric_actuator.pdf. U.S.
- Vaughan, M. E. (2001). The Design , Fabrication , and Modeling of a Piezoelectric Linear Motor by Master of Science. *Mechanical Engineering*.
- Wallis, J. R., & Loveday, P. W. (2004). Strain / Electrical Potential Transducer. United States.
- Williams, E. F., Loveday, P. W., & de Villiers, M. F. R. (2010). Development of an Efficient Piezoelectric Inchworm Motor. In *12th International Conference on New Actuators* (pp. 647–651).
- Yang, E., Dekany, R., & Padin, S. (n.d.). *Design and Fabrication of a Large Vertical Travel Silicon Inchworm Microactuator for the Advanced Segmented Silicon Space Telescope. Design*.

Yi, K. A., & Veillette, R. J. (2005). A Charge Controller for Linear Operation of a Piezoelectric Stack Actuator. *IEEE Transaction on Control System Technology*, 13(4), 517–526.

Yokohama, T. M. (1990). Drive Apparatus and Motor Unit Using the Same. U.S.

Zhang, B. (1994). Design of an inchworm-type linear piezomotor. *Proceedings of SPIE*, 2190, 528–539.
doi:10.1117/12.175214

10 Appendices

A. Behaviour of a piezoelectric element

Piezoelectric actuators exhibit highly capacitive electrical characteristics. The circuit shown in Figure 95 is an electric circuit equivalent for a piezoelectric element, as given by the IEEE Standards on Piezoelectricity (Meeker, 1996). In this circuit C_0 is the static or parallel capacitance and the parallel RLC branch represents one electromechanical resonance. In the small region near a particular resonance, R_1 , L_1 , and C_1 are constant. In order to model other resonances, additional RLC branches can be added. By adding additional RLC components, a fairly accurate model of the piezoelectric element is generated. For many power electronic design situations, however, the piezoelectric load may be considered to be purely capacitive.

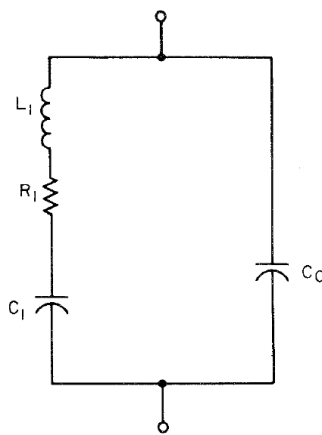


Figure 95: Equivalent electrical circuit of a piezoelectric vibrator (Meeker, 1996)

The relationship between electrical charge, voltage and current for a (pure) capacitor is given by the following equations:

$$q = C \cdot V \quad \text{Equation 10-1}$$

$$\frac{dq}{dt} = C \cdot \frac{dV}{dt}$$

$$I = \frac{dq}{dt}$$

$$I = C \cdot \frac{dV}{dt} \quad \text{Equation 10-2}$$

Where C is the capacitance of the piezo element (Farad), q is the electrical charge (coulomb), I is the current flowing in the piezo element (Ampere), $\frac{d}{dt}$ is the time derivative, P is power (watt) and V is the voltage applied to the piezo stack (volt).

The power consumption (P) is obtained by multiplying the current by the voltage.

$$P = V \cdot I \quad \text{Equation 10-3}$$

Also, the electrical charge (q) applied to a piezoelectric element is calculated as the sum of the charge on a pure capacitor and the product of the displacement (δ) and the piezoelectric constant (θ). The latter is because of the piezoelectric effect that couples displacement with electrical charge. For simulation, a linear relationship is assumed.

$$q = \theta \cdot \delta + C \cdot V \quad \text{Equation 10-4}$$

Consider the 1DOF representation of the system. Also consider an instance where a zero voltage is applied ($V = 0$) and a constant non-zero force is applied to the system. Once a steady state condition is reached, the velocity will be zero and the system reduces to a simple force-applied-to-a-spring system, i.e. the final displacement equals the force divided by the total stiffness. The electrical charge will also have a constant value, but the current will be zero and no power is consumed. If a different constant force is applied, only the displacement and electrical charge changes to a different constant value (in the steady state). Now, if a constant voltage is also applied and steady state is reached, the electrical charge will change to a new constant value (Equation 10-1) and a new constant displacement value (Equation 2-7), but the current and power consumption will still be zero. This example illustrates the ability of piezoelectric devices, such as an IWM, to hold a load in a position without consuming power. (In practice, however, minor power will be consumed due to the driving electronics and the internal resistance of the piezo element.)

By using a linear equation to model the 1DOF piezoelectric system, a linear relationship between voltage and displacement is implied. A plot of voltage against displacement will be a straight line. In reality, this relationship is not a straight line in that a significant amount of hysteresis is evident.

Testing a piezoelectric stack

To investigate the behaviour of a piezo element, a simple test was constructed. A PSt 150/5X5/20 piezo stack was used. This piezo element is commercially available from PIEZOMECHANIK (Piezomechanik, 2011). Its properties are listed in Table 10.

The test consists of a piezo stack loaded in a vice together with a load cell as shown in Figure 96. The stiffness of the load cell was determined by increasing the load and recording the displacement, which was found to be approximately 13 400 N/m. In Table 10, the stiffness of the piezo element is 59.3×10^6 N/m, roughly 4 500 times more than the load cell stiffness!

The loading during testing was increased at approximately 15 kg intervals. A -30 V to 150 V amplitude sine signal at 2 Hz was then applied to the stack. The low frequency was necessary so that dynamic effects were not included. The voltage and current were measured.

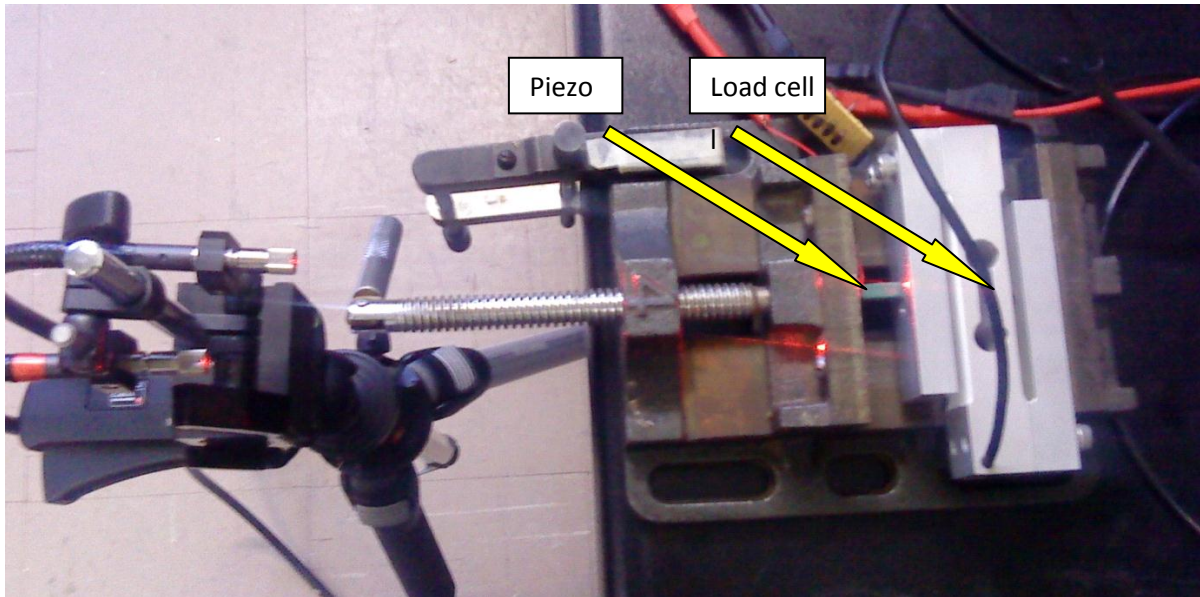


Figure 96: Testing of preloaded piezo element

The measured results showed that as the mean applied force increased from 10.4 kg to 74.9kg, the RMS current increased from 1.84 mA to 2.18mA, and the RMS power consumption of the piezo stack also increased from 115 mW to 145 mW.

The measured output from the load cell is shown in Figure 97. The load cell was zeroed when no load was applied. The second graph in Figure 97 shows the average loading for each test.

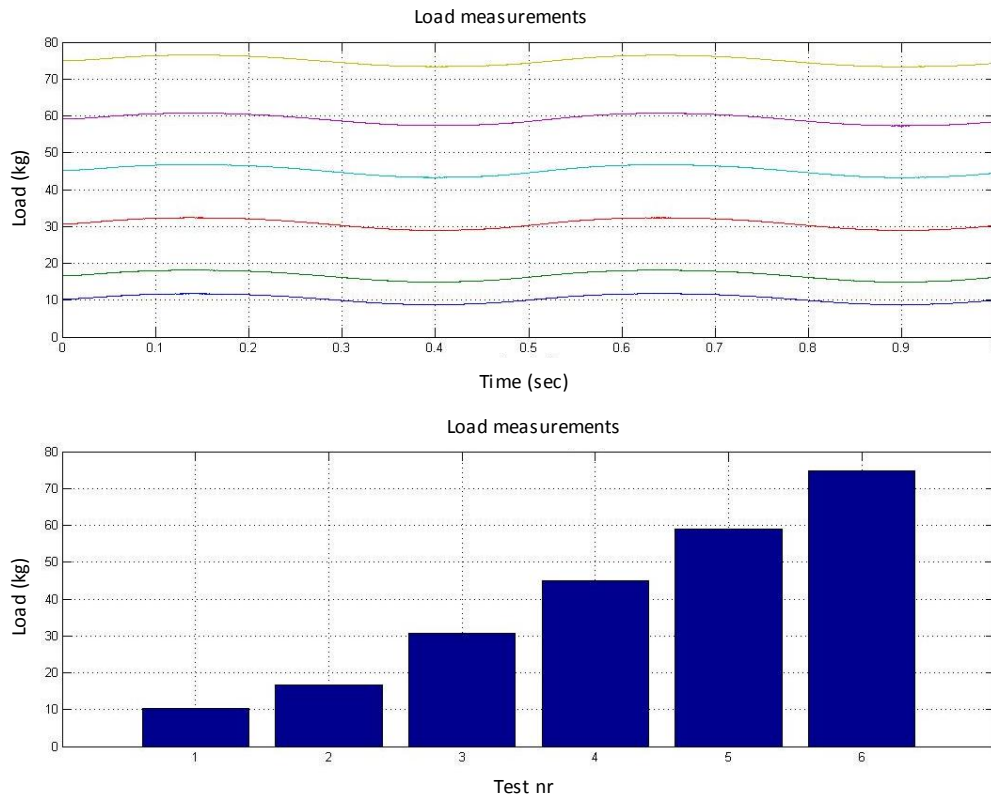


Figure 97: Load measurements on a single piezo stack

The displacement measurements were zeroed for each load adjustment. The measured values are shown in Figure 98. The blue bars on the second graph show the total displacement range. There is little change in displacement between the six measurements. The free displacement (zero loading) of the piezo stack that was tested was $27 \mu\text{m}$. The average displacement between all six measurements when the piezo was preloaded was also $27 \mu\text{m}$. The increased loading had little effect on the displacement range when the sine voltage signal was applied.

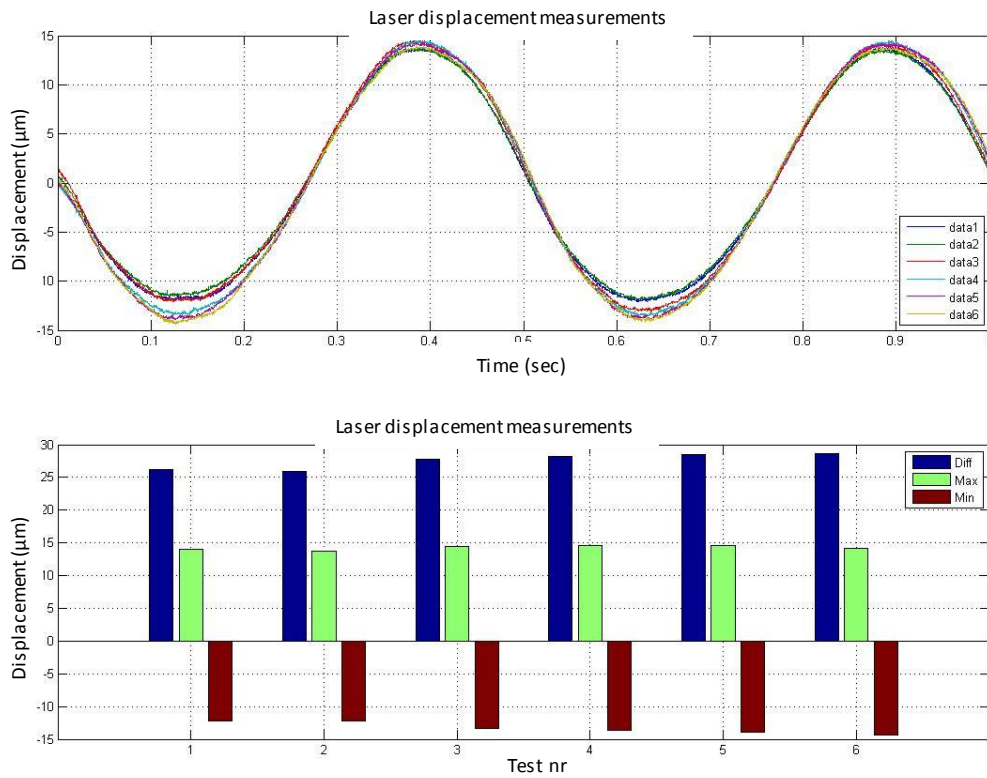


Figure 98: Laser displacement measurement

The voltage supplied to the piezo stack was kept the same between the six measurements as illustrated in Figure 99. Some difference between the current measurements can be seen on the current graph. Current peak values increased with loading. Also note that the current is not a cosine wave as predicted by a linear analytic model.

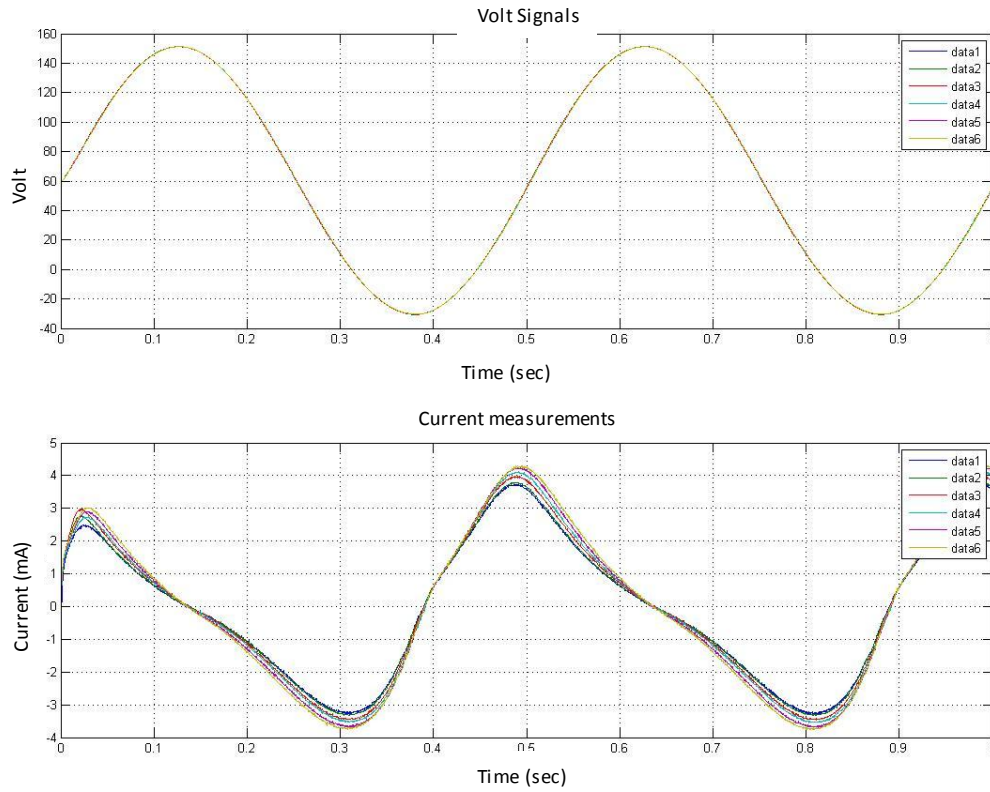


Figure 99: Voltage and current measurement for a single piezo stack

An increase in power consumption with increased loading due to the increased current consumption can be clearly seen below.

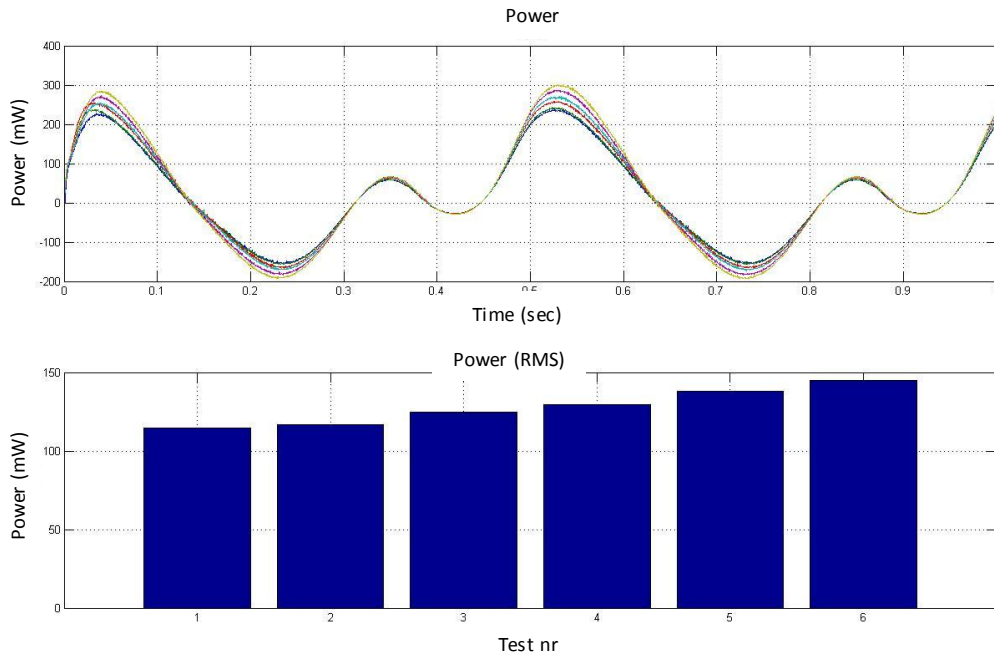


Figure 100: Power calculation from measured voltage and current for a single piezo stack

Comparison between measured and simulated results

The behaviour of a piezoelectric element was simulated using the formulation developed. The displacement output is calculated using Equation 10-10. See Appendix 0 for a Matlab program using Equation 10-10. The current and power can be calculated from Equation 10-2 and Equation 10-3.

The graphs plotted in Figure 101 to Figure 105 compare the measured and simulated results. The displacement is plotted in Figure 101. The measured results compare well with the simulated results, although the total displacement was somewhat larger in the simulation.

The hysteresis effect between the voltage and displacement is shown in Figure 104. The measured response shows some similarities with the published response in Figure 31. A piezo stack may be at one of two positions for a given voltage, depending on whether the voltage value is reached from a high voltage or a low voltage.

The effect of the non-linearity can also be clearly seen when the measured and calculated currents are plotted together (Figure 102). Again the simulation showed somewhat higher peaks than what was measured. It is also interesting to note the difference in results when the current is plotted against the driving signal as shown in Figure 105. The effect of the non-linearity resulted in the orbit of the graph not following the circle predicted by the linear simulation. The maximum and minimum current values also occur at different voltage values than predicted. For a given voltage value, one of two current conditions may occur, depending on the direction of current flow. The current values for the two conditions are also not symmetrical for the physical system. Also note that the maximum absolute current value is higher when the current is positive than when it is negative.

The power consumption calculated in the simulation is conservative when compared with the power calculated from the measured results. The root mean square power for the graphs in Figure 103 is 176 mW for the simulated results, and it increased from 115 mW to 145 mW with increased loading for the different tests for the measured results.

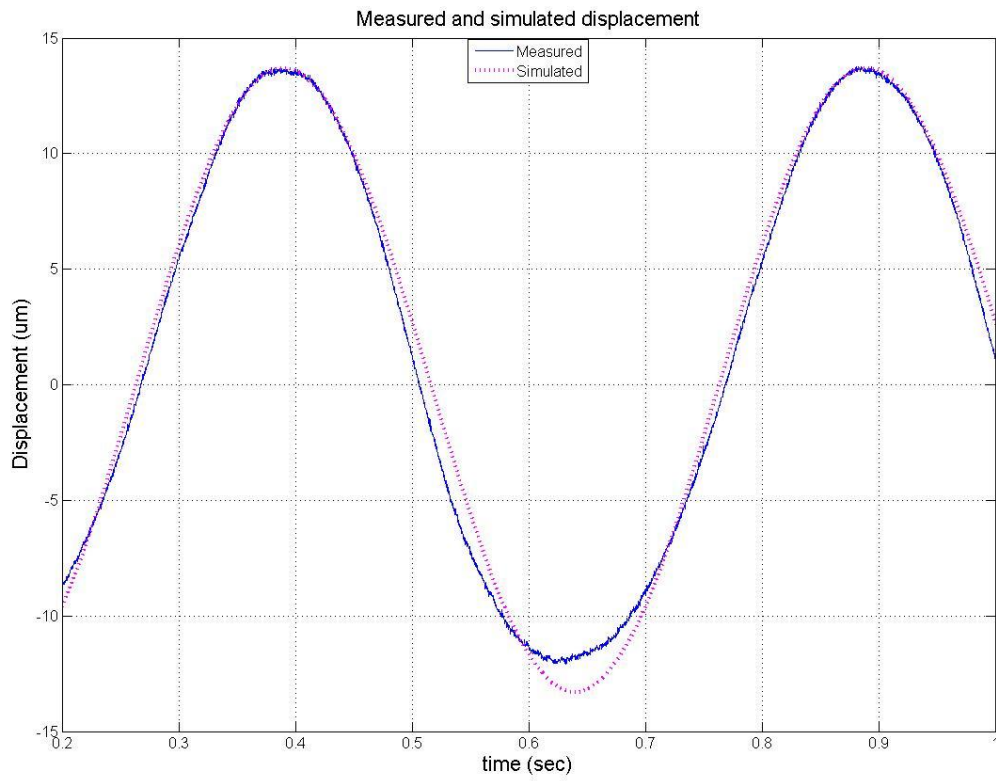


Figure 101: Comparison between measured and simulated displacement

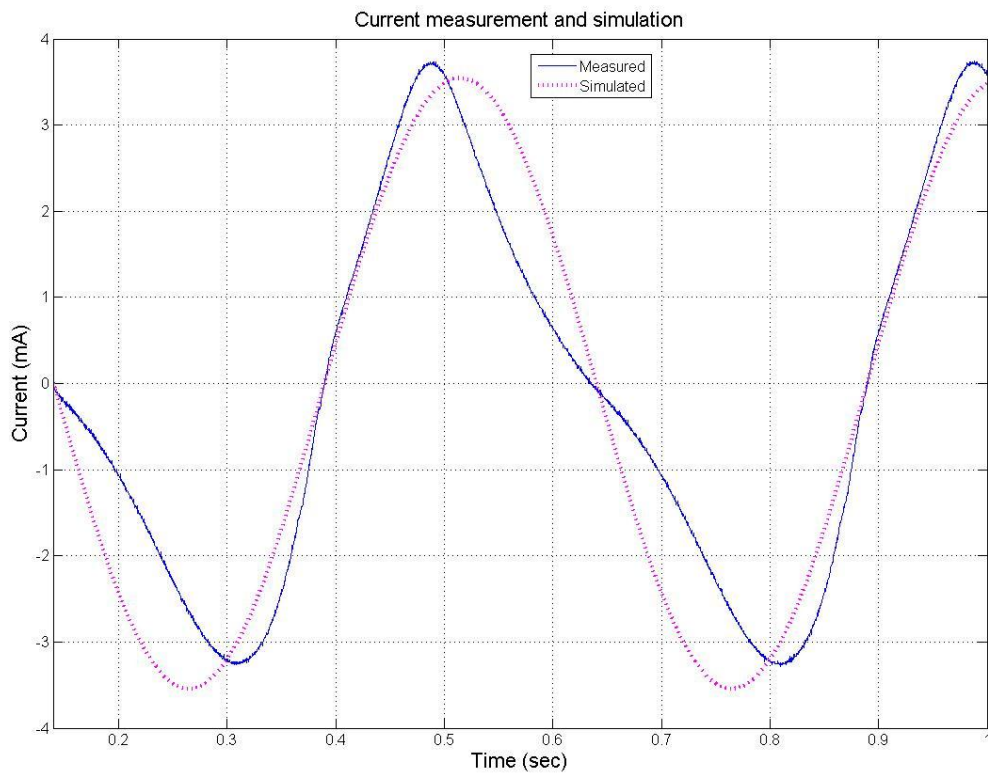


Figure 102: Comparison between measured and simulated current

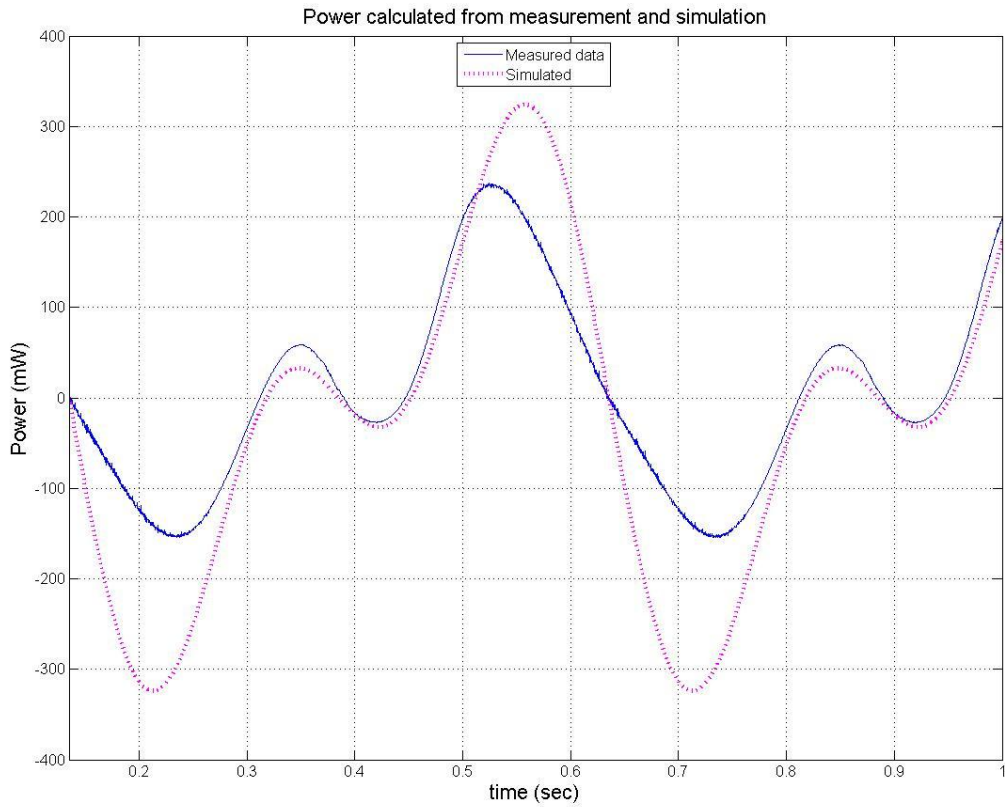


Figure 103: Comparison between measured and simulated power

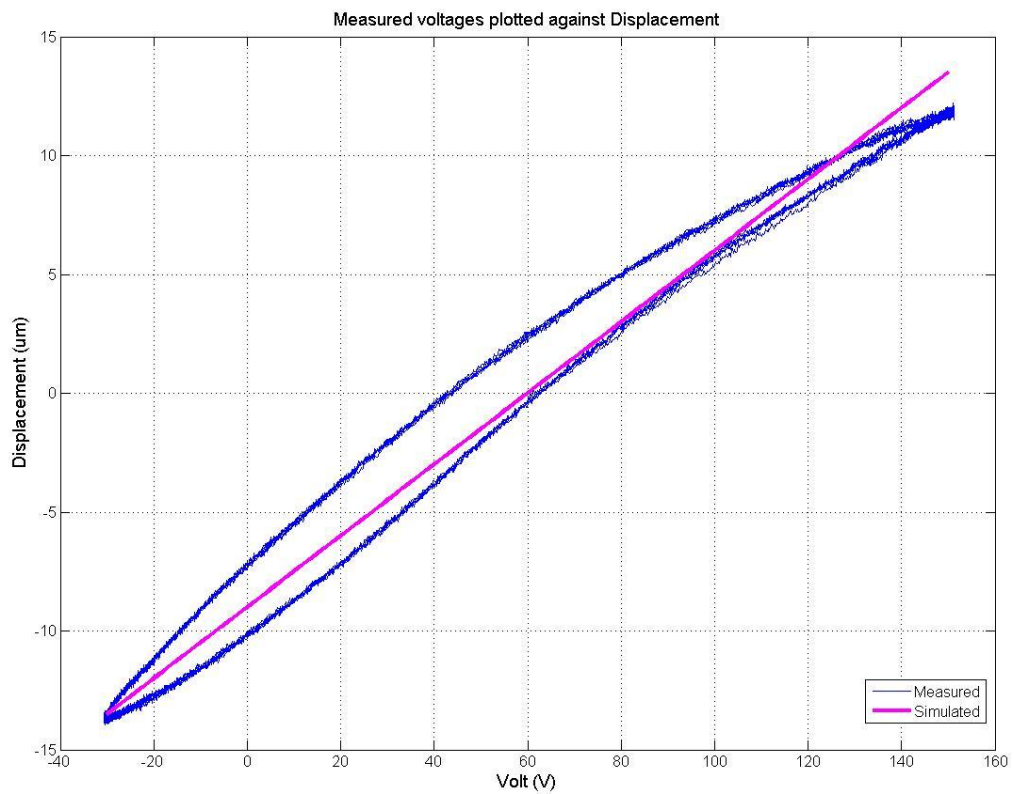


Figure 104: Hysteresis effect

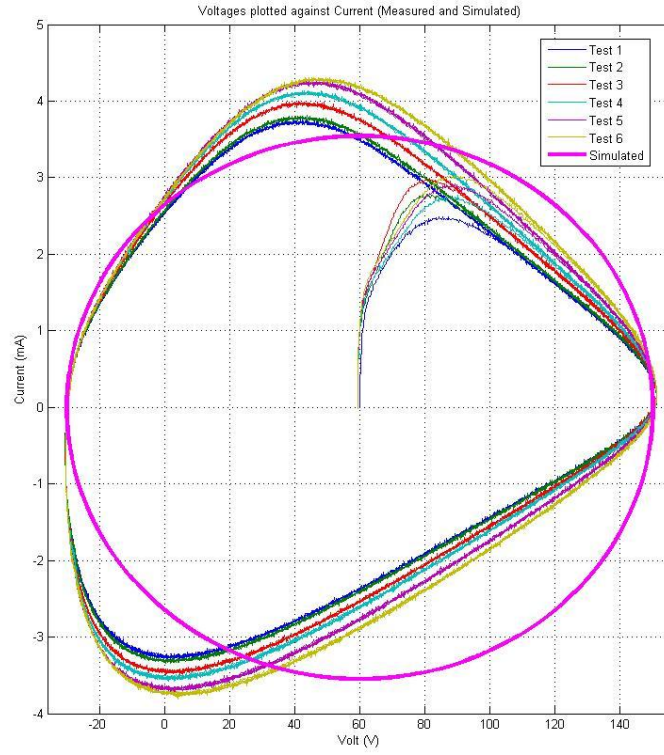


Figure 105: Comparison voltage and current for measured and simulated results

B. Matlab programs

Inchworm motor driving and testing program

```

%~~~~~
% Title: Test program for testing the demonstrator inchworm actuator
% Description: Creates block signals for the inchworm actuator
% and sends it to NI 6110 card, and receives back data and plots the data.
% Date: 2009 - 01 - 07
% Created by: Eddie Williams
% Comments: A single switch cycle is divided into six zones. The time
% duration for each zone can be adjusted by the user (CYCLETIME). The
% status for two clamps and the extender can be adjusted between engage
% (1) or off (-1). A signal is generated for one second and loaded into the
% buffer. The buffer is repeated for the required time. The output from the
% test setup is three signal channels from the piezo stacks, load,
% displacement and velocity

clc; clear all; daqreset; clf

%~~~~~
% User Input
% Weighted time intervals for one cycle
cycletime = [1 1 3 1 1 3];

% Select movement direction
dir = input('Direction (1 or 2)? ');

if dir == 1
    direc = 'up';
elseif dir ==2
    direc = 'down';
else
    disp('Nope (wrong entry)')
    return
end

% Switching vectors (1 for on, -1 for off)
clamp_one = [ 1  1  1  1 -1 -1];
extend = [-1 -1  1  1  1 -1];
clamp_two = [ 1 -1 -1  1  1  1];

time = 4;                % Duration of signal
signal_freq = 5;        % Signal frequency [Hz]
sample_freq_want = 6000; % Sampling frequency wanted[Hz]

% Calibration
v_error = [0 0 0 0 0 0 0]; % Calibration factors

% Number of input channels
in_chan = 4;

% Amplitude
ampe = 3;                % Extender amps
ampc = 3;                % Clamp amps

% Filter controls
wse = 10;                % Extender filter
wsc = 10;                % Clamp filter

```

```

% Conversions reduction
outr = 15; % Voltage reduction factor

% Displacement range
disran = 0.5; % mm/V

% Load
loadcon = 25.75/0.254; % Load cell conversion

filename = input('Enter file name for data storage: ','s');
%~~~~~

% Voltage limit
if abs(ampe) > 3
    ampe = 1;
    disp('VOLTAGE LIMIT ON.')
end
if abs(ampc) > 3
    ampc = 1;
    disp('VOLTAGE LIMIT ON.')
end

[sigout,sigin,tt,ttplot]=InchWorm_Act_switch_mod3...
    (direc,cycletime,clamp_one,extend,clamp_two,tyd,signal_freq,...
    sample_freq_want,v_error,in_chan,ampe,ampc,wse,wsc);

% Filter displacement data

disfil = filter(ones(1,5)/5,1,sigout(:,4));
displace = disfil*disran;

%loadfil = filter(ones(1,80)/80,1,sigout(:,5));

%load cell = loadcon*loadfil;

%Plot data for three outputs and three inputs.
figure(1);
subplot(3,1,1); plot(ttplot,sigin(:,1),'-',ttplot,sigin(:,2),'-',...
    ttplot,sigin(:,3),'-',ttplot,sigin(:,4),'-c');
    title('Input signals for 1 sec');...
    legend('Clamp1','Extender 1','Extender 2','Clamp2');
    ylabel('Volt'); grid;
subplot(3,1,2); plot(tt,sigout(:,1)*outr,tt,sigout(:,2)*outr,...
    tt,sigout(:,3)*outr,'c');
    title('Output signals'); legend('Clamp1','Extender 1','Clamp2');
    ylabel('Volt'); grid;

subplot(3,1,3); plot(tt,displace);
    ylabel('Displacement (mm)')
    title('Clamp Displacement measurement'); grid; xlabel('time (sec)');

    figure(2);
plot(tt,displace);
    ylabel('Displacement (mm)')
    title('Clamp Displacement measurement'); grid; xlabel('time (sec)');

disp('Done plotting')
% Save data
hgsave([1 2],filename); % Save graphics

```

```
save(filename,'sigin','sigout','displace','ttplot','tt')
disp('Done with data storage.')
Function program for "Inchworm motor driving and testing program"
function [getin,sendout,tyd_in,tt]=InchWorm_Act_switch_mod3...
    (direc,cycletime,clamp_one,extend,clamp_two,tyd,signal_freq,...
    sample_freq_want,v_error,in_chan,ampe,ampc,ws1,ws2)
```

```

%~~~~~
% Title: Signal Generator
% Description: Creates block signals for the inchworm actuator
% and sends it to NI 6110 card.
% Date: 2008 - 11 - 21
% Created by: Eddie Williams
%~~~~~

% Select clamp sequence for selected direction

if strcmp(direc,'up')
    clamp1 = clamp_one;
    clamp2 = clamp_two;
elseif strcmp(direc,'down')
    clamp1 = clamp_two;
    clamp2 = clamp_one;
else
    disp('fout')
end

blocks = length(clamp1);

% Time stuff
sample_freq = ceil(sample_freq_want/blocks/signal_freq)*blocks*signal_freq;
                % Real Sampling frequency [Hz]
tt = 0:(1/sample_freq):(1-1/sample_freq);
                % Time vector for 1 sec

numdata = length(tt);
wcycletime = cycletime./sum(cycletime);

ret = 0;                % Programming flag

% Creating an Analog Input Object
ail = analoginput('nidaq','Dev1');

% Creating an Analog Output Object
aol = analogoutput('nidaq','Dev1');

% Adding Channels to an Analog Input Object
chansin = addchannel(ail,0:in_chan-1);
% Adding Channels to an Analog Output Object
chansout = addchannel(aol,0:3);

% Find the range of valid sampling rates for hardware
%ValidRates = propinfo(aol,'SampleRate');
%ValidRates.ConstraintValue;
%out = daqhwinfo(aol)

% Setting the Sampling Rate
set(aol,'SampleRate',sample_freq);
set(ail,'SampleRate',sample_freq);
%ActualRate = get(ail,'SampleRate'); % Get Actual Sample Rate

% Change the time between consecutive channels to eliminate ghosting
set(ail,'channelskew',4e-5);

% Generate signal
intsize = numdata/signal_freq; % Size of signal
sigsteps = ceil(intsize.*wcycletime);
dif = sum(sigsteps) - sum(intsize);
sigsteps(3) = sigsteps(3) - dif; % Size correction

for w = 2:length(sigsteps)

```

```

    sigsteps(w) = sigsteps(w-1)+sigsteps(w);
end
sig = [1 sigsteps];

for tel = 1:blocks
    data1(sig(tel):sig(tel+1)) = clamp1(tel);
    data2(sig(tel):sig(tel+1)) = clamp2(tel);
    data3(sig(tel):sig(tel+1)) = extend(tel);
    data4(sig(tel):sig(tel+1)) = -extend(tel);
end

% Apply amplifications
data1t = data1.*ampc*1.5;           % Mod for x20 Amp
data2t = data2.*ampc;
data3t = data3.*ampe;
data4t = data4.*ampe;

c1t = data1.*ampc*1.5;           % Mod for x20 Amp
c2t = data2.*ampc;
e1t = data3.*ampe;
e2t = data4.*ampe;

for q = 1:signal_freq-1
    c1t = [c1t data1t];
    c2t = [c2t data2t];
    e1t = [e1t data3t];
    e2t = [e2t data4t];
end

c1 = c1t';
c2 = c2t';
e1 = e1t';
e2 = e2t';

% Filter signals
a1 = filter(ones(1,ws2)/ws2,1,c1);
c1ff = filter(ones(1,ws2)/ws2,1,a1);
a2 = filter(ones(1,ws2)/ws2,1,c2);
c2ff = filter(ones(1,ws2)/ws2,1,a2);
a3 = filter(ones(1,ws1)/ws1,1,e1);
e1ff = filter(ones(1,ws1)/ws1,1,a3);
a4 = filter(ones(1,ws1)/ws1,1,e2);
e2ff = filter(ones(1,ws1)/ws1,1,a4);

% Fix start of signal that gets messed up by the filters.
c1f = [c1ff(intsize+1:intsize*2); c1ff(intsize+1:end)];
c2f = [c2ff(intsize+1:intsize*2); c2ff(intsize+1:end)];
e1f = [e1ff(intsize+1:intsize*2); e1ff(intsize+1:end)];
e2f = [e2ff(intsize+1:intsize*2); e2ff(intsize+1:end)];

% Output
sendout = [c1f e1f e2f c2f];

% Write data to NI
putdata(ao1,sendout)
set(ao1,'RepeatOutput',tyd-1)
set(ao1,'TriggerType', 'Manual'); % Set TriggerType to manual

% Set up input
set(ai1,'SamplesPerTrigger',sample_freq*tyd);
set(ai1,'TriggerType', 'Manual');

% Start

```

```
start([a1l a0l]);
trigger([a1l a0l]);

try
    %Wait for the completion of ao, and ai_device object
    wait(a0l,tyd*1.5)
    wait(a1l,tyd*1.5)

    % Get data from NI
    [data_in,tyd_in] = getdata(a1l);
    % Data correction
    getin = zeros(size(data_in));
    for j = 1:in_chan
        getin(:,j) = data_in(:,j) - v_error(j);
    end
    %getin = data_in;

catch
    %If timeout occurs, display an error message
    display('Timeout!')
    ret = -1;
end

if(ret == -1)
    stop(a1l);
    stop(a0l);
end

% Clean up
delete ([a0l a1l]);
clear a0l chansout; %clear ao_channels/device
clear a1l chansin; %clear ai_channels/device

disp('Done with data generation and capturing')
```

Program to model a Piezoelectric stack. Properties for PSt 150/5x5/20.

(Requires Matlab's Control Systems toolbox)

```
%~~~~~
% Program to model a Piezoelectric stack. Properties for PSt 150/5x5/20
% have been used.
% Based on state space method for a 1DOF system.
% 2011-06
% EF williams
%~~~~~

clc; clear; close all

%~~~~~
% Inputs
% Mechanical inputs
kstruck = 13400;
m = 1;

% Damping
dr = 1;           % Damping ratio
cc = 2*sqrt(m*kstruck); %Critical damping
c = dr*cc;

% Piezo inputs
% Measured Actuator characteristics
Fb = 1600;        % Blocked Force [N]
delf = 27e-6;     % Free stroke [m]
Cap = 1800e-9;    % Capacitance [F] from catalogue
Vmax = 90;        % Drive Voltage [V]
Ka = Fb/delf;     % Actuator Mechanical stiffness
theta = Ka*delf/180; % Piezo constant

% Signal
Fs = 1000;        % Sampling frequency
L = 100000;       % Length of signal
dtp = 10;         % Fraction of 'on' time for slopes

% Constant Load
Lload = 0;        % Load (N)
%~~~~~
k = kstruck + Ka; % Total stiffness

% State space system
A = [0 1; -k/m -c/m];
B = [0; theta/m];
C = [1 0; 0 1];
D = [0; 0];
F = [0; 1/m];     % Noise coefficient matrix

sys1 = ss(A,B,C,D);
tfsys1 = tf(sys1);
P = ctrb(A,B);     % Check for controlability
Pdet = det(P);
Pcond = cond(P);

% Open loop system with noise
Aol = A;
Bol = [B F];
```



```

sys2 = ss(Aol,Bol,eye(2),zeros(2,2));

[wn,z,p] = damp(sys2);
freq = wn/2/pi

% Obtain filtered and unfiltered signal
%[tfsig,tsig,sigf,sig]=Sig_Power_Square(Vmax,Fs,L,ntp); % Square wave
%[tfsig,tsig,sigf,sig]=Sig_Power_Sin(Vmax,Fs,L,ntp); % Square with Sine
[tfsig,tsig,sigf,sig,inde]=Just_Sine(Vmax,Fs,L,ntp); % Just a sine wave

tf = tfsig - tfsig(1);
t = tsig - tfsig(1);

% Noise (Load) signal
%xn(:,1) = zeros(length(t),1);
xn(:,1) = Lload*ones(length(t),1);

% Desired state signal
vin = sig';
xin = [vin xn]';
vinf = sigf';
xinf = [vinf xn]';

% Calculating the response
xs = lsim(sys2,xin,t);
xsf = lsim(sys2,xinf,tf);

% Input to system 1 (OL system)
u = vin';
uf = vinf';

% Electrical properties
q = theta*xs(:,1)' + Cap*u;
qf = theta*xsf(:,1)' + Cap*uf;
%I = diff(q)./diff(tfil);
I = gradient(q)/(t(2)-t(1));
If = gradient(qf)/(tf(2)-tf(1));

% Calculate the Power
P = sig.*I;
%Pef = mean(abs(P));
Pf = sigf.*If;
%Peff = mean(abs(Pf));

% Plots
figure(1)
subplot(3,2,1);plot(t,vin,tf,vinf);
grid; title('Inputs to OL system'); ylabel('Volt [V]');
legend('Unfiltered','Filtered')

% Ignore quick start
t = t(inde:end);
tf = tf(inde:end);
xn = xn(inde:end,:);
xs = xs(inde:end,:);
xsf = xsf(inde:end,:);
q = q(inde:end);
qf = qf(inde:end);
I = I(inde:end);
If = If(inde:end);
P = P(inde:end);
Pf = Pf(inde:end);

```

```

Pef = sqrt(mean((P).^2));
%Pef = norm(P)/sqrt(length(P))
Peff = norm(Pf)/sqrt(length(Pf));

subplot(3,2,2);plot(t,xn(:,1));
    grid; title('Inputs to OL system'); ylabel('Load [N]')
subplot(3,1,2);plot(t,xs(:,1)*1e6,tf,xsf(:,1)*1e6);
    grid; title('Displacement Output'); ylabel('Displacement [um]');
    legend('Unfiltered','Filtered')
subplot(3,1,3);plot(t,xs(:,2)*1000,tf,xsf(:,2)*1000)
    grid; title('Velocity Output'); ylabel('Velocity [mm/s]')
    legend('Unfiltered','Filtered')

figure(2)
incon = [1 0]';
tin = 0:1e-6:0.01;
initial(sys1,'b',incon,tin); grid, hold on
initial(sys2,'r',incon,tin);
hold off

figure(3)
subplot(3,1,1);plot(t,q,tf,qf)
    grid; title('Charge'); ylabel('Coulomb [C]');
    legend('Unfiltered','Filtered')
subplot(3,1,2);plot(t,I*1000,tf,If*1000)
    grid; title('Current'); ylabel('Ampere [mA]')
    legend('Unfiltered','Filtered')
subplot(3,1,3); plot(t,P*1000,tf,Pf*1000);
S = strvcats(strcat('POWER RMS          = ',num2str(Pef*1000),' mW'),...
    strcat('POWER RMS FIL = ',num2str(Peff*1000),' mW'));
grid; title('Power'); ylabel('Power (mW)'); text(max(t)/2,max(P),S);
xlabel('Time (sec)'); legend('Unfiltered','Filtered')

figure(4)
bode(sys2); grid

```

C. State space representation of a Single Degree of Freedom (SDOF) piezoelectric system

A Single Degree of Freedom (SDOF) system is used to simulate a piezoelectric element that actuates a mechanical system. A schematic is shown in Figure 106.

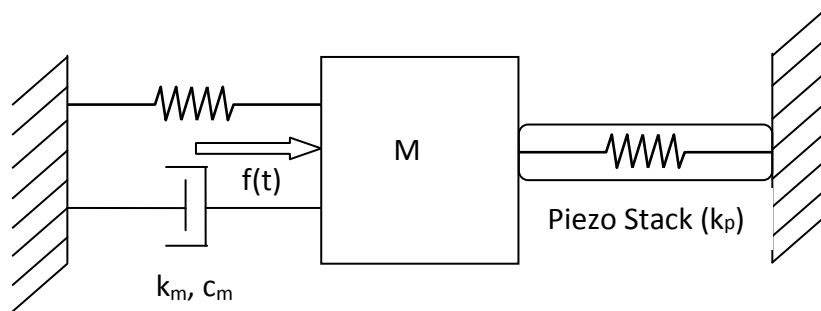


Figure 106: Diagram for SDOF system

The equation of motion for this system is given by :

$$m \cdot \ddot{x} + c_m \cdot \dot{x} + k \cdot x = f(t) + \theta \cdot V(t) \quad \text{Equation 10-5}$$

where

- m : Mass (kg)
- $k = k_m + k_p$: Sum of the mechanical and piezo stack stiffness (N/m)
- c_m : Mechanical damping (Ns/m)
- $f(t)$: External force (N)
- $V(t)$: Voltage applied to piezo stack (V)
- θ : Piezoelectric constant (N/V)

State space equations:

The equations of motion need to be in the state space form:

$$\dot{X} = A \cdot X + B \cdot u(t) \quad \text{Equation 10-6}$$

and general output equation:

$$Y = C \cdot X + D \cdot u(t) \quad \text{Equation 10-7}$$

now if

$$m \cdot \dot{x} - m \cdot \dot{x} = 0$$

and

$$m \cdot \ddot{x} + c_m \cdot \dot{x} + k \cdot x = f(t) + \theta \cdot V(t)$$

Equation 10-8

Then

$$\begin{bmatrix} m & 0 \\ 0 & m \end{bmatrix} \cdot \begin{Bmatrix} \dot{x} \\ \ddot{x} \end{Bmatrix} + \begin{bmatrix} 0 & -m \\ k & c_m \end{bmatrix} \cdot \begin{Bmatrix} x \\ \dot{x} \end{Bmatrix} = \begin{bmatrix} 0 \\ 1 \end{bmatrix} \cdot f(t) + \begin{bmatrix} 0 \\ \theta \end{bmatrix} \cdot V(t)$$

Equation 10-9

Or

$$\begin{Bmatrix} \dot{x} \\ \ddot{x} \end{Bmatrix} = \begin{bmatrix} 0 & 1 \\ -k/m & -c_m/m \end{bmatrix} \cdot \begin{Bmatrix} x \\ \dot{x} \end{Bmatrix} + \begin{bmatrix} 0 & 0 \\ 1/m & \theta/m \end{bmatrix} \cdot \begin{Bmatrix} f(t) \\ V(t) \end{Bmatrix}$$

Equation 10-10

also if the output vector is selected as x , and

$$y = x$$

Equation 10-11

Then

$$\begin{Bmatrix} y \\ \dot{y} \end{Bmatrix} = [\bar{I}] \cdot \begin{Bmatrix} x \\ \dot{x} \end{Bmatrix} + [\bar{O}]$$

Equation 10-12

where $[\bar{I}]$ is a two-by-two identity matrix and $[\bar{O}]$ is a two-by-two zero matrix.

Therefore:

$$X = \begin{Bmatrix} x \\ \dot{x} \end{Bmatrix}$$

$$Y = \begin{Bmatrix} y \\ \dot{y} \end{Bmatrix}$$

$$A = \begin{bmatrix} 0 & 1 \\ -k/m & -c/m \end{bmatrix}$$

$$B = \begin{bmatrix} 0 & 0 \\ 1/m & \theta/m \end{bmatrix}$$

$$C = \begin{bmatrix} 1 & 0 \\ 0 & 1 \end{bmatrix}$$

$$D = \begin{bmatrix} 0 & 0 \\ 0 & 0 \end{bmatrix}$$

$$u(t) = \begin{bmatrix} f(t) \\ V(t) \end{bmatrix}$$

Equation 10-13

These equations are used to simulate a SDOF mechanical system containing a piezoelectric element.

D. Spring acting through a ratio

Consider the instance where a spring (k_i) acts onto a system through a ratio ($N = \frac{a}{b}$), as indicated in Figure 107. If the displacement at the spring is x_i , and the output displacement is x_o , then the equivalent stiffness of the system (k_{eq}) can be calculated as follows:

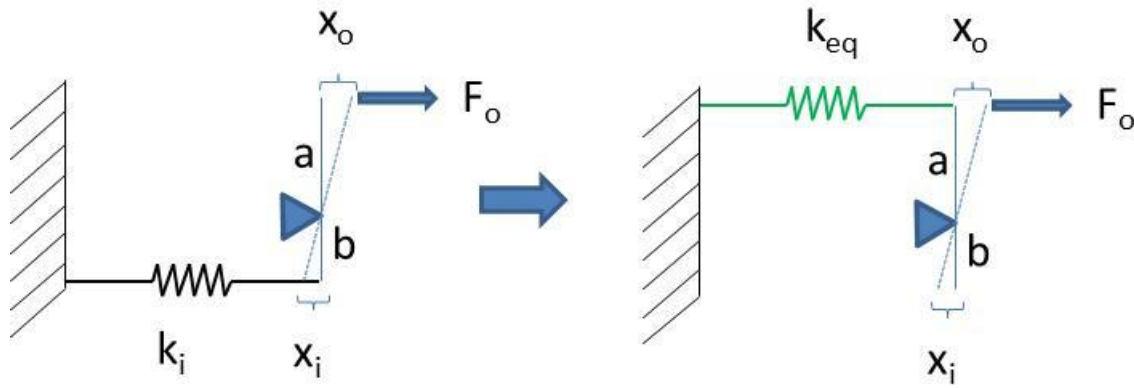


Figure 107: Spring acting through a ratio

$$N = \frac{x_o}{x_i} = \frac{a}{b}$$

$$F_i = k_i \cdot x_i$$

$$F_o = k_{eq} \cdot x_o$$

$$\sum \text{Moments} = 0$$

$$F_o \cdot a = F_i \cdot b$$

$$k_{eq} \cdot x_o \cdot a = k_i \cdot x_i \cdot b$$

$$k_{eq} := \frac{k_i \cdot x_i \cdot b}{x_o \cdot a}$$

$$k_{eq} := \frac{k_i}{N^2}$$

E. Material and load properties

Piezoelectric properties

The piezoelectric stack used was: PSt 150/5x5/20 (Piezomechanik, 2008).

Table 10: Properties for PSt 150/5x5/20

Blocked force	1 600 N (at voltage range of -30V to +150V)
Free displacement	27 μm (at voltage range of -30V to +150V)
Length	18 mm
Cross-section	5 mm x 5 mm
Stiffness	59.3 N/ μm
Capacitance	1 800 nF

For modal analysis a density is required. This was obtained by weighing a stack and dividing the weight by the volume that the FEA element representing the stacks measures. The density used was 7 600 kg/m³.

Table 11: Table of available piezoelectric stacks (Piezomechanik, 2008)

type osi-stack (+) U_{max} 150 V	ceramic- crosssection $a \times b / \text{mm}^2$	length L ¹⁾ mm	Max. Stroke ²⁾ μm	capacitance nF	Resonance frequency kHz	stiffness N/ μm	Blockingforce ³⁾ N	Max. load force N
PSt 150/2x3/5	2 x 3	5	6.5/5	70	150	45	300	300
PSt 150/2x3/7	2 x 3	9	13/9	170	100	25	300	300
PSt 150/2x3/20	2 x 3	18	28/20	340	50	12	300	300
PSt 150/3.5x3.5/7	3.5 x 3.5	9	13/9	350	100	50	800	800
PSt 150/3.5x3.5/20	3.5 x 3.5	18	28/20	800	50	25	800	800
PSt 150/5x5/7	5 x 5	9	13/9	800	100	120	1600	2000
PSt 150/5x5/20	5 x 5	18	28/20	1800	50	60	1600	2000
PSt 150/7x7/7	7 x 7	9	13/9	1800	100	240	3500	4000
PSt 150/7x7/20	7 x 7	18	28/20	3600	50	120	3500	4000
PSt 150/10x10/7	10 x 10	9	13/9	3600	100	500	7000	8000
PSt 150/10x10/20	10 x 10	18	28/20	7200	50	250	7000	8000
PSt 150/14x14/18	14 x 14	20	25/18	10500	47	500	10000	16000
PSt 150/25x25/18	25 x 25	20	25/18	35000	47	1500	30000	40000
Ring-actuators (+) U_{max} 150 V	Diameters $a \times b$							
HPSt 150/14-10/12	14 x 10	13.5	16/12	2600	75	250	4500	7000
HPSt 150/20-15/12	20 x 15	13.5	16/12	5000	75	450	8000	12000

The elastic properties are based on PZT-4.

The piezoelectric equation used is in the form:

$$\begin{Bmatrix} T_1 \\ T_2 \\ T_3 \\ T_4 \\ T_5 \\ T_6 \end{Bmatrix} = \begin{bmatrix} c_{11}^E & c_{12}^E & c_{13}^E & 0 & 0 & 0 \\ c_{12}^E & c_{22}^E & c_{13}^E & 0 & 0 & 0 \\ c_{13}^E & c_{13}^E & c_{33}^E & 0 & 0 & 0 \\ 0 & 0 & 0 & c_{44}^E & 0 & 0 \\ 0 & 0 & 0 & 0 & c_{44}^E & 0 \\ 0 & 0 & 0 & 0 & 0 & c_{66}^E \end{bmatrix} \cdot \begin{Bmatrix} S_1 \\ S_2 \\ S_3 \\ S_4 \\ S_5 \\ S_6 \end{Bmatrix} - \begin{bmatrix} 0 & 0 & e_{31} \\ 0 & 0 & e_{31} \\ 0 & 0 & e_{33} \\ 0 & e_{15} & 0 \\ e_{15} & 0 & 0 \\ 0 & 0 & 0 \end{bmatrix} \cdot \begin{Bmatrix} E_1 \\ E_2 \\ E_3 \end{Bmatrix}$$

The constants for PZT-4 are (Berlincourt, Krueger, & Near, n.d.):

Table 12: Properties for PZT-4

c^E - ELASTIC STIFFNESS AT CONSTANT ELECTRIC FIELD						
N/m ²						

1.39E+11	7.78E+10	7.43E+10	0	0	0	0
7.78E+10	1.39E+11	7.43E+10	0	0	0	0
7.43E+10	7.43E+10	1.15E+11	0	0	0	0
0	0	0	2.56E+10	0	0	0
0	0	0	0	2.56E+10	0	0
0	0	0	0	0	0	3.06E+10

e -PIEZOELECTRIC CONSTANT						
C/m2						

0	0	0	0	12.7	0	0
0	0	0	12.7	0	0	0
-5.2	-5.2	15.1	0	0	0	0

The commercial piezoelectric stacks used are made up of many layers of piezoelectric material and electrodes. It is, however, modelled as a single orthotropic solid state material. Because of this, the PZT-4 material properties are not directly applicable for these stacks. To apply material properties that will result in the correct blocked force and free displacement values, the PZT elastic material properties are used as a guide and then scaled down to obtain the correct behaviour from the FEA model. It was found that 37.1% of the value of the elastic properties for PZT-4 resulted in a blocked force for the stack of 1 600 N.

The values used in the analysis are therefore:

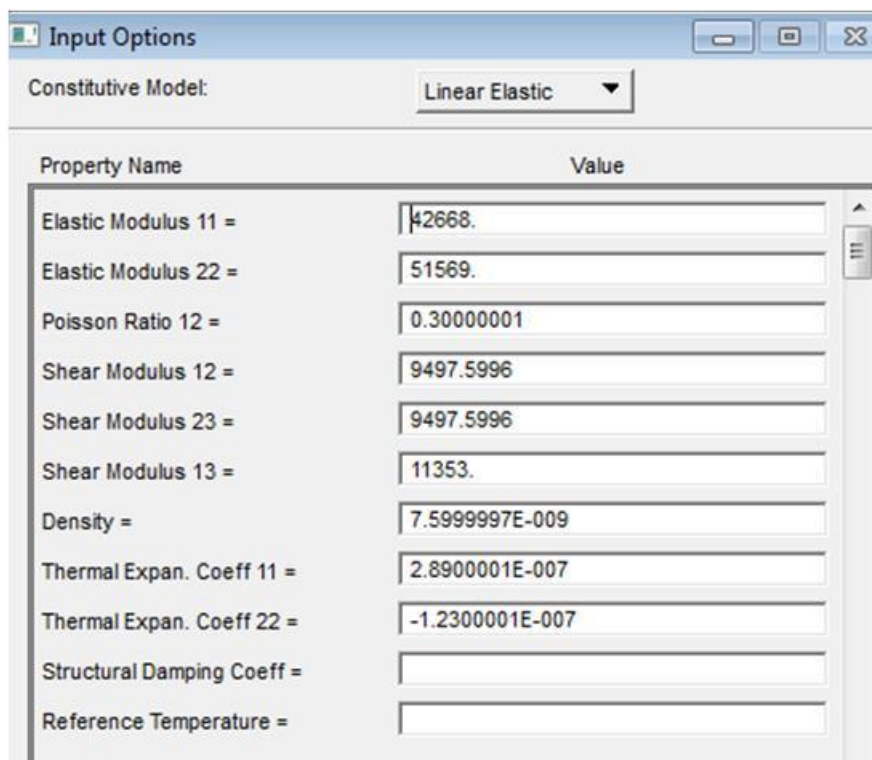
Table 13: Values used for the piezoelectric stacks' material properties

Elasticity			N/mm ²		
5.1569E+04	2.8864E+04	2.7565E+04			
2.8864E+04	5.1569E+04	2.7565E+04			
2.7565E+04	2.7565E+04	4.2665E+04			
			9.4976E+03		
				9.4976E+03	
					1.1353E+04

Piezoelectric constants			mm/V		
				4.9600E-07	
			4.9600E-07		
-1.2300E-07	-1.2300E-07	2.8900E-07			

To show how the properties were entered for the analysis, the Patran input form is shown:

Table 14: Patran input form for the piezoelectric stacks' material properties



Input Options

Constitutive Model: Linear Elastic

Property Name	Value
Elastic Modulus 11 =	42668.
Elastic Modulus 22 =	51569.
Poisson Ratio 12 =	0.30000001
Shear Modulus 12 =	9497.5996
Shear Modulus 23 =	9497.5996
Shear Modulus 13 =	11353.
Density =	7.5999997E-009
Thermal Expan. Coeff 11 =	2.8900001E-007
Thermal Expan. Coeff 22 =	-1.2300001E-007
Structural Damping Coeff =	
Reference Temperature =	

Metal properties

The actuator is made of Stainless Steel 431. The properties used are shown in Table 15.

Table 15: Patran input form for the stainless steel properties

Input Options

Constitutive Model: Linear Elastic

Property Name	Value
Elastic Modulus =	200000.
Poisson Ratio =	0.30000001
Shear Modulus =	76923.078
Density =	7.7499998E-009
Thermal Expan. Coeff =	
Structural Damping Coeff =	
Reference Temperature =	

F. Piezoelectric load input in Nastran

Nastran does not directly support piezoelectricity, i.e. no FEA element is defined within Nastran that uses piezoelectric variables as input. To get around this problem, the piezoelectric properties were modelled using the temperature cards in Nastran. A thermal analogy was used to model piezoelectric behaviour. It is thus required that the temperature input be calculated that will correlate to an electrical field input.

The equation for thermal expansion of a material is:

$$\Delta L = \alpha \cdot L_0 \cdot \Delta T$$

$$\Delta \begin{bmatrix} L_1 \\ L_2 \\ L_3 \end{bmatrix} = \begin{bmatrix} \alpha_1 \\ \alpha_2 \\ \alpha_3 \end{bmatrix} \cdot L_0 \cdot \Delta T$$

Equation 10-14

Where L_0 and ΔL are the original length and change in length and α is the coefficient of thermal expansion.

The equation used for piezoelectric behaviour is (see Equation 2-2):

$$S = s^E \cdot T + d^t \cdot E$$

When this equation can be expanded and applied to PZT, it becomes:

$$\begin{Bmatrix} S_1 \\ S_2 \\ S_3 \\ S_4 \\ S_5 \\ S_6 \end{Bmatrix} = \begin{bmatrix} s_{11}^E & s_{12}^E & s_{13}^E & 0 & 0 & 0 \\ s_{12}^E & s_{22}^E & s_{13}^E & 0 & 0 & 0 \\ s_{13}^E & s_{13}^E & s_{33}^E & 0 & 0 & 0 \\ 0 & 0 & 0 & s_{44}^E & 0 & 0 \\ 0 & 0 & 0 & 0 & s_{44}^E & 0 \\ 0 & 0 & 0 & 0 & 0 & s_{66}^E \end{bmatrix} \begin{Bmatrix} T_1 \\ T_2 \\ T_3 \\ T_4 \\ T_5 \\ T_6 \end{Bmatrix} + \begin{bmatrix} 0 & 0 & d_{31} \\ 0 & 0 & d_{31} \\ 0 & 0 & d_{33} \\ 0 & d_{15} & 0 \\ d_{15} & 0 & 0 \\ 0 & 0 & 0 \end{bmatrix} \begin{Bmatrix} E_1 \\ E_2 \\ E_3 \end{Bmatrix}$$

When modelling a piezoelectric stack, shear behaviour may be ignored, and the previous equation simplifies to:

$$\begin{Bmatrix} S_1 \\ S_2 \\ S_3 \end{Bmatrix} = \begin{bmatrix} s_{11}^E & s_{12}^E & s_{13}^E \\ s_{12}^E & s_{22}^E & s_{13}^E \\ s_{13}^E & s_{13}^E & s_{33}^E \end{bmatrix} \begin{Bmatrix} T_1 \\ T_2 \\ T_3 \end{Bmatrix} + \begin{bmatrix} 0 & 0 & d_{31} \\ 0 & 0 & d_{31} \\ 0 & 0 & d_{33} \end{bmatrix} \begin{Bmatrix} 0 \\ 0 \\ E_3 \end{Bmatrix}$$

Now the thermal analogy variables can be introduced:

$$\begin{Bmatrix} S_1 \\ S_2 \\ S_3 \end{Bmatrix} = \begin{bmatrix} s_{11}^E & s_{12}^E & s_{13}^E \\ s_{12}^E & s_{22}^E & s_{13}^E \\ s_{13}^E & s_{13}^E & s_{33}^E \end{bmatrix} \begin{Bmatrix} T_1 \\ T_2 \\ T_3 \end{Bmatrix} + \begin{bmatrix} 0 & 0 & \alpha_1 \\ 0 & 0 & \alpha_1 \\ 0 & 0 & \alpha_3 \end{bmatrix} \begin{Bmatrix} 0 \\ 0 \\ \Delta T \end{Bmatrix}$$

Where E, the electrical field, is replaced with ΔT , the temperature difference. The coefficient of thermal expansion is replaced by the piezoelectric coefficients.

To obtain a free displacement of 27 μm , a “temperature” of 5190.3 units should be applied. This correlates to a volt input of 180 V associated with the required displacement. The piezoelectric constant used is $d_{33} = 2.89 \times 10^{-10} \text{ m/V}$ (Berlincourt et al., n.d.).

$$\Delta L = \alpha \cdot L_0 \cdot \Delta T$$

$$27 \times 10^{-6} = 2.89 \times 10^{-10} \cdot 18 \times 10^{-3} \cdot \Delta T$$

$$\Delta T = 5190311.4^\circ\text{C} \text{ _or_ } V/m$$

$$\Delta T = 5190.3114^\circ\text{C} \text{ _or_ } V/mm$$

G. Detail design of the flextensional actuator

This actuator is a well-known type of piezoelectric actuator known as a flextensional or Moonie actuator (Newnham et al., 1993). The geometry is such that the input displacement of the piezo elements results in an amplified output perpendicular to the input. A commercially available device is shown in Figure 108 (“Cedrat Technologies,” 2012). The output amplification is largely determined by the angle of the structural arms.

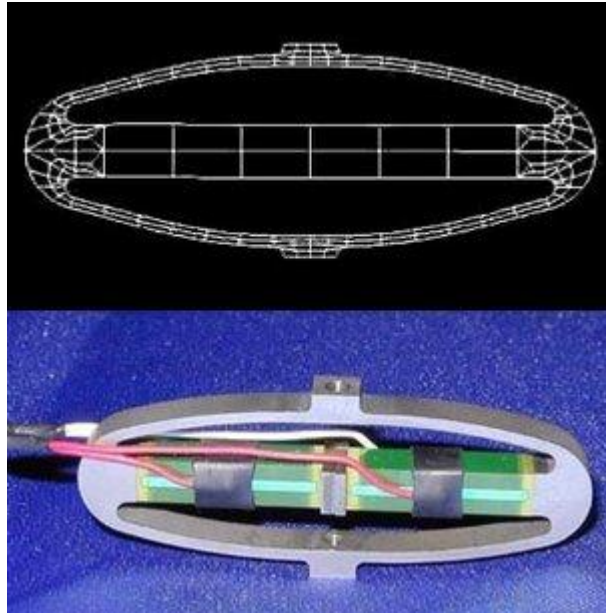


Figure 108: Flextensional actuator from Cedrat Technologies (“Cedrat Technologies,” 2012)

For designing a flextensional actuator to be used in an IWM, it was decided to use topology optimisation to determine the optimal compliancy mechanism for the design. The actuator is designed to amplify the piezoelectric stack displacement by a factor of four. This amplification is an input for the topology optimisation which then calculates the material distribution that would result in a minimum compliance design with such an amplification factor.

Due to symmetry, a quarter model could be used to lower the demands on computer resources. The material properties in Appendix E apply here as well. Nastran solver SOL 200 was used for topology optimisation. A relatively high-density element domain was created using QUAD 4 elements (four node plate elements) and is shown in Figure 109. The constraints are also shown in Figure 109 as well as the output position to be maximized (by minimizing Equation 10-15).

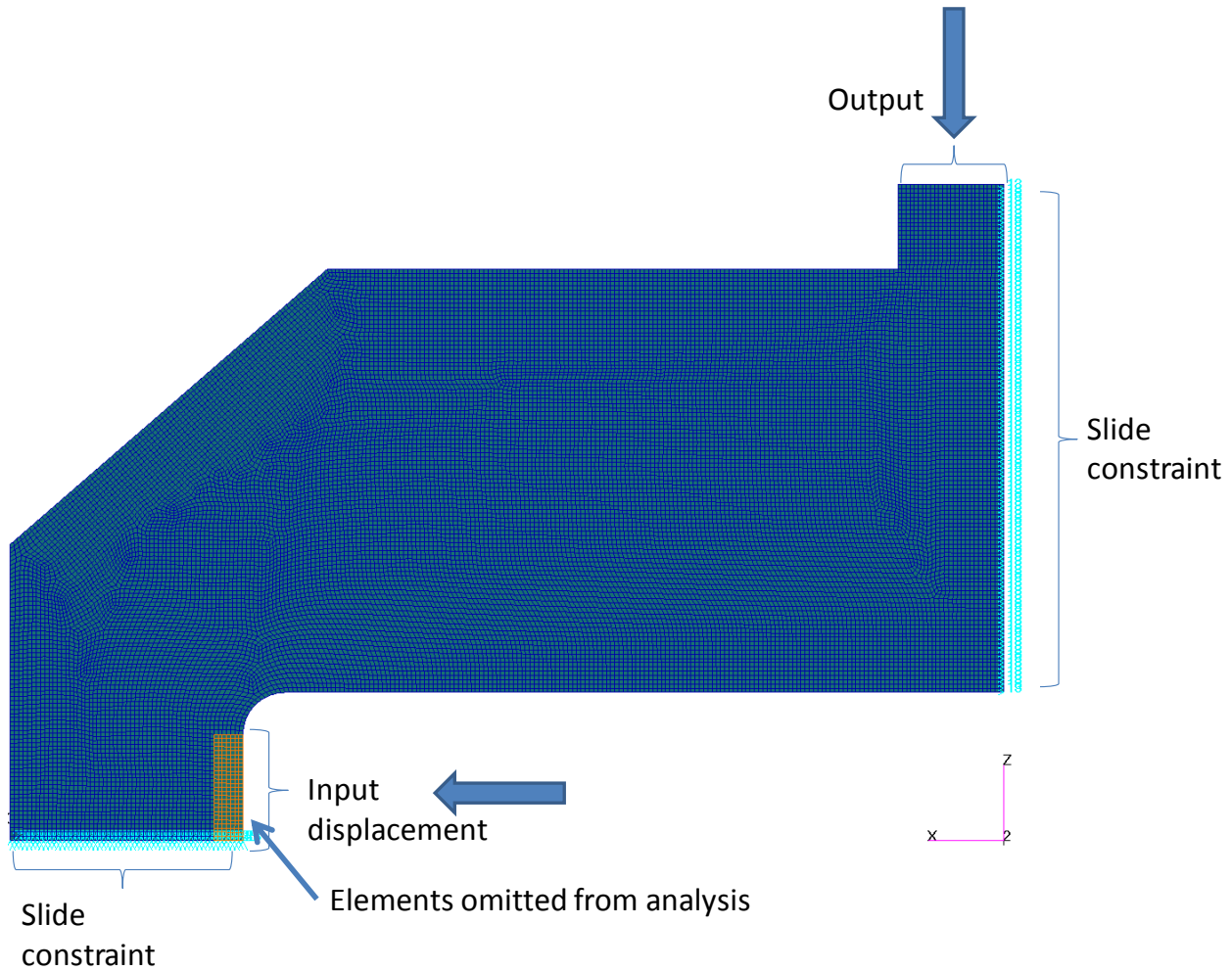


Figure 109: Domain used in the topology optimisation

To realize a 4X amplification, it was necessary to constrain the output as a function of the input to obtain a 4X multiplication. The following primary objective function was used for this:

$$F1 = (A + 4 \cdot \delta_{disp})^2 \quad \text{Equation 10-15}$$

Where F1 is the displacement output, A is the displacement input as a variable, and δ_{disp} is the displacement as a constant. Note that the “+” in Equation 10-15 is because an input displacement with a positive value in the x-direction would result in a output displacement with a negative value in the z-direction as defined in Figure 109. The use of a quadratic equation is necessary, so that the optimisation algorithm can find the minima of the derivative of this equation, i.e. Equation 10-15 will be minimized. The optimisation algorithm (i.e. Nastran) attempts to find the minimum compliance geometrical solution that will result in the constrained condition set by Equation 10-15 to equal zero. The analysis will attempt to converge to a minimum compliance geometry where the output is four times the input displacement. A mass fraction of 20% was chosen as a secondary objective function, and a minimum element thickness of 0.6mm was used as a further constrain.

The relevant Nastran cards that are needed for inputs to Nastran are shown below.

File name: Moonie 1_4h
 PELAS 111 100.

```

DOPTPRM DESMAX 300 CONV1 1.e-7
$ Design Variables for TOPOLOGY Optimization :
TOPVAR 1 PSHELL PSHELL .1 1
TDMIN .6
$ Global Target Constraints : MASS FRACTION
DCONSTR 1 10001 0.200000
DRESP1 10001 FRM FRMASS
$11111112222222233333333444444445555555566666666777777778888888899999999
DRESP1 111 DISPY DISP 2 50000
DRESP2 222 DispErr 333
DRESP1 111
DEQATN 333 F1(A) = (A+4.0*27.e-3)**2

```

The analysis converged in 33 cycles. The topology result is shown in Figure 110. Two interesting non-obvious observations can be made. The first is the appearance of two “flexures” at either ends of the arm, opposed to a single cantilever beam as is the case in Figure 108. The second is that the analysis has moved the one flexure away from the displacement input position point. It is believed that a high stress area exists at this location. By moving the lower flexure away from this area, a more optimal design is realised in terms of lower stresses.

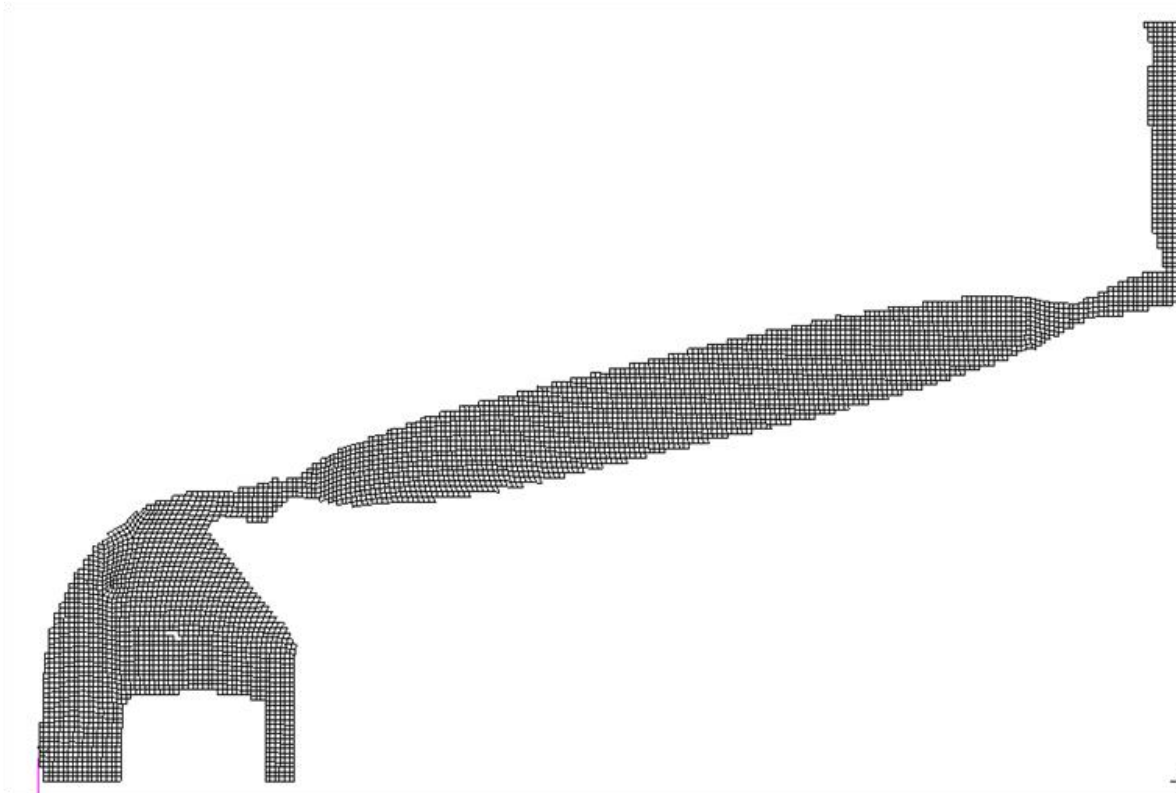


Figure 110: Result of the topology optimisation

The topology result is exported to CAD and used as input for the flextensional actuator design shown in Figure 111. The next step was to verify that the required displacement was achieved, that the stresses were not excessive, and to calculate the blocked force and stiffness of the actuator. The free displacement result is shown in Figure 112, and the stresses are shown in Figure 113 and Figure 114 for the free displacement condition and the blocked force condition respectively. The calculated blocked force is shown graphically in Figure 115, but must be multiplied by two due to the quarter model being used.

The constraints and input for the stiffness calculation are shown in Figure 116, and the stiffness displacement result is shown in Figure 117. The applied voltage was zero for the stiffness calculation.

A summary of the results is shown in Table 2, and repeated in Table 16.

Table 16: Summary of FEA results for the flextensional actuator

Blocked force	187.4 N
Free displacement	220 μm
Maximum stress (free displacement)	206 MPa
Maximum stress (blocked)	302 MPa
Stiffness in actuating direction	847.5 N/mm
Amplification (mechanical)	4.074

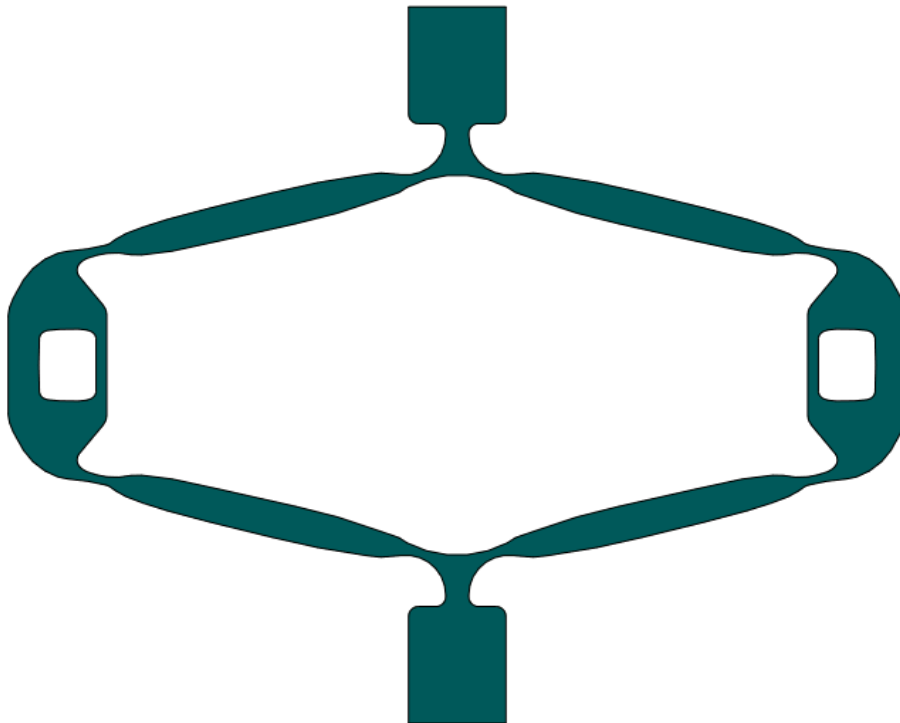


Figure 111: Final design of the flextensional actuator

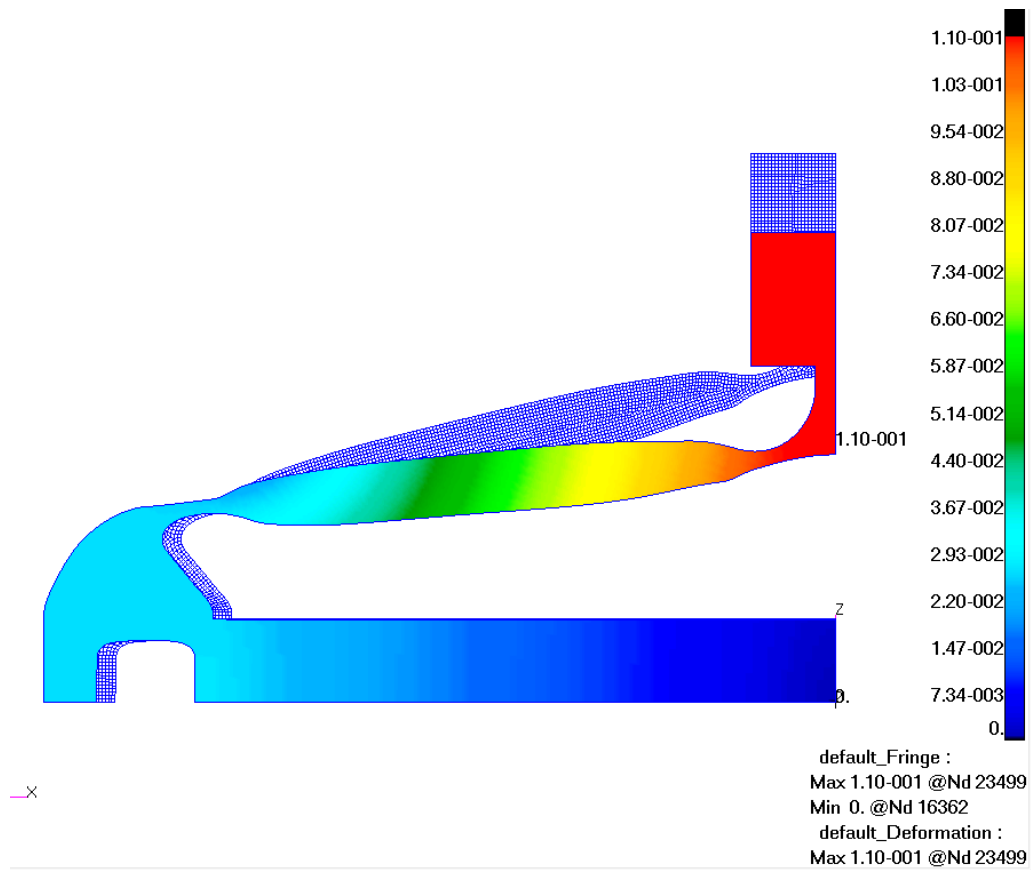


Figure 112: Free displacement

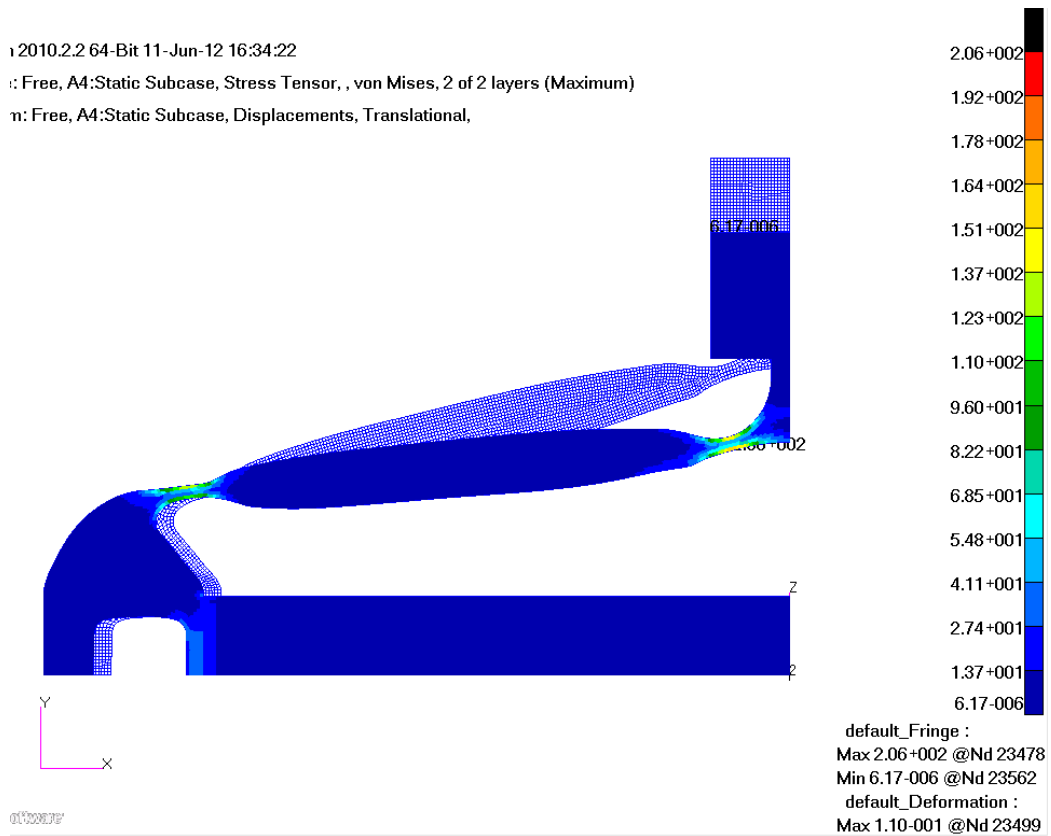


Figure 113: Free displacement stresses

tran 2010.2.2 64-Bit 11-Jun-12 16:36:03

nge: Block, A4:Static Subcase, Stress Tensor, , von Mises, 2 of 2 layers (Maximum)

form: Block, A4:Static Subcase, Displacements, Translational,

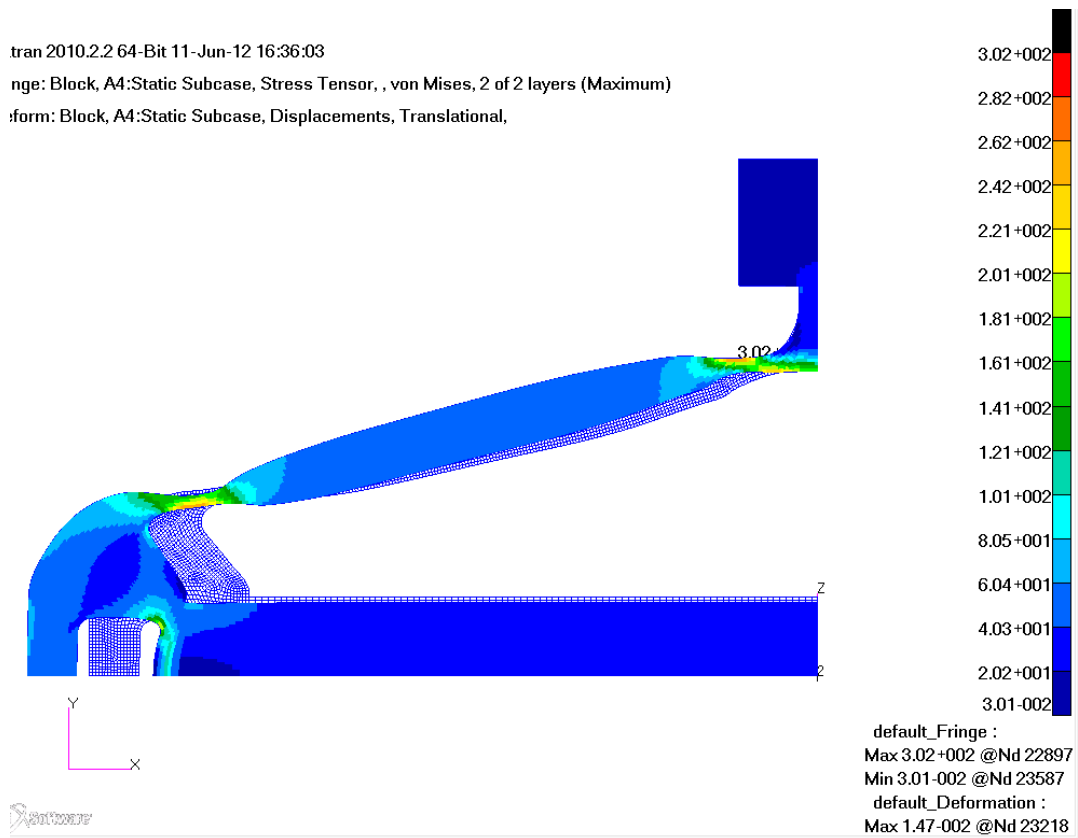


Figure 114: Blocked stresses

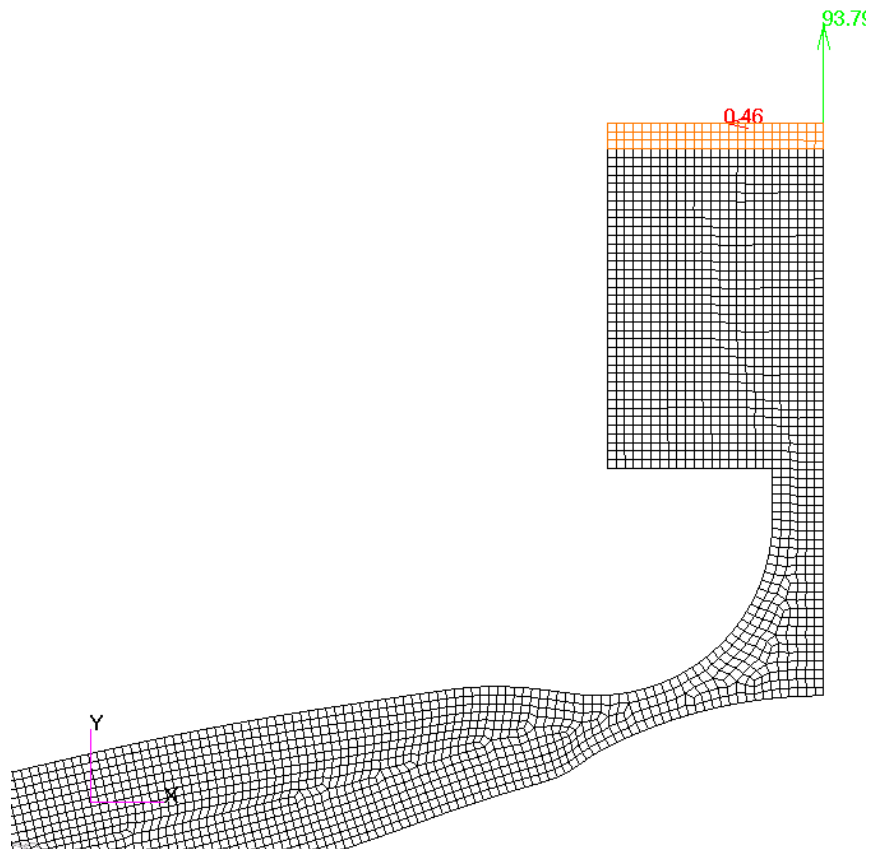


Figure 115: Blocked force reaction

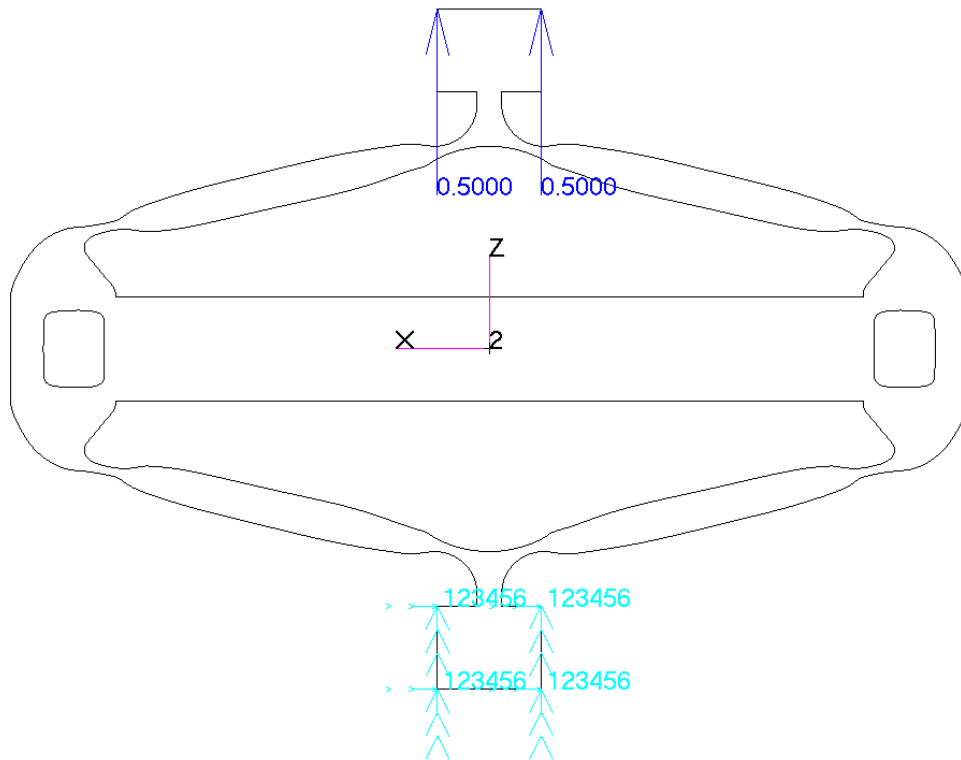


Figure 116: Force applied and constraints used for the stiffness calculation

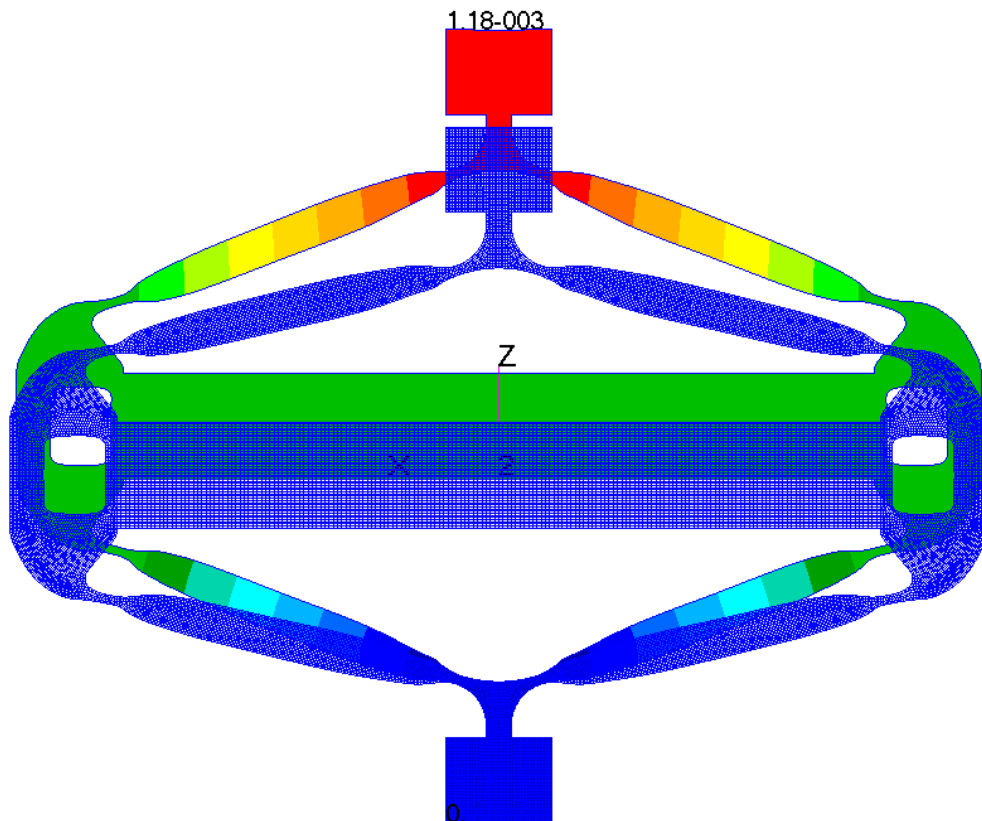


Figure 117: Displacement due to unit load (stiffness analysis)

To calculate the stiffness of the frame without the compliance effects of the piezo stacks included, the piezo stack in the FEA model is replaced with a rigid element. The NASTRAN RBE2 rigid elements are used as shown in Figure 118 with the displacement results presented in Figure 119.

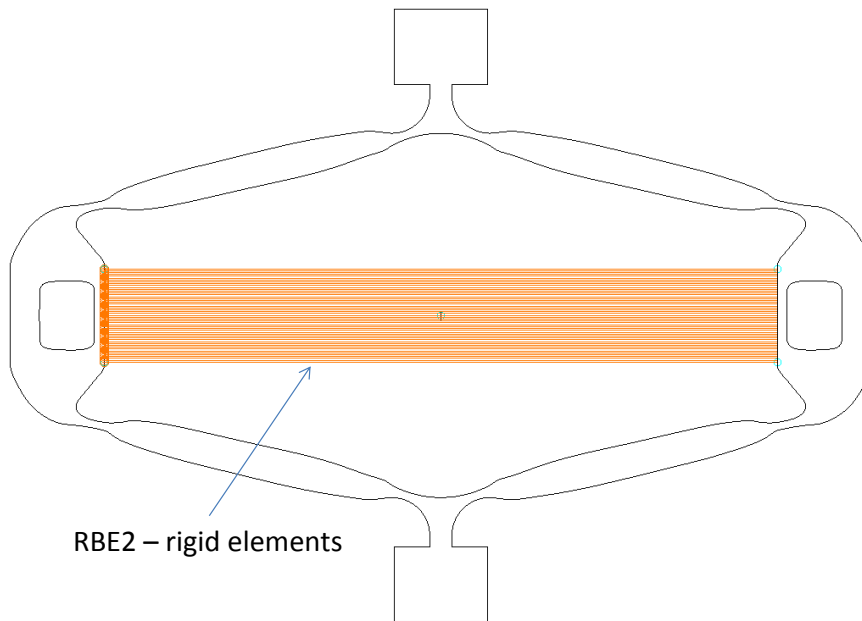


Figure 118: The element representing the piezo stacks is replaced with rigid elements

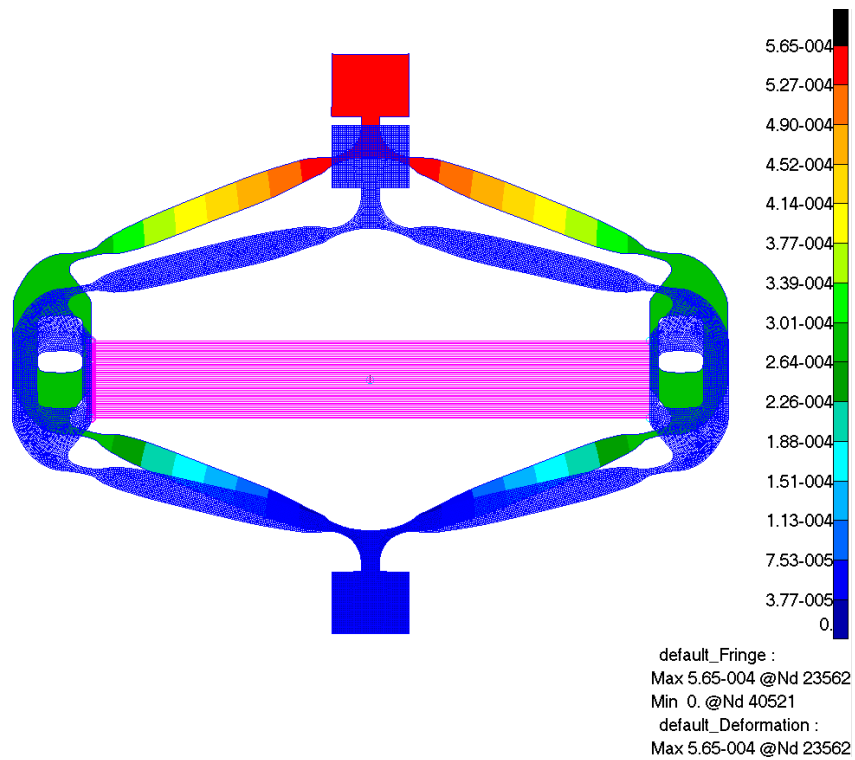


Figure 119: Displacement of the frame with rigid elements due to an applied unit force

For the modal calculation, the piezo-stack properties are used, replacing the rigid RBE2 elements.

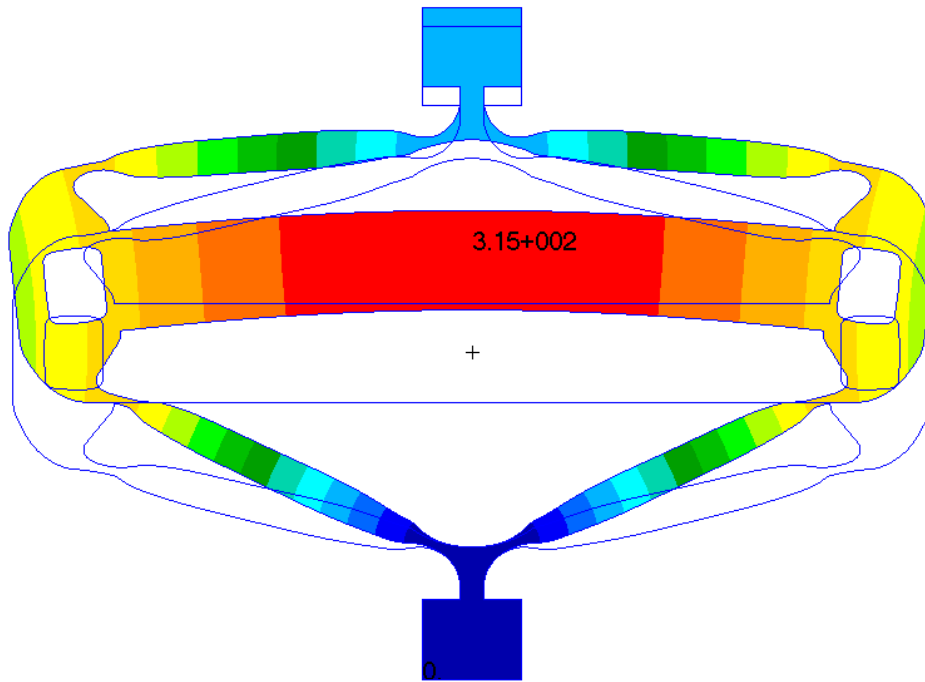


Figure 120: First natural mode at 831 Hz

H. Detail design of the beam actuator with force duplicator mechanism

The FEA model used in the analysis is shown in Figure 121. How the piezoelectric load was applied is discussed in Appendix F and the material properties are given in Appendix D. The constraints used are shown in Figure 122. The constraint at the load attachment point is required for only the blocked analysis, but only restraint the one translation degree of freedom. A model without the clamp mechanism was used to calculate the stiffness of only the extender mechanism for comparison with stiffness measurements.

The displacement shape for the blocked force and free displacement is shown in Figure 123 and Figure 124. The stresses generated during free displacement conditions and blocked force conditions are shown in Figure 125 and Figure 126.

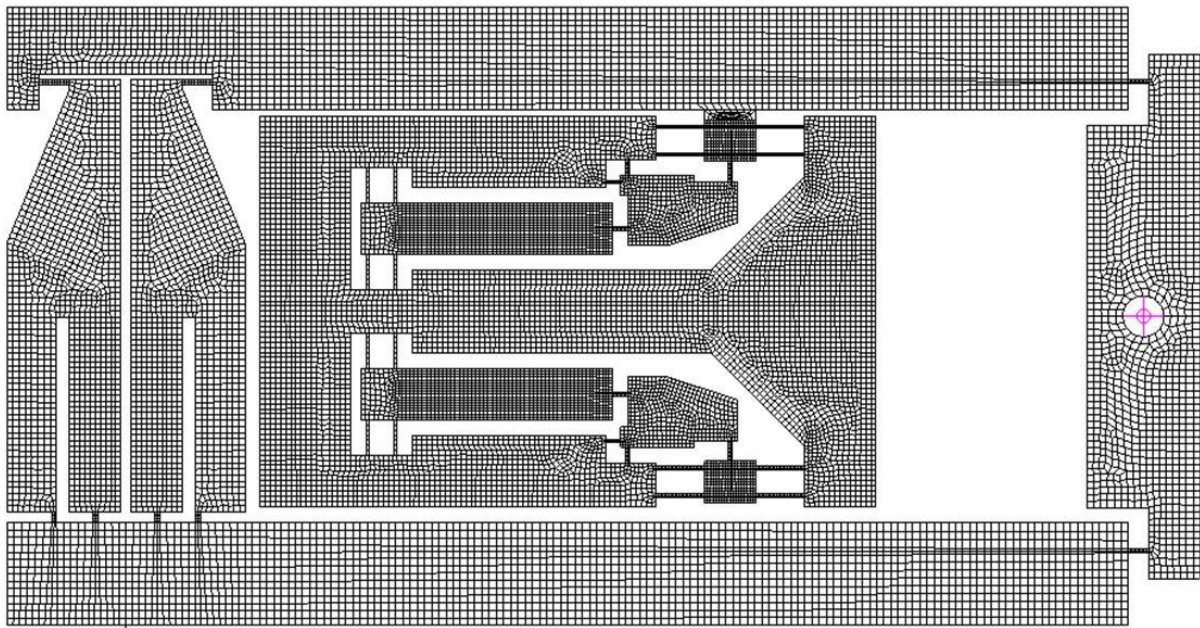


Figure 121: FEA model of extender

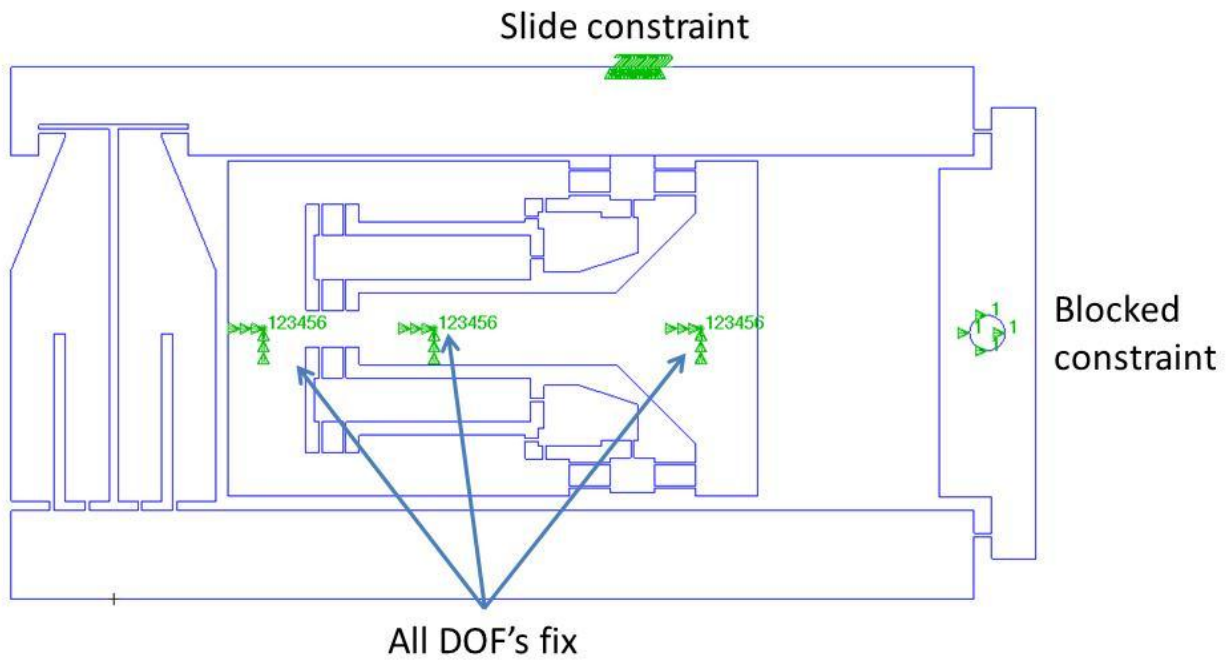


Figure 122: Constraints used in the analysis

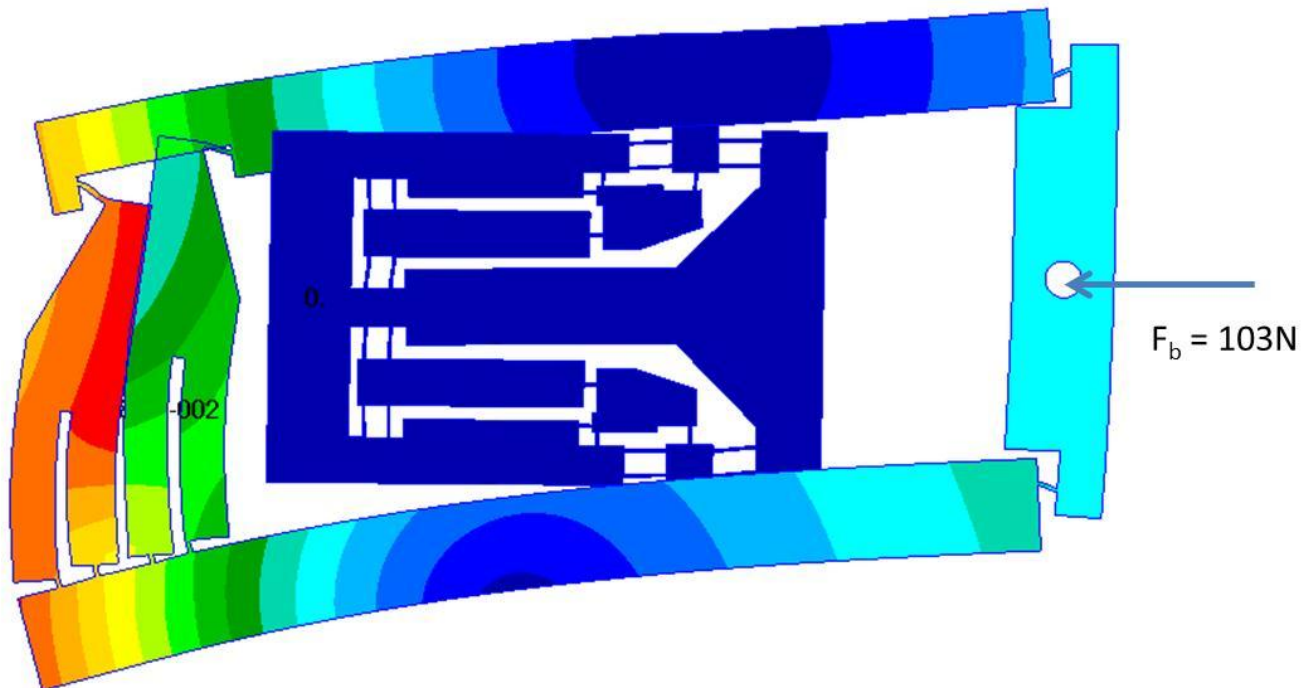


Figure 123: Exaggerated Displacement at Blocked force

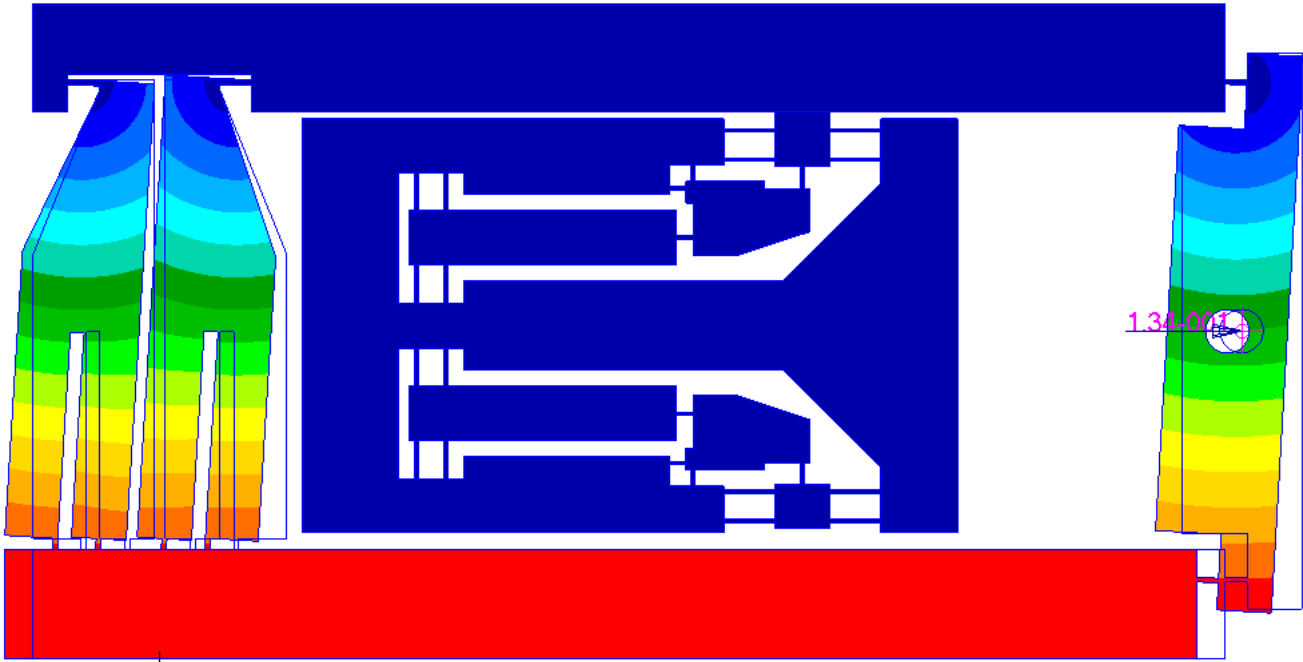


Figure 124: Free displacement

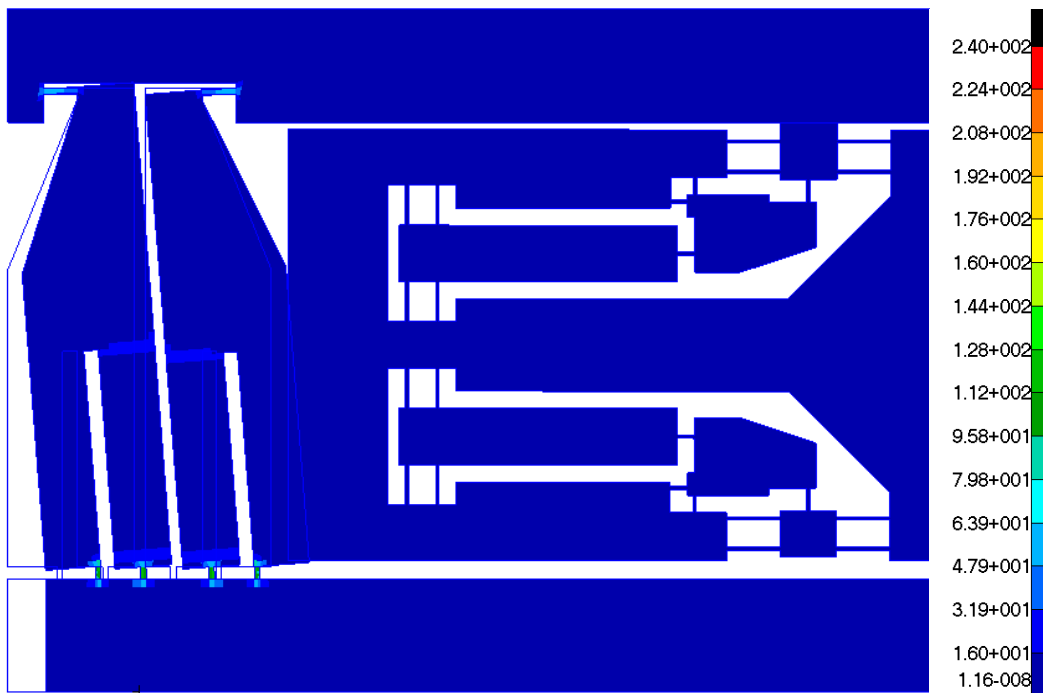


Figure 125: Stresses due to free displacement

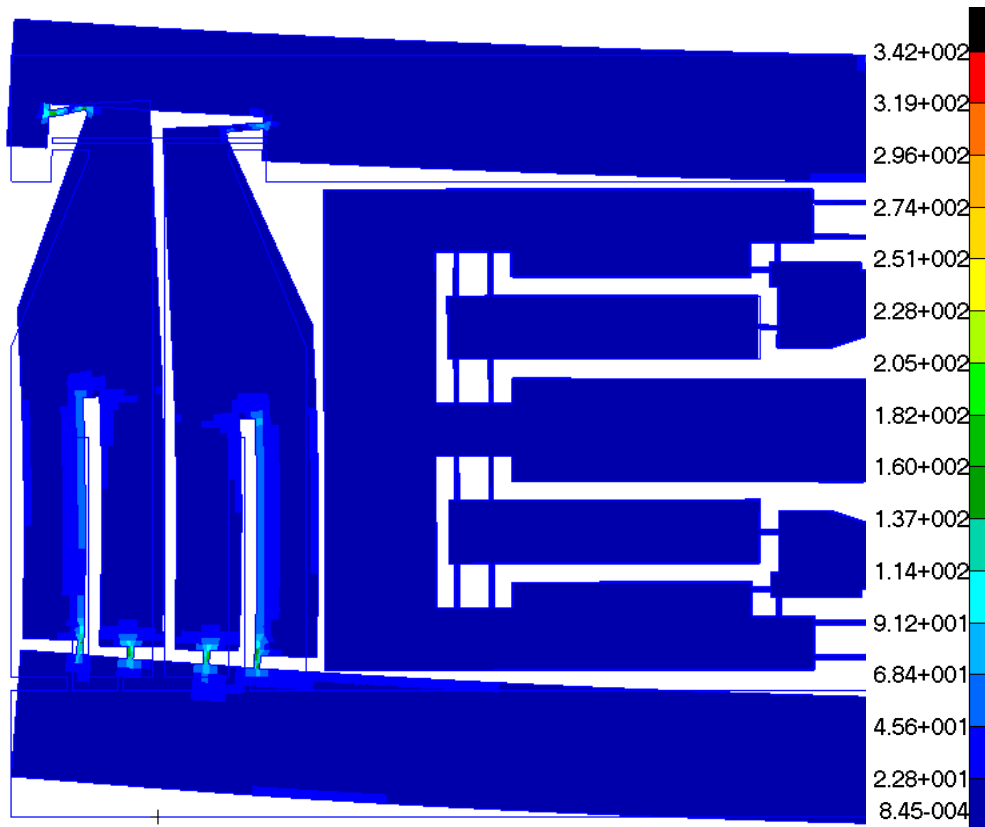


Figure 126: Stresses due to blocked force conditions

The FEA model is used to calculate the response of the IWM due to an applied unit force. The constraint was applied at the clamp position to simulate sliding and a fixed constraint as indicated in Figure 127. The unit load was applied at the load attachment point. The input to the FEA element that represents the piezoelectric stack corresponds to a zero voltage. The displacement shape due to the unit force is shown in Figure 128.

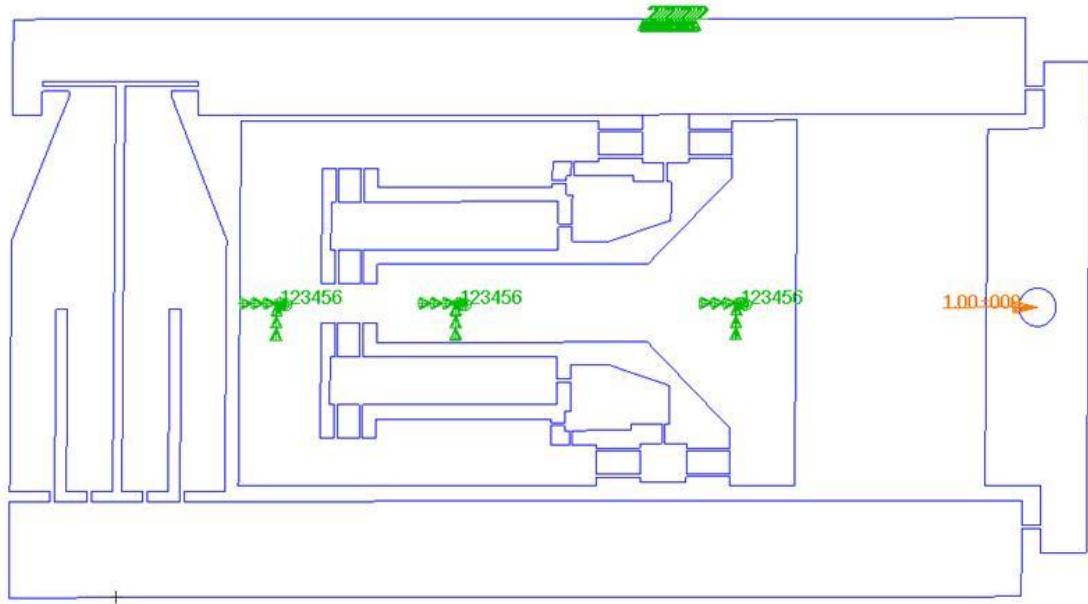


Figure 127: Constraint and force applied for stiffness calculation

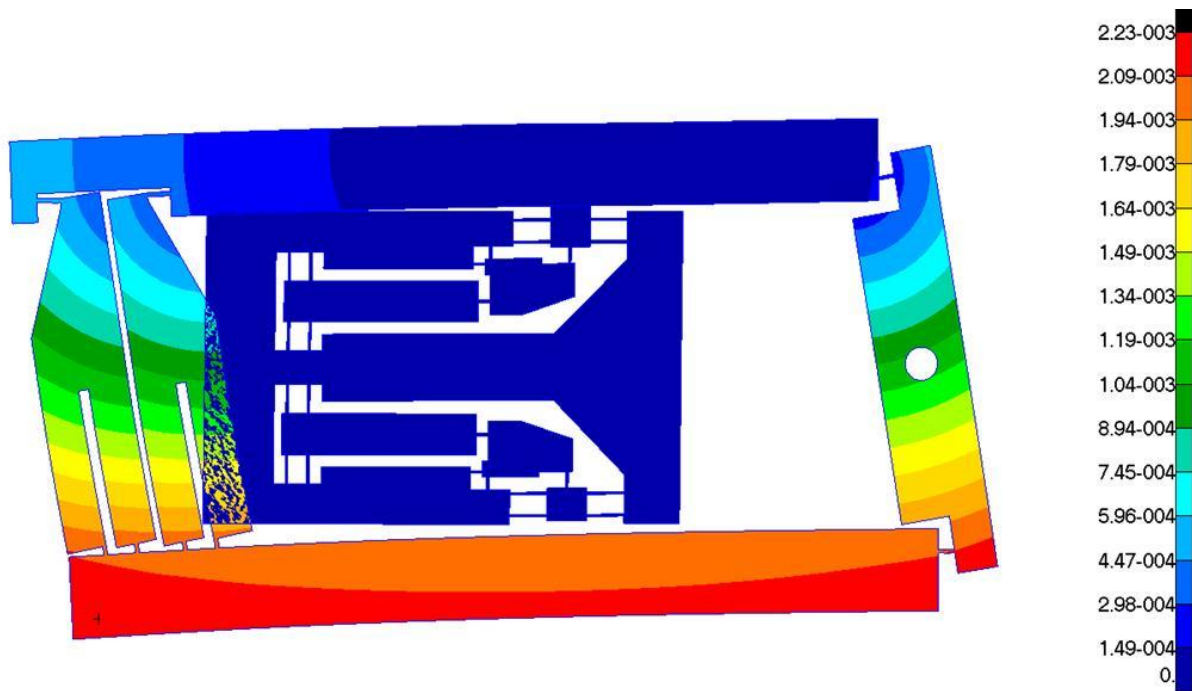


Figure 128: Displacement result due to unit force

For comparing the stiffness measurements of only the extender to calculated values, it was necessary to analyse a model that excluded the clamp mechanisms, and have similar constrains as was used during testing. The constraints and the displacement results is shown in Figure 129 and Figure 130.

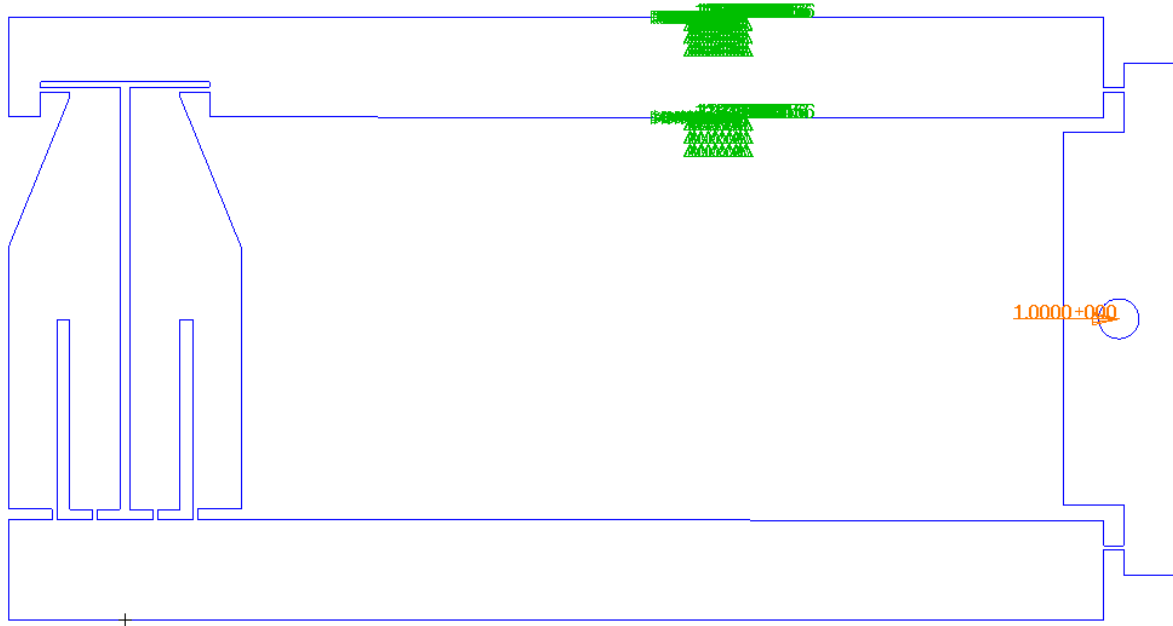


Figure 129: Constraint and force applied for stiffness calculation of only the extender

Patran 2010.2.2 64-Bit 20-Oct-11 14:23:24

Fringe: Stiffness, A3:Static Subcase, Displacements, Translational, Magnitude, (NON-LAYERED)

Deform: Stiffness, A3:Static Subcase, Displacements, Translational,

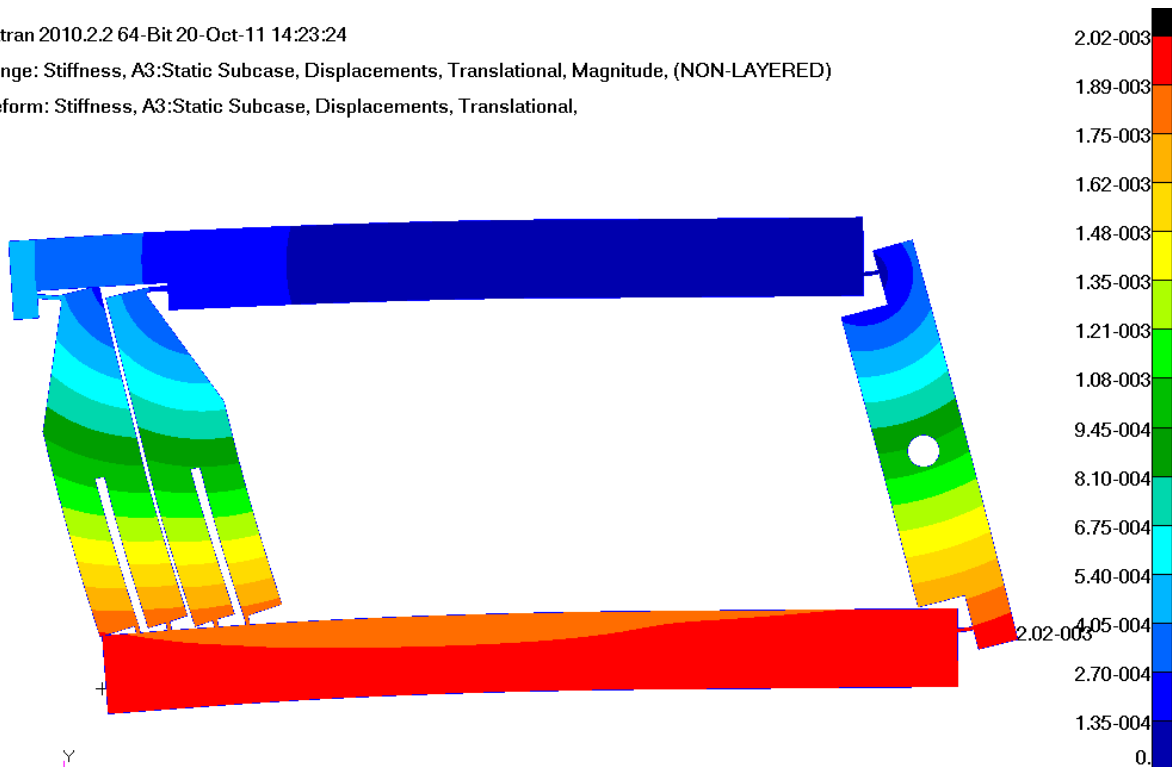


Figure 130: Displacement result due to unit force of only the extender

To calculate the stiffness of the frame without the compliance effects of the piezo stacks included, the piezo stack in the FEA model was replaced with a rigid element. The NASTRAN RBE2 rigid elements were used as shown in Figure 131, and the displacement results are presented in Figure 132. The displacement at the load attachment point was $0.934 \mu\text{m}$.

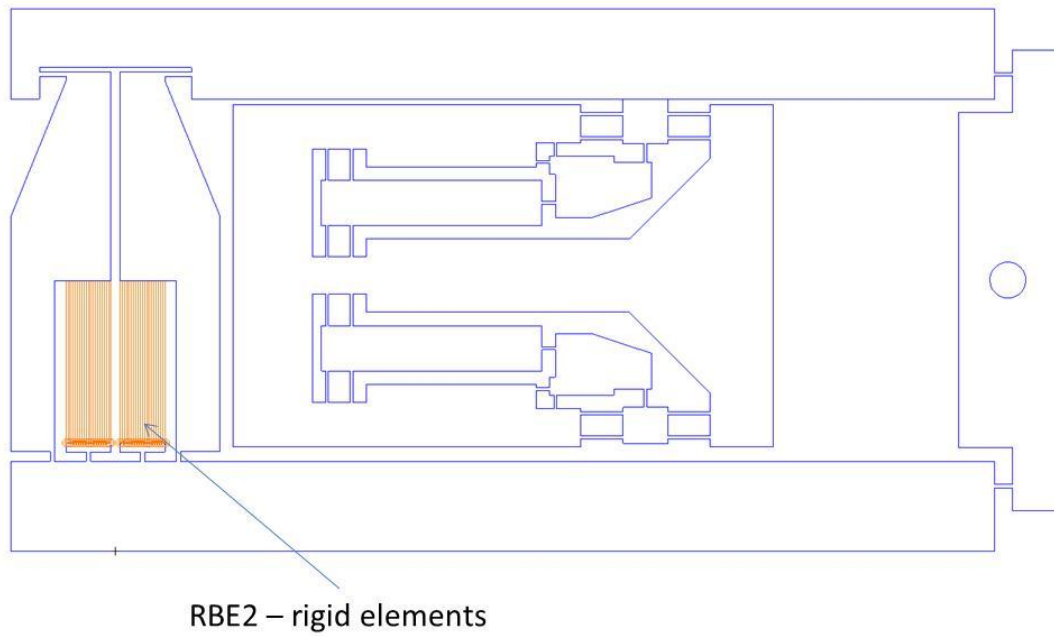


Figure 131: Element representing the piezo stacks is replaced with rigid elements

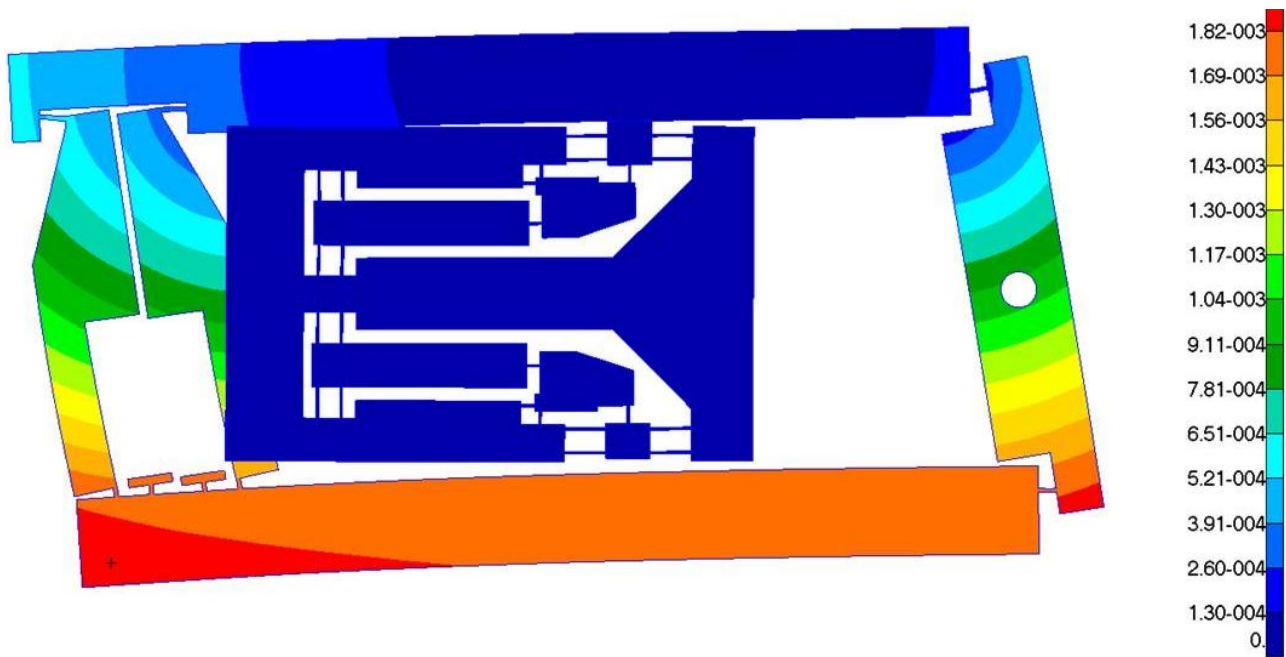


Figure 132: Displacement of the frame with rigid elements due to an applied unit force

The results of the analysis are summarised in Table 17.

Table 17: Summary of FEA results for the beam actuator with force duplicator mechanism

Blocked force (at load attachment point)	103 N
Blocked force (between top and bottom beams)	51.5 N
Free displacement (at load attachment point)	134 μm
Free displacement (between top and bottom beams)	268 μm
Maximum stress (free displacement)	240 MPa
Maximum stress (blocked)	342 MPa
Stiffness in actuating direction (at load attachment point)	768 N/mm
Stiffness in actuating direction with rigid stacks (at load attachment point)	1071 N/mm
Stiffness in actuating direction of the extender only (at load attachment point)	997.3 N/mm
Amplification (beam mechanical)	9.92
Amplification (at load attachment point)	4.96

The first modal mode (in the translation direction) is calculated to be at 335 Hz. Since this IWM was operated below 30 Hz, no dynamic resonant behaviours are envisaged.

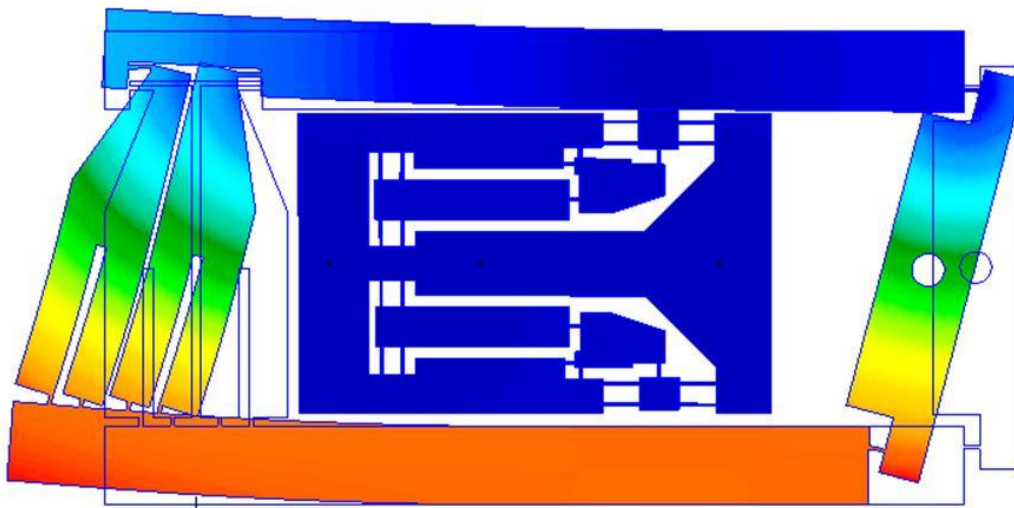


Figure 133: First modal shape at 335 Hz

I. Measurement equipment

The equipment listed below was used during testing.

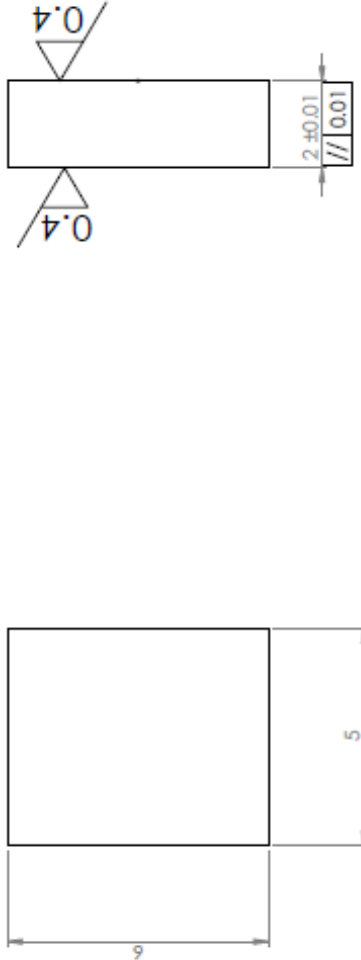
Table 18: Testing equipment

	Description	Serial no.
1	PosiCon.an 150-3 Power Amplifier	11203/1127
2	HP 6235A Triple Output Power Supply	2005A-03677
3	Tektronic TDS 2004B Oscilloscope	C035013
4	A-303 High Voltage Amplifier and Modulator	
5	A-303 High-Voltage Amplifier and Modulator	
6	Polytec PSV-400 Junction Box	0123713
7	Polytec OFV-552 Fiber Vibrometer	6060321
8	Polytec Data Management System	0126938
9	Polytec OFV-5000 Vibrometer Controller	0123679
10	Polytec PSV - I - 400 Scanning Head	0123681
11	National Instrument PCIe – 6259 A/D Data Acquisition board	0x1373CFA
	National Instrument BNC connector box 2110 with cable	CB3177
	National Instrument connector box BNC 2120 with cable	DA958A
12	Dell Optiflex 755 Computer	8D54L3J
13	Fluke Multimeter 117	92430312
14	TTi TG2000 20MHz Function Generator	?
16	HBM Scout 55 Transducer Amplifier	149928012
17	HBM Force Transducer: S9M/1 kN	30854350
18	ZEISS Axiovert 200M Laser Scanning Microscope	

J. Manufacturing drawings for the conventional IWM

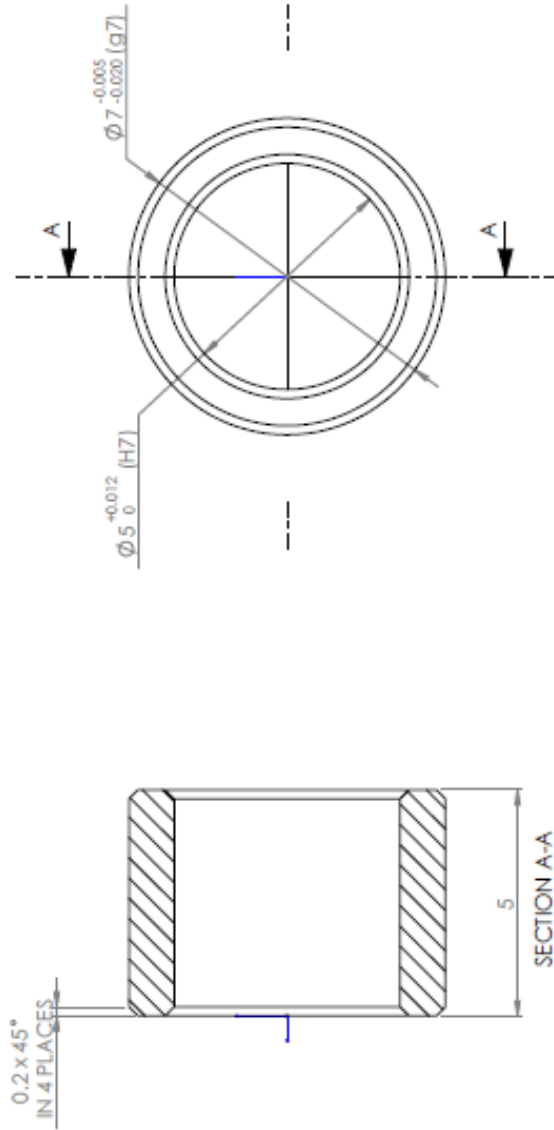
DO NOT SCALE

WHEN IN DOUBT, ASK

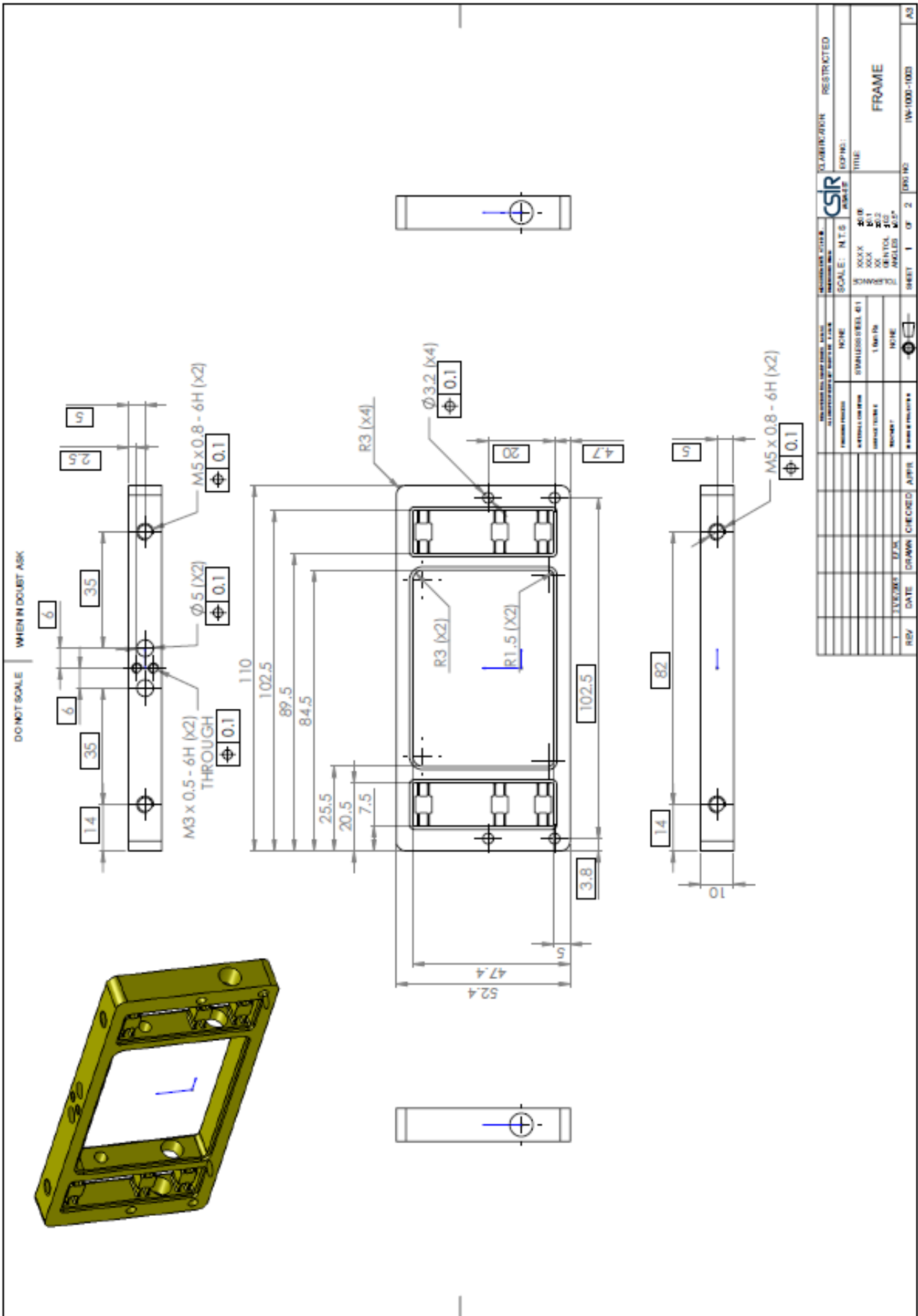


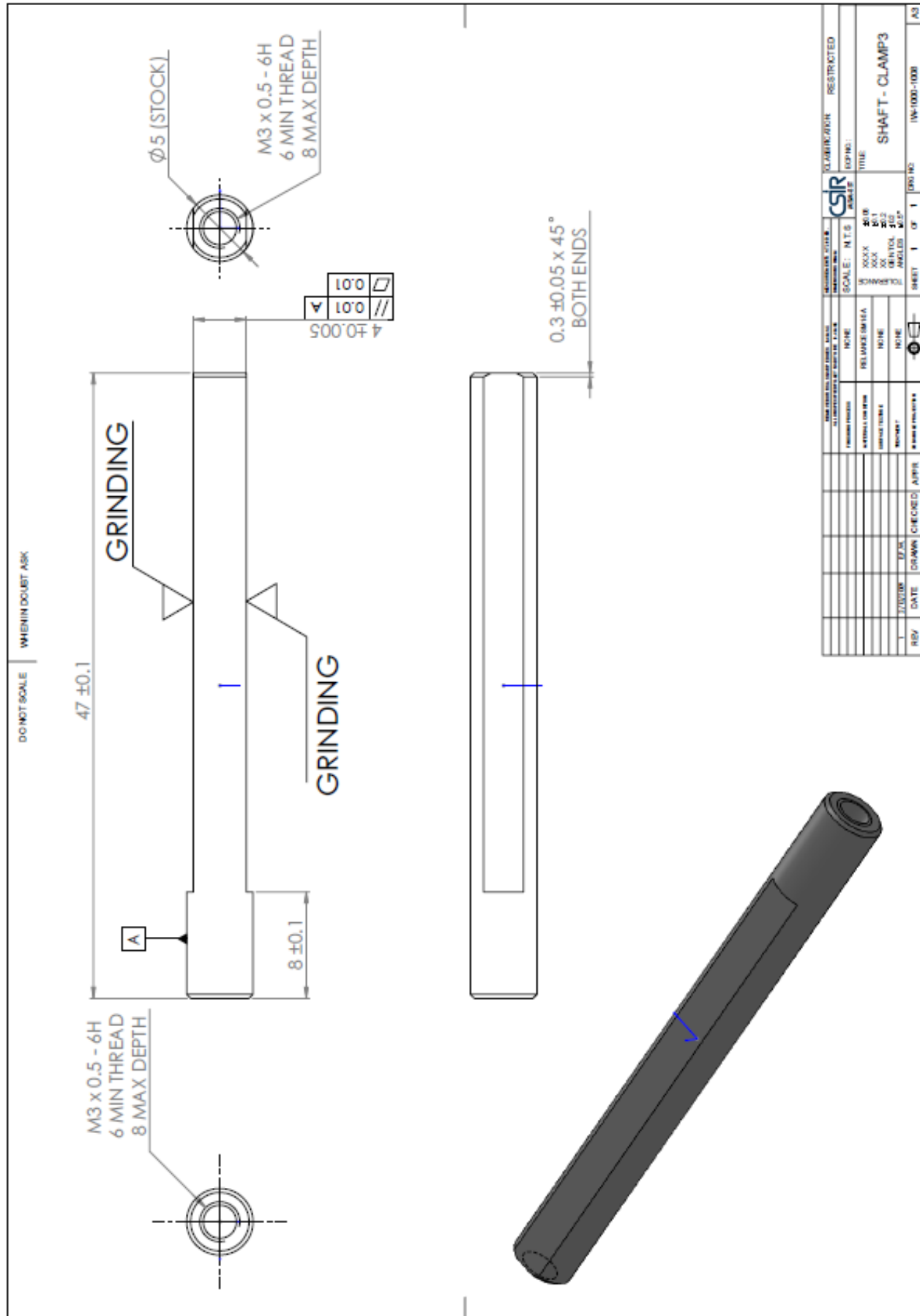
UNIVERSITY OF PRETORIA		UNIVERSITEIT VAN PRETORIA		YUNIBESITHI YA PRETORIA	
SCALE:	N.T.S.	CSIR		CLASSIFICATION:	RESTRICTED
FORMING METHOD:	NONE	DATE:	2008	DRAWN BY:	
ALUMINUM DIECAST		DATE:	2008	TITLE:	SHOE
UNIT OF MEASURE:	MILLIMETERS	DATE:	2008	CLASSIFICATION:	
REVISIONS:		DATE:	2008	PROJECT NO.:	IWM-1000-1000
REVISION:		DATE:	2008	SHEET 1 OF 1	
DATE:		DATE:			

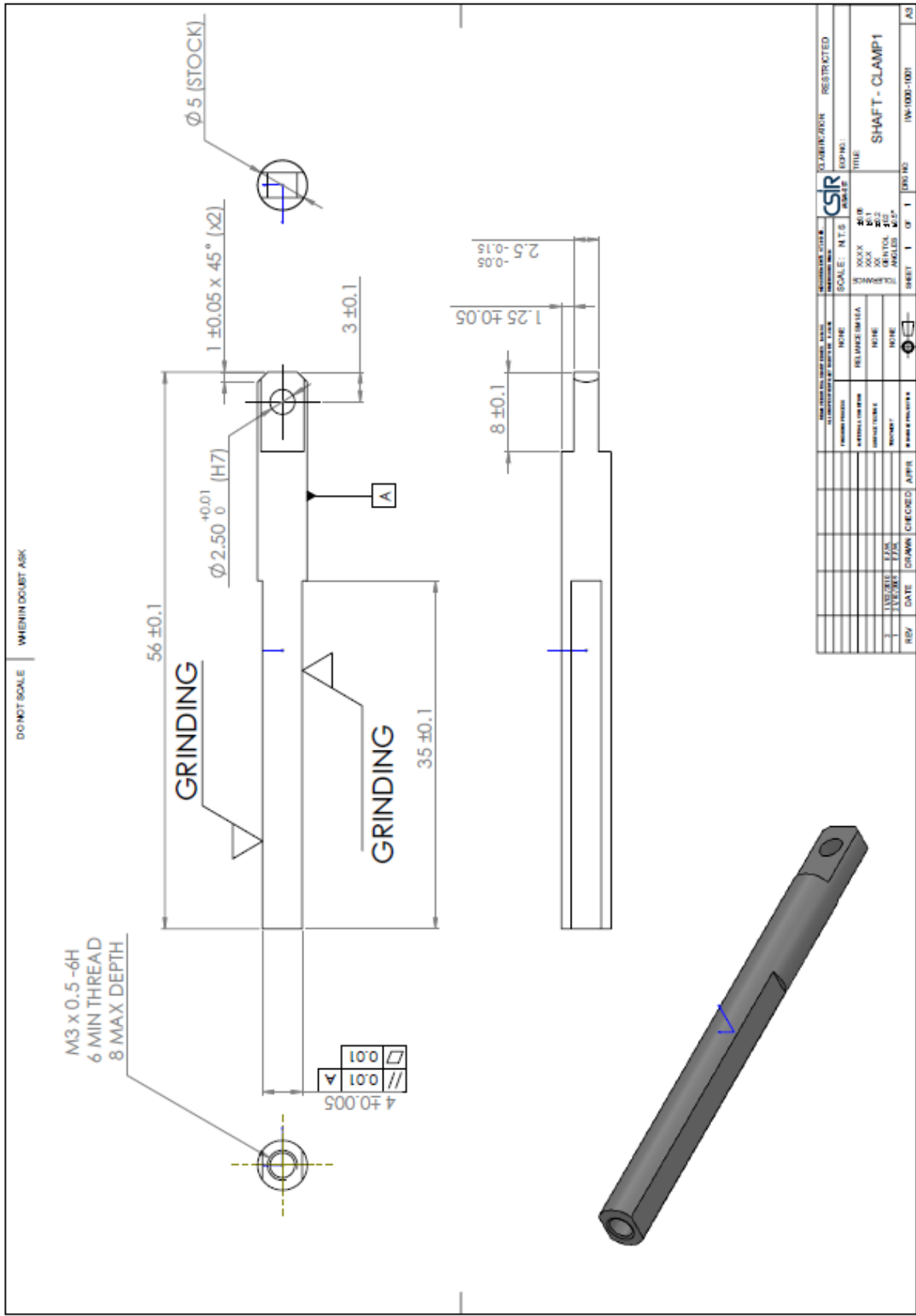
DO NOT SCALE WHEN IN DOUBT ASK

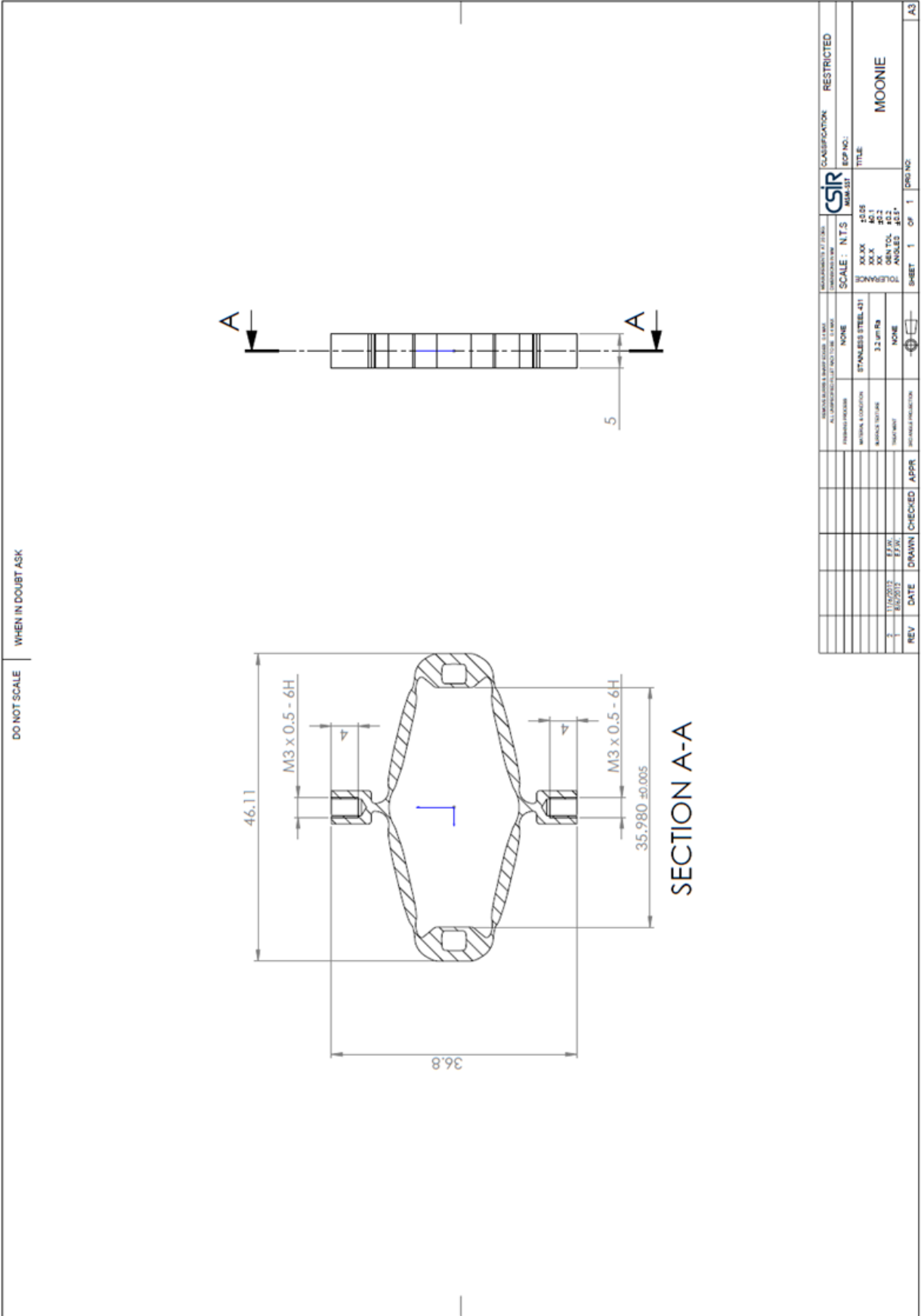



REVISIONS	DATE	BY	CHECKED	APPROVED	REVISIONS	DATE	BY	CHECKED	APPROVED
1									
PROJECT TITLE: BEARING SCALE: M.T.S SWMS/STL: XXX ANGLES: XXX DIMENSIONS: XXX UNIT: MM TOLERANCES: XXX SURFACE FINISH: XXX MATERIAL: XXX					DRAWING NO: W-1005-1007 SHEET: 1 OF 1 TITLE: BEARING STATUS: RESTRICTED				

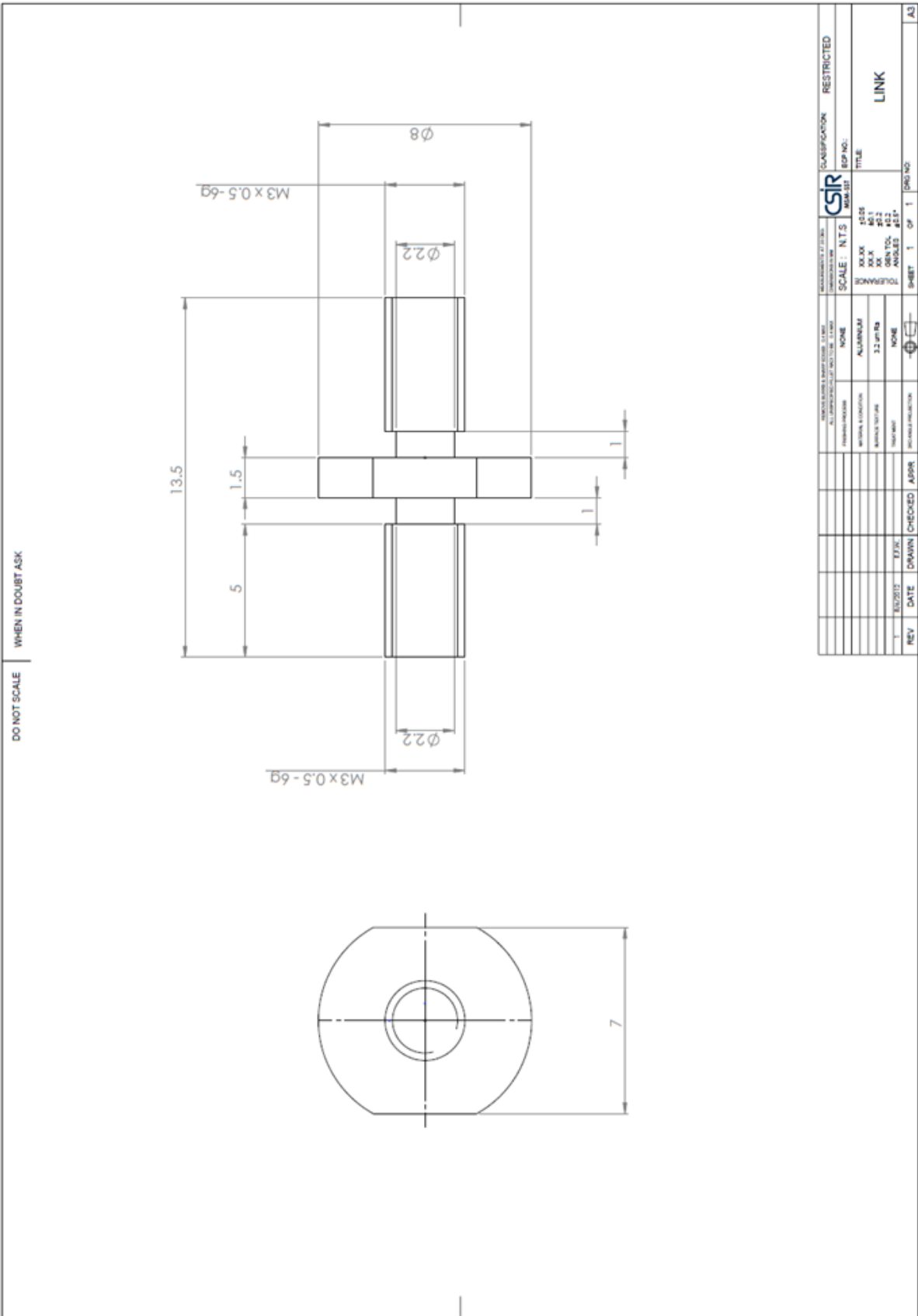




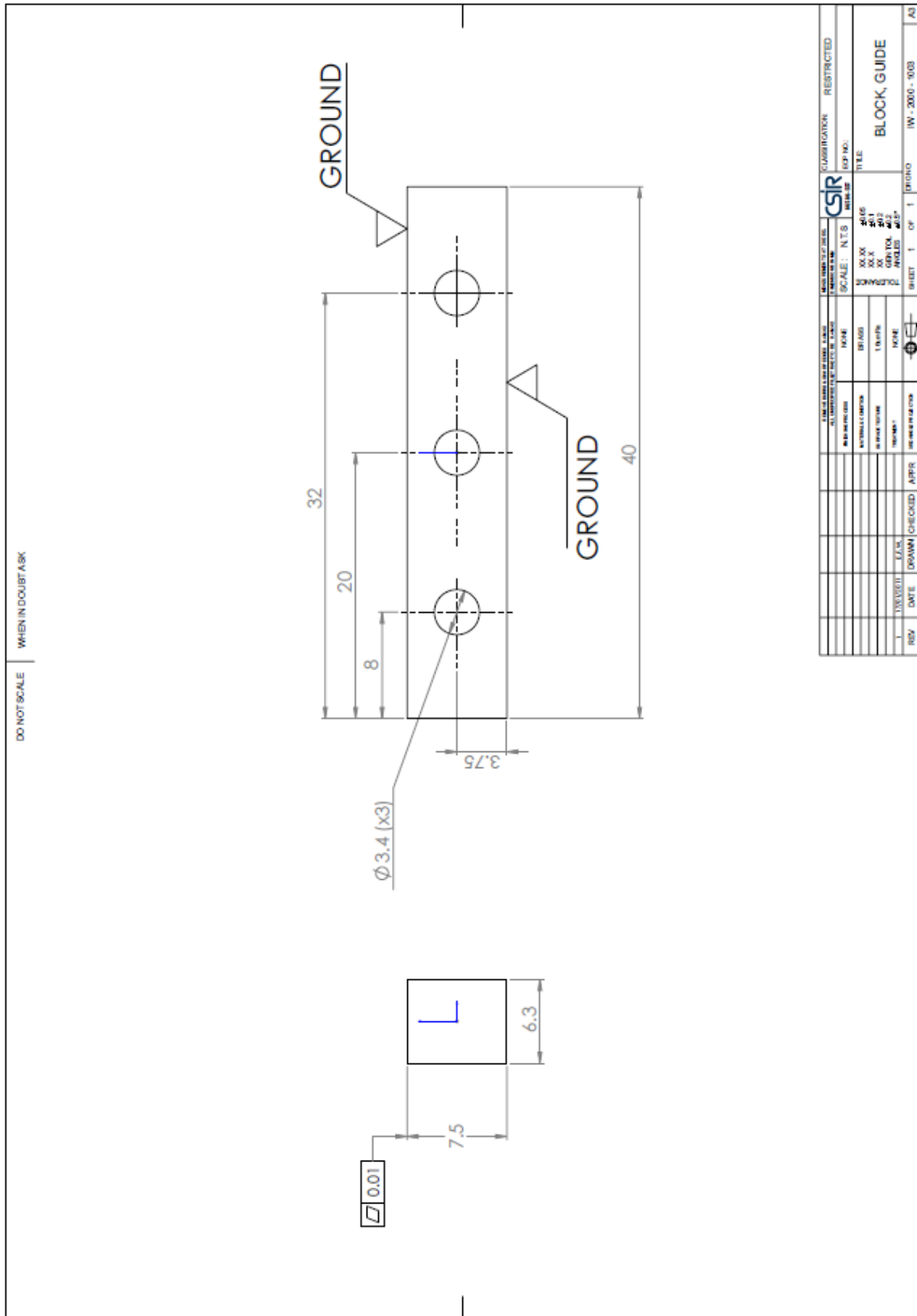


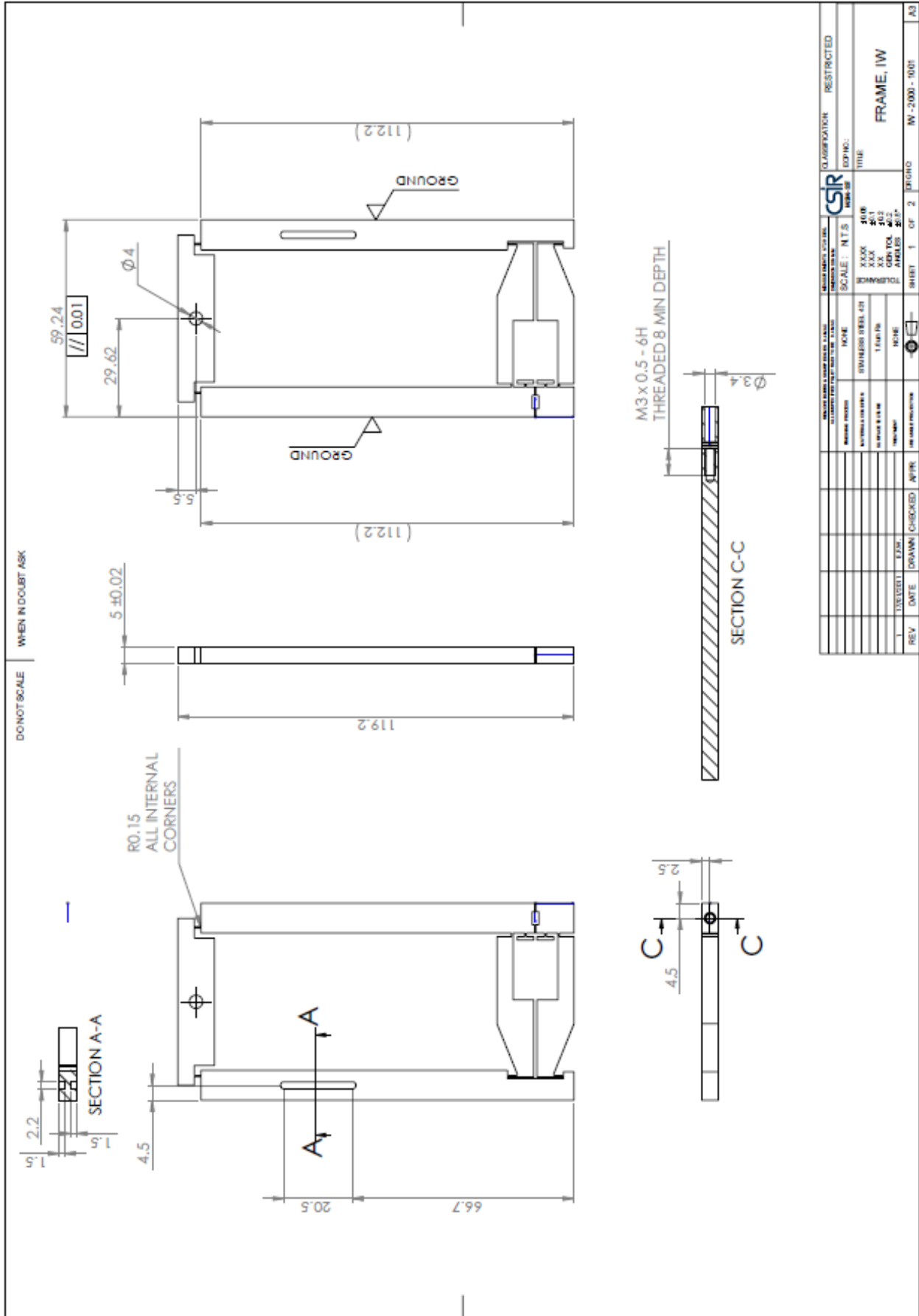


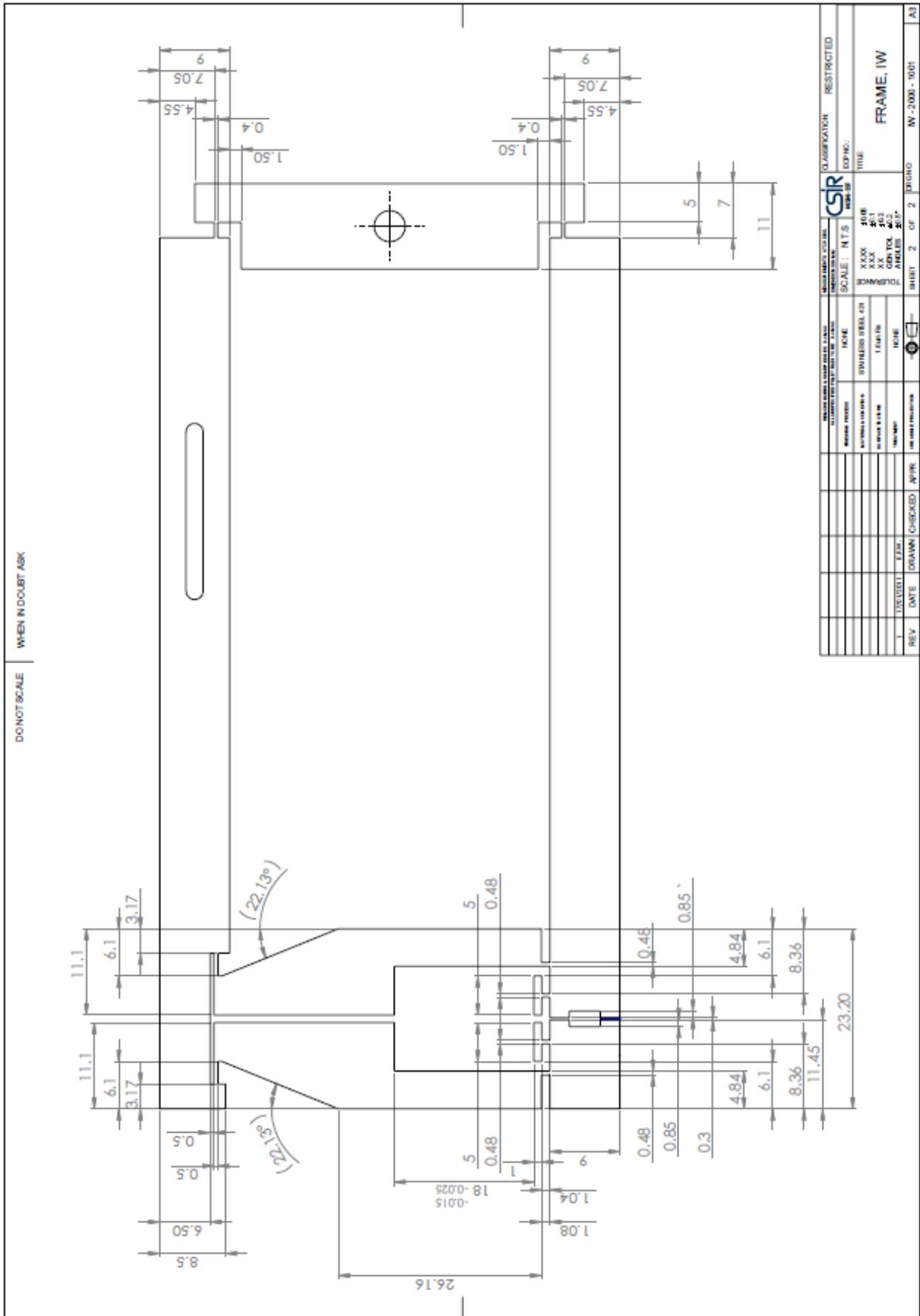
UNIVERSITY OF PRETORIA		CLASSIFICATION: RESTRICTED	
 CSIR MAM-57		EDP NO.: TITLE:	
SCALE: N.T.S		TOLERANCE	
NONE		±0.08	
FINISH PRECISION		±0.1	
MATERIAL SPECIFICATION		±0.2	
STAINLESS STEEL-316		±0.3	
MATERIAL CONDITION		±0.4	
NONE		±0.5	
TREATMENT		±0.6	
NONE		±0.7	
DIMENSIONAL PRECISION		±0.8	
NONE		±0.9	
NONE		±1.0	
NONE		±1.1	
NONE		±1.2	
NONE		±1.3	
NONE		±1.4	
NONE		±1.5	
NONE		±1.6	
NONE		±1.7	
NONE		±1.8	
NONE		±1.9	
NONE		±2.0	
NONE		±2.1	
NONE		±2.2	
NONE		±2.3	
NONE		±2.4	
NONE		±2.5	
NONE		±2.6	
NONE		±2.7	
NONE		±2.8	
NONE		±2.9	
NONE		±3.0	
NONE		±3.1	
NONE		±3.2	
NONE		±3.3	
NONE		±3.4	
NONE		±3.5	
NONE		±3.6	
NONE		±3.7	
NONE		±3.8	
NONE		±3.9	
NONE		±4.0	
NONE		±4.1	
NONE		±4.2	
NONE		±4.3	
NONE		±4.4	
NONE		±4.5	
NONE		±4.6	
NONE		±4.7	
NONE		±4.8	
NONE		±4.9	
NONE		±5.0	
NONE		±5.1	
NONE		±5.2	
NONE		±5.3	
NONE		±5.4	
NONE		±5.5	
NONE		±5.6	
NONE		±5.7	
NONE		±5.8	
NONE		±5.9	
NONE		±6.0	
NONE		±6.1	
NONE		±6.2	
NONE		±6.3	
NONE		±6.4	
NONE		±6.5	
NONE		±6.6	
NONE		±6.7	
NONE		±6.8	
NONE		±6.9	
NONE		±7.0	
NONE		±7.1	
NONE		±7.2	
NONE		±7.3	
NONE		±7.4	
NONE		±7.5	
NONE		±7.6	
NONE		±7.7	
NONE		±7.8	
NONE		±7.9	
NONE		±8.0	
NONE		±8.1	
NONE		±8.2	
NONE		±8.3	
NONE		±8.4	
NONE		±8.5	
NONE		±8.6	
NONE		±8.7	
NONE		±8.8	
NONE		±8.9	
NONE		±9.0	
NONE		±9.1	
NONE		±9.2	
NONE		±9.3	
NONE		±9.4	
NONE		±9.5	
NONE		±9.6	
NONE		±9.7	
NONE		±9.8	
NONE		±9.9	
NONE		±10.0	
NONE		±10.1	
NONE		±10.2	
NONE		±10.3	
NONE		±10.4	
NONE		±10.5	
NONE		±10.6	
NONE		±10.7	
NONE		±10.8	
NONE		±10.9	
NONE		±11.0	
NONE		±11.1	
NONE		±11.2	
NONE		±11.3	
NONE		±11.4	
NONE		±11.5	
NONE		±11.6	
NONE		±11.7	
NONE		±11.8	
NONE		±11.9	
NONE		±12.0	
NONE		±12.1	
NONE		±12.2	
NONE		±12.3	
NONE		±12.4	
NONE		±12.5	
NONE		±12.6	
NONE		±12.7	
NONE		±12.8	
NONE		±12.9	
NONE		±13.0	
NONE		±13.1	
NONE		±13.2	
NONE		±13.3	
NONE		±13.4	
NONE		±13.5	
NONE		±13.6	
NONE		±13.7	
NONE		±13.8	
NONE		±13.9	
NONE		±14.0	
NONE		±14.1	
NONE		±14.2	
NONE		±14.3	
NONE		±14.4	
NONE		±14.5	
NONE		±14.6	
NONE		±14.7	
NONE		±14.8	
NONE		±14.9	
NONE		±15.0	
NONE		±15.1	
NONE		±15.2	
NONE		±15.3	
NONE		±15.4	
NONE		±15.5	
NONE		±15.6	
NONE		±15.7	
NONE		±15.8	
NONE		±15.9	
NONE		±16.0	
NONE		±16.1	
NONE		±16.2	
NONE		±16.3	
NONE		±16.4	
NONE		±16.5	
NONE		±16.6	
NONE		±16.7	
NONE		±16.8	
NONE		±16.9	
NONE		±17.0	
NONE		±17.1	
NONE		±17.2	
NONE		±17.3	
NONE		±17.4	
NONE		±17.5	
NONE		±17.6	
NONE		±17.7	
NONE		±17.8	
NONE		±17.9	
NONE		±18.0	
NONE		±18.1	
NONE		±18.2	
NONE		±18.3	
NONE		±18.4	
NONE		±18.5	
NONE		±18.6	
NONE		±18.7	
NONE		±18.8	
NONE		±18.9	
NONE		±19.0	
NONE		±19.1	
NONE		±19.2	
NONE		±19.3	
NONE		±19.4	
NONE		±19.5	
NONE		±19.6	
NONE		±19.7	
NONE		±19.8	
NONE		±19.9	
NONE		±20.0	
NONE		±20.1	
NONE		±20.2	
NONE		±20.3	
NONE		±20.4	
NONE		±20.5	
NONE		±20.6	
NONE		±20.7	
NONE		±20.8	
NONE		±20.9	
NONE		±21.0	
NONE		±21.1	
NONE		±21.2	
NONE		±21.3	
NONE		±21.4	
NONE		±21.5	
NONE		±21.6	
NONE		±21.7	
NONE		±21.8	
NONE		±21.9	
NONE		±22.0	
NONE		±22.1	
NONE		±22.2	
NONE		±22.3	
NONE		±22.4	
NONE		±22.5	
NONE		±22.6	
NONE		±22.7	
NONE		±22.8	
NONE		±22.9	
NONE		±23.0	
NONE		±23.1	
NONE		±23.2	
NONE		±23.3	
NONE		±23.4	
NONE		±23.5	
NONE		±23.6	
NONE		±23.7	
NONE		±23.8	
NONE		±23.9	
NONE		±24.0	
NONE		±24.1	
NONE		±24.2	
NONE		±24.3	
NONE		±24.4	
NONE		±24.5	
NONE		±24.6	
NONE		±24.7	
NONE		±24.8	
NONE		±24.9	
NONE		±25.0	
NONE		±25.1	
NONE		±25.2	
NONE		±25.3	
NONE		±25.4	
NONE		±25.5	
NONE		±25.6	
NONE		±25.7	
NONE		±25.8	
NONE		±25.9	
NONE		±26.0	
NONE		±26.1	
NONE		±26.2	
NONE			

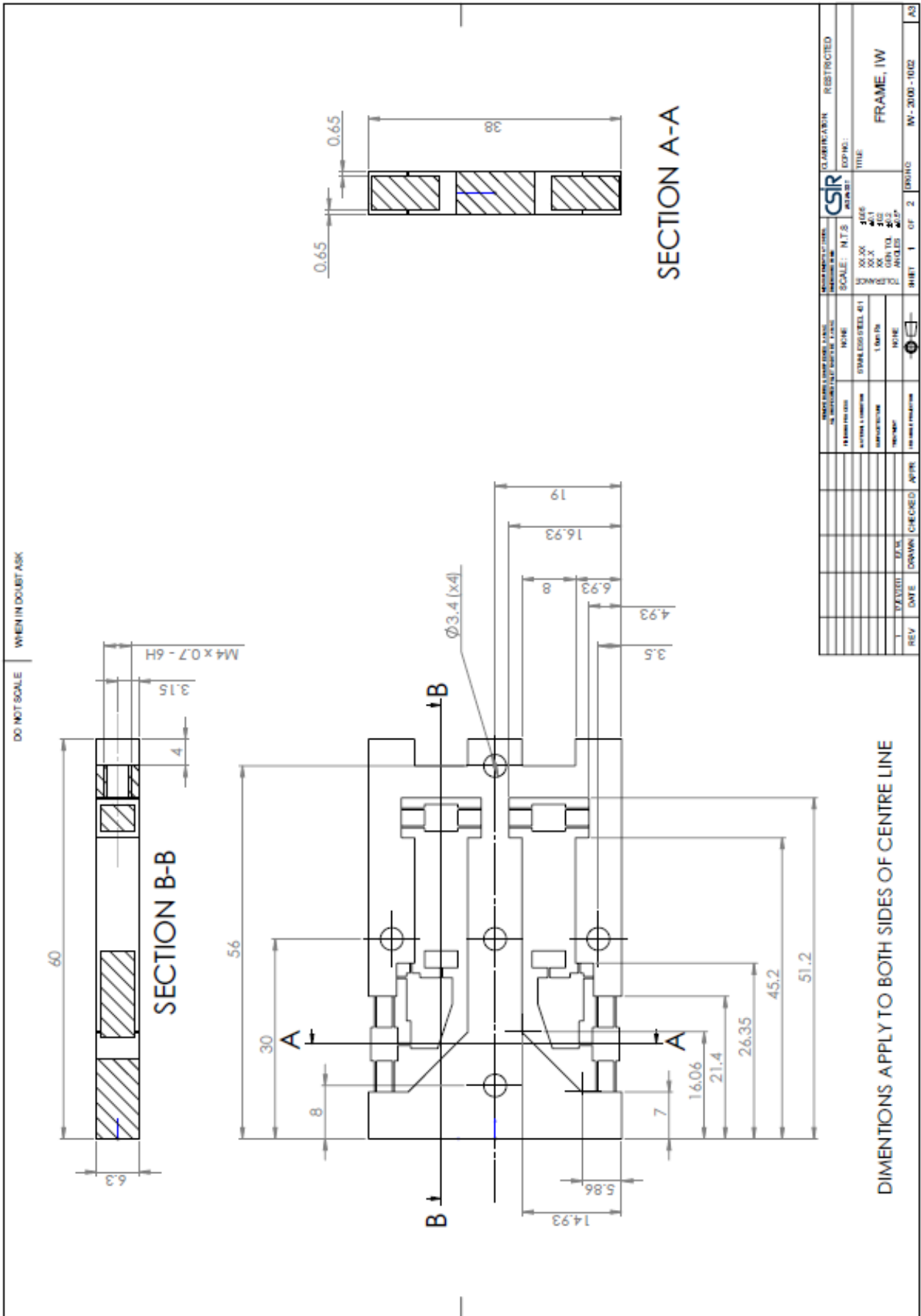


K. Manufacturing drawings for the IWM with force duplicator

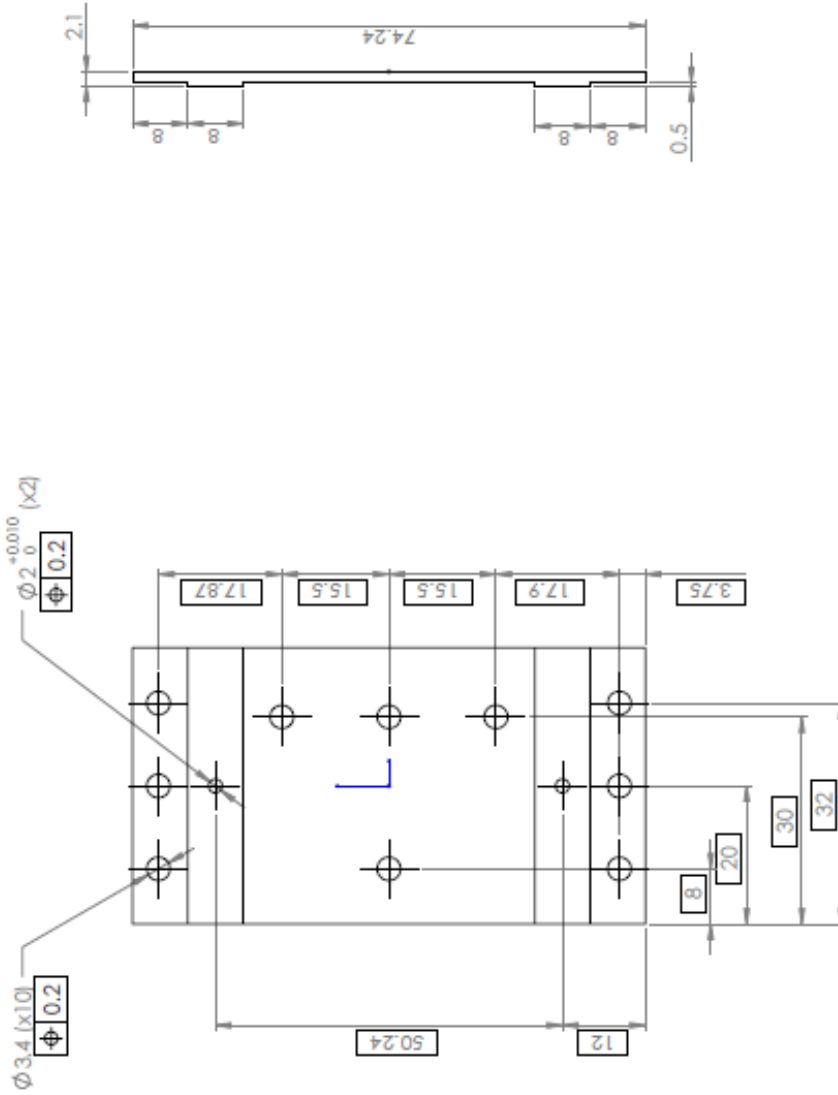








DO NOT SCALE WHEN IN DOUBT ASK



REVISIONS	DATE	DRAWN	CHECKED	APPR.	REV	DATE	DRAWN	CHECKED	APPR.
1									
PROJECT NAME: CLIENT: DRAWING NO: SCALE: N.T.S. SHEET NO: TITLE:					CLASSIFICATION: RESTRICTED DRAWING NO: TITLE:				
MATERIAL: FINISH: TOLERANCES: DIMENSIONS: SURFACE FINISH: HOLE FINISH:					CSIR 2008 2008 2008 2008 2008 2008				
SHEET 1 OF 1					DRAWING NO: W-2000-1004 TITLE: PLATE				

L. UAV outline

